Doctoral Dissertations

Graduate School

5-2021

Numerical Studies of Superconductivity and Charge-Density-Waves: Progress on the 2D Holstein Model and a Superconductor-Metal Bilayer

Philip M. Dee
The University of Tennessee, Knoxville, pdee@vols.utk.edu

Follow this and additional works at: https://trace.tennessee.edu/utk_graddiss

Part of the Condensed Matter Physics Commons

To the Graduate Council:

I am submitting herewith a dissertation written by Philip M. Dee entitled "Numerical Studies of Superconductivity and Charge-Density-Waves: Progress on the 2D Holstein Model and a Superconductor-Metal Bilayer." I have examined the final electronic copy of this dissertation for form and content and recommend that it be accepted in partial fulfillment of the requirements for the degree of Doctor of Philosophy, with a major in Physics.

Steven S. Johnston, Major Professor

We have read this dissertation and recommend its acceptance:

Takeshi Egami, Adriana Moreo, Adolfo G. Eguiluz

Accepted for the Council:

Dixie L. Thompson

Vice Provost and Dean of the Graduate School

(Original signatures are on file with official student records.)

Numerical Studies of Superconductivity and Charge-Density-Waves: Progress on the 2D Holstein Model and a Superconductor-Metal Bilayer

A Dissertation Presented for the

Doctor of Philosophy

Degree

The University of Tennessee, Knoxville

Philip M. Dee

May 2021

To my wife, Hannah

Acknowledgments

I do not envy those graduate students who began their research in 2020. After a full year of communicating with collaborators via digital means only, it is becoming clear that science is much more satisfying in the company of others. The eccentric hive mind that is an office filled with Ph.D. students and postdocs is a powerful motivator and catalyst for ideas. I have so many people to thank for enriching and supporting my years at UT, and I cannot possibly name them all.

First, I express my deepest gratitude to my Ph.D. advisor Prof. Steve Johnston. Steve showed me what it takes to become a productive scientist and an effective communicator, as well as what it takes to be a reliable and understanding group leader. He was actually the first faculty I met on my visit to UT in 2014. It was only a couple of years later that I returned to his office to discuss joining his group, and it was the best decision I could have made. Steve's extensive knowledge of theory and experiment really showed us how to become well-rounded theorists, and I am grateful for his mentorship.

Early in my Ph.D. research, I was but a helpless know-nothing that couldn't write code to save my life, but I got up to speed thanks in part to Yan Wang, Ken Nakatsukasa, and Shaozhi Li. The group office was often abuzz with hotly-contested debate, typically instigated by Umesh. I'd be lying if I said I didn't miss it. It was a pleasure to share a space with the Eguiluz group, who added some ab initio spice to our lives. Of them, I would like to acknowledge Casey Eichstaedt, the first graduate student I really got to know. From our exhaustive quantum mechanics whiteboard sessions to the occasional rejuvenating "Battlefront-and-skate-day" to musings about pie-in-the-sky physics, we really made the most of graduate school. Of the current group, I thank Jinu, Gus, and Trevor for making

me feel old but not obsolete. The weekly walk-and-talks at Lakeshore Park with Jinu really helped to stave off the isolating effects of quarantine.

I had the fortune of spending over a year at ORNL until the pandemic sent us all home. For this experience, I am most indebted to Thomas Maier. Thomas is a first-rate physicist, and I have learned much from him. By extension, I should thank the current and former members of the SciDAC collaboration for helping me get my footing with the DCA++ and Summit. I would like to acknowledge Peizhi Mai, Seher Karakuzu, Peter Doak, Arghya Chatterjee, Urs Hähner, Giovanni Balduzzi, Ying-Wai Li, and Doug Scalapino for the wealth of insight. Peizhi and Seher were my closest companions at the lab, and I am grateful we all keep in touch. I will greatly miss our lunches at SNS with Thomas, Tom, Peter, Paul, Miguel, and the visitors such as Jenny and Shinbali that kept things fresh.

I would be remiss if I didn't acknowledge a few of my other collaborators. My foray into machine learning was much improved by the opportunity to work with Ehsan Khatami. Ehsan's early source code really helped move the needle in constructing the neural networks from scratch. Early and recent collaborations with the members of Professor Devereaux's group at Standford, such as Ben Nosarzewski and Edwin Huang, and Ilya Esterlis, helped to form my current thoughts on the Holstein problem. Jenny Coulter so generously lent her DFT expertise to support our model machinations of nonlinear electron-phonon coupling. Lastly, I would like to thank Kevin Kleiner and Isaac Ownby, two talented undergrads who learned to swim in the deep end.

During the second and third year of my Ph.D., I was privileged enough to work with the PHYS 136 and 137 Honors students. I thank Dr. Jim Parks and Dr. Christine Cheney-Parks for giving me the opportunity to teach freely. I only hope the students learned more from me than I did from them.

Life in physics was made more enjoyable by many friends and family members I spent my "free time" with. To Nate, Joe, Sean, and Bobby, thanks for the many meandering cosmic psych-rock jam sessions we accumulated over the years. Everyone needs a purely creative outlet, and that was mine. Special thanks to my family in Ohio and elsewhere for all the encouragement they provided us from afar. To my parents, I could not have asked

for a stronger backbone of support and encouragement. Not many grad students get lucky enough to have family less than a half-hour drive away.

My wife and I moved to Knoxville less than a week after our wedding day. So much of our life has changed since that time, but Hannah's unwavering love and support has not. I may spend the rest of my life paying off the debt of gratitude I owe her for keeping us afloat. I am excited for the next chapter of life with Hannah and our cats Muon, Pion, and Norbert, as well as our daughter, who I can't wait to meet.

Abstract

The problem of superconductivity has been central in many areas of condensed matter physics for over 100 years. Despite this long history, there is still no theory capable of describing both conventional and unconventional superconductors. Recent experimental observations such as the dilute superconductivity in $SrTiO_3$ and near room-temperature superconductivity in hydride compounds under extreme pressure have renewed interest in electron-phonon systems. Adding to this is evidence that electron-phonon coupling may play a supporting role in unconventional systems like the cuprates and monolayer FeSe on $SrTiO_3$.

One way to make sense of these observations is to construct simple models that capture the essential physics. Among the models with electron-phonon interactions, the simplest and most studied is the two-dimensional Holstein model. It describes a single band of electrons that hop between sites on a square lattice and interact with atomic oscillators by coupling linearly to their displacements. This model gives rise to superconductivity and charge-density-wave order spanning different regions of doping. Surprisingly, even this model is not entirely understood.

First, we present a comprehensive study of the Holstein model phase diagram using self-consistent many-body perturbation theory. We then discuss one potential avenue for accelerating non-perturbative quantum Monte Carlo simulations of electron-phonon models using artificial neural networks. Following these topics, we wrap up the electron-phonon-related part by discussing the importance of nonlinear interaction terms and moving beyond the Holstein model.

The last problem of this dissertation revisits a proposal by Steve Kivelson. He hypothesized and later showed that coupling a superconductor with a large pairing scale but low phase stiffness to a metal raises the transition temperature (T_c). Expanding on previous

work, we studied a more general case with a 2D negative-U Hubbard model coupled with a metallic layer via single-particle tunneling. Here, we use the dynamical cluster approximation to estimate T_c, finding it is maximal for finite tunneling values, thereby confirming Kivelson's hypothesis in the general case. Collectively, the results in this dissertation shed new light on superconductivity in conventional systems and demonstrate a need to incorporate more aspects of real materials into models.

Table of Contents

List of Tables

List of Figures

Chapter 1

Introduction

This dissertation covers four published projects completed during my Ph.D. research. Three of these papers are concerned with simple models and methods for studying electron-phonon (e-ph) coupled systems [1, 2, 3], and the other revisits a model for interface enhanced superconductivity [4]. A common thread through all of these works aims to find updated perspectives on older problems in superconductivity. With modern theoretical and experimental tools, we now have access to more of the problem space of e-ph mediated superconductivity and associated phenomena. This chapter aims to explain the motivation by providing a broad historical and contemporary context. A large part of this motivation comes from a renewed interest in the e-ph problem in conventional and unconventional superconductivity, especially in the dilute limit [5]. As will be explained, there are good reasons not to ignore the role of e-ph interactions in strongly correlated systems. While this is an essential direction of study, I will argue the utility of revisiting basic models without strong correlations. Lastly, the discussion will turn to layered superconducting systems.

1.1 Superconductivity

Building a comprehensive theoretical framework of superconductivity is a central issue in condensed matter physics. At the time of writing, 110 years have passed since the first experiments showing vanishing resistivity at low temperature in simple elemental metals. Since then, the field has advanced considerably through several breakthroughs both in

theory and experiment, but much remains unsolved. This last fact is especially remarkable when one considers the multiple generations of researchers devoted to this effort. However, the continued interest surrounding superconductivity is unique in that its high application potential is well known to the world. In particular, any deep understanding that leads to sustained room-temperature superconductivity under ambient pressure is among the highest goals in condensed matter physics. Such a development would revolutionize power delivery around the world and increase innovation potential for emerging quantum technologies.

Recently, room-temperature superconductivity prevailed in a carbonaceous sulfur-hydride compound under extremely high pressure (267 GPa) [6]. This milestone caps a string of increasingly ambitious high-pressure experiments in hydrogen-rich compounds with transition temperatures above 100-200 K. The light elements within these materials suggest that conventional e-ph interactions play a significant role in the resulting superconductivity, but the mechanism is still unconfirmed. That elements like hydrogen could find themselves at the core of a high-temperature superconductor was originally suggested by Neil Ashcroft [7]. Given the high-pressures required to boost the critical temperature T_c in these systems, they are unlikely to see any widespread usage in modern technology. This caveat raises several questions about the role these hydride systems play in the quest for high-T_c under ambient conditions. On the one hand, they show that room temperature superconductivity is accessible but in very contrived and impractical environments. On the other hand, a detailed understanding of these systems under high-pressure may lead to new insights for systems under one atmosphere of pressure.

It is not just the unusually high pressures that allow these hydride systems to stand out. These materials may be extreme examples of conventional superconductivity, the latter of which is typically regarded as understood. Over the past few decades, research has focused more on unconventional superconductors and other exotic phenomena. It was not long after the introduction of Bardeen, Cooper, and Schrieffer's (BCS) theory of superconductivity [8] that alternative pairing symmetries became a topic of study. Work done on superfluid ^{3}He [9, 10, 11, 12] introduced Cooper pairs with anisotropic pairing and spin-triplet states, in contrast to the conventional picture of singlet s-wave pairs. Several groups [13, 14, 15, 16, 9, 10] postulated this anisotropic pairing simultaneously and used bare

nuclear interactions in the BCS theory framework. Many thought that the leading pairing channel was the $l = 2$, d-wave channel. However, in 1972, nuclear magnetic resonance (NMR) experiments revealed superfluidity in ^{3}He with a T_c of 2.65 mK. Anomalies in the NMR response revealed a high-temperature "A phase" and low-temperature "B phase" characterized by a vanishing magnetic response. Careful interpretation of these NMR measurements led Anthony Leggett [17, 18, 19] to show that the A phase possessed a p-wave pair symmetry, partially vindicating earlier theories about anisotropic symmetry but correcting the original d-wave hypothesis.

Superfluid ^{3}He inspired much of the research around higher angular momentum pairing channels, but it was not the only unconventional system responsible for a paradigm shift. A sizable fraction of today's research in unconventional superconductors is concerned with copper-oxide materials (cuprates), spearheaded by the Nobel prize-winning discovery of superconductivity in $La_{2-x}Ba_xCuO_4$ at $T_c = 30$ K by Bednorz and Müller in 1986 [20]. Their experiments ushered in a new era of "high-T_c" superconductivity, where additional cuprate compounds with critical temperatures higher than that of liquid nitrogen ($T = 77$ K) and liquid Argon ($T = 87$ K) were eventually discovered (e.g., YBCO $T_c = 93$ K [21], BSCCO $T_c = 91 - 105$ K [22, 23], triple-layer $HgBa_2Ca_2Cu_3O_{8+\delta}$ $T_c = 93$ K [24] at ambient pressure & $T_c = 164$ K [25] at 31 GPa).

While the cuprates currently boast some of the highest transition temperatures of any superconductor under ambient conditions, they are far from the only unconventional superconducting materials. Iron-based superconductors [26, 27, 28, 29, 30], heavy fermion superconductors [31, 32], organic superconductors [33, 34], nickelates [35, 36], twisted-bilayer graphene [37, 38], and several other systems are considered unconventional [39]. These superconductors elude the conventional description of BCS theory and its extensions. In many of these systems, a sole e-ph pairing mechanism fails to describe what is observed in experiments, leading many to suspect other mechanisms like electron-electron repulsion and spin-fluctuations. However, it is still possible that e-ph interactions play a supporting role, even if not the main one.

1.1.1 Is electron-phonon coupling important in unconventional superconductors?

One such scenario is the ongoing effort to understand the high-T_c of monolayer FeSe on an $SrTiO_3$ (STO) substrate. These systems can host superconductivity as high as 55-75 K [40, 41, 42], which is far greater than the critical temperature of bulk FeSe $T_c \sim 8$ K [43]. Recently, some have focused on the roles of interfacial e-ph coupling and spin-fluctuations on the superconducting transition [44, 45, 46, 47]. The interlayer e-ph coupling occurs between FeSe electrons and optical oxygen phonon modes in the STO substrate. It is important to note that this e-ph interaction is not isotropic and is biased toward forward (small-$\mathbf{q}$) scattering [44]. This forward-peaked interaction is known to mediate pairing in anisotropic pairing channels such as those with d-wave symmetry [48].

The role of e-ph coupling in cuprates is also an open question. Like the iron-based superconductors, strong electronic correlations make theoretical studies of the cuprates difficult. The phononic and electronic degrees of freedom in these systems are highly entangled, giving rise to a strongly correlated electron liquid. While electron-electron interactions appear to be primarily responsible for superconductivity in cuprates, other pair-driving excitations may act to enhance T_c further [49, 50, 51, 52, 53, 54]. There is good reason to consider the role of lattice vibrations in particular. For one, it is possible to induce transient superconductivity by optical pumping of apical oxygen phonons [55, 56, 57]. These mid-infrared pulses can drive vibrations into the anharmonic regime and increase T_c. This subfield of "nonlinear phononics" has been expanded to the idea that such dynamics could lead to enhanced e-ph coupling [58, 59]. Second, there are intense modulations in the low-energy acoustic and high-energy Cu-O bond stretching phonon branch spectrum around the CDW wave vector [60, 61].

Electron-phonon coupling in the cuprates is not weak and cannot be dismissed easily by such arguments. The relevant phonons are higher energy optical breathing and breathing modes, and the oscillations live in the copper-oxygen planes. These vibrations are associated with copper-oxygen bond-stretching, apical oxygen phonons, and oxygen B_{1g} buckling phonons [62]. These phonons may contribute to the d-wave superconductivity.

Despite these indications of phononic contributions, the cuprates and other strongly correlated materials draw little resemblance to traditional metals [63]. They are poorly conductive at room temperature and become robust insulating antiferromagnets through chemical composition shifts. This magnetism arises from significant repulsive magnetic interactions at the microscopic level, contrasting with the BCS theory's attractive interaction. At temperatures well above T_c, the measured conductivity in cuprates has an unusual frequency and temperature dependence. This behavior has granted them the classification of a "strange metal". Lastly, there is some semblance of gap formation at temperatures above T_c, characterized by suppression in the electronic density of states (DOS) near the Fermi level. Oddly, this pseudogap regime appears without any (apparent) occurrence of broken symmetry. One possible explanation for the pseudogap regime is that it hosts pre-formed electron pairs without long-range phase coherence, an idea we revisit in the motivation for Chapter 5.

All this is to say that very few, if anyone, believes that conventional models of superconductivity should describe such materials. After all, the theoretical workhorse for capturing some qualitative physics featured in the cuprates is the single-band Hubbard model [64, 65, 66], which includes electron hopping and a highly-local repulsive electron-electron interaction, omitting lattice dynamics entirely. Many qualitative features of the cuprate phase diagram also appear in various parts of the 2D Hubbard model phase diagram. For this and other reasons, simple models like the Hubbard model are of high interest to theorists. They provide a tunable platform to study how the microscopic picture manifests ordered phases and other emergent phenomena on a macroscopic scale. However, our principal interest here is *not* the repulsive Hubbard model or any related models with magnetic correlations.

1.1.2 Layered superconductors

Both the cuprates and pnictides offer another avenue of inquiry regarding the role of material layers and high-temperature superconductivity. In the previous section, we mentioned the monolayer FeSe on an STO substrate with an impressively high-T_c compared with bulk FeSe. Adding more layers of FeSe lowers T_c toward its bulk value [67, 68, 69], suggesting the

essential physics occurs at the interface. One can find a maximal T_c in the cuprates with some optimal number of copper-oxide layers (usually 3) [70]. This observation raises several questions about the interface's underlying phenomenology between two compounds and the longer-range correlations formed over several layers.

One of these questions, inspired by the cuprates, asks if it is possible to raise T_c in a strongly phase fluctuating superconductor by coupling it to a metal [71]. In the underdoped cuprates, superconducting pairs form at much higher temperatures than the actual T_c, where long-range phase coherence finally succeeds. Contrast this with simple metallic superconductors where pairing and phase coherence happen nearly simultaneously. Of course, unlike metals, the cuprates host strong correlations and large thermal phase fluctuations [72]. In the underdoped regime where the pseudogap exists for temperatures above the critical temperature, fluctuations of the pair-field are manifest in calculations of the superconducting susceptibility [73]. This system has a large pairing scale characterized by the superconducting gap but a low phase stiffness. The metal has precisely the opposite problem. It has a high phase stiffness but a small pairing scale. By growing a metallic film atop the correlated superconductor, could we significantly raise T_c? This question was posed by Steven Kivelson [71] and is the primary concern of Chapter 5, where we use state-of-the-art numerics to access a parameter regime seldom studied for this problem.

1.2 Models

The study of model Hamiltonians offers a valuable means for the understanding of superconductivity and strongly correlated phenomena. They can be material-specific models that use experimental or first principles-based estimates of the bare parameters, or they can be more general and simplistic. The former procedure can result in realistic models, which may be too challenging to study unless the calculation makes significant compromises, such as downfolding the Hilbert space to a subspace with fewer bands and highly local interactions. Those downfolded models look more like the toy models people study generally, but the parameters are specially tuned. The toy models are valuable because they provide much-needed intuition for the interplay between microscopic degrees of freedom and how that

gives rise to the emergent macroscopic state. However, even the most popular models are not always fully mapped out and understood.

This fact brings us to a key motivation of this dissertation. While the future of condensed matter theory indeed entails the study of more realistic and complex many-body systems, we cannot yet claim to have understood the simpler models that will comprise them. The recent large-scale efforts [74, 75, 76, 77] to make sense of the repulsive 2D Hubbard model [64, 65, 66] exemplifies this sentiment best. The parameter regimes considered in these works present analytical and numerical challenges. There, the interaction is neither weak nor strong, eliminating methods based on perturbation theory. Worse is the debilitating Fermion sign problem that arises in Monte Carlo simulations for such parameters. This highly entangled region of the phase space is fraught with competing intertwined orders and non-Fermi-liquid physics [78].

1.2.1 The Holstein model

The Hubbard model is often referred to as the "standard model of condensed matter", for it includes (arguably) the minimum ingredients to describe interacting mobile electrons on a lattice.[1] As stated previously, this model completely ignores the lattice degrees of freedom and their interactions with electrons. If there were an equivalent title to be issued for a model of electron-lattice interactions, it would undoubtedly go to the Holstein model [79, 80]. It describes a single band of electrons that hop from site to site and interact with the lattice by coupling linearly to the ion displacement. The ions[2] are treated in the simplest conceivable way barring their omission entirely. Each lattice site has an ion, all identical, and all of which vibrate harmonically and independently of each other (i.e., ion-ion interactions are neglected). There is just one orbital per ion for the valence electrons to occupy, hosting two electrons at most. For a static and perfect lattice, Bloch electrons move without interference

---

[1]Perhaps a better title would be the "standard model of electronic correlations".

[2]As pointed out by Mahan [81],

> "The word *ion* is not meant to imply a particular charge state. In metals, the atoms are ions, while in covalently bonded semiconductors they are something else. We use ion to encompass all these possibilities."

from the ions. However, the displaced ions couple linearly to the density of the electrons on a site.

Mathematically, the Holstein model can be written as

$$\hat{H} = -t \sum_{\langle i,j \rangle, \sigma} \left(\hat{c}_{i,\sigma}^{\dagger} \hat{c}_{j,\sigma} + \hat{c}_{j,\sigma}^{\dagger} \hat{c}_{i,\sigma} \right) - \mu \sum_{i,\sigma} \hat{n}_{i,\sigma} + \sum_{i} \left[\frac{\hat{P}_i^2}{2M} + \frac{1}{2} M \Omega^2 \hat{X}_i^2 \right] - \alpha \sum_{i,\sigma} \hat{n}_{i,\sigma} \hat{X}_i, \quad (1.1)$$

where $\hat{c}_{i,\sigma}^{\dagger}$ ($\hat{c}_{i,\sigma}$) creates (annihilates) an electron on site i with spin σ, and the number operator $\hat{n}_{i,\sigma} = \hat{c}_{i,\sigma}^{\dagger} \hat{c}_{i,\sigma}$. The transfer integral ("hopping-t") $-t$ is shorthand for the one-particle hopping matrix element $\langle i | \hat{H}_0 | j \rangle$ for different states i and j. Conceptually, one arrives at this simplification by assuming that each on-site electronic orbital is highly localized. The amplitude to tunnel between sites decays exponentially with the distance between the two locations, thereby permitting us to omit all but the nearest-neighbor hopping [3]. This hopping has a negative sign because it stems from the overlap integral between the wavefunctions and the negative crystalline potential. The notation $\langle i, j \rangle$ in the first sum indicates that the site indices are restricted to nearest neighbors only. We always work in the grand canonical ensemble, so the chemical potential μ serves to tune the average density of electrons in the system. The ion momentum and position operators at site i are given by $\hat{P}_i$ and $\hat{X}_i$, respectively. They act as identical independent harmonic oscillators located at each site with a dispersionless frequency Ω and mass M. Lastly, these ions interact with electrons occupying the same site with an interaction strength α. Throughout much of this work, the units are such that $\hbar = k_{\mathrm{B}} = M = a = 1$, where a is the lattice spacing. We will restore some quantities with appropriate units when it proves useful.

The Hamiltonian form given by Eqn. (1.1) is particularly well suited for quantum Monte Carlo (QMC) simulations since the coordinates X can be simulated directly as configurations. Alternatively, one may quantize the lattice vibrations using the creation and annihilation operators well known to all who have studied the quantum harmonic oscillator. Here, $\hat{P}$ and $\hat{X}$ are given by

$$\hat{X}_i = \sqrt{\frac{\hbar}{2M\Omega}} \left(\hat{a}_i + \hat{a}_i^{\dagger} \right) \qquad \text{and} \qquad \hat{P}_i = i \sqrt{\frac{M\hbar\Omega}{2}} \left(-\hat{a}_i + \hat{a}_i^{\dagger} \right), \qquad (1.2)$$

---

[3]Later, we will include next-nearest-neighbor hopping and discuss it's consequences on the Holstein model.

where $\hat{a}_i^\dagger$ and $\hat{a}_i$ are bosonic operators (i.e., $\left[\hat{a}_i^\dagger, \hat{a}_j^\dagger\right] = \left[\hat{a}_i, \hat{a}_j\right] = 0$ and $\left[\hat{a}_i, \hat{a}_j^\dagger\right] = \delta_{i,j}$). With these substitutions, the ionic energy terms can be simplified as

$$\hat{H}_{\text{ion}} = \sum_i \frac{\hat{P}_i^2}{2M} + \frac{1}{2}M\Omega^2\hat{X}_i^2 = \sum_i \hbar\Omega\left(\hat{a}_i^\dagger\hat{a}_i + \frac{\hat{\mathbb{I}}}{2}\right), \tag{1.3}$$

which includes the zero-point energy and all additional phonon quanta. In general applications, the dispersionless phonon energy is too simple to describe real materials accurately. However, it captures the qualitative physics of higher energy optical phonon modes, which are relatively flat compared with acoustic modes, particularly in materials with complex unit cells like the cuprates. Precision calculations aimed at matching experimental values would be much improved using a dispersion $\hbar\Omega_{\mathbf{q},\nu}$ where $\mathbf{q}$ is the momentum of a particular mode and ν is a phonon branch index. In d dimensions, with $N_{\text{ions-uc}}$ per unit cell and N unit cells, there are $d \times N_{\text{ions-uc}} \times N$ independent oscillators. In this work, we will only require the Einstein phonons in $d = 2$ for calculations. Here, we take one oscillator per unit cell, and so the number of oscillators is just N.

Using the first equation in Eqns. (1.2), the electron-ion interaction can be written as an e-ph interaction

$$\hat{H}_{\text{e-ph}} = -g\sum_{i,\sigma} \hat{n}_{i,\sigma}\left(\hat{a}_i + \hat{a}_i^\dagger\right) \tag{1.4}$$

where $g := \alpha\sqrt{\frac{\hbar}{2M\Omega}}$ is called the (Holstein) e-ph coupling.

It is advantageous to obtain the Fourier transform of the Holstein model when using methods other than the DQMC. The details of this transform are in Appendix A, and the result (setting $\hbar = 1$) is given by

$$\hat{H} = \sum_{\mathbf{k},\sigma} \epsilon_{\mathbf{k}}\hat{c}_{\mathbf{k},\sigma}^\dagger\hat{c}_{\mathbf{k},\sigma} + \Omega\sum_{\mathbf{k}}\left(\hat{a}_{\mathbf{k}}^\dagger\hat{a}_{\mathbf{k}} + \frac{\hat{\mathbb{I}}}{2}\right) - g\sum_{\mathbf{k},\mathbf{q},\sigma} \hat{c}_{\mathbf{k}+\mathbf{q},\sigma}^\dagger\hat{c}_{\mathbf{k},\sigma}\left(\hat{a}_{\mathbf{q}} + \hat{a}_{-\mathbf{q}}^\dagger\right). \tag{1.5}$$

This form will be useful for the self-consistent Migdal approximation (SCMA), which is treated using many-body perturbation theory (MBPT).

There is something curious about the way the Holstein model appears in modern literature. It is widespread to use dispersionless Einstein modes and refer to optical modes with no additional details surrounding the atoms in the unit cell. Most physics students

encounter Einstein phonons while studying the oscillating diatomic chain. The relatively flat optical branch dispersion is one of two solutions for longitudinal oscillations, with the other being dispersive acoustic modes. Really, the Holstein model was derived with a molecular-crystal in mind, where each site is a polar molecule. In that context, the oscillations correspond to the molecule's internal displacements and not overall displacements with respect to the lattice sites. The physics in this model extends beyond these specifics. As we will show later, the phase diagram reveals a simplified picture of competing for charge-density and superconducting instabilities. Such competition is relevant for many material systems, even ones where the Holstein model is hardly the appropriate minimal Hamiltonian.

1.2.2   Some details on electron-phonon coupling

Like Einstein phonons' simplicity, the Holstein model's e-ph interaction is the least complicated possible choice. The coupling is taken to be constant, and results in isotropic scattering. A more flexible choice for the e-ph interaction would be that of the single-band Fröhlich Hamiltonian [82, 83] given by

$$\hat{H}_{\text{e-ph}} = \sum_{\mathbf{k},\mathbf{q},\sigma,\nu} g_{\mathbf{q},\nu}\, \hat{c}^{\dagger}_{\mathbf{k}+\mathbf{q},\sigma} \hat{c}_{\mathbf{k},\sigma} \left(\hat{a}_{\mathbf{q},\nu} + \hat{a}^{\dagger}_{-\mathbf{q},\nu} \right) \qquad \text{(Fröhlich interaction)}. \qquad (1.6)$$

For the most general form [84], one can restore the complete momentum, band, and branch dependence to the e-ph coupling matrix element $g_{n'n,\nu}(\mathbf{k},\mathbf{q})$ given by

$$g_{n'n,\nu}(\mathbf{k},\mathbf{q}) \equiv g^{\mathbf{q},\nu}_{\mathbf{k}+\mathbf{q},n';\mathbf{k},n} \propto \langle \mathbf{k}+\mathbf{q}, n', \sigma | \, \Delta_{\mathbf{q},\nu} \hat{V}_{\text{e-i}} \, | \mathbf{k}, n, \sigma \rangle, \qquad (1.7)$$

where an electron in band n with crystal momentum $\mathbf{k}$ is scattered by a phonon (in this case, absorbing it) of momentum $\mathbf{q}$ in branch ν into a final band n' with momentum $\mathbf{k}+\mathbf{q}$. Such matrix elements can be calculated within the Kohn-Sham formalism of density-functional theory (DFT).

There is a considerable amount of detail hidden away in Eqn. (1.7). For one, the electronic states that bookend this matrix element are generally taken to be Bloch-periodic components

of the Kohn-Sham electron wave functions.[4] The scattering potential operator $\Delta_{\mathbf{q},\nu}\hat{V}_{\text{e-i}}$ is the slight phonon-induced variation of the self-consistent potential experienced by the electrons. This potential is a complicated object, accounting for electronic screening effects in the presence of the oscillating ions/nuclei in a very general and self-consistent manner. The most up-to-date formalism for evaluating these matrix elements instead relies on a real-space picture made possible in part by Wannier functions. Since our models are much simpler than what is generally prescribed by DFT, we instead refer the reader to Ref. [84] for the latest treatments.

The derivation of the e-ph coupling contribution to the Hamiltonian is covered in most condensed matter textbooks [86, 81, 87, 88, 89, 85], and we will recall just a few essential points from those discussions. Our starting point is the electron-ion Hamiltonian is given by

$$\hat{H}_{\text{e-i}} = \sum_{i=1}^{N} \hat{h}_{\text{e-i}}(\mathbf{r}_i), \tag{1.8}$$

where

$$\hat{h}_{\text{e-i}}(\mathbf{r}_i) = \sum_{\kappa,p} \hat{V}_{\text{e-i}}(\mathbf{r}_i - \mathbf{R}_{\kappa,p}), \tag{1.9}$$

is the sum over all individual interactions $\hat{V}_{\text{e-i}}(\mathbf{r}_i - \mathbf{R}_{\kappa,p})$ between the i-th electron located at position $\mathbf{r}_i$ and an ion at position $\mathbf{R}_{\kappa,p}$. For now, we use the indices $p = 1, \ldots, N$ and $\kappa = 1, \ldots, N_{\text{ions-uc}}$ to denote a particular unit cell and the ion's designation within that cell, respectively. If we take the ionic oscillator equilibrium position to be $\mathbf{R}_{\kappa,p}^0$ and the associated displacement to be $\mathbf{X}_{\kappa,p}$, then $\mathbf{R}_{\kappa,p} = \mathbf{R}_{\kappa,p}^0 + \mathbf{X}_{\kappa,p}$. Rewriting the electron-ion interaction

---

[4]In fact, when the coupling depends only on the momentum transfer [i.e., $g_\nu(\mathbf{q})$], the electrons are effectively plane waves. The more general form $g_{n'n,\nu}(\mathbf{k}, \mathbf{q})$ arises when the Bloch wave functions of the electron band replace the plane-wave functions [85].

terms as $\hat{V}_{\text{e-i}}(\mathbf{r}_i - \mathbf{R}^0_{\kappa,p} - \mathbf{X}_{\kappa,p})$, we then expand in terms of $\mathbf{X}_{\kappa,p}$, giving us

$$
\begin{aligned}
\hat{h}_{\text{e-i}}(\mathbf{r}_i) &= \sum_{\kappa,p} \hat{V}_{\text{e-i}}(\mathbf{r}_i - \mathbf{R}^0_{\kappa,p} - \mathbf{X}_{\kappa,p}) \\
&= \sum_{\kappa,p} \left[\hat{V}_{\text{e-i}}(\mathbf{r}_i - \mathbf{R}^0_{\kappa,p}) - \sum_{\alpha=1}^{d} \hat{X}_{\alpha,\kappa,p} \frac{\partial \hat{V}_{\text{e-i}}(\mathbf{r}_i - \mathbf{R}^0_{\kappa,p})}{\partial r_\alpha} \right. \\
&\quad \left. + \frac{1}{2} \sum_{\alpha=1}^{d} \sum_{\beta=1}^{d} \hat{X}_{\alpha,\kappa,p} \hat{X}_{\beta,\kappa,p} \frac{\partial^2 \hat{V}_{\text{e-i}}(\mathbf{r}_i - \mathbf{R}^0_{\kappa,p})}{\partial r_\alpha \partial r_\beta} + O(\hat{X}^3) \right],
\end{aligned} \tag{1.10}
$$

where α and β are indices for Cartesian coordinates in d-dimensions.

For the expansion to be meaningful, the displacements $\hat{X}_{\alpha,\kappa,p}$ should be small enough to render the higher-order terms as negligible. How small is small enough? In practice, sufficient grounds for omitting higher-order terms are that they do not appreciably change results after their inclusion. To the degree that higher-order terms can be dealt with at all, we may only have the means to check the next leading order contribution. For now, we will limit the series to the linear term only and will revisit the nonlinear terms shortly. Incidentally, the first term (i.e., $\hat{h}^{(0)}_{\text{e-i}}(\mathbf{r}_i) \equiv \sum_{\kappa,p} \hat{V}_{\text{e-i}}(\mathbf{r}_i - \mathbf{R}^0_{\kappa,p})$) is just the interaction between the electrons and the frozen lattice configuration. This term contributes to the periodic crystal potential whose Hamiltonian contribution $\hat{H}^{(0)}_{\text{e-i}} = \sum_i \hat{h}^{(0)}_{\text{e-i}}(\mathbf{r}_i)$ is typically solved first, yielding Bloch states as its eigenfunctions. In the Holstein Hamiltonian and many others, the effects of $\hat{H}^{(0)}_{\text{e-i}}$ are accounted for à la tight binding.

By far, the most common way to deal with Eqn. (1.10) is to employ the linear approximation: $\hat{h}_{\text{e-i}}(\mathbf{r}_i) \approx \hat{h}^{(0)}_{\text{e-i}}(\mathbf{r}_i) + \hat{h}^{(1)}_{\text{e-i}}(\mathbf{r}_i)$, where

$$
\hat{h}^{(1)}_{\text{e-i}}(\mathbf{r}_i) = -\sum_{\kappa,p} \sum_{\alpha=1}^{d} \hat{X}_{\alpha,\kappa,p} \frac{\partial \hat{V}_{\text{e-i}}(\mathbf{r}_i - \mathbf{R}^0_{\kappa,p})}{\partial r_\alpha}. \tag{1.11}
$$

Alternatively, this can be written in vector notation as

$$
\hat{h}^{(1)}_{\text{e-i}}(\mathbf{r}_i) = -\sum_{\kappa,p} \hat{\mathbf{X}}_{\kappa,p} \cdot \nabla_\mathbf{r} \hat{V}_{\text{e-i}}(\mathbf{r}_i - \mathbf{R}^0_{\kappa,p}). \tag{1.12}
$$

Without further qualification, the potential $\hat{V}_{\text{e-i}}(\mathbf{r}_i - \mathbf{R}^0_{\kappa,p})$ corresponds to the unscreened electron-ion potential. Electron-electron interactions act to reduce this potential via

12

screening in real materials [81]. As indicated previously, ab initio methods include the effects of electronic screening and additional contributions such as exchange and correlation at this stage [84]. The lowest order approximation would be to replace $\hat{V}_{\text{e-i}}$ with a screened interaction $\hat{V}_{\text{e-i}}/\varepsilon$ where ε is the dielectric constant.

Let us perform the Fourier transform of of the interaction potential using $\hat{V}_{\text{e-i}}(\mathbf{r}) = \frac{1}{\mathcal{V}}\sum_{\mathbf{q}'}\hat{V}_{\text{e-i},\mathbf{q}'}e^{i\mathbf{q}'\cdot\mathbf{r}}$ so the gradient becomes

$$\nabla\hat{V}_{\text{e-i}}(\mathbf{r}_i - \mathbf{R}^0_{\kappa,p}) = \frac{1}{\mathcal{V}}\sum_{\mathbf{q}'}(i\mathbf{q}')\hat{V}_{\text{e-i},\mathbf{q}'}e^{i\mathbf{q}'\cdot(\mathbf{r}_i-\mathbf{R}^0_{\kappa,p})}, \tag{1.13}$$

where $\mathcal{V}$ is the volume of the crystal. Writing $\mathbf{q}'$ as the sum of a reciprocal lattice (RL) vector $\mathbf{G} \in$ RL and a wave vector $\mathbf{q}$ in the first Brillioun zone (FBZ), as in $\mathbf{q}' = \mathbf{q} + \mathbf{G}$, we have

$$\nabla\hat{V}_{\text{e-i}}(\mathbf{r}_i - \mathbf{R}^0_{\kappa,p}) = \frac{i}{\mathcal{V}}\sum_{\mathbf{q}\in\text{FBZ}}\sum_{\mathbf{G}\in\text{RL}}(\mathbf{q}+\mathbf{G})V_{\text{e-i},\mathbf{q}+\mathbf{G}}e^{i(\mathbf{q}+\mathbf{G})\cdot(\mathbf{r}_i-\mathbf{R}^0_{\kappa,p})}. \tag{1.14}$$

The e-ph interaction operator becomes

$$\hat{h}^{(1)}_{\text{e-i}}(\mathbf{r}_i) = -\frac{i}{\mathcal{V}}\sum_{\mathbf{q}\in\text{FBZ}}\sum_{\mathbf{G}\in\text{RL}}\sum_{j}\hat{\mathbf{X}}_j\cdot(\mathbf{q}+\mathbf{G})V_{\text{e-i},\mathbf{q}+\mathbf{G}}e^{i(\mathbf{q}+\mathbf{G})\cdot(\mathbf{r}_i-\mathbf{R}^0_j)}, \tag{1.15}$$

where we have opted for a single index for the all the ions $j = 1,\ldots,N_{\text{ions}}$ with $N_{\text{ions}} = N_{\text{ions-uc}}N$.

We can now replace the displacement operator by is occupation number representation [87]

$$\hat{\mathbf{X}}_j = \frac{1}{\sqrt{N}}\sum_{\mathbf{p}\in\text{FBZ}}\sum_{\nu}\sqrt{\frac{\hbar}{2M\Omega_{\mathbf{p},\nu}}}\left(\hat{a}_{\mathbf{p},\nu} + \hat{a}^\dagger_{-\mathbf{p},\nu}\right)\boldsymbol{\epsilon}_{\mathbf{p},\nu}e^{i\mathbf{p}\cdot\mathbf{R}^0_j}, \tag{1.16}$$

which is a linear combination of solutions from the harmonic phonon eigenvalue problem. These solutions cover the $d \times N_{\text{ion-uc}}$ phonon modes, of which there are d acoustical modes and $d \times (N_{\text{ion-uc}} - 1)$ optical modes. Each mode is described by a branch dispersion $\Omega_{\mathbf{p},\nu}$ appearing in the phonon Hamiltonian given by $\hat{H}_{\text{ph}} = \sum_{\mathbf{p},\nu}\hbar\Omega_{\mathbf{p},\nu}\left(\hat{a}^\dagger_{\mathbf{p},\nu}\hat{a}_{\mathbf{p},\nu} + \frac{1}{2}\right)$. For each branch index ν, $\Omega_{\mathbf{p},\nu}$ is defined in N discrete points in $\mathbf{p}$-space. The polarization vector $\boldsymbol{\epsilon}_{\mathbf{p},\nu}$ determines the direction of of the displacement relative to the wave vector $\mathbf{p}$. Note also that

since the displacements $\hat{\mathbf{X}}_j$ are real, we must have $\boldsymbol{\epsilon}^*_{\mathbf{p},\nu} = \boldsymbol{\epsilon}_{-\mathbf{p},\nu}$. Most often, we deal with longitudinal modes for which $\boldsymbol{\epsilon}_{\mathbf{p},\nu} \parallel \mathbf{p}$. The transverse modes ($\boldsymbol{\epsilon}_{\mathbf{p},\nu} \perp \mathbf{p}$) do not to produce significant e-ph coupling in most applications.

After substituting Eqn. (1.16) into Eqn. (1.15), we can simplify the sum over j using $\sum_j \mathrm{e}^{\mathrm{i}(\mathbf{p}-(\mathbf{q}+\mathbf{G}))\cdot\mathbf{R}_j^0} = N\delta_{\mathbf{p},\mathbf{q}+\mathbf{G}}$. Since phonon wave vectors are only defined within the FBZ, we can drop the reciprocal lattice vector from the appropriate terms and write

$$\hat{h}^{(1)}_{\text{e-i}}(\mathbf{r}_i) = -\sum_{\mathbf{q},\nu}\sum_{\mathbf{G}} g_{\mathbf{q},\mathbf{G},\nu}\left(\hat{a}_{\mathbf{q},\nu} + \hat{a}^\dagger_{-\mathbf{q},\nu}\right)\mathrm{e}^{\mathrm{i}(\mathbf{q}+\mathbf{G})\cdot\mathbf{r}_i}, \tag{1.17}$$

where we have introduced the e-ph coupling strength $g_{\mathbf{q},\mathbf{G},\nu}$ given by

$$g_{\mathbf{q},\mathbf{G},\nu} = \frac{\mathrm{i}}{\mathcal{V}}\sqrt{\frac{N\hbar}{2M\Omega_{\mathbf{p},\nu}}}\boldsymbol{\epsilon}_{\mathbf{q},\nu}\cdot(\mathbf{q}+\mathbf{G})V_{\text{e-i},\mathbf{q}+\mathbf{G}}. \tag{1.18}$$

If we define the e-ph Hamiltonian under the linear approximation as

$$\hat{H}_{\text{e-ph}} = \sum_i \hat{h}^{(1)}_{\text{e-i}}(\mathbf{r}_i), \tag{1.19}$$

then we can expand the sum in second quantized notation for the fermion operators[5]:

$$\hat{H}_{\text{e-ph}} = \sum_{\mathbf{k},\mathbf{k}',n,n',\sigma} \langle \mathbf{k}',n',\sigma|\,\hat{h}^{(1)}_{\text{e-i}}\,|\mathbf{k},n,\sigma\rangle\, \hat{c}^\dagger_{\mathbf{k}',n',\sigma}\hat{c}_{\mathbf{k},n,\sigma}. \tag{1.20}$$

Here, we have used a generic Bloch basis and assumed that the spin remains unchanged after e-ph scattering events (i.e., $\sigma' = \sigma$). Inserting a completeness relation $\hat{\mathbb{1}} = \int \mathrm{d}\mathbf{r}\,|\mathbf{r}\rangle\langle\mathbf{r}|$, we

---

[5]Any fermionic one-body Hamiltonian of the form $\hat{H}_1 = \sum_{i=1}^N \hat{h}(i)$, can expressed in a basis $\{|\phi_\nu\rangle\}$ with operators $\hat{c}^\dagger_\nu$ and $\hat{c}_\nu$ via

$$\hat{H}_1 = \sum_{\nu,\mu} \langle\phi_\mu|\,\hat{h}\,|\phi_\nu\rangle\, \hat{c}^\dagger_\mu\hat{c}_\nu.$$

have

$$\hat{H}_{\text{e-ph}} = \sum_{\mathbf{k},\mathbf{k}',n,n',\sigma} \left(\int d\mathbf{r} \langle \mathbf{k}', n', \sigma | \mathbf{r} \rangle \langle \mathbf{r} | \hat{h}_{\text{e-i}}^{(1)} | \mathbf{k}, n, \sigma \rangle \right) \hat{c}_{\mathbf{k}',n',\sigma}^{\dagger} \hat{c}_{\mathbf{k},n,\sigma}$$

$$= -\sum_{\mathbf{q},\nu} \sum_{\mathbf{G}} \sum_{\mathbf{k},\mathbf{k}',n,n',\sigma} \left(\int d\mathbf{r} \, \phi_{\mathbf{k}',n',\sigma}^{*}(\mathbf{r}) g_{\mathbf{q},\mathbf{G},\nu} e^{i(\mathbf{q}+\mathbf{G})\cdot\mathbf{r}} \phi_{\mathbf{k},n,\sigma}(\mathbf{r}) \right) \left(\hat{a}_{\mathbf{q},\nu} + \hat{a}_{-\mathbf{q},\nu}^{\dagger} \right) \hat{c}_{\mathbf{k}',n',\sigma}^{\dagger} \hat{c}_{\mathbf{k},n,\sigma},$$

where $\phi_{\mathbf{k},n,\sigma}(\mathbf{r}) = e^{i\mathbf{k}\cdot\mathbf{r}} u_{n,\mathbf{k}}(\mathbf{r}) | \sigma \rangle$ is a Bloch function and $u_{n,\mathbf{k}}(\mathbf{r})$ has the same periodicity as the lattice.

Let us make some simplifying approximations. We can start by dropping the band index, n, and work within a single partially filled band (like the Holstein model). In such a case, we can approximate $u_{n,\mathbf{k}}(\mathbf{r}) \approx 1/\sqrt{\mathcal{V}}$, and take the so-called "effective mass approximation" where $\epsilon_{\mathbf{k}} = \hbar^2 k^2 / 2m^*$, where m^* is the usual effective electron mass [89]. This is a reasonable approximation for metals since $m^* \approx m$, but it may be dubious for other materials such as semiconductors. Using these approximations, we have

$$\hat{H}_{\text{e-ph}} = -\sum_{\mathbf{q},\nu} \sum_{\mathbf{G}} \sum_{\mathbf{k},\mathbf{k}',\sigma} g_{\mathbf{q},\mathbf{G},\nu} \underbrace{\left(\frac{1}{\mathcal{V}} \int d\mathbf{r} \, e^{i(\mathbf{k}+\mathbf{q}+\mathbf{G}-\mathbf{k}')\cdot\mathbf{r}} \right)}_{=\delta_{\mathbf{k}',\mathbf{k}+\mathbf{q}+\mathbf{G}}} \left(\hat{a}_{\mathbf{q},\nu} + \hat{a}_{-\mathbf{q},\nu}^{\dagger} \right) \hat{c}_{\mathbf{k}',\sigma}^{\dagger} \hat{c}_{\mathbf{k},\sigma}$$

$$= -\sum_{\mathbf{q},\nu} \sum_{\mathbf{G}} \sum_{\mathbf{k},\mathbf{k}',\sigma} g_{\mathbf{q},\mathbf{G},\nu} \left(\hat{a}_{\mathbf{q},\nu} + \hat{a}_{-\mathbf{q},\nu}^{\dagger} \right) \hat{c}_{\mathbf{k}+\mathbf{q}+\mathbf{G},\sigma}^{\dagger} \hat{c}_{\mathbf{k},\sigma}. \tag{1.21}$$

Some comments about the wave vectors are necessary here. Each of the wave vectors $\mathbf{q}$, $\mathbf{k}$, and $\mathbf{k}+\mathbf{q}+\mathbf{G}$ must fall within the first Brillouin zone. There is only one reciprocal lattice vector for any fixed $\mathbf{k}$ and $\mathbf{q}$, which, when added to $\mathbf{k}+\mathbf{q}$, maps the vector sum back to the FBZ. If $\mathbf{k}+\mathbf{q}$ already resides in the FBZ, then $\mathbf{G} = 0$; otherwise, $\mathbf{G}$ is nonzero. It is customary to keep only the "normal processes" where $\mathbf{G} = 0$, and neglect all Umklapp processes where $\mathbf{G}$ is nonzero. The primary reasons for this are two-fold: (1) the potential $V_{\mathbf{q}+\mathbf{G}}$ is small with inverse squared dependence (i.e., $\propto (\mathbf{q}+\mathbf{G})^{-2}$), and (2) the phase space for Umklapp type processes is negligible at low temperatures [87].

Finally, dropping the $\mathbf{G}$ dependence based on the arguments above, we have

$$\hat{H}_{\text{e-ph}} = -\sum_{\mathbf{q},\nu} \sum_{\mathbf{k},\mathbf{k}',\sigma} g_{\mathbf{q},\nu} \, \hat{c}_{\mathbf{k}+\mathbf{q},\sigma}^{\dagger} \hat{c}_{\mathbf{k},\sigma} \left(\hat{a}_{\mathbf{q},\nu} + \hat{a}_{-\mathbf{q},\nu}^{\dagger} \right). \tag{1.22}$$

15

All of the material specific information lives within the e-ph coupling $g_{\mathbf{q},\nu}$. With this derivation, we can better understand how the intricate details of e-ph interactions get smeared out or lost entirely in the Holstein model. Many approximations were made along the way:
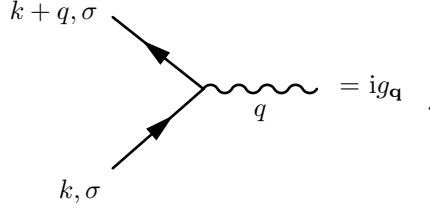
- **Linear approximation:** We expanded the electron-ion interaction potential $\hat{V}_{\text{e-i}}(\mathbf{r}_i - \mathbf{R}_j)$ in the displacement $\hat{\mathbf{X}}_j$, keeping only the lowest order terms up to order $O(\hat{X})$.

- **Fourier Transform of $\hat{V}_{\text{e-i}}(\mathbf{r})$:** We assume a perfect crystal lattice without anomalies such that the Fourier transform of $\hat{V}_{\text{e-i}}(\mathbf{r}) \to \hat{V}_{\text{e-i},\mathbf{q}'}$ exists.

- **Harmonic lattice:** We use the normal coordinate representation of $\hat{X}_j$ in Eqn. (1.16), which relies on solving the harmonic lattice problem. If anharmonicities between pairwise interactions of atoms are significant, the treatment should account for them properly.

- **Bloch electrons:** In order to make further sense of Eqn. (1.20), we introduced Bloch state electrons and then proceeded to fix the function $u_{n,\mathbf{k}}(\mathbf{r}) \approx 1/\sqrt{\mathcal{V}}$.

- **Singleband only:** We do not consider e-ph scattering events that take an electron from one band to another and omit all but one band in total.

- **No Umklapp processes:** Any processes for which $\mathbf{k} + \mathbf{q}$ falls outside the FBZ are not included in the sums. However, in applications, we need not be so restrictive by allowing $\mathbf{k} + \mathbf{q}$ outside the FBZ, but restricting the sum to $\mathbf{G} = 0$ only.

The Holstein model introduces two more approximations:

- **Single branch:** Since we only consider one dispersionless optical phonon branch, we drop the index ν from all quantities and $\Omega_{\mathbf{q},\nu} \to \Omega$.

- **Momentum independent coupling:** The coupling $g_{\mathbf{q}}$ is replaced by constant g. In model calculations, one is more concerned about the relative size of g to other model parameters, such as the hopping t.

1.2.3 The effective electron-electron interaction
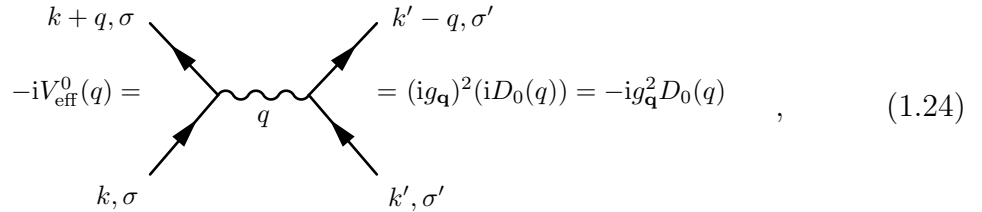
The e-ph coupling plays the role of the bare interaction vertex. Using Feynman diagrams, this vertex is given by [6]

$$k + q, \sigma \qquad \qquad = \mathrm{i}g_{\mathbf{q}} \qquad . \qquad (1.23)$$

Here, the right hand side (rhs) came from the product $(\mathrm{i})^3 \times -g_{\mathbf{q}}$ where each factor of i comes from one of the three propagators. As depicted, an electron in state $|k, \sigma\rangle$ is scattered into a state $|k + q, \sigma\rangle$ by absorbing (emitting) a phonon of wave vector $\mathbf{q}$ $(-\mathbf{q})$. We use the compact notation $k \equiv (\mathbf{k}, \mathrm{i}\omega_n)$ and $q \equiv (\mathbf{q}, \mathrm{i}\nu_n)$, where the fermionic and bosonic Matsubara frequencies are given by $\omega_n = (2n+1)\pi T$ and $\nu_n = 2n\pi T$, respectively (note that $n \in \mathbb{Z}$). We will discuss the treatment of the electron-interaction vertex more generally in short order.

This vertex permits us to discuss the exchange of a phonon between two electrons.

$$-\mathrm{i}V_{\mathrm{eff}}^0(q) = \qquad \qquad = (\mathrm{i}g_{\mathbf{q}})^2 (\mathrm{i}D_0(q)) = -\mathrm{i}g_{\mathbf{q}}^2 D_0(q) \qquad , \qquad (1.24)$$

where we have used the free phonon propagator

$$D_0(q) = \frac{2\Omega_{\mathbf{q}}}{(\mathrm{i}\nu_n)^2 - \Omega_{\mathbf{q}}^2}. \qquad (1.25)$$

The induced bare effective interaction between two *electrons* as mediated by a phonon can written as

$$V_{\mathrm{eff}}^0(\mathbf{q}, z) = g_{\mathbf{q}}^2 \frac{2\Omega_{\mathbf{q}}}{z^2 - \Omega_{\mathbf{q}}^2}, \qquad (1.26)$$

where $z \in \mathbb{C}$ is a frequency.

---

[6]For the purposes of generality, we have temporarily restored some momentum dependence to the coupling $g_{\mathbf{q}}$ and—in a moment—the phonon frequency $\Omega_{\mathbf{q}}$.

At this level, we can highlight a few characteristics about the interaction above. For one, it depends much more strongly on frequency than momentum, reflecting the retarded nature of the e-ph interaction and its spatial locality (though there are cases where $g_{\mathbf{q}}$ is strongly peaked, such as the forward scattering problem [90]). The time scale for restitution with respect to the e-ph related to Debye frequency ω_{D}, as in $\tau_{\text{e-ph}} \sim 1/\omega_{\mathrm{D}}$. In comparison, the corresponding relaxation time associated with the repulsive Coulomb interaction is $\tau_{\text{e-e}} \sim 1/\epsilon_{\mathrm{F}}$, where ϵ_{F} is the Fermi energy. The ratio of these two relaxation times is a rough measure of the adiabaticity, given by

$$\frac{\tau_{\text{e-e}}}{\tau_{\text{e-ph}}} \sim \frac{\omega_{\mathrm{D}}}{\epsilon_{\mathrm{F}}} \sim \sqrt{\frac{m}{M}} \sim \frac{1}{100}, \tag{1.27}$$

where m and M are the bare electron and ion masses, respectively. We will occasionally refer to $\omega_{\mathrm{D}}/\epsilon_{\mathrm{F}}$ (or, generically Ω/E_{F}) as the "adiabatic ratio." The bare dispersion $\Omega_{\mathbf{q}}$ is of order ω_{D} for acoustic phonons, and of order $\Omega \equiv \omega_{\mathrm{E}}$ for optical phonons (ω_{E} is the characteristic Einstein frequency). Consequently, this means that the interaction V_{eff}^0 is attractive when the $|z| < \omega_{\mathrm{D}}$. This attractive e-e interaction is the basis for superconductivity in conventional superconductors and relevant for the Holstein model. However, the phonon dispersion will begin to soften near particular wave vectors in the presence of a charge instability. As a result, the bare interaction V_{eff}^0 will be renormalized, thereby affecting the superconducting instability.

Ignoring the possibility of competing order for the moment, let us say more about the superconducting instability. It is well known from BCS theory that low-energy electrons close to the Fermi surface are responsible for driving the superconductivity. The energy transferred in these scatterings is close to zero; hence the frequency conservation in our diagrams above implies $\Delta\omega = z \approx 0$ in Eqn. (1.26). The effective interaction close to the Fermi surface is then equal to

$$V_{\text{eff}}^0(\mathbf{q}, 0) = -\frac{2g_{\mathbf{q}}^2}{\Omega_{\mathbf{q}}}. \tag{1.28}$$

The momentum dependence of $V_{\text{eff}}^0(\mathbf{q})$ depends strongly on the phonon branch and the origin of $g_{\mathbf{q}}$. For longitudinal acoustic phonons, this ratio is essentially momentum independent.

For longitudinal optical phonons, a flat Einstein phonon dispersion is often used, meaning that momentum dependence in $V_{\text{eff}}^0(\mathbf{q})$ primarily follows $g_{\mathbf{q}}^2$.

1.2.4 A dimensionless e-ph coupling constant λ

Of particular importance to this thesis is the introduction of the dimensionless e-ph coupling constant lambda. Replacing the momentum indices with their equivalence in $\mathbf{k}$ and $\mathbf{k}'$, we estimate this value using

$$\lambda = N_{\text{F}} \left\langle\!\!\left\langle \frac{2g_{\mathbf{k}-\mathbf{k}'}^2}{\Omega_{\mathbf{k}-\mathbf{k}'}} \right\rangle\!\!\right\rangle_{\text{FS}} = N_{\text{F}} \frac{\displaystyle\sum_{\mathbf{k},\mathbf{k}'} w(\mathbf{k},\mathbf{k}') \frac{2g_{\mathbf{k}-\mathbf{k}'}^2}{\Omega_{\mathbf{k}-\mathbf{k}'}} \delta(\epsilon_{\mathbf{k}}) \delta(\epsilon_{\mathbf{k}'})}{\displaystyle\sum_{\mathbf{k},\mathbf{k}'} w(\mathbf{k},\mathbf{k}') \delta(\epsilon_{\mathbf{k}}) \delta(\epsilon_{\mathbf{k}'})} \tag{1.29}$$

where the notation $\langle\!\langle \cdots \rangle\!\rangle_{\text{FS}}$ implies a double Fermi-surface average of the quantity inside the brackets over momentum[7] $\mathbf{k}, \mathbf{k}' \in \text{FS}$, $N_{\text{F}} \equiv N(0)$ is the electron density of states (DOS) evaluated at the Fermi level, and $w(\mathbf{k},\mathbf{k}')$ is a weight function to be specified. For superconductivity, $w = 1$ for the weight function, while other functions may be used for transport applications. In typical metals, $\lambda \sim 0.1$ - 2. Historically, these values are obtained through a mixture of first principles methods (e.g., local density approximation, energy bands, rigid ion approximation) and experiment [91].

In the Holstein model, $\frac{2g_{\mathbf{k}-\mathbf{k}'}^2}{\Omega_{\mathbf{k}-\mathbf{k}'}} \to \frac{2g^2}{\Omega}$, and the remaining sums in Eqn. (1.29) cancel each other, giving us

$$\lambda = \frac{2g^2}{\Omega} N_{\text{F}} = \frac{\alpha^2}{M\Omega^2} N_{\text{F}}. \tag{1.30}$$

This equation is often simplified further by using $N_{\text{F}} \approx 1/W$, where W is the electronic bandwidth:

$$\lambda = \frac{2g^2}{W\Omega} = \frac{\alpha^2}{WM\Omega^2}. \tag{1.31}$$

This dimensionless coupling is useful in several ways:

- It puts all of the model parameters on equal footing and allows easier comparison across different results stemming from different approaches.

---

[7]Actually, the most general form replaces $\mathbf{k}$ and $\mathbf{k}'$ with generic quantum numbers $\tilde{k}$ and $\tilde{k}'$, where (for example) $\tilde{k} \equiv (\mathbf{k}, n, \sigma)$.

- It appears as a prefactor within diagrammatic perturbation theory given by $\lambda \frac{\Omega}{\epsilon_{\mathrm{F}}}$. If this product of the dimensionless coupling constant and the adiabatic ratio $\Omega/\epsilon_{\mathrm{F}}$ is sufficiently small, we can use Migdal's approximation to neglect higher order corrections to the e-ph vertex [92].

- It has a direct connection with estimates of the e-ph coupling from tunneling measurements.

1.2.5 The nonlinear Holstein model

Of the many approximations used in our discussion of the e-ph interaction in Section 1.2.2, the linear approximation was the first one made. Even if one keeps the linear approximation but relaxes one or more of the others, it can be challenging to deal with the interaction. How then could it be sensible to add nonlinear terms? For the Holstein model, it is possible to add the next leading order term on the same footing as the linear term. We start by assuming that the part of our expansion in Eqn. (1.10) corresponding to the e-ph interaction (i.e., $\hat{H}_{\text{e-ph}} = \sum_i \sum_{k=1} \hat{h}_{\text{e-i}}^{(k)}(\mathbf{r}_i)$) can be expressed as

$$\hat{H}_{\text{e-ph}} = \sum_{i,k} \alpha_k \hat{n}_i \hat{X}_i^k = \sum_{i,k} g_k \hat{n}_i \left(\hat{a}_i^\dagger + \hat{a}_i \right)^k. \tag{1.32}$$

This Hamiltonian describes the e-ph interaction to k^{th} order in the atomic displacement at site i. Here, α_k and g_k are the e-ph interaction strengths in the two representations, which are related by $g_k = \alpha_k \left(\frac{\hbar}{2M\Omega} \right)^{\frac{k}{2}}$. In Chapter 4, we consider this interaction up to second order only. Comparing with the e-ph interactions of Eqns. (1.1) and (1.4), the nonlinear interaction to second order is

$$\hat{H}_{\text{e-ph}} = \sum_i \hat{n}_i \left[\alpha_1 \hat{X}_i + \alpha_2 \hat{X}_i^2 \right] = \sum_i \hat{n}_i \left[g_1 \left(\hat{a}_i^\dagger + \hat{a}_i \right) + g_2 \left(\hat{a}_i^\dagger + \hat{a}_i \right)^2 \right]. \tag{1.33}$$

Let us rewrite the terms after the second equals sign as

$$\hat{H}_{\text{e-ph}} = \sum_i g_1 \hat{n}_i \left(\hat{a}_i^\dagger + \hat{a}_i \right) \left[1 + \xi \left(\hat{a}_i^\dagger + \hat{a}_i \right) \right], \tag{1.34}$$

where $\xi := g_2/g_1$. The influence of this nonlinearity will depend greatly on the magnitude and sign of ξ. As we will discuss in Chapter 4, even small values of ξ can yield a significant departure from the results of the linear model.

1.2.6   The attractive Hubbard-metallic bilayer model

The models described up to now are concerned with the electron-phonon problem. In the Chapter 5, we shift gears and focus on a superconducting bilayer system where one layer has a sizable local attractive electron-electron interaction, and the other layer is metallic. This composite system consists of a correlated negative-U Hubbard layer and a non-interacting (metallic) layer connected through interlayer single-particle tunneling. Both layers have a square lattice geometry with identical lattice spacing. The connection to models in the previous sections is that the negative-U Hubbard model can be viewed as the $\Omega \to \infty$ limit of the Holstein model [93].

The composite bilayer Hamiltonian is defined as

$$\hat{H} = -\sum_{\langle ij \rangle, \alpha, \sigma} t_\alpha (\hat{c}_{i\alpha\sigma}^\dagger \hat{c}_{j\alpha\sigma} + \text{H.c}) - |U| \sum_i \hat{n}_{i1\uparrow} \hat{n}_{i1\downarrow} + \sum_{i,\alpha,\sigma} (\epsilon_2 \delta_{\alpha 2} - \mu) \hat{n}_{i\alpha\sigma} + t_\perp \sum_{i,\sigma} (\hat{c}_{i1\sigma}^\dagger \hat{c}_{i2\sigma} + \text{H.c.}),$$

(1.35)

where $\hat{c}_{i\alpha\sigma}^\dagger$ ($\hat{c}_{i\alpha\sigma}$) creates (destroys) an electron on the ith site of the $\alpha = 1$ or 2 layer with spin σ ($=\uparrow, \downarrow$) and $\hat{n}_{i\alpha\sigma} = \hat{c}_{i\alpha\sigma}^\dagger \hat{c}_{i\alpha\sigma}$; $-|U|$ is an attractive on-site interaction; t_α is the hopping *within* layer α; ϵ_2 is an on-site energy term in the metal; μ is the chemical potential; $t_\perp$ is the single-particle hopping/tunneling between layers.

Kivelson proposed the conceptual model [71] and later studied it with Berg et al [94]. In Ref. [94], this model was studied perturbatively for no hopping in the correlated (Hubbard) layer (i.e., $t_1 = 0$) and hopping in one direction (e.g., $t_{1,x} \neq 0$ and $t_{1,y} = 0$; a.k.a., "nanowires"). Later, Wachtel et al. [95] considered the former using quantum Monte Carlo and included the effects of disorder. A more general study using determinant quantum Monte Carlo addressed the model hopping in the correlated layer restored [96].

When the correlated sites are disconnected ($t_1 = 0$), and the tunneling is zero, the correlated layer has a vanishing T_c and zero superfluid stiffness. As tunneling increases, superconducting pairs can migrate to the metallic layer, which possesses a high phase

stiffness. The transition temperature increases until reaching a peak at some optimal tunneling value and then decreases monotonically. The earlier studies primarily explored the regime where the interaction was small compared to the electronic bandwidth, and here, the metal always helps boost the transition temperature. The only study to focus on the general problem with hopping in the correlated layer did not attempt to extract critical temperatures or their dependence on the tunneling.

We study this model for a more general case in Chapter 5. The goal is to determine if the metal offers a significant boost to the superconducting transition temperature when the correlated layer starts with a non-zero phase stiffness.

1.3 Methods

1.3.1 Migdal's Approximation

One of the critical breakthroughs on the e-ph problem was introducing an approximation to the e-ph interaction vertex made by Arkadii Migdal [92]. Much in the spirit of the Born-Oppenheimer approximation, which capitalizes on the velocity disparity between large slow-moving ions and fast-moving lightweight electrons, Migdal's approximation (a.k.a., Migdal's "theorem") shows that renormalization of the e-ph vertex is suppressed by a factor of $\sqrt{m/M} \sim 10^{-2}$ or more. To see how this result comes about, we will proceed with similar arguments made in Refs [97, 85].

The self-energy of the electron in the e-ph problem has a Feynman diagrammatic expansion given by

$$(1.36)$$

where the diagrams appearing just after the first equals sign are the fully dressed (abbreviated) self-energy. The shaded circle on the dressed self-energy diagram[8] is the full e-ph interaction vertex. In diagrams, the vertex part looks like

$$\Gamma(q) = \quad \text{(diagram)} \quad = \quad \text{(diagram)} \quad + \quad \text{(diagram)} \quad + \ldots \quad = \mathrm{i}g_{\mathbf{q}}(1 + \Gamma^{(2)}(q) + \ldots), \qquad (1.37)$$

where the second diagram after the second equals sign corresponds to the vertex correction

$$\Gamma^{(2)}(q) = T\sum_{k'}(\mathrm{i}g_{\mathbf{k}-\mathbf{k}'})^2 D_0(k - k')G_0(k' + q)G_0(k'). \qquad (1.38)$$

The quantities $G_0(k)$ and $D_0(k - k')$ are the noninteracting fermion and boson Green's functions given by

$$G_0(k) = \frac{1}{\mathrm{i}\omega_n - \epsilon_{\mathbf{k}}}, \qquad (1.39)$$

and

$$D_0(k - k') = -\frac{2\Omega_{\mathbf{k}-\mathbf{k}'}}{(\omega_n - \omega_{n'})^2 + \Omega^2_{\mathbf{k}-\mathbf{k}'}}, \qquad (1.40)$$

respectively. Note that we used frequency conservation to set $(\mathrm{i}\nu_n)^2 = -(\omega_n - \omega_{n'})^2$. The sum over $k' \equiv (\mathbf{k}', \mathrm{i}\omega_{n'})$ in Eqn. (1.38) is shorthand for $\sum_{\mathrm{i}\omega_{n'}} \int \frac{\mathrm{d}\mathbf{k}'}{(2\pi)^3}$. In the limit $T \to 0$, the sum over Matsubara frequencies becomes an integral: $T\sum_{\mathrm{i}\omega_{n'}} \to \int \frac{\mathrm{d}\omega_{n'}}{2\pi}$. If temperatures are low enough, the integral is still good approximation. Now we need to choose a frequency cutoff for this integral. At its largest, $\Omega_{\mathbf{k}-\mathbf{k}'}$ becomes comparable to the Debye frequency ω_{D}. Notice that when $|\omega_n - \omega_{n'}| > \omega_{\mathrm{D}}$, we can expand the bare phonon propagator in a series

$$D_0(k - k') \approx -2\left[\frac{\Omega_{\mathbf{k}-\mathbf{k}'}}{(\omega_n - \omega_{n'})^2} - \frac{\Omega^3_{\mathbf{k}-\mathbf{k}'}}{(\omega_n - \omega_{n'})^4} + O\left(\frac{1}{(\omega_n - \omega_{n'})^5}\right)\right], \qquad (1.41)$$

---

[8]The shaded vertex appears only on one side of the self-energy diagram because an additional circle on the other side would introduce topologically identical diagrams to those included within the other dressed vertex, leading to double counting.

which vanishes quickly as $(\omega_{n'})^{-2}$. We can restrict the frequency integral to a window from $-\omega_D$ to ω_D:

$$\Gamma^{(2)}(q) \approx \int_{-\omega_D}^{\omega_D} \frac{d\omega_{n'}}{2\pi} \int \frac{d\mathbf{k}'}{(2\pi)^3} (ig_{\mathbf{k}-\mathbf{k}'})^2 D_0(k-k') G_0(k'+q) G_0(k'). \tag{1.42}$$

Recall from Eqn. (1.29) that $g^2_{\mathbf{k}-\mathbf{k}'} \sim \frac{\lambda \Omega_{\mathbf{k}-\mathbf{k}'}}{2N_F}$. Since $D_0 \sim -2/\Omega_{\mathbf{k}-\mathbf{k}'}$ for $|\omega_n - \omega_{n'}| \ll \omega_D$, we should have that

$$g^2_{\mathbf{k}-\mathbf{k}'} D_0(\mathbf{k}-\mathbf{k}') \sim \frac{\lambda \Omega_{\mathbf{k}-\mathbf{k}'}}{2N_F} \times \left(-\frac{2}{\Omega_{\mathbf{k}-\mathbf{k}'}}\right) = -\frac{\lambda}{N_F}. \tag{1.43}$$

Updating the vertex, we have

$$\Gamma^{(2)}(q) \approx \frac{\lambda}{N_F} \int \frac{d\mathbf{k}'}{(2\pi)^3} \int_{-\omega_D}^{\omega_D} \frac{d\omega_{n'}}{2\pi} G_0(k'+q) G_0(k'). \tag{1.44}$$

The remaining frequency integral is just a product of two free-fermion Green functions, which can be expanded around zero frequency:

$$G_0(k'+q) G_0(k') \approx \frac{1}{\epsilon_{\mathbf{k}'+\mathbf{q}}\epsilon_{\mathbf{k}'}} + \frac{i(\epsilon_{\mathbf{k}'+\mathbf{q}} + \epsilon_{\mathbf{k}'})}{(\epsilon_{\mathbf{k}'+\mathbf{q}}\epsilon_{\mathbf{k}'})^2}\omega_{n'} - O((i\omega_{n'})^2). \tag{1.45}$$

At lowest order, the frequency integral is

$$\int_{-\omega_D}^{\omega_D} \frac{d\omega_{n'}}{2\pi} G_0(k'+q) G_0(k') \approx \frac{1}{\pi}\frac{\omega_D}{\epsilon_{\mathbf{k}'+\mathbf{q}}\epsilon_{\mathbf{k}'}} \propto \omega_D. \tag{1.46}$$

For free fermions, the dispersion is trivial $\epsilon_{\mathbf{k}'} \to \frac{\hbar^2(k')^2}{2m}$ and the remaining momentum space integral is approximately

$$\Gamma^{(2)}(q) \sim \frac{\lambda\omega_D}{N_F\pi}\frac{d\mathbf{k}'}{(2\pi)^3} 4\pi \underbrace{\int_0^{k_F} dk' (k')^2 \frac{1}{(\frac{\hbar^2}{2m})^2(k'+q)^2(k')^2}}_{\sim \frac{1}{(\frac{\hbar^2}{2m})^2 k_F} = \frac{k_F^3}{\epsilon_F^2}} = \frac{\lambda\omega_D k_F^3}{2\pi^3 N_F \epsilon_F^2}, \tag{1.47}$$

where we used spherical coordinates to evaluate the momentum integral. The density of states at the Fermi level can be approximated by $N_F \sim \frac{1}{\epsilon_F a^3}$ (a is the lattice spacing) and

the approximate vertex becomes

$$\Gamma^{(2)}(q) \sim \underbrace{k_{\mathrm{F}}^3 a^3}_{\sim 1} \frac{\lambda \omega_{\mathrm{D}}}{\epsilon_{\mathrm{F}}} \sim \lambda \frac{\omega_{\mathrm{D}}}{\epsilon_{\mathrm{F}}} \sim \lambda \sqrt{\frac{m}{M}}. \tag{1.48}$$

In other words, the vertex series has corrections that scale as $O\left(\sqrt{\frac{m}{M}}\right)$ or, equivalently, $O\left(\frac{\omega_{\mathrm{D}}}{\epsilon_{\mathrm{F}}}\right)$. When we neglect these higher order corrections, we are omitting so-called "crossing" diagrams from the self-energy expansion. A couple examples of such diagrams are depicted below:

$$\Sigma(\text{Neglected Diagrams}) \quad = \qquad\qquad\qquad + \qquad\qquad\qquad + \dots \qquad . \tag{1.49}$$

By no means have we proven anything rigorous with this hand-waving approximation of the vertex. A more careful treatment of this term is quite involved and outside the scope of this introduction. However, the prefactor proportional to $\lambda \frac{\omega_{\mathrm{D}}}{\epsilon_{\mathrm{F}}}$ still prevails. Issues arise in scattering events where the energies of scattered electrons are degenerate. Singularities that we have swept under the rug in our analysis can arise in the presence of charge and Cooper instabilities, two phenomena encountered frequently in our applications.

So when can we apply this approach? Some recent works demonstrate that abiding by the prefactor alone is misleading [98, 99, 100]. While the precise boundary of validity may never be known, it is clear that comparison with nonpertubative methods is sufficient in specific applications [98, 99, 3, 100].

In the next chapter, we will introduce a modern approach to performing calculations under Migdal's approximation. There, the goal is to calculate the electron and phonon propagators and two-particle susceptibilities self-consistently. Using a clever application of fast-Fourier transforms, we can numerically solve the many-body problem under Migdal's approximation for impressively large lattices and obtain estimates of quantities in the thermodynamic limit.

1.3.2   Determinant Quantum Monte Carlo

In Chapters 3 and 4, we employ determinant quantum Monte Carlo (DQMC) [101, 102, 103] as a nonperturbative means of studying the Holstein model and the nonlinear Holstein model, respectively. Much like the SCMA, the DQMC offers a means of estimating one- and two-particle propagators in finite-temperature many-body theory. However, the DQMC formalism stochastically sums all Feynman diagrams implicitly by sampling the exact partition function. The trade-off is that DQMC is resource-intensive and limited to smaller finite-size lattices and higher temperatures than many-body perturbation theory. As a consequence, some DQMC results are merely qualitative representations of the thermodynamic limit. In scenarios where the universality class of specific correlations is known, one can use finite-size scaling techniques over a range of lattice sizes to extract the thermodynamic limit result.

In this section, we discuss basic formalism and introduce formulas without proof. We focus on a generic nonlinear Holstein model that applies to the linear model when the nonlinear coupling is zero. For a more detailed discussion, including many derivations, we refer readers to the Appendix B. Other valuable references include but are not limited to Refs. [102, 104, 105]. Much of the following discussion is taken *verbatim* from the Supplemental Information of our Ref. [3].

The Hamiltonian assumed in this context has the form $\hat{H} = \hat{K} + \hat{H}_{\text{int}}$ where

$$\hat{K} = -t \sum_{\langle i,j \rangle, \sigma} \left(\hat{c}_{i,\sigma}^{\dagger} \hat{c}_{j,\sigma} + \hat{c}_{j,\sigma}^{\dagger} \hat{c}_{i,\sigma} \right) - \mu \sum_{i,\sigma} \hat{n}_{i,\sigma} + \sum_{i} \left[\frac{\hat{P}_i^2}{2M} + \frac{1}{2} M \Omega^2 \hat{X}_i^2 \right] \tag{1.50}$$

$$\hat{H}_{\text{int}} = -\sum_{i} \hat{n}_i \left[\alpha_1 \hat{X}_i + \alpha_2 \hat{X}_i^2 \right] \tag{1.51}$$

We can define the partition function as

$$Z = \text{Tr}(e^{-\beta \hat{H}}) = \text{Tr}(e^{-\beta \hat{K}} e^{-\beta \hat{H}_{\text{int}}})^L + O[(\Delta\tau)^2]. \tag{1.52}$$

Here, the Trotter-Suzuki decomposition was used to discretize the imaginary time interval $\tau \in [0, \beta)$ into L segments of size $\Delta\tau = \frac{\beta}{L}$, indexed by l. The Hamiltonian, and thus also

the action, is bilinear in electron operators. The fermion degrees of freedom and lattice momenta can then be traced out of the partition function [106, 101], leaving an integral over the displacement fields

$$Z = \int \mathcal{D}X \det \mathrm{M}^\uparrow \det \mathrm{M}^\downarrow e^{-\Delta\tau S_{\mathrm{ph}}}, \tag{1.53}$$

where $\int \mathcal{D}X$ is shorthand for integration over the continuous fields $X_{i,l}$, $\mathrm{M}^\sigma = I + \mathrm{B}^\sigma(L)\mathrm{B}^\sigma(L-1)\cdots\mathrm{B}^\sigma(1)$ and $\mathrm{B}^\sigma(l) = e^{-\Delta\tau[\alpha_1 \mathrm{X}(l)+\alpha_2 \mathrm{X}^2(l)]}e^{-\Delta\tau \mathrm{K}}$, $\mathrm{X}(l)$ is a *diagonal* matrix whose i^{th} diagonal element is $X_{i,l}$, K is the matrix form of noninteracting fermionic terms, and I is an $N \times N$ identity matrix. The bosonic action S_{ph} describes the bare kinetic and potential energy of the phonons and is given by

$$S_{\mathrm{ph}} = \frac{M}{2}\left(\frac{X_{i,l+1} - X_{i,l}}{\Delta\tau}\right)^2 + \frac{M\Omega^2}{2}X_{i,l}^2. \tag{1.54}$$

There is symmetry between the spin up and spin down electrons in our e-ph problem, which guarantees the product of determinants in Eqn. (1.53) is larger than zero. Consequently, the integrand of Z is genuinely a probability distribution eligible for sampling space-time configurations of phonon fields, and there is no fermion sign-problem.

Single-particle Green's function and single-site updates

The equal-time Green's function at time $\tau = l\Delta\tau$ is given by

$$
\begin{aligned}
G_{i,j}^\sigma(l) &= \langle \hat{T}_\tau \hat{c}_{i,\sigma}(\tau)\hat{c}_{j,\sigma}^\dagger(\tau)\rangle \\
&= [I + \mathrm{B}^\sigma(l)\cdots\mathrm{B}^\sigma(1)\mathrm{B}^\sigma(L)\cdots\mathrm{B}^\sigma(l+1)]_{i,j}^{-1}.
\end{aligned}
\tag{1.55}
$$

Computing the full Green's function (matrix) $G^\sigma(l)$ from scratch for a single time slice l has an operational cost of $O(N^3)$. However, once known, $G^\sigma(l)$ can be used to compute the Green's function on the next time slice $(l+1)$,

$$G^\sigma(l+1) = \mathrm{B}^\sigma(l+1)G^\sigma(l)[\mathrm{B}^\sigma(l+1)]^{-1}, \tag{1.56}$$

at a reduced operational cost of $O(N^2)$.

To perform a single-site update of the phonon field at a point (i, l), we first propose a field displacement update $X_{i,l} \rightarrow X'_{i,l} = X_{i,l} + \Delta X_{i,l}$, where $\Delta X_{i,l}$ is drawn from a box probability distribution function. Then, the proposed update is accepted with probability R given by

$$R = \frac{\det \mathrm{M}^{\uparrow\prime} \det \mathrm{M}^{\downarrow\prime}}{\det \mathrm{M}^{\uparrow} \det \mathrm{M}^{\downarrow}} \mathrm{e}^{-\Delta\tau\Delta S_{\mathrm{ph}}}, \tag{1.57}$$

where the prime in $\mathrm{M}^{\sigma\prime}$ corresponds to the updated configuration. Fast Sherman-Morrison updates [102] are performed on the equal-time Green's function by first updating the B-matrices

$$\mathrm{B}^{\sigma}(l) \rightarrow \mathrm{B}^{\sigma\prime}(l) = [I + \Delta^{\sigma}(i, l)]\mathrm{B}^{\sigma}(l). \tag{1.58}$$

Here, $\Delta^{\sigma}(i, l)$ is a matrix with elements generically given by $\Delta^{\sigma}_{j,k}(i, l) = \delta_{j,i}\delta_{k,i}[\exp(-\Delta\tau\Delta X_{i,l}) - 1]$, which is zero for all but one element, $\Delta^{\sigma}_{i,i}(i, l)$. It follows that the ratio of determinants can be computed using

$$R^{\sigma} = 1 + [1 - G^{\sigma}_{i,i}(l)]\Delta^{\sigma}_{i,i}(i, l). \tag{1.59}$$

If the phonon field displacement update is accepted, the updated Green's function is given by

$$[G^{\sigma}(l)]' = G^{\sigma}(l) - \frac{G^{\sigma}(l)\Delta^{\sigma}(i, l)[I - G^{\sigma}(l)]}{1 + [1 - G^{\sigma}_{i,i}(l)]\Delta^{\sigma}_{i,i}(i, l)}. \tag{1.60}$$

After updating all the fields for a particular time slice l, $G^{\sigma}(l)$ is used to find $G^{\sigma}(l+1)$ by using Eqn. (1.56).

Two-particle correlation functions

Our primary interest in DQMC calculations is the evaluation of finite temperature correlation functions. As we discussed, the electron Green's function is a central quantity responsible for much of the bottleneck in simulations. However, once we have Green's functions, we can use them to form correlation functions via Wick's theorem at little to no cost. As a simple example, we will show how the charge-density-wave (CDW) structure factor can be built directly from equal time Green's functions.

The CDW structure factor is an equal-time correlation function that measures periodic modulations of the electron density on the lattice. In DQMC, it is useful to formulate

measurements on the real space lattice and then Fourier transform them to momentum space when needed. The structure factor is one such quantity, and its definition is given by the connected correlation function

$$S_{\text{CDW}}(\mathbf{q}) = \frac{1}{N} \sum_{i,j} e^{i\mathbf{q}\cdot(\mathbf{r}_i - \mathbf{r}_j)} \left[\langle \hat{n}_i \hat{n}_j \rangle - \langle \hat{n}_i \rangle \langle \hat{n}_j \rangle \right], \tag{1.61}$$

where $\mathbf{q}$ is a momentum vector, $\mathbf{r}_i$ is a position vector to site i, $\hat{n}_i \equiv \hat{n}_{i,\uparrow} + \hat{n}_{i,\downarrow}$, and $\langle \cdots \rangle$ denotes an expectation value in the grand canonical ensemble. In some references, the definition of $S_{\text{CDW}}(\mathbf{q})$ does not explicitly include the subtraction of $\langle \hat{n}_i \rangle \langle \hat{n}_j \rangle$, which could reflect other details of its application in DQMC. We will omit the $\langle \hat{n}_i \rangle \langle \hat{n}_j \rangle$ term for the purposes of our demonstration.

We begin by evaluating the main density-density term:

$$
\begin{aligned}
\langle \hat{n}_i \hat{n}_j \rangle &= \Big\langle \sum_{\sigma,\sigma'} \hat{n}_{i,\sigma} \hat{n}_{j,\sigma'} \Big\rangle \\
&= \sum_{\sigma,\sigma'} \langle \hat{c}_{i,\sigma}^\dagger \hat{c}_{i,\sigma} \hat{c}_{j,\sigma'}^\dagger \hat{c}_{j,\sigma'} \rangle \\
&= \sum_{\sigma,\sigma'} \left[\langle \hat{c}_{i,\sigma}^\dagger \hat{c}_{i,\sigma} \rangle \langle \hat{c}_{j,\sigma'}^\dagger \hat{c}_{j,\sigma'} \rangle + \langle \hat{c}_{i,\sigma}^\dagger \hat{c}_{j,\sigma'} \rangle \langle \hat{c}_{i,\sigma} \hat{c}_{j,\sigma'}^\dagger \rangle \right] \qquad \text{Wick's theorem} \\
&= \sum_{\sigma,\sigma'} \left[(1 - G_{ii,\sigma})(1 - G_{jj,\sigma'}) + \delta_{\sigma,\sigma'}(\delta_{i,j} - G_{ji,\sigma})G_{ij,\sigma} \right].
\end{aligned}
$$

Expanding out the spin sums, regrouping terms, and a few lines of algebra allow us to write

$$\langle \hat{n}_i \hat{n}_j \rangle = (2 - \sum_{\sigma} G_{ii,\sigma})(2 - \sum_{\sigma'} G_{jj,\sigma}) - \sum_{\sigma} G_{ji,\sigma} G_{ij,\sigma} + \delta_{i,j} \sum_{\sigma} G_{ij,\sigma}, \tag{1.62}$$

which is precisely how it appears in the code. The Fourier transform can be carried out easily on the lattice, and thousands of measurements of $S_{\text{CDW}}(\mathbf{q})$ can be performed over the course of simulation. It is the Monte Carlo averaging that yields the final estimate.

Block updates for the phonon fields

Sampling the phonon fields also requires a block update scheme, which helps to move phonon configurations out of local minima at lower temperatures and reduces the autocorrelation

time. A lattice position for a given site is updated such that $X_{i,l} \to X_{i,l} + \Delta X$ for all $l \in [0, L]$. Here, ΔX is drawn from a separate box probability distribution than for single-site updates. Operationally speaking, the cost of this scheme is $O(N^3)$ as compared with the $O(N^2)$ using Eqn. (1.60) because $G^\sigma(l)$ must be recomputed from scratch. After each full sweep of single-site updates is performed, block updates are typically performed on several randomly selected sites. In this work, we applied block updates on *all* the lattice sites following each full spacetime sweep of single site updates.

1.3.3 The Dynamical Cluster Approximation

Many nonperturbative methods such as QMC, exact diagonalization, and density-matrix renormalization group work on a finite-size lattice of linear dimension L. Mean-field theories, on the other hand, are formulated in the thermodynamic limit: $L \to \infty$. The best known of these mean-field approaches is the dynamical mean-field theory (DMFT). In DMFT, the infinite lattice problem is mapped onto an effective impurity model, which is solved self-consistently. Since there is only one site interacting with a mean-field bath, the underlying self-energy is local in real space. In the limit of infinite dimensions, this approximation holds, and the solution is exact.

For many phenomena like superconductivity, nonlocal spatial fluctuations can are crucial for describing phase transitions. These fluctuations are reintroduced by promoting the single impurity site to a finite-size cluster embedded (self-consistently) in a mean-field bath. This procedure is the aim of cluster extensions of DMFT, for which there are several [107]. Of these methods, the dynamical cluster approximation (DCA) maps the bulk lattice problem to a finite-size periodic cluster embedded in a dynamical mean-field [107, 108, 109]. The finite-size cluster problem is amenable to solution via any aforementioned nonperturbative methods, but we use continuous-time quantum Monte Carlo (CTQMC) [110, 111, 112].

In this section, we provide a brief overview of the DCA method used in chapter 5. The specifics of the implementation used for our calculations are outlined in great detail within Ref. [113]. Most of this background material will very closely follow chapter 14 of Ref. [114].

The DCA approaches the lattice problem by partitioning the FBZ into $N_{\rm c}$ smaller **k**-space clusters of equal size located by the vector **K** at the center of each cell. Each *patch*
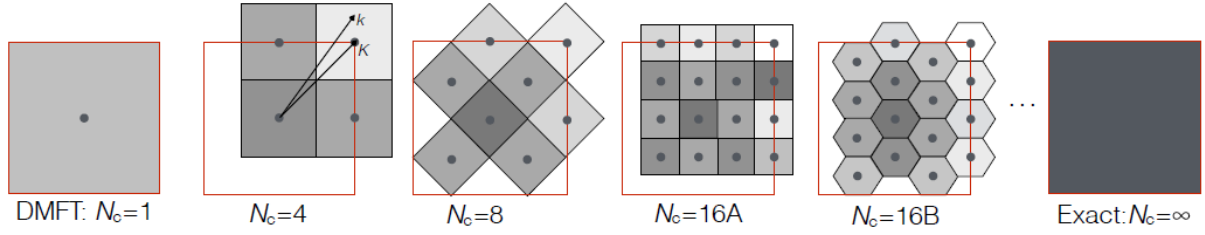
Figure 1.1: In the DCA, one partitions the first Brillouin zone into N_c patches over which the Green's function is 'coarse-grained' (averaged) to represent the system by a reduced number of N_c cluster DOF. The bulk DOF are absent in the cluster and introduced instead as a mean-field. The two limiting cases of $N_c \to 0$ and $N_c \to \infty$ correspond to the DMFT result and exact result respectively. In the original DCA, the location and shape of the coarse-graining patches, as illustrated for the $N_c = 16A$ and $N_c = 16B$ cases, can be different. Figure originally featured in Ref. [114].

has an associated function $\phi_{\mathbf{K}}(\mathbf{k})$, which is defined as

$$
\phi_{\mathbf{K}}(\mathbf{k}) = \begin{cases} 1 & \text{if } \mathbf{k} \text{ is in patch } \mathbf{K} \\ 0 & \text{otherwise}. \end{cases} \tag{1.63}
$$

The main purpose of the patch function is to restrict the sums over momenta $\mathbf{k}$ inside the $\mathbf{K}^{\text{th}}$-patch. These functions obey an orthogonality condition

$$
\frac{N_c}{\mathcal{V}_{\text{BZ}}} \int_{\text{BZ}} \mathrm{d}\mathbf{k} \, \phi_{\mathbf{K}}(\mathbf{k}) \phi_{\mathbf{K}'}(\mathbf{k}) = \delta_{\mathbf{K},\mathbf{K}'}, \tag{1.64}
$$

they must have equal size and shape,

$$
\phi_{\mathbf{K}}(\mathbf{k}) = \phi(\mathbf{k} - \mathbf{K}), \tag{1.65}
$$

and exhibit inversion symmetry,

$$
\phi(\mathbf{k} - \mathbf{K}) = \phi(\mathbf{K} - \mathbf{k}). \tag{1.66}
$$

In Fig.(1.1) we can see that the number of patches/clusters N_c can vary between the two limiting cases: 0 (DMFT), and ∞ (exact), where the size and shape of each cluster is also variable. The shape of the patch is not unique, and the results may depend slightly on a given shape—especially for smaller clusters. One difference between the DCA over DMFT is that the DCA includes momentum dependence in the self-energy. However, the DCA assumes that the self-energy is only weakly dependent on the momentum in such a way that it can be approximated by a coarse grid of $\mathbf{K}$-points of a finite cluster

$$
\Sigma(\mathbf{k}, i\omega_n) \simeq \Sigma_c(\mathbf{K}, i\omega_n), \qquad \forall \mathbf{k} \in \mathbf{K}. \tag{1.67}
$$

It is often possible to capture enough of the exact result using a sufficiently dense and manageable grid size.

In the many-body theory of electron Green's functions, the interactions between electrons modify the single-particle propagator by a feedback mechanism which shifts the effective mass and energy of propagating electron away from their respective bare values by introducing the self-energy. The single-particle propagator $G(\mathbf{k}, i\omega_n)$ with interactions turned on is functionally dependent on the non-interacting Green's function $G_0(\mathbf{k}, i\omega_n)$ and the self-energy through Dyson's equation

$$G(\mathbf{k}, i\omega_n) = \left[G_0^{-1}(\mathbf{k}, i\omega_n) - \Sigma(\mathbf{k}, i\omega_n)\right]^{-1}, \tag{1.68}$$

which can be rearranged to find $\Sigma(\mathbf{k}, i\omega_n) = \Sigma\left[G(\mathbf{k}, i\omega_n)\right]$. To keep all the DOF from the bulk lattice, we must calculate the cluster self-energy $\Sigma_c(\mathbf{K}, i\omega_n) = \Sigma[\bar{G}(\mathbf{K}, i\omega_n)]$ from a coarse-grained Green's function[9]

$$\bar{G}(\mathbf{K}, i\omega_n) = \frac{N_c}{N} \sum_{\mathbf{k}} \phi_{\mathbf{K}}(\mathbf{k}) G(\mathbf{k}, i\omega_n), \tag{1.69}$$

where N is the total number of sites and the lattice propagator is

$$G(\mathbf{k}, i\omega_n) = \frac{1}{i\omega_n - \epsilon_{\mathbf{k}} + \mu - \Sigma^{DCA}(\mathbf{k}, i\omega_n)}. \tag{1.70}$$

The DCA self-energy $\Sigma^{DCA}(\mathbf{k}, i\omega_n)$ is approximated by a constant self-energy $\Sigma_c(\mathbf{K}, i\omega_n)$ within the $\mathbf{K}^{\text{th}}$ patch, but can vary between the different patches:

$$\Sigma^{DCA}(\mathbf{k}, i\omega_n) = \sum_{\mathbf{K}} \phi_{\mathbf{K}}(\mathbf{k}) \Sigma_c(\mathbf{K}, i\omega_n). \tag{1.71}$$

The Green's function $\bar{G}(\mathbf{K}, i\omega_n)$ corresponds to a propagator in which the DOF outside the cluster are coarse-grained or averaged out. As such we can build a corresponding non-interacting Green's function G_0:

$$G_0(\mathbf{K}, i\omega_n) = \left[\bar{G}^{-1}(\mathbf{K}, i\omega_n) + \Sigma_c(\mathbf{K}, i\omega_n)\right]^{-1}, \tag{1.72}$$

---

[9]We will use an overbar on all coarse-grained quantities, e.g. $\bar{G}$.

which is readily obtained by setting the cluster self-energy to zero. Calculating the cluster self-energy $\Sigma_c(\mathbf{K}, \mathrm{i}\omega_n)$ requires that we set up an effective cluster model using a Hamiltonian $\hat{H} = \hat{H}_0 + \hat{H}_{\mathrm{int}}$ where $\hat{H}_0$ is the 'non-interacting' part and $\hat{H}_{\mathrm{int}}$ is the interacting part. Equipped with the form of $\hat{H}$ and a value for G_0, we now need to employ the cluster solver to get an estimate for the interacting propagator and use it to find the corresponding cluster self-energy $\Sigma_c(\mathbf{K}, \mathrm{i}\omega_n)$:

$$\Sigma_c(\mathbf{K}, \mathrm{i}\omega_n) = G_0^{-1}(\mathbf{K}, \mathrm{i}\omega_n) - G_c^{-1}(\mathbf{K}, \mathrm{i}\omega_n), \qquad (1.73)$$

where $G_c^{-1}(\mathbf{K}, \mathrm{i}\omega_n)$ came from the output of the cluster solver. Using this new result for $\Sigma_c(\mathbf{K}, \mathrm{i}\omega_n)$ as the new value for $\Sigma^{DCA}(\mathbf{k}, \mathrm{i}\omega_n)$ in Eqn.(1.70), iterating through the same order of operations self-consistently until $\Sigma_c(\mathbf{K}, \mathrm{i}\omega_n)$ converges within the QMC error $|\Sigma_c^{(n)} - \Sigma_c^{(n-1)}| < \varepsilon_{\mathrm{QMC}}$. The basic DCA calculation loop is shown in Fig.(1.2).

1.4 Summary

In this introduction, we have made contact with several topics relevant to this thesis. First, we discussed the state of superconductivity in broad terms, highlighting its history and introducing some of the nuance related to e-ph coupling in conventional and unconventional superconductors. Then we discussed the general interest in using layered materials as a route to better superconductors. Next, we introduced the Holstein model and the many details surrounding e-ph interactions. We emphasized many of the approximations used to arrive at the Holstein Hamiltonian to make its bearing on reality clearer. To move beyond the linear coupling of the Holstein model, we defined the simplest form of nonlinear e-ph coupling possible. The last model presented was a composite bilayer system aimed at boosting T_{c} by coupling a strong pairing scale superconductor—hindered by phase fluctuations—to a metal.

The methods section introduced the three primary tools used in this dissertation. Migdal's approximation underpins our "self-consistent Migdal approximation" approach introduced in the next chapter, and so we gave a non-rigorous tour of the steps that lead to his argument. DQMC was introduced in the context of the e-ph problem, and it will be

(1) Find total self-energy from individual clusters

$$\Sigma^{DCA}(\mathbf{k}, i\omega_n) = \sum_{\mathbf{K}} \phi_{\mathbf{K}}(\mathbf{k}) \Sigma_c(\mathbf{K}, i\omega_n)$$

(4) Cluster Solver uses $\mathcal{G}_0$ and $\hat{H}_{\text{int}}$ to obtain Σ_c .

$$\Sigma_c(\mathbf{K}, i\omega_n) = \mathcal{G}_0^{-1}(\mathbf{K}, i\omega_n) - \mathcal{G}_c^{-1}(\mathbf{K}, i\omega_n)$$

(2) Get the coarse-grained propagator with total self-energy.

$$\bar{\mathcal{G}}(\mathbf{K}, i\omega_n) = \frac{N_c}{N} \sum_{\mathbf{k}} \phi_{\mathbf{K}}(\mathbf{k}) \frac{1}{\mathcal{G}_0^{-1}(\mathbf{k}, i\omega_n) - \Sigma^{DCA}(\mathbf{k}, i\omega_n)}$$

(3) Find the current non-interacting propagator value.

$$\mathcal{G}_0(\mathbf{K}, i\omega_n) = \left[\bar{\mathcal{G}}^{-1}(\mathbf{K}, i\omega_n) + \Sigma_c(\mathbf{K}, i\omega_n) \right]^{-1}$$
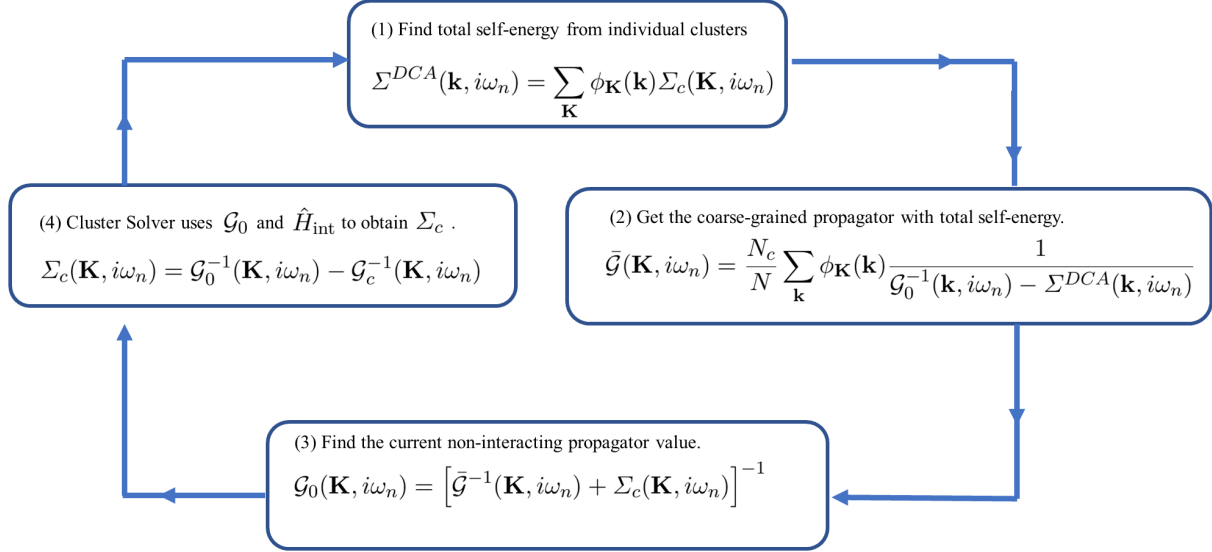
Figure 1.2: The basic algorithm for the DCA begins with a calculation of the self-energy $\Sigma^{DCA}(\mathbf{k}, i\omega_n)$ which can be approximated with an initial guess on the very first iteration (e.g. $\Sigma^{DCA}(\mathbf{k}, i\omega_n) = 0$). For step (2) we begin the coarse-graining process whereby an estimate for the propagator on each cluster is found using the non-interacting propagator of the system. (3) With the estimate for $\bar{G}(\mathbf{K}, i\omega_n)$ we use Dyson's equation to find the non-interacting propagator on each patch. (4) With the new value for $G_0^{-1}(\mathbf{K}, i\omega_n)$ and knowledge of the interaction $\hat{H}_{\text{int}}$ we can find the cluster self-energies by using the cluster solver. The new value of $\Sigma_c(\mathbf{K}, i\omega_n)$ can be inserted back into the calculation loop and iterated until the difference between the self-energies of subsequent iterations is less than the QMC error, $\left| \Sigma_c^{(n)} - \Sigma_c^{(n-1)} \right| < \varepsilon_{\text{QMC}}$.

important for Chapters 3 and 4. Lastly, an overview of the main ideas behind the DCA were presented. The DCA is the main technique used in Chapter 5, where we study a composite bilayer system.

Some of the primary research questions addressed in this dissertation are as follows:

- What is the nature of the Holstein model phase diagram as predicted by self-consistent Migdal theory?

- In that phase diagram, what can we understand about the superconducting dome?

- Perturbative methods like the SCMA are not applicable across a vast parameter space of the Holstein model. What improvements can be made to existing nonperturbative approaches like quantum Monte Carlo using modern machine learning tools?

- Is nonlinear e-ph coupling critical in the most relevant parameter space regions, and does this extend into the regime appropriate for Migdal's approximation?

- Are these nonlinear terms good or bad for superconductivity?

- Can we raise T_c in a composite Hubbard-metallic bilayer system in the regime where U is comparable to the electronic bandwidth?

Chapter 2

Temperature-filling phase diagram of the Holstein Model

This chapter aims to address the question, "what is the phase diagram of the 2D Holstein model under Migdal's approximation?" When this work began, we could not find any comprehensive study including a temperature phase diagram using the renormalized (self-consistent) Migdal's approximation in the literature. While we anticipated the Holstein model's dominant correlations, the phase boundaries were unconfirmed. We introduced a rapid algorithm based on fast-Fourier transforms capable of studying charge-density-wave and superconducting correlations in the thermodynamic limit to accomplish this goal. What follows is a discussion of the phase diagram and some essential quantities that help explain the phase diagram. This chapter features the work of Ref. [1], essentially verbatim.

2.1   Introduction

The electron-phonon (e-ph) interaction drives many physical phenomena and plays a central role in a wide range of solids. For example, it leads to the formation of lattice polarons at large e-ph coupling [115]; it is a significant factor in determining the electronic and thermal transport properties of many functional materials; it can drive broken symmetry states such as charge-density-wave (CDW) order [116] or conventional superconductivity [8, 117, 118,

119] with low [120] and high T_c[121, 122, 123, 124, 125, 126]; and, as recently demonstrated, it can even stabilize and control the location of Dirac cones in certain materials [127].

There has been remarkable progress in the accurate modeling of e-ph interactions in realistic materials using *ab-initio* methods [128, 84] based on density-functional theory and density-functional perturbation theory. Notwithstanding predictions for several superconducting transition temperatures T_c [129, 130, 131, 132, 133], *ab initio* methods usually lack the capability of describing ordered phases or resolving competing orders and are often hindered by large computational costs. Due to these limitations, many researchers turn to model Hamiltonian approaches, which capture the essential physics of the problem while remaining tractable and often easier to interpret. For e-ph coupled systems, the simplest model Hamiltonian is the Holstein model [79] (Eqn. 1.1), which treats the motion of the ions using independent harmonic oscillators and the electron-lattice interaction as a purely local coupling between the electron density and lattice displacement.

Except for a couple of extreme cases, e.g., the use of a two-site system [134, 135, 136] or the atomic limit (with hopping $t = 0$) [81], there are no exact analytical solutions for Holstein model. Nevertheless, it has been widely studied using approximate analytical methods including the modified variational Lang-Firsov transformation [137], diagrammatic expansions [92, 138, 139, 117, 140, 141] based on many-body perturbation theory (MBPT) [97], and variational methods. [142, 135, 143] The Holstein model has also been studied using several exact or approximate numerical techniques including quantum Monte Carlo (QMC) [144, 145, 140, 146, 147, 148, 141, 149, 150, 105, 151, 98, 152], variational Monte Carlo (VMC) [153, 154, 155], and dynamical mean-field theory (DMFT) [156, 157, 158, 159, 160, 161, 162, 163]. (Many of these numerical studies were conducted in the context of the Hubbard-Holstein model, or some other extension, where results for the pure Holstein model were obtained as a limiting case.) At half-filling, these studies find that the Holstein model is dominated by a $\mathbf{q} = (\pi/a, \pi/a)$ CDW phase, while doping away from half-filling leads to a competition between CDW and superconducting instabilities. Moreover, the transition temperatures for both phases vary as a function of the filling n, the phonon frequency Ω, the dimensionless e-ph coupling strength λ, and the Fermi surface (FS) topology. Detailed phase diagrams for Holstein(-Hubbard) model for these parameters

have been obtained by nonperturbative numerical methods in the spatial dimension $d = 1$ by density matrix renormalization group (DMRG) [164], $d = 2$ by VMC [155], and a Bethe lattice with infinite coordination number by DMFT [163].

Owing to its simplicity and lower computational cost, the Migdal approximation [92, 165] outlined in Sec. 1.3.1 is routinely used to capture the e-ph interaction effects in many materials. For instance, it is often used to estimate the superconducting transition temperatures in metals with the e-ph coupling matrix elements from *ab initio* calculations [84, 129, 133, 166, 167]. It is also widely employed to estimate electronic structure renormalization in several materials. [139, 168, 169, 170, 171, 172, 173] As discussed in Sec. 1.3.1, the Migdal approximation entails the omission of vertex corrections to the e-ph interaction. This approximation is typically justified by arguing that such corrections scale as $O\left(\lambda \frac{\hbar\Omega}{E_{\mathrm{F}}}\right)$, where E_F is the Fermi energy, and λ is a dimensionless factor quantifying the e-ph coupling strength. While this condition is satisfied by most metallic systems (because $\hbar\Omega/E_{\mathrm{F}} \ll 1$, i.e., adiabatic limit), there is a growing number of materials where it is not, such as the fullerides [174, 175], solid picene [176, 177], n-type $SrTiO_3$ [178, 179], and monolayer FeSe on $SrTiO_3$ [180, 44]. Interest in these systems, as well as the wide-ranging applications of the Migdal approximation, has invited intense scrutiny on its range of validity, resulting in many studies comparing its predictions with those of nonperturbative numerical methods such as QMC and DMFT [140, 159, 160, 161, 162, 98]. It is found that the Migdal approximation can still break down at large λ [181, 182, 160, 161, 162, 98], even within the adiabatic limit, near half filling. The effort to map out the validity of the Migdal approximation as a function of the e-ph coupling strength, phonon frequency, and the electron filling is ongoing [140, 162, 98].

The studies comparing exact numerical methods and MBPT are usually limited to relatively small lattice sizes for QMC or dimension $d = \infty$ for DMFT and are commonly focused at or close to half filling. It is, therefore, essential that we assess the finite-size effects for both the nonperturbative numerical methods and MBPT, and then extrapolate to the thermodynamic limit. But despite the large body of work surrounding the Holstein model, there is (to the best of our knowledge) no comprehensive study of the general temperature-filling phase diagrams by the full-fledged MBPT in the thermodynamic limit. Motivated by

this, we carried out a detailed study of the single-band two-dimensional Holstein model on a square lattice calculated with the self-consistent Migdal approximation, where the electron and phonon self-energies are both determined self-consistently [140].

Our implementation is based on the fast Fourier transform (FFT) between the momentum-frequency coordinates and the position-time coordinates, which is often used in fluctuation-exchange (FLEX) [183, 184] and DMFT calculations [185]. We show that the predicted CDW transition temperature T_c^{CDW} exhibits significant finite-size effects. To mitigate this problem, we determined the transition temperatures using large lattice sizes well beyond those used in previous studies to obtain a reliable extrapolation to the thermodynamic limit. We also found that the superconducting transition temperature T_c^{SC} exhibits non-monotonic behavior as a function of filling. Specifically, we found that it increases gradually as a function of filling n until it approaches a $\mathbf{q}_{\mathrm{max}} = (\pi, \pi)/a$ CDW phase boundary, where it is suppressed by competition with the CDW, leading to dome-like behavior.

The chapter is organized as follows. Section 2.2 provides a some details of the Holstein model in this context and its extension for momentum dependent coupling, inclusive of the expressions for the self-energies in the Migdal approximation. Section 2.3 documents the computational details and the implementation of our numerical algorithm. Section 2.4 presents the results for the temperature-filling phase diagrams for the Holstein model and other related cases. Section 2.5 summarizes our conclusions. Finally, our code was made publicly available as a set of MATLAB functions and scripts [1].

2.2 Models and Methods

2.2.1 Holstein Model

The Holstein Hamiltonian describes the electronic degrees of freedom using a single band tight-binding model. The lattice degrees of freedom are modeled using independent harmonic oscillators at each site with a spring constant $K = M\Omega^2$, where M is the ion mass, and Ω is the bare frequency of the oscillator. The e-ph interaction is introduced as a purely

---

[1] The MATLAB code is released at https://github.com/johnstonResearchGroup/Migdal

local coupling between the electrons and the atomic displacement. The specific form of the Holstein model studied in this Chapter is given by

$$\hat{H} = -\sum_{i \neq j, \sigma} t_{ij} \hat{c}^{\dagger}_{i,\sigma} \hat{c}_{j,\sigma} - \mu \sum_{i,\sigma} \hat{n}_{i,\sigma} \tag{2.1}$$

$$+ \sum_{i} \left[\frac{\hat{P}_i^2}{2M} + \frac{K\hat{X}_i^2}{2} \right] + \alpha \sum_{i,\sigma} \hat{X}_i \left(\hat{n}_{i,\sigma} - \frac{1}{2} \right), \tag{2.2}$$

where $\hat{c}^{\dagger}_{i,\sigma}$ ($\hat{c}_{i,\sigma}$) creates (annihilates) an electron with spin $\sigma = \uparrow$ or $\downarrow$ on site i, t_{ij} is the hopping integral between sites i and j, μ is the chemical potential, $\hat{n}_{i,\sigma} = \hat{c}^{\dagger}_{i,\sigma} \hat{c}_{i,\sigma}$ is the electron number operator, $\hat{X}_i$ and $\hat{P}_i$ are the lattice displacement and momentum operators, respectively, and α is the e-ph coupling strength. Throughout this chapter, we restrict the range of the hopping to nearest-neighbor (NN) (t) and next-nearest-neighbor (NNN) hopping (t'), only. For $t' = 0$, the Hamiltonian is particle-hole symmetric about half-filling, so we only consider $0 \leq n \leq 1$; for $t' \neq 0$, we consider $0 \leq n \leq 2$. Here, $n = \sum_{\sigma} \langle \hat{n}_{i,\sigma} \rangle$ is the electron filling. There are three differences between Eqn. 2.2 above and Eqn. 1.1 of the introduction: (1) we now include the option of NNN hopping; (2) the interaction term is written for particle-hole symmetry; (3) the minus sign in front of the interaction term is now absorbed into the e-ph coupling strength (i.e., $\alpha < 0$).

Fourier transforming the operators and introducing second quantized forms for the lattice operators $\hat{X}_i$ and $\hat{P}_i$ yields

$$\hat{H} = \sum_{\mathbf{k},\sigma} \xi_{\mathbf{k}} \hat{c}^{\dagger}_{\mathbf{k},\sigma} \hat{c}_{\mathbf{k},\sigma} + \hbar\Omega \sum_{\mathbf{q}} \left(\hat{a}^{\dagger}_{\mathbf{q}} \hat{a}_{\mathbf{q}} + \frac{1}{2} \right)$$

$$+ \frac{1}{\sqrt{N}} \sum_{\mathbf{k},\mathbf{q},\sigma} g \hat{c}^{\dagger}_{\mathbf{k}+\mathbf{q},\sigma} \hat{c}_{\mathbf{k},\sigma} \left(\hat{a}^{\dagger}_{-\mathbf{q}} + \hat{a}_{\mathbf{q}} \right), \tag{2.3}$$

where N is the number of lattice sites, $g = \alpha\sqrt{\frac{\hbar}{2M\Omega}}$, and $\xi_{\mathbf{k}} = \epsilon_{\mathbf{k}} - (\mu - \tilde{\mu})$ is the band dispersion measured relative to the chemical potential. The additional constant $\tilde{\mu} = \frac{\alpha^2}{K} = \frac{2g^2}{\hbar\Omega}$ arises from the fact that the displacement is coupled to $\hat{n}_{i,\sigma} - \frac{1}{2}$ instead of $\hat{n}_{i,\sigma}$ in Eq. (2.2). This shift restores the condition that $\mu = 0$ corresponds to half-filling when $t' = 0$, even in the e-ph coupled case. Physically, it amounts to shifting the zero of the lattice displacement operator $\hat{X}_i - \frac{\alpha}{K} \rightarrow \hat{X}_i$ when going from Eq. (2.2) to Eq. (2.3).

In what follows, we work on a two-dimensional (2D) square lattice with NN hopping t and NNN hopping t'. The resulting electron band dispersion is $\epsilon_\mathbf{k} = -2t\left[\cos(k_x a) + \cos(k_y a)\right] - 4t'\cos(k_x a)\cos(k_y a)$, where the bandwidth $W = 8t$ when $|t'| \leq 0.5t$. We use Eqn. 1.31 as our definition for the dimensionless e-ph coupling (i.e., $\lambda = 2g^2/(W\Omega)$) to facilitate easy comparisons with QMC calculations. Finally, we set our choice of units so that $\hbar = k_\mathrm{B} = a = M = 1$, where $\hbar$ is the reduced Planck constant, and k_B is the Boltzmann constant.

2.2.2 Momentum-Dependent Interactions

Our algorithm can treat momentum dependent interactions, wherein the e-ph coupling g in Eq. (2.3) depends on the phonon wavevector $\mathbf{q}$ with $|g(\mathbf{q})|^2 = g^2 f(\mathbf{q})$, where $f(\mathbf{q})$ is a shape function. Physically, such coupling constants arise when the e-ph interaction couples the electron density to neighboring atomic displacements. Motivated by the e-ph coupling to the oxygen phonon modes in the high-T_c cuprates [186, 187, 54], we will consider three different cases

$$
f(\mathbf{q}) =
\begin{cases}
1 & \text{(Isotropic)}, \\
\cos^2\left(\frac{q_x}{2}\right) + \cos^2\left(\frac{q_y}{2}\right) & \text{(Buckling)}, \\
\sin^2\left(\frac{q_x}{2}\right) + \sin^2\left(\frac{q_y}{2}\right) & \text{(Breathing)}.
\end{cases}
\tag{2.4}
$$

The "isotropic" case corresponds to the conventional Holstein model. The "buckling" case approximates the e-ph vertex expected for c-axis polarized Cu-O bond-buckling modes for in the cuprates while the "breathing" case approximates the momentum dependence expected for the Cu-O bond-stretching modes.

For a general momentum dependent e-ph coupling, we define the dimensionless e-ph coupling constant as $\lambda = [2g^2/(W\Omega)]\langle f(\mathbf{q})\rangle$, where $f(\mathbf{q})$ for the buckling and breathing modes both satisfy: $\langle f(\mathbf{q})\rangle = N^{-1}\sum_{\mathbf{q}\in\mathrm{FBZ}} f(\mathbf{q}) \approx \frac{1}{(2\pi)^2}\int_{-\pi}^{\pi} \mathrm{d}^2 q\, f(\mathbf{q}) = 1$.

2.2.3 Self-consistent Migdal Approximation

In this section we describe how the electron and phonon self-energies are computed self-consistently [140]. For convenience, we adopt the 4-vector notation $k \equiv (\mathbf{k}, i\omega_n)$ and $q \equiv (\mathbf{q}, i\nu_m)$ for the momentum-(Matsubara) frequency coordinates and $x \equiv (\mathbf{r}, \tau)$ for the position-(imaginary) time coordinates. The fermionic and bosonic Matsubara frequencies are given by $\omega_n = (2n+1)\pi T$ and $\nu_m = 2m\pi T$, respectively, with $n, m \in \mathbb{Z}$. The imaginary time is constrained to the range $\tau \in [0, \beta]$, where $\beta = 1/T$ is the inverse temperature.

The dressed single-particle electron Green's function $G(k)$ can be expressed using Dyson's equation as

$$
\begin{aligned}
G(k) &= \left[G_0^{-1}(k) - \Sigma(k) \right]^{-1} \\
&= \left[i\omega_n - \xi_{\mathbf{k}} - \Sigma(k) \right]^{-1},
\end{aligned}
\tag{2.5}
$$
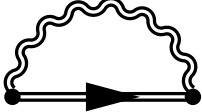
where $G_0(k) = (i\omega_n - \xi_{\mathbf{k}})^{-1}$ is the bare electron Green's function and $\Sigma(k)$ is the electron self-energy. The dressed phonon Green's function $D(q)$ is similarly given by
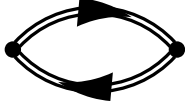
$$
\begin{aligned}
D(q) &= \left[D_0^{-1}(q) - \Pi(q) \right]^{-1} \\
&= -\left[\frac{\nu_m^2 + \Omega^2}{2\Omega} + \Pi(q) \right]^{-1},
\end{aligned}
\tag{2.6}
$$
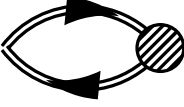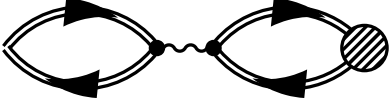
where $D_0(q) = -2\Omega/(\nu_m^2 + \Omega^2)$ is the bare phonon Green's function and $\Pi(q)$ is the phonon self-energy.

The skeleton diagram for the electron self-energy within Migdal approximation is shown in Fig. 2.1(a). Since the vertex corrections are neglected, the full electron self-energy includes only two terms $\Sigma(k) = \Sigma^{\mathrm{F}}(k) + \Sigma^{\mathrm{H}}$. The Fock term $\Sigma^{\mathrm{F}}(k)$ includes all non-crossing "rainbow" Feynman diagrams if the dressed G-skeleton is fleshed out with the self-energy diagrams, and the Hartree term Σ^{H} includes the dressed G-skeleton but with the bare phonon propagator D_0 instead of D to avoid double counting. According to rules for the Feynman diagrams, we have

$$
\Sigma^{\mathrm{F}}(k) = -\frac{1}{N\beta} \sum_q |g(\mathbf{q})|^2 D(q) G(k - q),
\tag{2.7}
$$
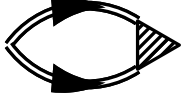
Figure 2.1: The Feynman diagrams for (a) the electron self-energy $\Sigma(k)$, (b) phonon self-energy $\Pi(q)$, (c) CDW susceptibility $\chi^{\text{CDW}}(\mathbf{q})$, (d) and pairing susceptibility χ^{SC}, evaluated within the self-consistent Migdal approximation. The lines (double lines) represent bare (dressed) electron propagators G_0 (G); the wiggly lines (double-wiggly lines) represent bare (dressed) phonon propagators D_0 (D). The black dot represents the bare e-ph coupling vertex. The equation in (c) defines a series of particle-hole ring diagrams and the recurrence equation in (d) defines a series of particle-particle ladder diagrams. Figure taken from our Ref. [1].

and

$$\begin{aligned}
\Sigma^{\mathrm{H}} &= \frac{2|g(\mathbf{0})|^2}{N\beta} D_0(0) \sum_{k'} G(k') \mathrm{e}^{\mathrm{i}\omega_{n'}0^+} \\
&= |g(\mathbf{0})|^2 D_0(0) n,
\end{aligned} \tag{2.8}$$

where

$$n = \frac{2}{N\beta} \sum_{k'} G(k') \mathrm{e}^{\mathrm{i}\omega_{n'}0^+} = 2G(\mathbf{r} = \mathbf{0}, \tau = 0^-). \tag{2.9}$$

The Hartree term is independent of k and thus a constant that is typically absorbed into the definition of the chemical potential $\mu - \tilde{\mu} \to \mu - \tilde{\mu} - \Sigma^{\mathrm{H}}$. Here, we refrain from this practice to facilitate easier comparisons to the chemical potentials used in QMC methods, which include all Feynman diagrams. Note that at half-filling ($n = 1$), $\Sigma^{\mathrm{H}} = -\tilde{\mu} = -2|g(\mathbf{0})|^2/\Omega$.

The skeleton diagram for the phonon self-energy within Migdal approximation is shown in Fig. 2.1(b) and has the analytical form

$$\Pi(q) = \frac{2|g(\mathbf{q})|^2}{N\beta} \sum_k G(k)G(k+q). \tag{2.10}$$

It is useful to use $\Pi(q)$ to define the irreducible charge susceptibility

$$\chi_0(q) = -\frac{\Pi(q)}{|g(\mathbf{q})|^2} = -\frac{2}{N\beta} \sum_k G(k)G(k+q), \tag{2.11}$$

which diagrammatically corresponds to Fig. 2.1(b) with two e-ph coupling vertices removed [i.e., the first term on the right-hand side of the equation in Fig. 2.1(c)].

2.2.4 Charge-density-wave and Pairing Susceptibilities

The charge-density correlation at a wavevector $\mathbf{q}$ is measured by the CDW susceptibility

$$\chi^{\mathrm{CDW}}(\mathbf{q}) = \frac{1}{N} \int_0^\beta \mathrm{d}\tau \left\langle \hat{\rho}_{\mathbf{q}}(\tau) \hat{\rho}_{\mathbf{q}}^\dagger(0) \right\rangle_{\mathrm{c}}, \tag{2.12}$$

where

$$\hat{\rho}_{\mathbf{q}}(\tau) \equiv \sum_{i,\sigma} \mathrm{e}^{-\mathrm{i}\mathbf{q}\cdot\mathbf{R}_i} \hat{c}_{i,\sigma}^{\dagger}(\tau) \hat{c}_{i,\sigma}(\tau). \tag{2.13}$$

In Eq.(2.12), we have used the notation for the connected correlation function defined as $\langle \hat{x}\hat{y} \rangle_{\mathrm{c}} = \langle \hat{x}\hat{y} \rangle - \langle \hat{x} \rangle \langle \hat{y} \rangle$. When significant charge-density correlations are present on the lattice, the CDW susceptibility becomes strongly peaked at an ordering vector $\mathbf{q} = \mathbf{q}_{\mathrm{max}}$. For this reason, we will primarily use and discuss the momentum-space representation $\chi^{\mathrm{CDW}}(\mathbf{q})$. For spin-singlet s-wave pairing due to e-ph coupling, the superconducting correlations are measured by the pairing susceptibility

$$\chi^{\mathrm{SC}} = \frac{1}{N} \int_0^{\beta} \mathrm{d}\tau \left\langle \hat{\Delta}(\tau)\hat{\Delta}^{\dagger}(0) \right\rangle, \tag{2.14}$$

where

$$\hat{\Delta}(\tau) \equiv \sum_i \hat{c}_{i,\uparrow}(\tau)\hat{c}_{i,\downarrow}(\tau). \tag{2.15}$$

In the thermodynamic limit, the temperatures at which the pair field and CDW susceptibilities diverge correspond to the transition temperatures $T_{\mathrm{c}}^{\mathrm{SC}}$ and $T_{\mathrm{c}}^{\mathrm{CDW}}$, respectively. In the case of a $\mathbf{q} = (\pi, \pi)$ CDW order, the temperature dependence of χ^{CDW} should follow the 2D Ising universality class, which can be used to find $T_{\mathrm{c}}^{\mathrm{CDW}}$ [see Sec. (2.3.2)]. By comparison, χ^{SC} diverges much more sharply as a function temperature. In the latter case, we can obtain an accurate measure of $T_{\mathrm{c}}^{\mathrm{SC}}$ by extrapolating $1/\chi^{\mathrm{SC}}(T)$ to zero.

The CDW susceptibility within the Migdal approximation is obtained by summing the particle-hole ring diagrams shown in Fig. 2.1(c), which is formally identical to the random-phase approximation (RPA) or the *GW* approximation for the Coulomb interaction in the electron gas. The CDW susceptibility is largest at zero-frequency, so to determine $T_{\mathrm{c}}^{\mathrm{CDW}}$ we calculate

$$\begin{aligned}
\chi^{\mathrm{CDW}}(\mathbf{q}) &= \frac{\chi_0(\mathbf{q}, 0)}{1 + |g(\mathbf{q})|^2 D_0(\mathbf{q}, 0)\chi_0(\mathbf{q}, 0)} \\
&= \frac{\chi_0(\mathbf{q}, 0)}{1 - \lambda W f(\mathbf{q})\chi_0(\mathbf{q}, 0)}.
\end{aligned} \tag{2.16}$$

Here, we have used $D_0(\mathbf{q}, 0) = -2/\Omega$, $|g(\mathbf{q})|^2 = g^2 f(\mathbf{q})$, and $\lambda = 2g^2/(W\Omega)$. In principle, the momentum dependence of a dispersive phonon mode $\Omega_{\mathbf{q}}$ can be included in the function $f(\mathbf{q})$. This is not the case, however, for any nonzero Matsubara frequencies [152].

The pairing susceptibility within the Migdal approximation is obtained by summing the particle-particle ladder diagrams shown in Fig. 2.1(d) and is given by

$$\chi^{\text{SC}} = \frac{1}{N\beta} \sum_k G(k)G(-k)\Gamma(k), \qquad (2.17)$$

where the vertex function $\Gamma(k)$ is obtained by solving the vertex equation

$$\Gamma(k) = 1 - \frac{1}{N\beta} \sum_{k'} |g(\mathbf{q})|^2 G(k')G(-k')D(q)\Gamma(k'), \qquad (2.18)$$

where $q = k - k'$.

2.3 Computational Details

2.3.1 Self-consistent Iterations with FFT

To obtain the dressed electron and phonon Green's functions, G and D, we self-consistently solve Eqs. (2.5)–(2.10), while the chemical potential μ is adjusted to fix the filling n after every iteration. Once the self-consistent solutions for G and D are obtained, we then evaluate the CDW and pairing susceptibilities using Eq. (2.16) and Eq. (2.17), respectively. An independent self-consistency loop is performed to solve for the pairing vertex function in Eq. (2.18) after the converged Green's functions are obtained. Both the momentum and Matsubara frequency summations in these equations can be viewed as convolutions and thus are evaluated efficiently using FFTs.

Our algorithm for self-consistent calculations of the Green's functions is summarized in the flowchart shown in Fig. 2.2. The input parameters include the temperature T, the filling n, the energy dispersion $\epsilon_{\mathbf{k}}$, the phonon frequency Ω, and the e-ph coupling function $|g(\mathbf{q})|^2$ [or equivalently the dimensionless coupling strength λ and the momentum dependent part of the coupling function $f(\mathbf{q})$]. We discretized the first Brillouin zone using a uniform

$N = n_{\mathbf{k}} \times n_{\mathbf{k}}$ momentum grid, which corresponds to a square lattice with N sites and periodic boundary condition in real space. For computational purposes, the fermionic and bosonic Matsubara frequencies $\omega_n = 2\pi(2n+1)/\beta$ and $\nu_m = 2\pi m/\beta$ are defined over a range defined by $-N_c \leq n, m \leq N_c - 1$. This cutoff corresponds to evenly dividing the imaginary time interval $0 \leq \tau \leq \beta$ into $2N_c$ parts, with $\tau_l = (l-1)\beta/(2N_c)$, where $1 \leq l \leq 2N_c + 1$. For the electron Green's function $G(\tau)$, the end points should be understood as 0^+ and β^- due to the discontinuities of $G(\tau)$ at these points. Here, N_c is determined by $N_c = \omega_c\beta/(2\pi)$, where ω_c is an energy cut-off that is much larger than the band width W. Most of the results obtained here used a cutoff $\omega_c \geq 100\Omega$ which implies that the cutoff was close to W for $\Omega = 0.1t$. We have checked that larger cutoffs produce no changes in the results. When in doubt, we recommend a more conservative cutoff $\omega_c \geq 10W$.

The iteration loop begins with an initial value for electron self-energy $\Sigma(k) = 0$ (or the converged Σ at the previous temperature T data point). The iteration loop then continues through the following steps in sequence:

1. The dressed electron Green's function $G(k)$ is computed by Dyson's equation with the chemical potential μ adjusted to fix the filling n at the input value.

2. The irreducible susceptibility is computed by $\chi_0(x) = -G(x)G(-x) = G(\mathbf{r}, \tau)G(\mathbf{r}, \beta - \tau)$ with $G(x)$ obtained from $G(k)$ by FFT and the spatial inversion symmetry assumed.

3. The dressed phonon Green's function $D(q)$ is computed by the Dyson's equation with $\chi_0(q)$ obtained from $\chi_0(x)$ by the inverse FFT (iFFT) and then an effective interaction $V(q) = -|g(\mathbf{q})|^2 D(q)$ is computed and transformed to $V(x)$ by FFT.

4. A new electron self-energy $\Sigma(x) = V(x)G(x)$ is computed and transformed back to $\Sigma(k)$ by iFFT.

Note that the addition of the constant Hartree term Σ^{H} to the self-energy is optional since μ is adjusted in every iteration. The final step of the iteration loop checks for convergence using $\max|\Sigma_{\mathrm{new}}(k) - \Sigma_{\mathrm{old}}(k)| < \varepsilon$, where the absolute error is typically $\varepsilon = 10^{-8}t$. If the self-energy $\Sigma(k)$ is converged, final values for the Green's functions G and D are recomputed and used to find the CDW and pairing susceptibilities. If not, a new dressed electron Green's function
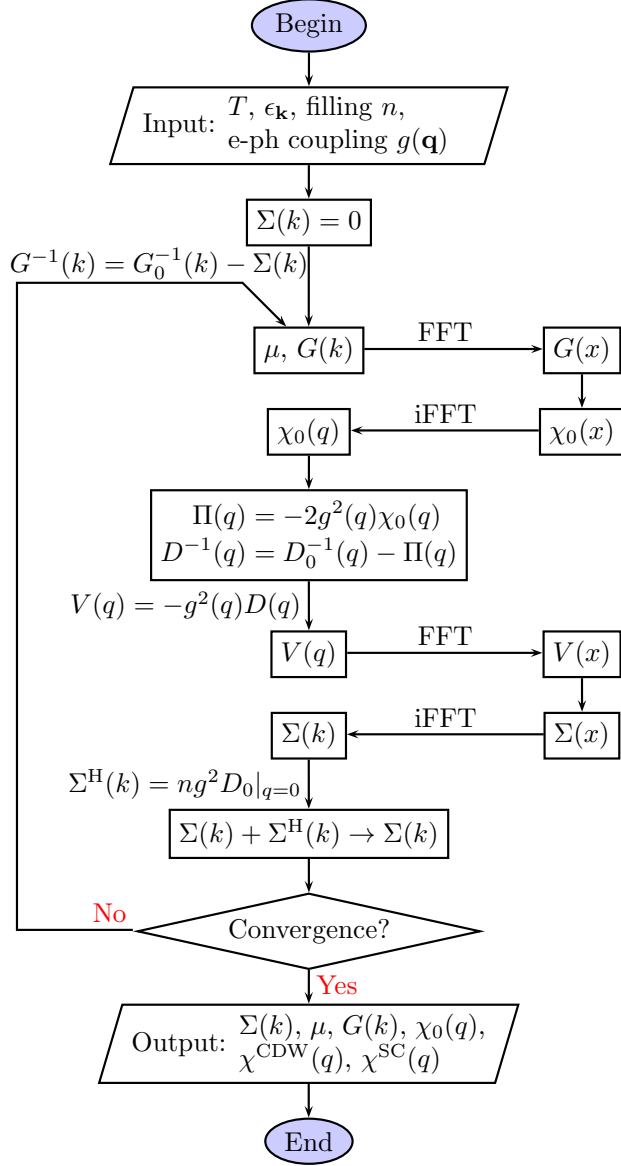
Figure 2.2: Algorithm for self-consistent iterations of Green's functions and self-energies with FFT. The Hartree self-energy $\Sigma^{\mathrm{H}} = n|g(\mathbf{q} = \mathbf{0})|^2 D_0(q = 0) = -2n|g(\mathbf{0})|^2/\Omega$ is a constant during iterations, and thus in practice the computation of Σ^{H} and the shift of electron self-energy $\Sigma(k) \to \Sigma(k) + \Sigma^{\mathrm{H}}$ can be moved outside the iteration loop and done after the convergence. Figure taken from our Ref. [1].

is computed by Dyson's equation, and the iteration loop continues. The self-consistency condition can usually be achieved within 20–100 iterations.

For the algorithm described above, three issues regarding our implementation deserve further remarks. The first remark concerns the Fourier transform of variables $k = (\mathbf{k}, i\omega_n) \xrightleftharpoons[\text{iFFT}]{\text{FFT}} x = (\mathbf{r}, \tau)$, where we need to consider the fact that the FFT only applies to discrete variables. In our case, the transform between $\mathbf{k}$ and $\mathbf{r}$ is straightforward for the lattice model, but the transform between ω_n and τ requires special care, especially for the electron Green's function. When transforming from $G(\omega_n)$ to $G(\tau)$, an infinite number of Matsubara frequencies must be summed to reproduce the discontinuity of $G(\tau)$ between $\tau = 0^+$ and $\tau = 0^-$. We accomplish such a feat by approximating $G(\omega_n)$ with the bare electron Green's function $G_0(\omega_n)$ for $|\omega_n| > \omega_c$, and thus the sum of Matsubara frequencies ω_n with $n \to \pm\infty$ can be carried out analytically. Transforming $G(\tau)$ to $G(\omega_n)$ requires a Fourier integral transform over the continuous variable $0 < \tau < \beta$. This Fourier integral is evaluated exactly following the interpolation of $G(\tau)$ using a continuous function such as spline or piecewise polynomial on the discrete τ grid. Further technical details on this procedure are provided in the supplemental section 2.6.

On a related note, Ref. [188] showed that if the effective interaction $V(\omega_n)$ has a simple analytical form, then the analytical form of the high frequency tail of $\Sigma(\omega_n)$ can be obtained and added to the sum with a finite frequency cut-off. As a result, the effect of the frequency cut-off is reduced, and a relatively low value can be chosen to speed up the computation together with an FFT similar to the one given here. However, comparing to Ref. [188], the major advantage of our algorithm is that it applies to any form of effective interaction $V(\omega_n)$, including ones where the bosonic self-energy modifies the interaction, without any additional cost. [2]

The second remark concerns the use of the Anderson acceleration (also called Anderson mixing) algorithm [190, 191, 192], which can be used to improve and accelerate the convergence of the simple fixed-point iteration scheme presented above. Conceptually,

---

[2]In our algorithm, the accuracy of the high frequency tail depends on the accuracy of the interpolant $G(\tau)$, which in turn depends on the τ-grid form and size, the type of interpolant, and the actual function $G(\tau)$ for a specific physical system. It is also possible to enforce the exact high frequency tail, for example, by imposing physical sum rules to the boundary conditions of a cubic spline interpolant. See Ref. [189]

Anderson mixing is a generalization of and an improvement to the simple mixing iteration method. In terms of our problem, the simple mixing dictates that $\tilde{G}_{\text{new}} = \alpha G_{\text{new}} + (1-\alpha)G_{\text{old}}$ is used in the next iteration instead of G_{new}, where $0 < \alpha < 1$ is a constant. Using Anderson mixing, values of G_{old} from the previous M iteration steps are mixed according to the coefficients $\{\alpha_i\}_{i=1}^{M}$, which are optimized for each iteration. In practice, we find that Anderson mixing is usually more efficient than simple mixing, even if an optimal α is chosen for simple mixing. Although both methods require a similar number of iterations to converge the self-energy, the Anderson mixing provides as much as a ten-fold reduction of the iterations required to converge the pairing vertex. For a detailed description of the algorithm, see Ref. [192].

The final remark concerns the behavior of our algorithm close to a phase transition T_{c} or sometimes simply at low T, where the initial input self-energy at the first iteration sometimes yields a diverged charge susceptibility. This premature divergence occurs when $\lambda W f(\mathbf{q})\chi_0(\mathbf{q}, 0) > 1$ for a few $\mathbf{q}$ points around the CDW ordering vector in the denominator of Eq. (2.16). To circumvent this problem we impose the condition $\lambda W f(\mathbf{q})\chi_0(\mathbf{q}, 0) \leq \tilde{\chi}$, where $\tilde{\chi}$ is a constant that is close to but less than unity. More specifically, we selectively change the value of $\chi_0(\mathbf{q}, 0)$ such that $\lambda W f(\mathbf{q})\chi_0(\mathbf{q}, 0) = \tilde{\chi}$ at the offending $\mathbf{q}$ points. Once the calculation is stabilized after a few iterations, this condition is removed. In practice, we allow $\tilde{\chi}$ to take values increasingly closer to unity, and usually in the range 0.995–0.99999. This cutoff is particularly important as the calculation approaches $T_{\text{c}}^{\text{CDW}}$, where we expect the charge density instabilities to be present. Establishing a proper cutoff sequence of $\tilde{\chi}$ can improve the quality of $T_{\text{c}}^{\text{CDW}}$ extrapolation.

2.3.2 Determination of Phase Transition Temperatures

To determine the phase transition temperatures $T_{\text{c}}^{\text{CDW}}$ and T_{c}^{SC}, we compute the CDW and pairing susceptibilities $\chi^{\text{CDW}}(\mathbf{q}, T)$ and $\chi^{\text{SC}}(T)$ with decreasing temperatures from above the phase transitions. In the thermodynamic limit ($N \to \infty$), the susceptibilities should diverge as $T \to T_{\text{c}}$. For a finite-size lattice, this divergence is limited once the correlation length ξ becomes comparable to the lattice size. Our goal is to determine T_{c} in the thermodynamic
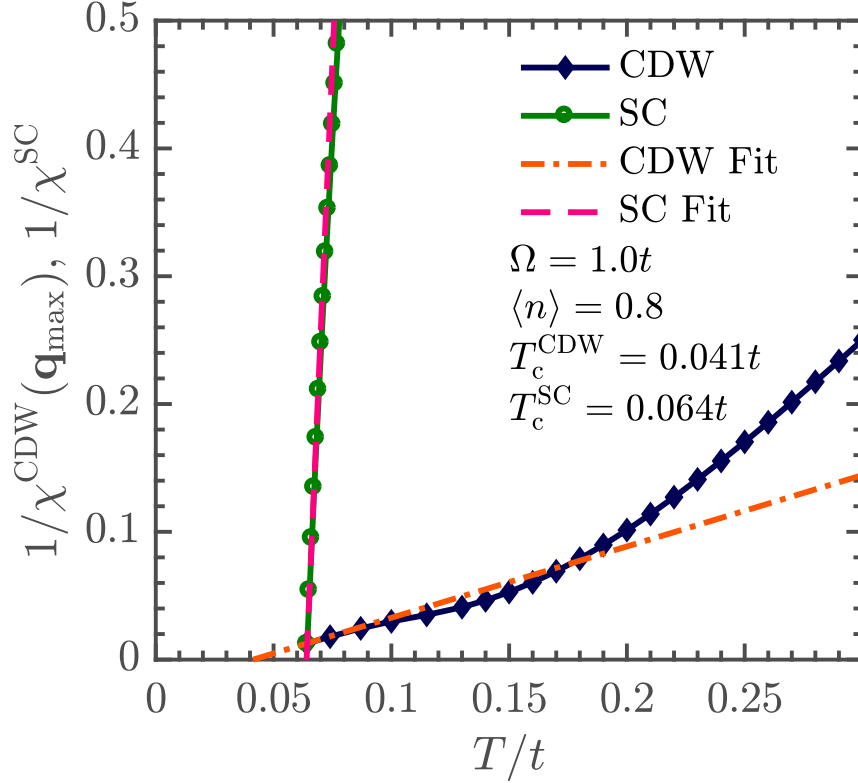
Figure 2.3: An example of extrapolating the inverse CDW and pairing susceptibilities to zero to obtain T_c on a lattice with $N = 64 \times 64$ and a coupling constant $\lambda = 0.3$. The dashed and dashed-dotted lines are linear fits to the three lowest temperature points and their intercepts on T-axis are the respective estimated T_c's in this procedure. This extrapolation is accurate for the superconducting T_c^{SC}; however, the more gradual approach of $1/\chi^{CDW}(\mathbf{q}_{max})$ to the T_c region makes T_c^{CDW} more susceptible to over(under)-estimation. Therefore, we use a different procedure to estimate T_c^{CDW} by fitting the low temperature $\chi^{CDW}(T)$ to the T-dependence of the 2D Ising universality class (See Sec. 2.3.2). Figure taken from our Ref. [1].
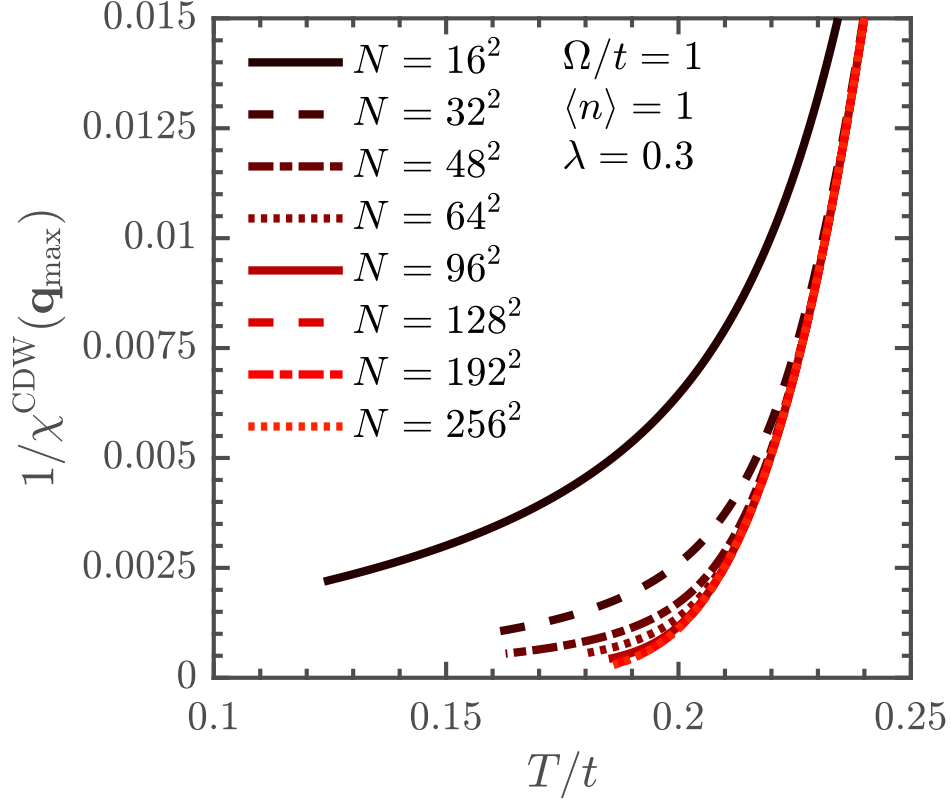
Figure 2.4: The dependence of $1/\chi^{\mathrm{CDW}}$ on the size of the lattice near T_c^{CDW}. For smaller lattice sizes, the temperature dependence deviates strongly from what is expected in the thermodynamic limit ($N \to \infty$). Consequently, the critical temperatures T_c^{CDW} found by fitting $\chi^{\mathrm{CDW}}(\mathbf{q}_{\mathrm{max}})$ with a model function $\chi^{\text{2D-Ising}}(T)$, depends strongly on the value of N (see Fig. 2.5). Figure taken from our Ref. [1].

limit by using sufficiently large lattice sizes such that a reliable extrapolation to $N \to \infty$ limit can be performed.

These values can be extracted in one of two ways: (i) by extrapolating the low T behavior of the inverse susceptibilities $1/\chi^{\mathrm{CDW}}(\mathbf{q}_{\mathrm{max}})$ and $1/\chi^{\mathrm{SC}}$ to zero as a function of temperature (e.g. Fig. 2.3); or (ii) by fitting the susceptibilities near the transition temperature with the appropriate asymptotic forms expected for their universality class in 2D.

It is well known [145] that the pairing susceptibility in a 2D system has a similar behavior to the Kosterlitz-Thouless [193] phase transition. However, we do not use this universality class in practice to find T_c^{SC} because we have found that the extrapolation of $1/\chi^{\mathrm{SC}}$ to the temperature axis provides a reliable estimate for T_c^{SC} (e.g., see Fig. 2.3) because of the relatively sharp divergence of the pairing susceptibility within the Migdal approximation. On the other hand, this same extrapolation procedure offers a T_c^{CDW} with a rather tenuous justification. As seen in Fig. 2.3, extrapolating the last few points in $1/\chi^{\mathrm{CDW}}(\mathbf{q}_{\mathrm{max}})$ tends to estimate the T_c^{CDW} significantly lower than the last obtainable point in the numerical calculation. Close to the transition, $\chi^{\mathrm{CDW}}(\mathbf{q}_{\mathrm{max}} = (\pi, \pi))$ is expected to follow the Ising universality class [146], which follows $\chi^{\mathrm{2D\text{-}Ising}}(T) = A \left| \frac{T - T_c}{T_c} \right|^{-\gamma}$, where $\gamma = 7/4$. The critical temperatures can thus be obtained by fitting the CDW susceptibility results to this model. Notice that the slope $1/\chi^{\mathrm{2D\text{-}Ising}}(T)$ approaches zero as $T \to T_c^+$. This partially explains the potential inaccuracy of linear extrapolation for T_c^{CDW} since it is expected that $1/\chi^{\mathrm{CDW}}(\mathbf{q}_{\mathrm{max}})$ will not sharply cross the temperature axis.

The accuracy of the Ising fit to χ^{CDW} significantly depends on the lattice-size. In fact, at smaller sizes such as 4×4 and 8×8, the model above is a remarkably poor descriptor of the χ^{CDW} results. As we increase the lattice to 128×128 and above, we see that the susceptibility more closely follows the expected Ising form (See Fig. 2.4). The resulting finite size dependence of T_c^{CDW} is shown in Fig. 2.5 for the isotropic coupling case, with $\Omega/t = 1$, at half-filling. Here, the changes in T_c^{CDW} are pronounced until $N \sim 128^2$ while T_c^{SC} is approximately flat for $N \geq 16^2$. Furthermore, as shown in Fig. 2.3, for fillings very close to the CDW and superconductivity phase boundary, the comparable values for T_c^{CDW} and T_c^{SC} make the careful extrapolation more important. We adhere to a convention that
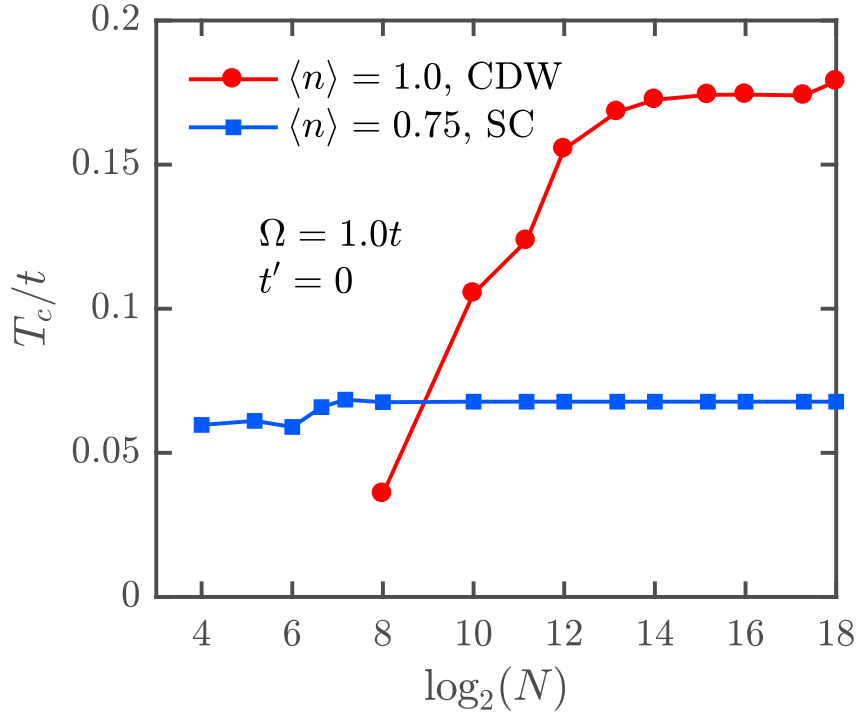
Figure 2.5: The finite size dependence of T_c on the logarithm of the total number of sites $\log_2(N)$ for the Holstein model (isotropic e-ph coupling). The fillings $n = 1.0$ and $n = 0.75$ correspond to parts of the phase diagram that yield CDW and SC phases, respectively, for $\Omega/t = 1.0$, $\lambda = 0.3$, and $t' = 0$. The value of T_c^{SC} has converged for $N = 16 \times 16$, whereas T_c^{CDW} has significant dependence on lattice size N. The value of T_c^{CDW} was obtained from the model fit $\chi^{\text{2D-Ising}}(T)$. For $\log_2(N) \geq 8$, the values of N are identical to those shown in the legend of Fig. 2.4. Five additional smaller lattice sizes ($\sqrt{N} = 4, 6, 8, 10, 12$) are plotted for T_c^{SC} to show the variations due to finite size effects Figure taken from our Ref. [1].

when the CDW and superconducting phases have comparable transition temperatures, the winning phase is determined by the larger of the extrapolated T_c^{CDW} and T_c^{SC}.

2.4 Results

2.4.1 Temperature-filling Phase Diagram

First, we report the full temperature-filling phase diagram within the Migdal approximation for the 2D Holstein model with isotropic e-ph coupling $g(\mathbf{q}) = g$ and only the NN hopping t. Fig. 2.6 shows results for hole-doped case with filling $0 \leq n \leq 1$ and three different phonon frequencies. The electron-doped side is identical due to particle-hole symmetry. The phase boundaries in all three panels in Fig. 2.6 are plotted together in Fig. 2.7 for an easy comparison.

As expected, we observe the competition between CDW and superconducting (SC) ground states, where the CDW phase dominates close to half-filling. For large phonon frequencies, the CDW phase always appears at $\mathbf{q}_{\text{max}} = (\pi, \pi)$ but is rapidly suppressed for a small degree of doping away from half-filling. For the smallest phonon frequency ($\Omega = 0.1t$), we find larger values of T_c^{CDW} indicating a slight decrease in χ_0. Moreover, we observe an incommensurate CDW phase for filling levels below $n \approx 0.8$. This incommensurate ordering can be distinguished from the commensurate case by noting that when $T \to T_c^{\text{CDW}}$, the function $\chi^{\text{CDW}}(\mathbf{q})$ develops peaks at $\mathbf{q}_{\text{max}} = (\pi, \kappa\pi)$ with $0 < \kappa \leq 1$ (and its symmetry equivalent positions). These four peaks split off from a single broader peak originally centered at (π, π) at high temperatures as $T \to T_c^{\text{CDW}}$. At intermediate temperatures, these four peaks largely overlap resulting in a plateau centered at (π, π). In the commensurate case, $\chi^{\text{CDW}}(\mathbf{q})$ has a single global maximum at (π, π) for nearly all the temperatures examined. We also observe strong incommensurate charge correlations when Ω is large but in this case the superconducting phase forms before the long-range incommensurate charge order forms.

Once the CDW correlations are sufficiently suppressed at lower values of n, the s-wave superconducting correlations dominate. Our results show that superconducting transition temperature T_c^{SC} depends strongly on the phonon frequency Ω. The fact that T_c^{SC} strongly
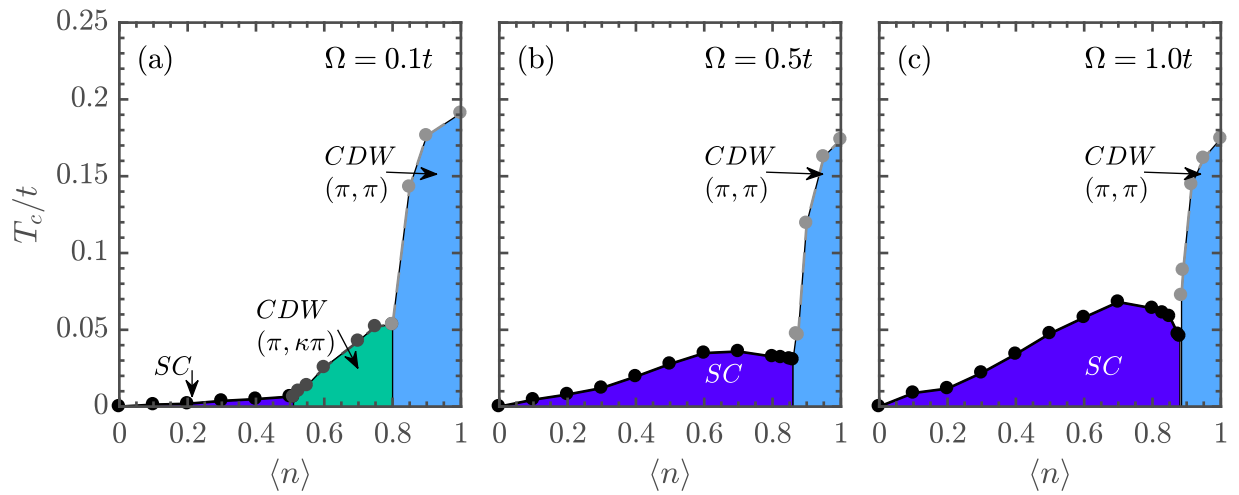
Figure 2.6: The temperature-filling phase diagram for the Holstein model for (a) $\Omega = 0.1t$, (b) $\Omega = 0.5t$, and (c) $\Omega = t$. Results were obtained on a $N = 128^2$-site lattice and for a dimensionless coupling $\lambda = 0.3$. Figure taken from our Ref. [1].
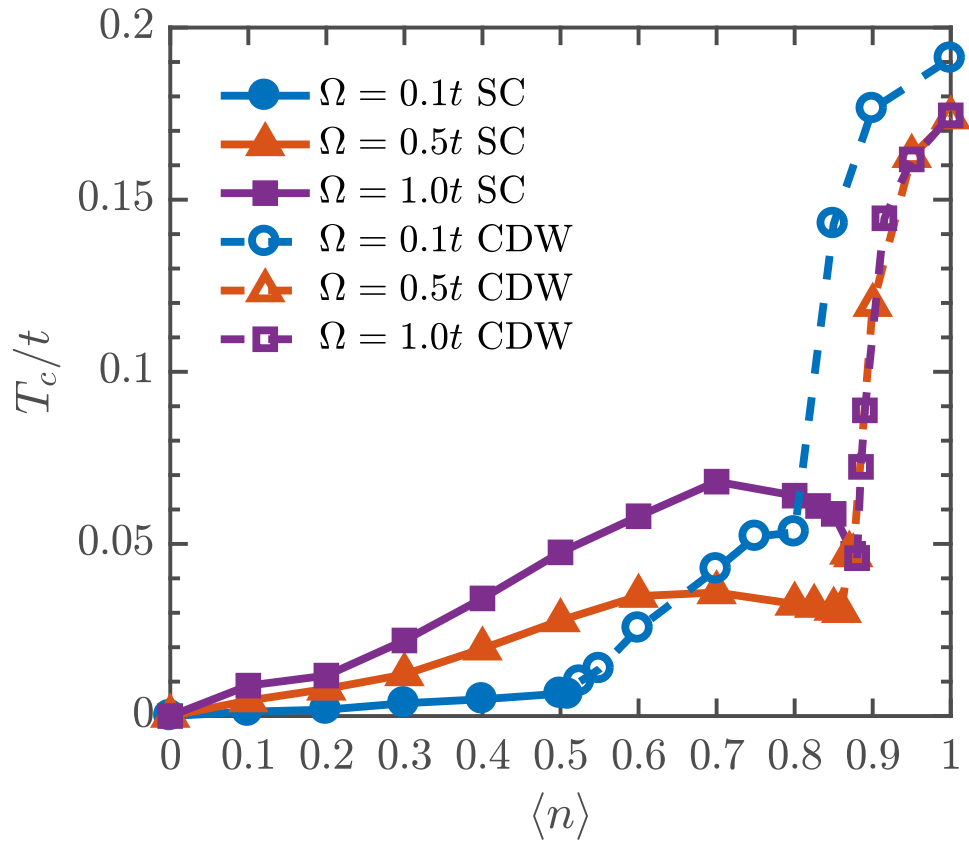
Figure 2.7: A comparison of the three phase diagrams shown in Fig. 2.6. Figure taken from our Ref. [1].

depends on Ω while T_c^{CDW} depends more on electronic properties is in qualitative agreement with solutions to the Holstein model in the infinite dimensional limit [156]. Interestingly, we observe non-monotonic behavior in the superconducting T_c, where the maximum value of T_c occurs for fillings away from the CDW phase boundary. This "dome" in the superconducting region of the phase diagram becomes more pronounced as the phonon frequency increases. We will discuss the origin of this behavior in Sec. 2.4.5.

2.4.2 The effects of longer-range hopping on the phase diagram

Previous studies of the Holstein model [147] and the attractive Hubbard model [194] found that enhanced pairing occurs when the Fermi level E_{F} lies near the Van Hove singularity once NNN hopping is included. With this motivation, we now turn our attention to the effects of t' on the phase diagram. In this case, the lack of particle-hole symmetry requires us to consider the temperature-filling phase diagram across the full range of electronic fillings, as shown in Fig. 2.8. We consider two representative values $\Omega = 0.1t$ [Figs. 2.8(a) and 2.8(c)] and $\Omega = t$ [Figs. 2.8(b) and 2.8(d)] and fix $t' = -0.25t$, chosen to reflect a phase factor of opposite sign commonly encountered in diagonal hopping scenarios. We note that a choice of opposite sign merely creates a mirror image (with respect to $n = 1$) of depicted the phase diagrams, i.e., changing $n \to 2 - n$ in the x-axis.

Many of the effects of t' can be understood from its influence on the bare electronic structure. The Van Hove singularity in the bare 2D electronic density of states (DOS) shifts below (above) the middle of the band when $t' < 0$ ($t' > 0$) and, moreover, the Fermi surface inherits curvature that weakens nesting near half-filling. These changes, which are not mutually exclusive, are collectively associated with the suppression of charge-density correlations near half-filling. Upon hole doping, the Fermi surface for $t' < 0$ moves towards the Van Hove singularity, thus increasing the electron energy degeneracy where strong pairing correlations are already present and enhancing the superconducting correlations on the hole-doped side of the phase diagram. Conversely, the superconducting state on the electron-doped side of the phase diagram is suppressed. These changes are most prominent for large Ω and clearly seen in the contrast between the top (for $t' = 0$) and the bottom row (for $t' \neq 0$) in Fig. 2.8.
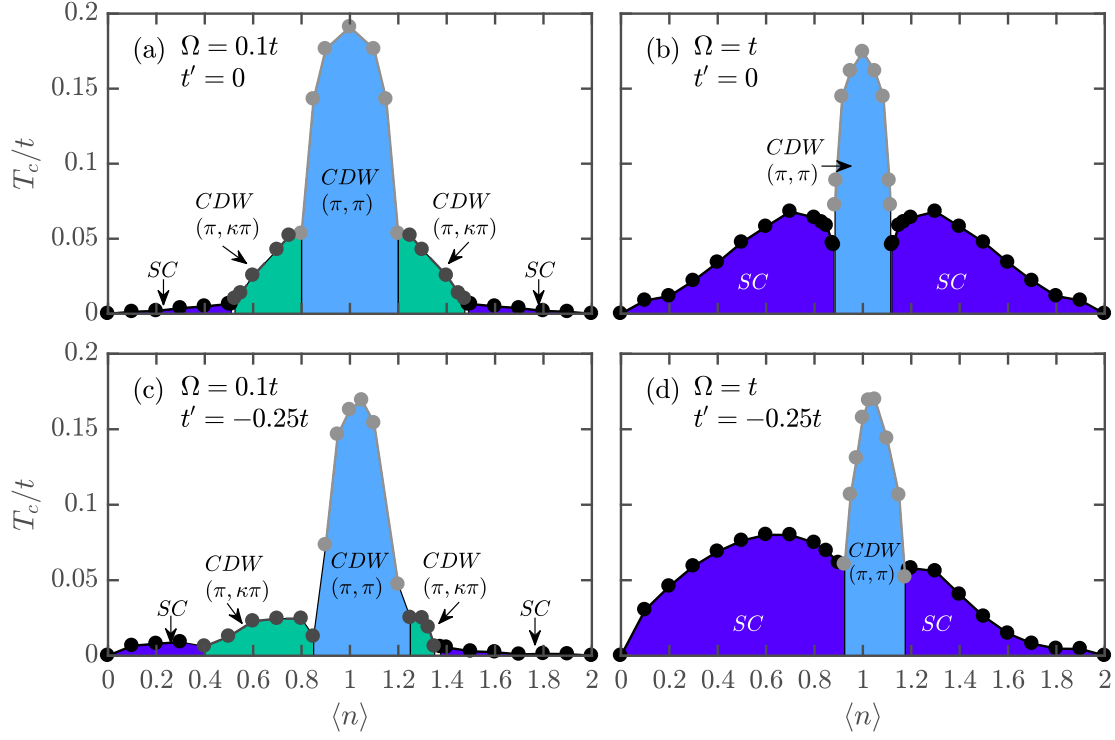
Figure 2.8: Comparison of the temperature-filling phase diagrams for Holstein model with or without NNN hopping t'. (a) $\Omega = 0.1t$, $t' = 0$; (b) $\Omega = t$, $t' = 0$; (c) $\Omega = 0.1t$, $t' = -0.25t$; and (d) $\Omega = 0.1t$, $t' = -0.25t$. Results were obtained on a $N = 128^2$ site lattice and for a dimensionless coupling $\lambda = 0.3$. Figure taken from our Ref. [1].

The effects of a longer-range hopping are more subtle for the smaller phonon frequency $\Omega = 0.1t$. Here, t' lowers the transition temperatures of the commensurate and incommensurate CDW phases both for all dopings. At the same time, the boundary of the incommensurate CDW region is modified such that it extends towards smaller values of n with hole doping. Likewise, the SC phase on the hole-doped side is confined to a smaller region of fillings but with an enhanced superconducting T_c. On the electron-doped side, the superconducting region also extends over a broader range of fillings but the overall T_c is suppressed.

Similar asymmetric features in the phase diagram can result from other modifications/extensions of the Holstein model. For instance, adding a small anharmonic term to the Holstein Hamiltonian also results in an asymmetric phase diagram with a larger SC phase and suppressed CDW phase on one side of half-filling [195]. In that case, the changes in the phase diagram are the result of the modified phonon potential, which constrains the phonon displacements and enhances superconductivity. A more recent study focused on the electron effective mass m^* [196]; however, in the 2D weak coupling case, the changes to m^* resulting from $t' \neq 0$ are quite small and effectively negligible. We also note that NNN hopping can influence the competition between charge density and pairing correlations. In some real materials (e.g., transition metal dichalcogenides) it can be difficult to determine whether CDW and SC correlations are working together or competing for order [197]. In this simple model calculation, we find evidence for the latter through the absence of *both* large pairing and charge density correlations together near a critical temperature, as well as a decreasing T_c^{SC} near the SC-CDW phase boundary.

2.4.3 Momentum Dependent Electron-Phonon Coupling

The traditional Holstein model can be easily extended by introducing fermionic ($\mathbf{k}$) and bosonic ($\mathbf{q}$) momentum dependence to the e-ph coupling constant $g \to g(\mathbf{k}, \mathbf{q})$. As mentioned in section (2.2.2), our FFT-based algorithm can easily incorporate models where the vertex depends on the boson wavevector $g(\mathbf{q})$. In general, we have found that convergence of the self-consistent equations is more challenging for such models near phase transitions, and it can become difficult to develop a full temperature dependence for the susceptibilities across

all fillings relative to the isotropic coupling case. Nevertheless, we have obtained results for several popular models for the high-T_c cuprates with a momentum dependent $g(\mathbf{q})$, which we present in this section.

The behavior of the susceptibilities χ^{CDW} and χ^{SC} for a given $g(\mathbf{q})$ is examined across a small range of λ values in Fig. 2.9 and Fig. 2.10, respectively. All of the results were obtained using a 32×32 lattice with $\Omega/t = 0.5$, and NN-hopping only ($t' = 0$). The first, second, and third rows of the figures correspond to isotropic, buckling, and breathing models, respectively (see Sec. 2.2.2). The individual columns show results for temperatures $T/t = 0.4$, 0.2, and 0.1 from left to right. The white regions indicate parameter ranges where no data is plotted. The vertical axis in Fig. 2.9 and Fig. 2.10 contain data points for ten values of λ separated by increments of $\Delta\lambda = 0.02\bar{2}$. Although the spacing in filling points along the horizontal axis is comparable ($\Delta n = 0.025$), the plot range is larger, making it appear as though $\Delta\lambda$ was disproportionately coarse. As a result, we see that the boundary separating the susceptibility contours from the white region is jagged in appearance. Although the boundary is expected, it should be smooth in the limit where $\Delta\lambda \to 0$. Therefore, no physical meaning should be attributed to the uneven nature of the boundary. Despite this unwanted cosmetic detail, the white region beyond the (colored) contours is, to a good approximation, where the system would have settled into a charge ordered phase peaked at some vector $\mathbf{q}_{\mathrm{max}}$.

For the isotropic and breathing cases, we find that the CDW correlations are strongest at $\mathbf{q}_{\mathrm{max}} = (\pi, \pi)$. These results are expected since $\mathbf{q} = (\pi, \pi)$ corresponds to a strong nesting condition near half-filling and $g(\mathbf{q})$ for the breathing mode is largest at this wavevector. For the buckling case, we find the CDW correlations are strongest at $\mathbf{q}_{\mathrm{max}} = (0, 0)$. This is also not surprising since $g(\mathbf{q})$ for this model places most of the scattering weight on $\mathbf{q}_{\mathrm{max}} = (0, 0)$ and none on the nesting vector (at half-filling) (π, π). We interpret large charge correlations at $\mathbf{q}_{\mathrm{max}} = (0, 0)$ as a reflection of a tendency towards phase separation since we are considering a single-orbital model without the possibility for any intracell charge order.

By comparing the results at different temperatures it becomes clear that the momentum dependent models yield higher T_c^{CDW}'s than the isotropic case. For the Hosltein coupling [Figs 2.9(a)–(c)] the CDW correlations build somewhat tightly around half-filling whereas
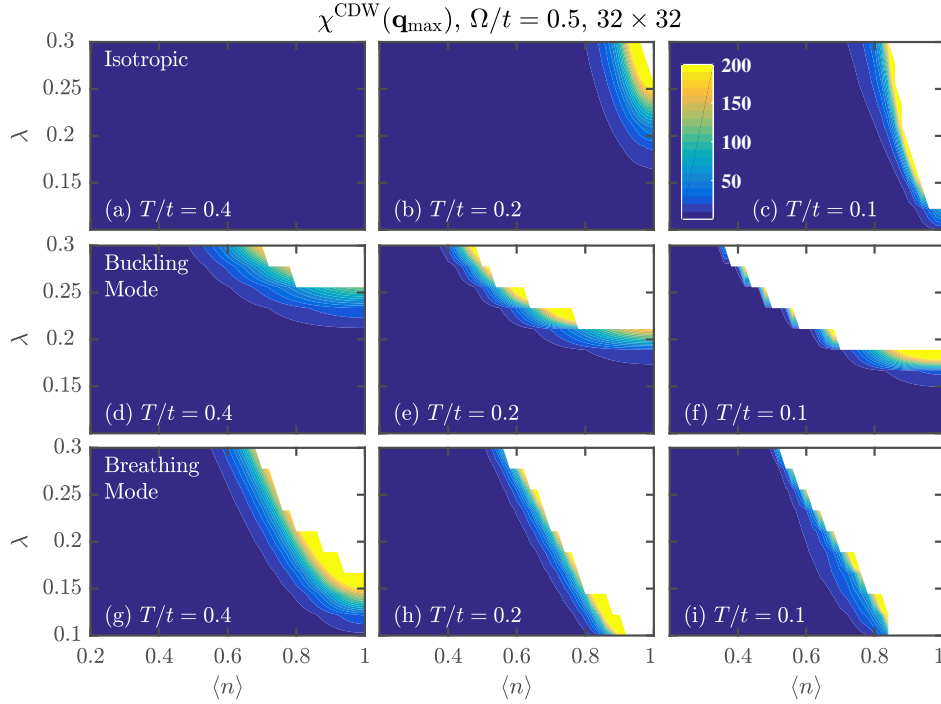
Figure 2.9: The charge susceptibility for three decreasing temperatures plotted using contours over a window of λ vs n. Panels (a)–(c) show the Holstein (isotropic) coupling case, where a strong CDW susceptibility peaked at $\mathbf{q}_{max} = (\pi, \pi)$ emerges near and at half-filling. Panels (d)–(f) show results for the buckling case, which reveal the onset of susceptibility peaked at $\mathbf{q}_{max} = (0, 0)$. This is not representative of a CDW with long range order and could be an indication of phase separation. The last row of panels (g)–(i) show results for the breathing mode coupling, which strongly favors a CDW phase peaked at $\mathbf{q}_{max} = (\pi, \pi)$ for larger regions of the parameter space. Introducing the breathing and buckling mode $\mathbf{q}$-dependence into the e-ph coupling has significant influence over the competition between pairing correlations and charge-density correlations. Figure taken from our Ref. [1].
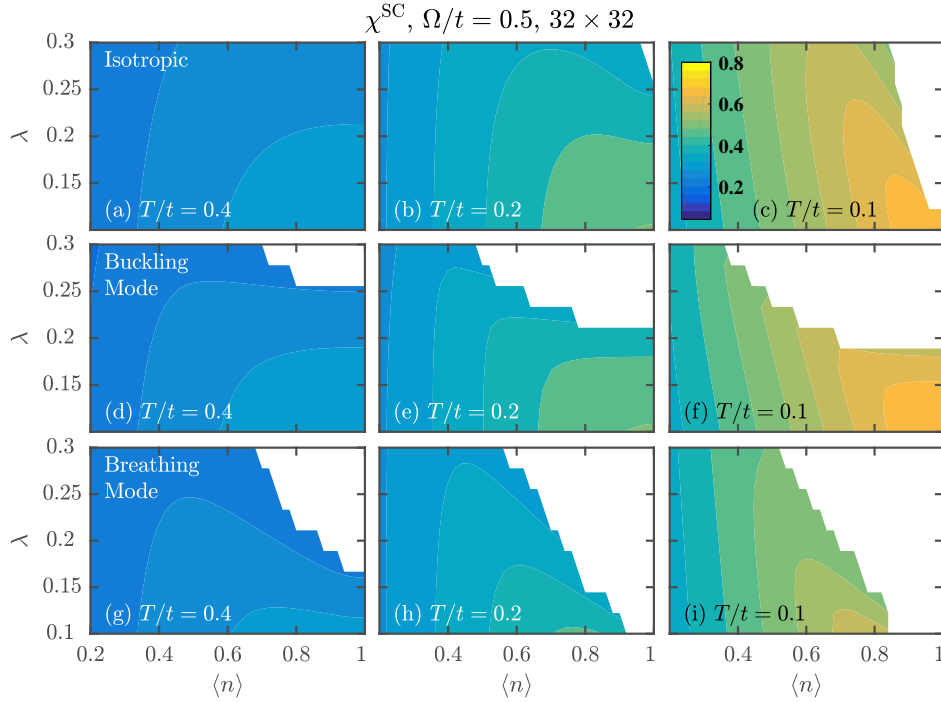
Figure 2.10: The pairing susceptibility for three decreasing temperatures plotted using contours over a window of λ vs n. Similar to Fig. 2.9, panels (a)–(c) correspond to the Holstein (isotropic) coupling case, panels (d)–(f) for the buckling mode coupling, and panels (g)–(i) for the breathing mode coupling. Each temperature progression shares qualitatively similar features with pairing correlations largely suppressed at these temperatures. However, it should be noted that the Holstein case is unique. With the CDW region so closely confined to the half-filling region, pairing correlations can develop at higher temperatures. A superconducting phase does emerge for each of the $g(\mathbf{q})$ cases, but the strong charge density correlations in the buckling and breathing mode cases push the SC boundary to lower values of n. Figure taken from our Ref. [1].

they extend much further as a function of both n and λ once a momentum dependent coupling is introduced. A momentum dependent coupling also influences the s-wave pairing tendencies. As shown in Fig. 2.10, the contour lines for large values of χ_c^{SC} extend over larger n and λ in the Holstein case. We have performed other calculations confirming that the s-wave superconducting correlations generally shift to more dilute fillings and lower T once the e-ph vertex depends on $\mathbf{q}$. It should be emphasized that the contours in Fig. 2.10 can be somewhat deceptive since the temperatures at which χ^{SC} are plotted are well above T_c^{SC}. For instance, χ^{SC} seems to be peaked at occupancies of $n \sim 0.8 - 1$ and couplings $\lambda \sim 0.1$ in Fig. 2.10, but this peak actually shifts to lower fillings and larger λ values as the temperature is lowered further. When we decrease the temperature so that $T \approx T_c^{SC}$, we see a rapid growth of χ^{SC} near the phase boundary as shown in Fig. 2.11(b). This figure reveals that the highest T_c^{SC} occurs for larger λ (for the range shown) and the features leading to the SC dome in Fig. 2.6(b) can be seen. If we were to superimpose Fig. 2.11(b) onto Fig. 2.11(a), the correlations for pairing and a CDW would form a valley in-between the domes for each phase, reminiscent of the phase diagrams presented earlier.

2.4.4 Renormalized Phonon Dispersions at Half-filling

Until now we have largely focused on the electronic properties of the model. It is also instructive, however, to consider the renormalization of the phononic properties in proximity to the CDW phase. In this section, we present the spectral properties of the phonons, which are obtained by analytically continuing the phonon Green's function to the real axis using Padé approximants [198]. Fig. 2.12 shows the phonon spectral function $B(\mathbf{q}, \omega) = -\Im D(\mathbf{q}, i\nu_m \to \omega + i0^+)/\pi$ as a function of temperature along the high-symmetry path of the first Brillouin zone. Here, we are considering the case of a momentum-independent Holstein coupling, half-filling $n = 1.0$, $\lambda = 0.19$, and $\Omega/t = 1.0$. These spectra compare well with the results obtained from determinant QMC simulations [199] carried out for comparable values of λ but on a smaller lattice ($\lambda = 0.25$, 8×8).

Our first observation is that the overall energy of the phonon branch has softened significantly due to the electron-phonon coupling. Due to the proximity of the CDW phase, the phonon spectral function also has a pronounced Kohn-like anomaly, where spectral weight
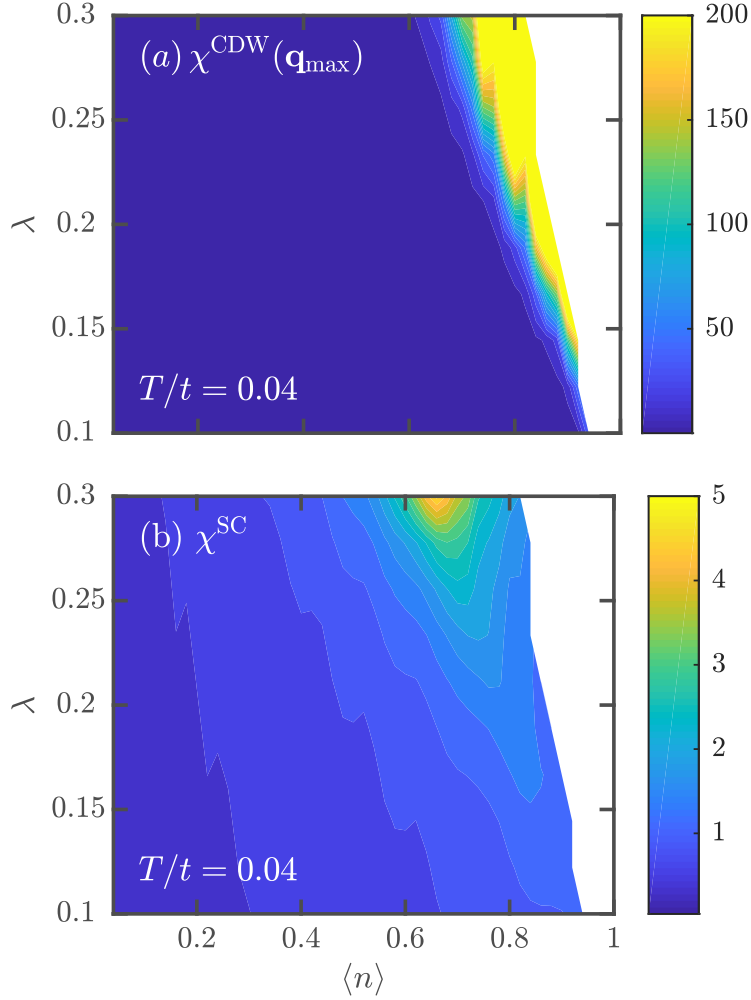
Figure 2.11: For the isotropic coupling case with $\Omega = 0.5t$, $T = 0.04t$, and $t' = 0$, we plot the (a) charge-density wave susceptibility $\chi^{\mathrm{CDW}}(\mathbf{q}_{\max})$ and (b) singlet-pairing susceptibility χ^{SC} using a 32×32 lattice. At this lower temperature we see the pairing correlations becoming more significant around $\lambda = 0.3$ and $n \approx 0.66$, which corresponds to a point near the top of the $T_{\mathrm{c}}^{\mathrm{SC}}$-dome in Fig. 2.6. Figure taken from our Ref. [1].

becomes concentrated at $\mathbf{q} = (\pi, \pi)$ and $\omega \approx 0$. As the temperature is lowered, and the charge correlations grow, spectral weight is redistributed to lower energies and the Kohn anomaly becomes sharper. Although it is not shown here, we have also found that in the case of the buckling mode coupling, the spectral weight indeed concentrates at $\mathbf{q} = \mathbf{0}$.

We expect that the renormalization of the phononic properties will influence the superconducting phase in nontrivial ways. For example, within weak coupling BCS theory, the superconducting transition temperature is given by $T_{\mathrm{c}} \propto \Omega \exp(-1/\lambda)$. The phonon dispersion enters this expression twice, once in the prefactor and once in the dimensionless coupling constant $\lambda \propto 1/\Omega$. The softening of the phonon branch observed in Fig. 2.12 will, therefore, simultaneously reduce the energy scale of the Cooper pairs and enhance the pairing strength. Which of these effects dominates is a nontrivial question, which is addressed in the following section.

2.4.5 Origin of the Superconducting Dome

As we noted in Sec. 2.4.1, we observe a non-monotonic behavior in the superconducting T_{c}, where the maximum value of T_{c} occurs for fillings away from the boundary of the CDW phase. This "dome" in the superconducting region of the phase diagram becomes more pronounced as the phonon frequency increases and arises from an interplay of the renormalized phononic and electronic properties.

To better understand how the dome appears, we examined several quantities commonly linked to pairing. These include the electronic density of states (DOS) $N(\omega)$ (per spin), the Eliashberg function $\alpha^2 F(\omega)$, the renormalized e-ph coupling $\lambda^{\alpha^2 F}$, the logarithmic average frequency $\omega_{\log}$, and the superconducting critical temperature T_{c} (estimated by various approaches from the quantities examined here). All of these quantities are calculated and shown in Fig. 2.13 over a range of electron occupancy $n \in [0.6, 0.8]$ using a fixed momentum $\mathbf{k}$-grid $N = 64 \times 64$, [3] $t' = 0$, a bare phonon frequency $\Omega = t$, and a bare dimensionless e-ph coupling $\lambda = 0.3$. Note that for panels 2.13(a) and 2.13(b), the calculations are performed on

---

[3] As indicated by the blue line in Fig. 2.5, this size is sufficiently large to discuss the superconductivity at the fillings considered. Except for the lattice size, all input parameters used in Fig. 2.13 are the same as Fig. 2.6(c). Therefore, the T_{c} dome within the same filling range in Fig. 2.6(c) and Fig. 2.13(c) (square symbols in the plot) are comparable, if not identical.
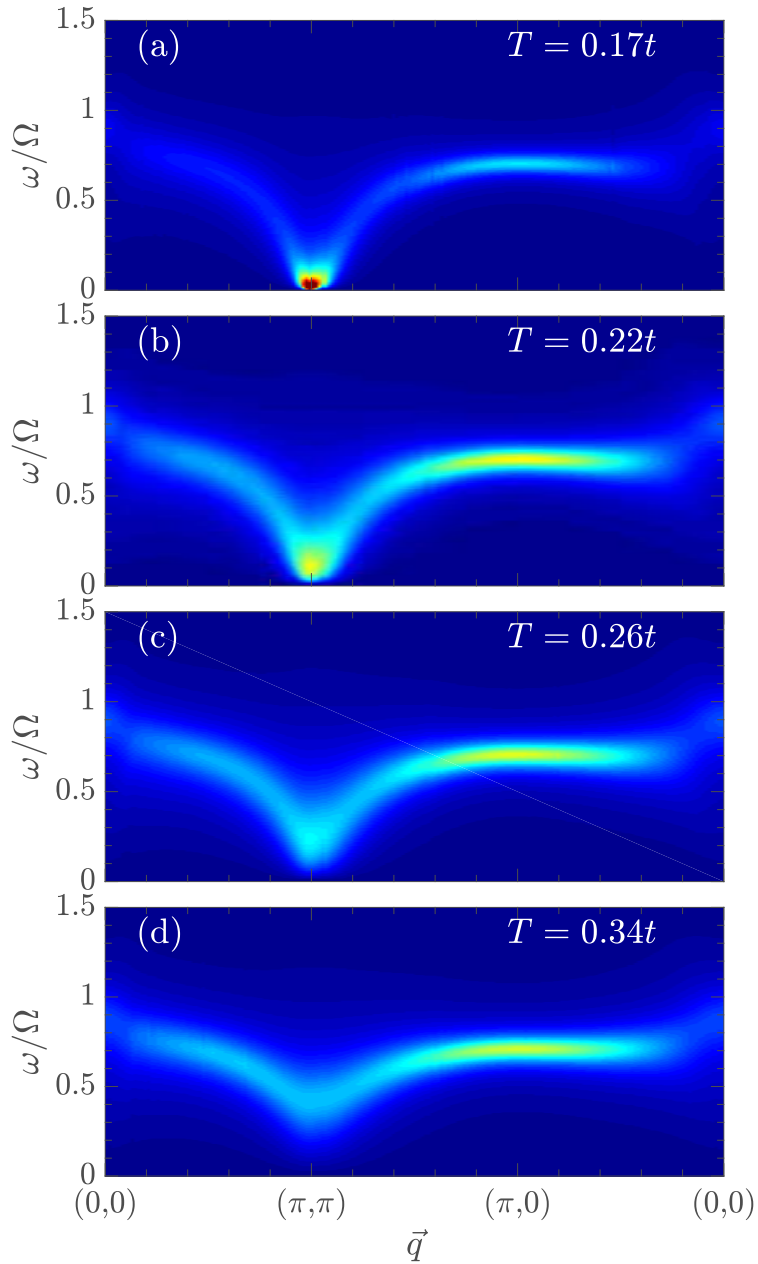
Figure 2.12: The temperature dependence of the phonon spectral function $B(\mathbf{q}, \omega) = -\Im D(\mathbf{q}, i\nu_m \to \omega + i0^+)/\pi$ for the half-filled Holstein model with $\lambda = 0.1875$. Results were obtained on an $N = 128^2$ cluster and the analytic continuation was performed using Padé approximants. The actual CDW transition temperature is $T_{\mathrm{c}}^{\mathrm{CDW}} = 0.144t$. Figure taken from our Ref. [1].

the imaginary frequency axis at a temperature $T = 0.07t$, [4] and then analytically continued onto the real frequency axis using Padé approximants [198] with a small imaginary part $\eta = 0.005t$. Moreover, the frequency ω in these two plots is measured with respect to the chemical potential μ. The calculation of μ occurs on the imaginary axis, and any shifts in μ stemming from the Padé procedure, if they exist, are negligibly small since the filling from integrating the DOS over ω is essentially unchanged.

The DOS is calculated by summing the electron spectral function $A(\mathbf{k}, \omega) = -\text{Im}[G(\mathbf{k}, \omega)]/\pi$ over momentum and is given by

$$N(\omega) = \frac{1}{N} \sum_{\mathbf{k}} A(\mathbf{k}, \omega), \tag{2.19}$$

where $G(\mathbf{k}, \omega) \equiv G(\mathbf{k}, i\omega_n \to \omega + i0^+)$. In Fig. 2.13(a), the solid curves represent $N(\omega)$ at various fillings, with the bright (dark) colors corresponding to smaller (larger) values of n. The two dash-dotted curves are the noninteracting DOS for the lowest filling $n = 0.6$ (light blue) and the highest filling $n = 0.8$ (dark blue) and are obtained from the exact result at $T = 0$ (elliptic integral function for a cosine band structure). Although not shown here, a plot of the non-interacting DOS for $T \neq 0$ using a finite $\mathbf{k}$-grid would also exhibit a broadened profile similar to $N(\omega)$; however, unlike the interacting case, the peak position would remain at half-filling (i.e. the Van Hove singularity). The effect of filling in the non-interacting case is just a rigid band shift of μ, while the shape of the interacting DOS, has a strong dependence on the filling. In fact, the interacting DOS at the ω corresponding to half-filling is strongly suppressed to a small hump for $n = 0.6$, and even disappears for $n = 0.8$. Lastly, and perhaps most importantly, the DOS near and at the Fermi level $N_{\text{F}} = N(0)$ has a non-monotonic dependence on the filling n. More specifically, the peak actually shifts from $\omega > 0$ for $n \sim 0.6$ to $\omega < 0$ for $n \sim 0.8$. In other words, this shift of the peak in $N(\omega)$ approximately follows the T_{c} dome over n as it moves from $\omega > 0$ to $\omega < 0$.

The isotropic Eliashberg function $\alpha^2 F(\omega)$, also known as the electron-phonon spectral function, can be obtained by taking a double Fermi-surface average of the product between the squared e-ph coupling $|g(\mathbf{q})|^2$, the phonon spectral function $B(\mathbf{q}, \omega)$, and the DOS at

---

[4]This temperature is slightly greater the T_{c} dome. We have checked by solving the eigenvalue problem that the pairing vertex at this T is enhanced proportional to the T_{c} at each respective filling considered.
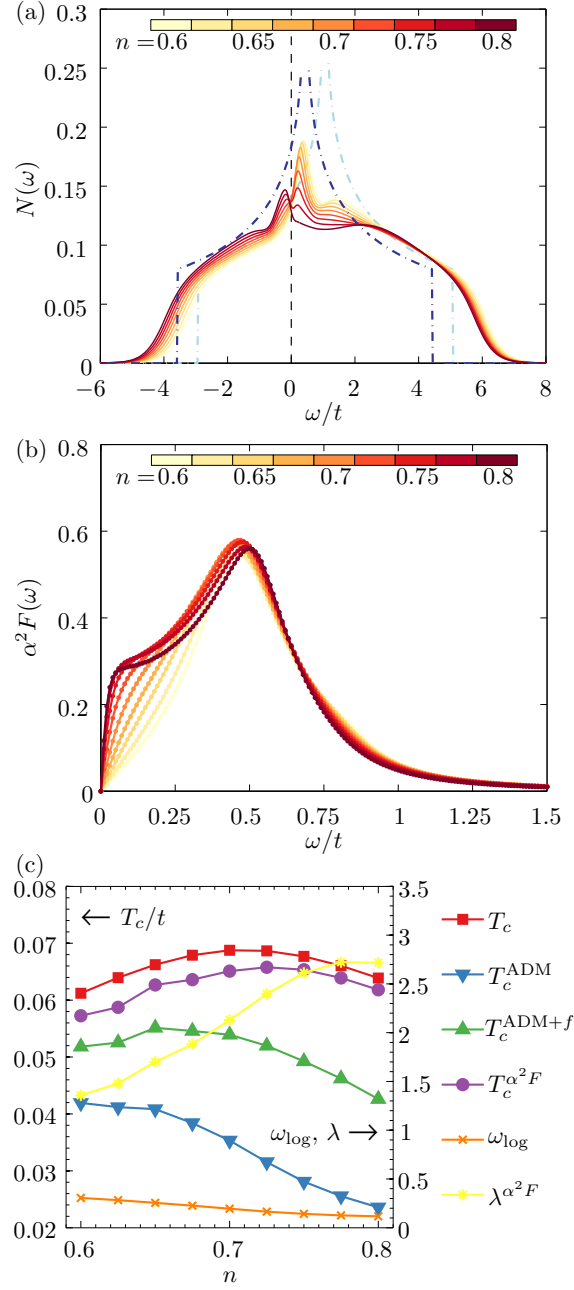
Figure 2.13: (a) the electron density of states $N(\omega)$, (b) the Eliashberg function $\alpha^2 F(\omega)$ multiplied by a factor of N_F/N_F^{fd}, and (c) T_c, $\omega_{\log}$, and λ as a function of n. A factor of N_F/N_F^{fd} is included in $\alpha^2 F(\omega)$ and $\lambda^{\alpha^2 F(\omega)}$. The factor of N_F/N_F^{fd} is used to account for differences between the exact DOS and the DOS estimated by a sum of delta functions. Figure taken from our Ref. [1].

the Fermi-level $N_F = N^{-1} \sum_{\mathbf{k}} \delta(\xi_{\mathbf{k}'})$, given by

$$\alpha^2 F(\omega) = \langle\langle N_F | g(\mathbf{k} - \mathbf{k}')|^2 B(\mathbf{k} - \mathbf{k}', \omega)\rangle\rangle_{FS}, \tag{2.20}$$

where the double Fermi surface average is defined by

$$\langle\langle f(\mathbf{k} - \mathbf{k}')\rangle\rangle_{FS} = \frac{\displaystyle\sum_{\mathbf{k}}\sum_{\mathbf{k}'} f(\mathbf{k} - \mathbf{k}')\delta(\xi_{\mathbf{k}})\delta(\xi_{\mathbf{k}'})}{\displaystyle\sum_{\mathbf{k}}\sum_{\mathbf{k}'} \delta(\xi_{\mathbf{k}})\delta(\xi_{\mathbf{k}'})}. \tag{2.21}$$

Here, the phonon spectral function $B(\mathbf{q}, \omega)$ is calculated from the renormalized phonon Green's function as defined in Section 2.4.4. The delta functions appearing in Eq. (2.21) and in other calculations are not true Dirac delta functions but are instead "smeared" delta functions, denoted as $\tilde{\delta}(x)$. These approximate delta functions are used when the system is constrained to a finite $\mathbf{k}$-grid. We use a Fermi-Dirac smearing given by

$$\tilde{\delta}_{fd}(x) = -\frac{d}{dx}\left(\frac{1}{e^{x/\sigma} + 1}\right) = \frac{1}{4\sigma \cosh^2\left(\frac{x}{2\sigma}\right)},$$

which we use to obtain a DOS at the Fermi-level $N_F^{fd} = N^{-1} \sum_{\mathbf{k}} \tilde{\delta}_{fd}(\xi_{\mathbf{k}})$ with the broadening parameter $\sigma = T$. The family of curves in Fig. 2.13(b) shows the change in $\alpha^2 F(\omega)$ over a range in n. We have included factor of N_F/N_F^{fd} in $\alpha^2 F(\omega)$ to account for the differences between the exact DOS

Notice that $\alpha^2 F(\omega)$ in Fig. 2.13(b) (for all fillings shown) is peaked at a frequency lower than the bare frequency $\Omega = 1.0t$, indicating that the phonon branch has renormalized. Recall from Fig. 2.12 that phonon spectral weight shifts to lower frequency as the temperature is lowered, indicating corrections to the dispersion stemming from the formation of a CDW. For fillings relevant to the T_c-dome, the dispersion also shows signatures of competing CDW order developing, but now it is *incommensurate*. This implies that the system can approach a superconducting phase and simultaneously show signatures of CDW driven renormalization of the phonon dispersion. Referring back to Fig. 2.7, the T_c^{CDW} for the incommensurate CDW ($\Omega = 0.1t$) is smaller than the T_c^{SC}-dome at $\Omega = 1.0t$. Thus, at larger values of Ω,

the incommensurate CDW correlations and their effects are present but never fully develop before the system becomes superconducting.

The dimensionless e-ph coupling constant $\lambda^{\alpha^2 F}$ can be derived from the Eliashberg function via

$$\lambda^{\alpha^2 F} = 2 \int_0^\infty \mathrm{d}\omega \frac{\alpha^2 F(\omega)}{\omega}. \tag{2.22}$$

This quantity measures the effective electron-phonon coupling after the phonon dispersion and the electron spectrum are renormalized by the interaction. It is plotted in Fig. 2.13(c) and includes the same factor of $N_\mathrm{F}/N_\mathrm{F}^\mathrm{fd}$ introduced for $\alpha^2 F(\omega)$. The approximately monotonic increase in this coupling across the range of filling n is generally favorable for pairing and thus also T_c. In the same figure, we also show the filling dependence on the logarithmic average frequency ω_log, given by

$$\omega_\mathrm{log} = \exp\left(\frac{2}{\lambda} \int_0^\infty \frac{\mathrm{d}\omega}{\omega} \alpha^2 F(\omega) \ln(\omega)\right). \tag{2.23}$$

The value of ω_log monotonically decreases across the filling range, reflecting the softening of the phonon branch as the CDW correlations develop. Since $T_\mathrm{c} \propto \omega_\mathrm{log}$, we might expect a reduction in T_c, however, there will be additional interplay with the change in $\lambda^{\alpha^2 F}$.

To supplement our results for the superconducting T_c obtained within the Migdal approximation we have also estimated the superconducting critical temperatures using three appr oaches commonly found in the literature. First, we obtained $T_\mathrm{c}^{\alpha^2 F}$ by solving the linearized gap equation [Eq. (2.34)] using the computed $\alpha^2 F(\omega)$ as input. In Fig. 2.13(c), the data for $T_\mathrm{c}^{\alpha^2 F}$ most closely follows the T_c found within the Migdal approximation, exhibiting dome-like behavior. If we exclude the corrective factor of $N_\mathrm{F}/N_\mathrm{F}^\mathrm{fd}$ in $\alpha^2 F(\omega)$, which accounts for the renormalization of the electron spectral function at the Fermi-level, the calculated $T_\mathrm{c}^{\alpha^2 F}$ exhibits a monotonic increasing dependence on the filling n within the range considered here. For the second and third estimates, we used the Allen-Dynes-modified McMillan (ADM) formula [Eq. (2.36)] [200], which we denote $T_\mathrm{c}^\mathrm{ADM}$, and the ADM+$f$ formula [Eq. (2.37)] to find $T_\mathrm{c}^{\mathrm{ADM}+f}$. Both of these formulas underestimate the critical temperature significantly, and only the $T_\mathrm{c}^{\mathrm{ADM}+f}$ results exhibit non-monotonicity. The wide discrepancy between the various methods for calculating T_c should be taken in to account

when estimating the superconducting transition temperature from simplified, Fermi-surface averaged, isotropic Migdal-Eliashberg equations.

From this analysis, we conclude that the T_{c}^{SC} dome is tied to the competition of three renormalized quantities: the monotonic rise in $\lambda^{\alpha^2 F}$ which enhances pairing, the decrease in $\omega_{\log}$ which weakens the energy scale of pairing, and the non-monotonic filling dependence of the DOS around the Fermi-level. In particular, it is interesting to note how the quasiparticle properties are renormalized at different fillings and how this affects the value of T_{c}. While it is sometimes claimed in the literature that a superconducting dome is indicative of an unconventional pairing mechanism [201], our results indicate that this is not necessarily the case. A superconducting dome can be obtained in proximity to competing phases and this behavior will be more common in materials with narrow bandwidths (i.e., large values of Ω/t).

Effective Interaction

The bare effective electron-electron interaction for the Holstein model is purely local in real space and consequently uniform in momentum space. However, in the fully self-consistent approach, the effective interaction is related to the renormalized phonon propagator as shown by the double-wiggly line in the Migdal self-energy in Fig. 2.1(a). Thus the formation of a momentum dependent renormalized phonon branch indicates that the effective electron-electron interaction must develop some real space structure and become nonlocal, and a deeper understanding of this interaction will shed light on the factors for enhancing or suppressing transition temperatures. In this section we therefore examine the static effective interaction $V(\mathbf{q}) \equiv V(\mathbf{q}, i\nu_n = 0)$ in momentum space, and its (discrete) Fourier transform $V(\mathbf{r} = \mathbf{R}_i)$ on the lattice.

Defining the bare interaction parameter $v(\mathbf{q}) = 2g^2/\Omega \equiv v_0$, we rewrite the bare e-ph coupling constant $\lambda = v_0/W$, where W is the band width. The renormalized interaction can thus be related to the CDW susceptibility in Eq. (2.16) as

$$V(\mathbf{q}) = V(\mathbf{q}, i\nu_m = 0) = \frac{v_0}{1 - v_0 \chi_0(\mathbf{q})} \tag{2.24}$$

where $\chi_0(\mathbf{q}) \equiv \chi_0(\mathbf{q}, i\nu_m = 0)$. In momentum space $V(\mathbf{q})$ has either a single peak or quadruple peaks depending on whether the dominant CDW correlations occur at the commensurate vector $\mathbf{q}_{\text{max}} = (\pi, \pi)$ or the incommensurate vectors given by $\mathbf{q}_{\text{max}} = (\pi, \kappa\pi)$, and its symmetry-related points. In this case, we are again interested in the range of fillings $n \in [0.6, 0.8]$ relevant to the SC-dome where we always observe an incommensurate structure. To better understand the analytical properties of the interaction, we have fit $V(\mathbf{q})$ with a sum of four 2D Lorentzians

$$V(\mathbf{q}) \approx \sum_{s=1}^{4} \frac{v_{\text{max}}}{\xi^2 |\mathbf{q} - \mathbf{q}_{\text{max},s}|^2 + 1}, \tag{2.25}$$

where $\mathbf{q}_{\text{max},s}$ denotes all points related to $\mathbf{q}_{\text{max}} = (\pi, \kappa\pi)$ by rotational symmetries, and ξ, κ, ' and v_{max} are fitting parameters obtained by a least-squares fit to the data. The symmetry of $V(\mathbf{q})$ and its associated fit permit us to look along one cut of the 2D-momentum space $\mathbf{q} = (q_x, 1)\pi$ as shown in Fig. 2.14(a). As the filling is increased for fixed $\Omega = t$, and $T = 0.07t$, we see that the ordering vectors approach $\mathbf{q}_{\text{max}} = (\pi, \pi)$ and the effective interaction peak value v_{max} becomes increasingly larger.

The real-space structure of the effective interaction can be obtained form the Fourier transform $V(\mathbf{r}) = N^{-1} \sum_{\mathbf{q} \in \text{BZ}} V(\mathbf{q}) e^{i\mathbf{q} \cdot \mathbf{r}}$. Applying this procedure to the Lorentzian fits gives a functional form

$$V(\mathbf{r}) \approx \frac{v_{\text{max}}}{\pi \xi^2} R(r_x, r_y) K_0 \left(\frac{|\mathbf{r}|}{\xi} \right) \tag{2.26}$$

where $\mathbf{r} = (r_x, r_y)$, $R(r_x, r_y) = \cos(\pi r_x + \pi r_y)[\cos(|\kappa - 1|\pi r_x) + \cos(|\kappa - 1|\pi r_y)]$, and $K_\nu(z)$ is the modified Bessel function of the second kind with $\nu = 0$. The effective interaction $V(\mathbf{r})$ obtained from our self-consistent Migdal calculations and its corresponding fits are plotted in Fig. 2.14(b) along the r_x-axis, extending from the origin to a point where the effective interaction amplitudes taper off. At low filling the interaction $V(\mathbf{r})$ is noticeably weaker and has a shorter estimated range $\xi \approx 0.5$ (lattice spacing $a = 1$) making it essentially local in extent. As the filling increases, we see the emergence of oscillatory behavior and a more extended effective interaction. Between $0.7 \leq n \leq 0.8$, on the decreasing side of the T_c dome, the correlation length approximately ranges from $2.3 \leq \xi \leq 5.7$.
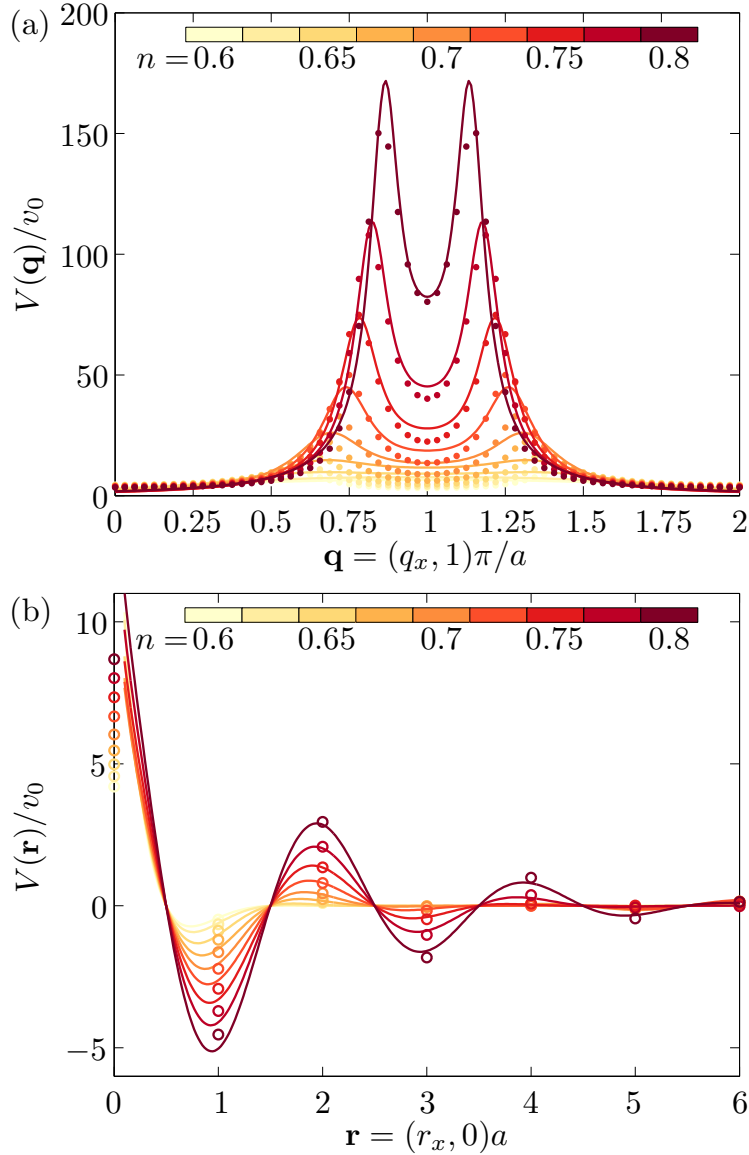
Figure 2.14: The effective interaction V normalized by the bare interaction parameter $v_0 = 2g^2/\Omega$ for various fillings n in (a) momentum space $V(\mathbf{q}, i\nu_m = 0)$, and (b) along the r_x-direction in real space $V(r_x, r_y = 0, i\nu_m = 0)$. In (a), the data points are obtained from self-consistent calculations and the solid lines are from the corresponding fit to Lorentzian functions with the method of least squares. In (b), the open circles are from the discrete Fourier transform of $V(\mathbf{q})$ (dots) in panel (a); the lines are a cosine Fourier integral transform of the fitted Lorentzian function in panel (a). The sign convention for the effective interaction in this figure is $V > 0$ ($V < 0$) for attractive (repulsive) interaction. The colors of the lines or symbols indicate the value of the filling with bright (dark) color for small (large) filling n. The bare phonon frequency $\Omega = t$, the bare e-ph coupling constant $\lambda = v_0/W = 0.3$, and the temperature is fixed at $T = 0.07t$ which is close to the superconducting critical temperatures for the chosen range of electron filling n. Figure taken from our Ref. [1].

A recent paper [202] by Langmann *et al.* proposed that a superconducting dome is not necessarily associated with competing orders or exotic superconductivity, but instead can be the result of a finite-range potential. Notably, they used a few phenomenological forms in real space for these finite-range potentials without self-consistently renormalizing them at different fillings across the dome. Although we observe a finite-range potential and a T_c-dome, we cannot deduce such a causation between them within our approach. As was discussed in the previous section, the filling dependence of the interacting DOS $N(\omega)$, the coupling $\lambda^{\alpha^2 F}$, and $\omega_{\log}$ support the role of competing orders for our problem. Moreover, the real-space structure of the effective interaction is directly linked to the formation of a **q**-dependent phonon dispersion due to the formation of long-range CDW correlations.

Comparison to Previous Findings

Although we do not aim to present a comprehensive review of the literature surrounding the Holstein model and Holstein-like models, there are some other studies whose results can further contextualize the relevant physics in these models. For instance, some features of the temperature filling phase diagram have been explored by using different approaches such as the modified variational Lang-Firsov transformation [137], strong-coupling expansions [203], and QMC [195]. These studies are not explicitly focused on the weak-coupling regime where the Migdal approximation is most applicable, but there are some similarities worth noting.

In Ref. [137], a large CDW dome near half-filling and a small SC phase at lower fillings are found; however, in the phase diagram there are additional *inhomogeneous* phases including a CDW+NO phase (consisting of phase separated CDW and Non-Ordered regions) and a CDW+SC phase (consisting of phase separated CDW and SC regions). On the other hand, Ref. [163] found in the phase diagram a *homogeneous* supersolid (SS) phase where the CDW and SC orders coexist. It is beyond the scope of the present work to study the SS phase since it requires considering coexisting CDW and SC orders in the symmetry broken states. However, such an investigation is possible using our theory and numerical implementation after considering the anomalous Green's function. In the range of parameters used, we did not observe any indication of phase separation for the Holstein model. A phase separation transition is an analog to the condensation transition between gas and liquid. In lattice

models, it was first studied and observed in the extended Hubbard model [204, 205, 206] with a nearest-neighbor Hubbard interaction, later in the Hubbard model [207, 208], and in a e-ph coupled case, the Hubbard-Holstein model [209, 210]. Unlike CDW order, for a phase separation transition $\chi^{\mathrm{CDW}}(\mathbf{q})$ diverges at $\mathbf{q} = \mathbf{0}$. Therefore, for an anisotropic e-ph coupling with strong forward scattering, it is possible to find a phase separation transition [211]. We note that we do see indications for this physics for our buckling mode case.

Two previously mentioned references [203, 195] focus on the addition of anharmonic phonon oscillations and find that anharmonicity enhances the overall size and spread of the SC region of the phase diagram. However, the maximum T_{c} is not enhanced significantly beyond that of the maximal values attained in the truly harmonic (Holstein) model. This result parallels the changes we discussed in section 2.4.2 when diagonal hopping is permitted. Although setting $t' \neq 0$ enhances the pairing (and thus $T_{\mathrm{c}}^{\mathrm{SC}}$) relative to $t' = 0$, the improvement in the greatest value of $T_{\mathrm{c}}^{\mathrm{SC}}$ is modestly small.

2.5 Summary and Conclusions

In this chapter, we have presented a detailed analysis of the Holstein model within a fully self-consistent Migdal approximation, where both the renormalization of the electron and phonon properties are treated on an equal (approximate) footing. Using an efficient implementation based on fast Fourier transforms, we were able to simulate the model on lattice sizes much larger than those considered in the past. Our results revealed significant finite size effects when determining the CDW transition temperatures. This result should be kept in mind when simulating the Holstein model using numerically exact methods such as QMC that are limited to smaller lattice sizes.

Comprehensive phase diagrams were mapped as a function of filling, revealing a mix of expected and unexpected features. For large phonon frequencies, the dominant CDW ordering vector occurs at $\mathbf{q}_{\mathrm{max}} = (\pi, \pi)$; however, at smaller frequencies, superconducting T_{c}'s are lowered sufficiently far to allow an incommensurate CDW phase to occupy a small range of fillings adjacent to the commensurate CDW phases near half-filling. The *s*-wave superconducting phase was present at lower values of the filling and was enhanced with

increasing Ω. Moreover, the filling dependence of T_c^{SC} was non-monotonic with a peak near $n \approx 0.7$. We addressed the possible factors responsible for this dome by studying the filling dependence of the interacting DOS, the renormalized e-ph coupling, and $\omega_{\log}$, and found that all three have competing effects on the pairing. The DOS around the Fermi-surface exhibits non-monotonicity akin to T_c^{SC} across the same range of n, while the renormalized e-ph coupling and the $\omega_{\log}$ increased and decreased over this range respectively. The latter two changes generally enhance and suppress pairing correlations, respectively, hence, they provide a measure of the competition. Characterization of the effective electron-electron interaction V over both momentum and position space show that a very local (short range) interaction becomes further extended by several lattice constants as n approaches half-filling. We cannot, however, attribute the origin of our superconducting T_c dome to this finite-range interaction in contrast to other approaches [202].

The addition of a nonzero NNN hopping $t' < 0 \, (t' > 0)$ to the electronic band promotes larger pairing correlations in the SC phase for $n < 1 \, (n > 1)$ and suppresses the charge density correlations. Asymmetry in the phase diagram across the full range of filling is consistent with the asymmetry in the DOS due to $t' \neq 0$ which makes more states available for pairing at fillings away from half-filling. Moreover, the NNN hopping also weakens nesting at the Fermi surface, which in turn suppresses the CDW and thus reduces competition between the SC and CDW phases. In addition, anisotropic e-ph couplings and the corresponding correlations are compared. Lastly, we showed that $g(\mathbf{q})$ modeling the breathing and buckling oxygen modes in the high-T_c cuprates induce a much larger range of charge density correlations and a suppression of superconductivity relative to the isotropic coupling.

Implementation of the fully self-consistent Migdal-Eliashberg equations has been made freely available to the public[5].

---

[5]The MATLAB code is released at https://github.com/johnstonResearchGroup/Migdal.

2.6 Supplemental: Fast Fourier Transform of Physical Quantities

We consider the Fourier transform

$$f(\mathbf{r}, \tau) = \frac{1}{N\beta} \sum_{\mathbf{k}} \sum_{n=-\infty}^{\infty} e^{i(\mathbf{k}\cdot\mathbf{r}-\omega_n\tau)} f(\mathbf{k}, i\omega_n), \qquad (2.27)$$

where we choose the plane wave $e^{ik\cdot x} = e^{i(\mathbf{k}\cdot\mathbf{r}-\omega t)} = e^{i(\mathbf{k}\cdot\mathbf{r}-\omega_n\tau)}$, and the inverse Fourier transform

$$f(\mathbf{k}, i\omega_n) = \sum_{\mathbf{r}} \int_0^\beta d\tau \, e^{-i(\mathbf{k}\cdot\mathbf{r}-\omega_n\tau)} f(\mathbf{r}, \tau). \qquad (2.28)$$

Note that $\omega_n\tau = \omega t$ because the mappings between imaginary and real time-frequency variables are $\tau \to it$ and $i\omega_n \to \omega$, respectively. Since the summations of $\mathbf{k}$ and $\mathbf{r}$ range over the discretized first Brillouin zone and the lattice sites $\mathbf{R}_i$, respectively, the discrete Fourier transform using FFT is straightforward. Therefore, we need only discuss FFT between time and frequency domains. As such, $\mathbf{r}$ and $\mathbf{k}$ arguments will be suppressed in the function f which stands for the Green's function G, self-energy Σ, the effective interaction V, or the irreducible susceptibility χ_0. As stated in the main text, $\omega_n = (2n+1)\pi/\beta$ is fermionic Matsubara frequency in $G(i\omega_n)$ and $\Sigma(i\omega_n)$, and $\omega_n = 2n\pi/\beta$ is bosonic Matsubara frequency in $V(i\omega_n)$ and $\chi_0(i\omega_n)$. In the self-consistent iterations, we perform a FFT on $G(i\omega_n)$ and $V(i\omega_n)$, and an iFFT on $\Sigma(\tau)$ and $\chi_0(\tau)$.

For a practical calculation using the FFT we must use a finite number of Matsubara frequencies in the sum. The uniform fermionic and bosonic Matsubara frequency grids $\omega_n = (2n+1)\pi/\beta$ and $\omega_n = 2n\pi/\beta$, where $-N_c \le n \le N_c - 1$, are used in the sum for $G(i\omega_n)$ and $V(i\omega_n)$, respectively. Since $G(i\omega_n) \sim O(\frac{1}{\omega_n})$ for large frequency, the Fourier transform featured in Eq. (2.27) has convergence issues for $G(i\omega_n)$ (see the discussion in the last part of Chapter 3 in Ref. [97]). Therefore, we subtract a function $G_0^\xi(i\omega_n) = 1/(i\omega_n - \xi)$ with the same large frequency dependence as $G(i\omega_n)$, use the fact that $\beta^{-1} \sum_{n=-\infty}^{\infty} e^{-i\omega_n\tau} G_0^\xi(i\omega_n) =$

$-\mathrm{e}^{(\beta-\tau)\xi}/(\mathrm{e}^{\beta\xi}+1)$ for $\tau > 0$, and obtain the final formula for the Fourier transform

$$G(\tau > 0) = \frac{1}{\beta} \sum_{n=-N_c}^{N_c-1} \mathrm{e}^{-\mathrm{i}\omega_n \tau} \tilde{G}(\mathrm{i}\omega_n) - \frac{\mathrm{e}^{(\beta-\tau)\xi}}{\mathrm{e}^{\beta\xi}+1}, \tag{2.29}$$

where $\tilde{G}(\mathrm{i}\omega_n) = G(\mathrm{i}\omega_n) - G_0^\xi(\mathrm{i}\omega_n)$. Any constant value ξ can be used, provided that $|\xi| \ll \omega_{n=N_c}$. In our calculations, we use $\xi = \xi_{\mathbf{k}}$, i.e., the band dispersion. This choice is usually more accurate and requires smaller cut-off number N_c than other choices. Setting $\xi = 0$, one recovers the familiar formula

$$\lim_{\tau\to 0} G(\tau) = \frac{1}{\beta} \sum_{n=N_c}^{N_c-1} G(\mathrm{i}\omega_n) - \frac{1}{2}\operatorname{sgn}\tau. \tag{2.30}$$

which is Eq. (17.36) on page 153 of Ref. [97].

For iFFT, we must reformulate the Fourier integral transform $f(\mathrm{i}\omega_n) = \int_0^\beta \mathrm{d}\tau\, \mathrm{e}^{\mathrm{i}\omega_n \tau} f(\tau)$ into a discrete Fourier transform. The pitfall and the method for doing this are discussed in Chapter 13.9 of Ref. [212] and in Chapter 2.10.2 of Ref. [213]. As mentioned in the main text, the correct way to accomplish this task is to compute the Fourier integral exactly after interpolating $f(\tau)$ on the discrete τ grid using a continuous function such as spline or piecewise polynomial. Here, we choose the piecewise polynomial (Lagrange polynomial) and provide the explicit formula for the second (quadratic) order, which appears to be absent from literature.

Denote $\delta = \beta/N_\tau$, the τ grid $\tau_l = (l-1)\delta$, where $1 \leq l \leq N_\tau + 1$, $f_l = f(\tau_l)$, and $\tilde{f}_l = \mathrm{e}^{\mathrm{i}\omega_n \tau_l} f(\tau_l)$. If the discontinuity exists at $\tau = 0$ and β, the end points should be understood as 0^+ and β^-. The quadratic Lagrange polynomial used for interpolation is

$$\begin{aligned} f(\tau) \approx\ & f_l \frac{(\tau - \tau_{l+1})(\tau - \tau_{l+2})}{(\tau_l - \tau_{l+1})(\tau_l - \tau_{l+2})} \\ & + f_{l+1} \frac{(\tau - \tau_l)(\tau - \tau_{l+2})}{(\tau_{l+1} - \tau_l)(\tau_{l+1} - \tau_{l+2})} \\ & + f_{l+2} \frac{(\tau - \tau_l)(\tau - \tau_{l+1})}{(\tau_{l+2} - \tau_l)(\tau_{l+2} - \tau_{l+1})}, \end{aligned} \tag{2.31}$$

where $\tau_l \le \tau \le \tau_{l+2}$. Using the above interpolating function, the final result for the Fourier integral transform is

$$f(\mathrm{i}\omega_n) = (c_1 + c_2 + c_3) \sum_{l=1}^{N_\tau} \tilde{f}_l - (p_3 + c_3) f_\Delta$$
$$+ (s_1 - c_2 + p_3) \tilde{f}_1 + (s_2 - c_3) \tilde{f}_2 + s_3 \tilde{f}_3$$
$$+ p_1 \tilde{f}_{N_\tau - 1} + (p_2 - c_1) \tilde{f}_{N_\tau}, \tag{2.32}$$

where

$$f_\Delta = f(\tau = 0^+) - f(\tau = 0^-) = \tilde{f}_1 - \tilde{f}_{N_\tau + 1},$$
$$c_1 = \frac{\delta}{4}(I_{22} - 3I_{12} + 2I_{02}), \quad c_2 = -\frac{\delta \mathrm{e}^{-\mathrm{i}\omega_n \delta}}{2}(I_{22} - 2I_{12}),$$
$$c_3 = \frac{\delta \mathrm{e}^{-2\mathrm{i}\omega_n \delta}}{4}(I_{22} - I_{12}), \quad s_1 = \frac{\delta}{4}(I_{21} - 3I_{11} + 2I_{01}),$$
$$s_2 = -\frac{\delta \mathrm{e}^{-\mathrm{i}\omega_n \delta}}{2}(I_{21} - 2I_{11}), \quad s_3 = \frac{\delta \mathrm{e}^{-2\mathrm{i}\omega_n \delta}}{4}(I_{21} - I_{11}),$$
$$p_1 = \frac{\delta \mathrm{e}^{\mathrm{i}\omega_n \delta}}{4}(I_{21} - I_{11}), \quad p_2 = -\frac{\delta}{2}(I_{21} - I_{01}),$$
$$p_3 = \frac{\delta \mathrm{e}^{-\mathrm{i}\omega_n \delta}}{4}(I_{21} + I_{11}),$$

and $I_{vu} = \int_0^{u\delta} \mathrm{d}x\, \mathrm{e}^{\mathrm{i}\omega_n x} x^v / \delta^{v+1}$, $(v \in \{0, 1, 2\})$, for which the closed analytical form can be found using integration by parts. At this point, the sum in Eq. (2.32) is suitable for evaluation by a FFT.

Note that for $\omega_n = 0$ (only for bosonic frequencies), we should use $I_{vu} = u^{v+1}/(v+1)$ and thus $(c_1, c_2, c_3) = (1, 4, 1)\delta/6$, $(s_1, s_2, s_3) = (p_3, p_2, p_1) = (5, 8, -1)\delta/24$. Then Eq. (2.32) becomes the usual composite Simpson's rule that applies to both even and odd number of intervals:

$$f(\mathrm{i}\omega_n = 0) = \delta \Bigg[\frac{3}{8} f_1 + \frac{7}{6} f_2 + \frac{23}{24} f_3 + \sum_{l=4}^{N_\tau - 2} f_l + \frac{23}{24} f_{N_\tau - 1}$$
$$+ \frac{7}{6} f_{N_\tau} + \frac{3}{8} f_{N_\tau + 1} \Bigg], \tag{2.33}$$

which is a formula also found in Ref. [212].

2.7 Supplemental: Linearized Isotropic Gap Equation and Modified McMillan T_c Formulas

The linearized isotropic gap equation is given by [214, 200]

$$\Phi_n = \sum_{n'} K_{n,n'} \Phi_{n'}, \tag{2.34}$$

where $K_{n,n'} = \pi T(\lambda_{n,n'} - \mu^*)/(|\omega_{n'}|Z_{n'})$, $Z_n = 1 + (\pi T/\omega_n)\sum_{n'} \lambda_{n,n'}\omega_{n'}/|\omega_{n'}|$, and $\lambda_{n,n'}$ is given by the Eliashberg spectral function $\alpha^2 F(\omega)$

$$\lambda_{n,n'} = \int_0^\infty \mathrm{d}\omega \frac{2\omega\alpha^2 F(\omega)}{(\omega_n - \omega_{n'})^2 + \omega^2}. \tag{2.35}$$

Here, ω_n and $\omega_{n'}$ are the fermionic Matsubara frequencies. The frequency dependent gap function is defined as $\Delta_n = \Phi_n/Z_n$. In this work, we set Coulomb pseudopotential $\mu^* = 0$ when solving the linearized gap equation for T_c, which is defined as the temperature when the largest eigenvalue of the matrix $K_{n,n'}$ reaches unity from below.

The Allen-Dynes-modified McMillan (ADM) T_c formula [200] for weak coupling strength reads

$$T_c = \frac{\omega_{\log}}{1.2} \exp\left(-\frac{1.04(1+\lambda)}{\lambda - \mu^*(1+0.62\lambda)}\right). \tag{2.36}$$

For intermediate coupling strength, Allen and Dynes further modified the above formula with two additional coefficients f_1 and f_2. The corresponding T_c formula [200] (ADM+f) is

given by

$$T_c = \frac{f_1 f_2 \omega_{\log}}{1.2} \exp\left(-\frac{1.04(1+\lambda)}{\lambda - \mu^*(1 + 0.62\lambda)}\right), \tag{2.37a}$$

$$f_1 = \left[1 + \left(\frac{\lambda}{2.46(1 + 3.8\mu^*)}\right)^{3/2}\right]^{1/3}, \tag{2.37b}$$

$$f_2 = 1 + \frac{(\overline{\omega}_2/\omega_{\log} - 1)\lambda^2}{\lambda^2 + [1.82(1 + 6.3\mu^*)(\overline{\omega}_2/\omega_{\log})]^2}. \tag{2.37c}$$

Here, $\overline{\omega}_2 = [(2/\lambda) \int_0^\infty \omega \alpha^2 F(\omega) d\omega]^{1/2}$ and $\lambda = \lambda_{n,n} = \lambda^{\alpha^2 F}$. Again, it should be noted that we set $\mu^* = 0$ when calculating T_c.

Chapter 3

Neural Network Monte Carlo

Monte Carlo (MC) simulations are essential computational approaches with widespread use throughout all areas of science. We present a method for accelerating lattice MC simulations using fully-connected and convolutional artificial neural networks that are trained to perform *local* and *global* moves in configuration space, respectively. Both networks take local spacetime MC configurations as input features and can, therefore, be trained using samples generated by conventional MC runs on smaller lattices before being utilized for simulations on larger systems. This new approach is benchmarked for the case of determinant quantum Monte Carlo (DQMC) studies of the two-dimensional Holstein model. We find that both artificial neural networks are capable of learning an unspecified effective model that accurately reproduces the MC configuration weights of the original Hamiltonian and achieve an order of magnitude speedup over the conventional DQMC algorithm. Our approach is broadly applicable to many classical and quantum lattice MC algorithms. The content of this chapter stems from our Ref. [2], essentially verbatim.

3.1   Introduction

As their full potential becomes apparent, machine learning algorithms are assuming more prominent roles in the process of scientific discovery. Meanwhile, the boundary lines between industry applications of machine learning, data and computer science, and other disciplines have blurred. Applications ranging from the high-quality feature extraction from

astrophysical images of galaxies [215] to helping with the real-time data analysis of particle accelerators [216, 217, 218] at the Fermilab [216] and the Large Hadron Collider [217] to discovering phases of matter [219, 220, 221] have emerged.

A series of early studies have underscored the potential for machine learning in the context of condensed matter physics by using artificial neural networks and dimension-reduction techniques to locate phase transitions [219, 220], or represent ground states of quantum many-body systems [222]. Machine learning algorithms have also been employed to help gain more insight into classical and quantum systems [223, 224, 225, 226, 227, 228, 229, 230, 231] as well as accelerate specific numerical algorithms [232, 233, 234, 235, 236, 237]. These applications are not only helping to automate and streamline scientific processes that could take many years to accomplish with more conventional computational approaches, but they are also uncovering previously inaccessible phenomena.

One machine learning application that has attracted significant attention is in accelerating MC simulations [232, 238, 233, 239, 240, 241, 242, 243, 244, 245]. For example, in the so-called self-learning Monte Carlo (SLMC) method [238], an effective bosonic model is trained to mimic the statistics of the original Hamiltonian. Once trained, the effective model is then used to perform the same simulations much more efficiently. The primary advantage of this approach is that the action of the effective model is often much easier to compute than the action for the full fermion model, thus granting access to larger system sizes. This approach has also been extended to include correlations in both the real space and imaginary time domains [239, 240]. Despite their power, however, the SLMC methods require that the form of the effective model be known *a priori.* This limitation can be significant as different effective models may be required for the same fermionic model as the model parameters, system size, or simulation temperature changes, and the overall effectiveness of these approaches is severely limited if the wrong effective model is chosen. To overcome this problem, several groups have used artificial neural networks to learn the form of the model in some instances [241, 243, 244, 245] (*e.g.* QMC simulations of the Anderson impurity model); however, generalizing this approach to lattice QMC problems has not yet been achieved. One reason for this is the fact that such problems typically involve thousands of auxiliary

spacetime fields and any neural network using that many input features will often generalize poorly.

Here, we show how to design artificial neural networks that can be trained to represent an effective bosonic model for lattice QMC simulations. Inspired by applications of the traveling cluster approximation to spin-fermion models [246, 247], we design fully-connected and convolutional neural networks that only require information from surrounding auxiliary fields (see. Fig. 3.1) to perform both *local* and *global* moves of the MC configurations. This method does not suffer from the scaling issues restricting other self-learning methods and can be easily generalized across models and parameter regimes without changes in the underlying algorithm, provided the neural networks are versatile enough to learn the effective models. As such, this approach can be integrated directly into existing MC codes. To demonstrate the efficiency of this approach, here we apply it to determinant quantum Monte Carlo (DQMC) simulations of the two-dimensional Holstein model. This problem is particularly challenging owing to long autocorrelation times [248], the need for both local and global MC moves to ensure ergodicity [249, 105], and competition between charge-density-wave (CDW) and superconducting ground states [1] that may require different effective boson models. Reproducing known results, we obtain an order of magnitude of speedup with our algorithm.

3.2 Model and Methods

Model — The single-band Holstein Hamiltonian [79] is $H = H_0 + H_{\text{lat}} + H_{\text{e-ph}}$, where $H_0 = -t \sum_{\langle i,j \rangle, \sigma} \hat{c}_{i,\sigma}^\dagger \hat{c}_{j,\sigma} - \mu \sum_{i,\sigma} \hat{n}_{i,\sigma}$, $H_{\text{lat}} = \sum_i \left(\frac{1}{2M} \hat{P}_i^2 + \frac{M\Omega^2}{2} \hat{X}_i^2 \right)$, and $H_{\text{e-ph}} = g \sum_{i,\sigma} \hat{X}_i \hat{n}_{i,\sigma}$. Here, $\langle \cdots \rangle$ denotes a summation over nearest neighbors; $\hat{c}_{i,\sigma}^\dagger$ ($c_{i,\sigma}$) creates (annihilates) an electron with spin σ on site i; $\hat{n}_{i,\sigma} = \hat{c}_{i,\sigma}^\dagger \hat{c}_{i,\sigma}$ is the particle number operator; t is the nearest-neighbor hoping integral; M is the ion mass and Ω is the phonon frequency; $\hat{X}_i$ and $\hat{P}_i$ are the lattice position and momentum operators, respectively; and g is the strength of the e-ph coupling. Throughout, we set $M = t = 1$ as the unit of mass and energy, and we study this Hamiltonian on an $N = N_x^2$ square lattice, where N_x is the linear size of the cluster.
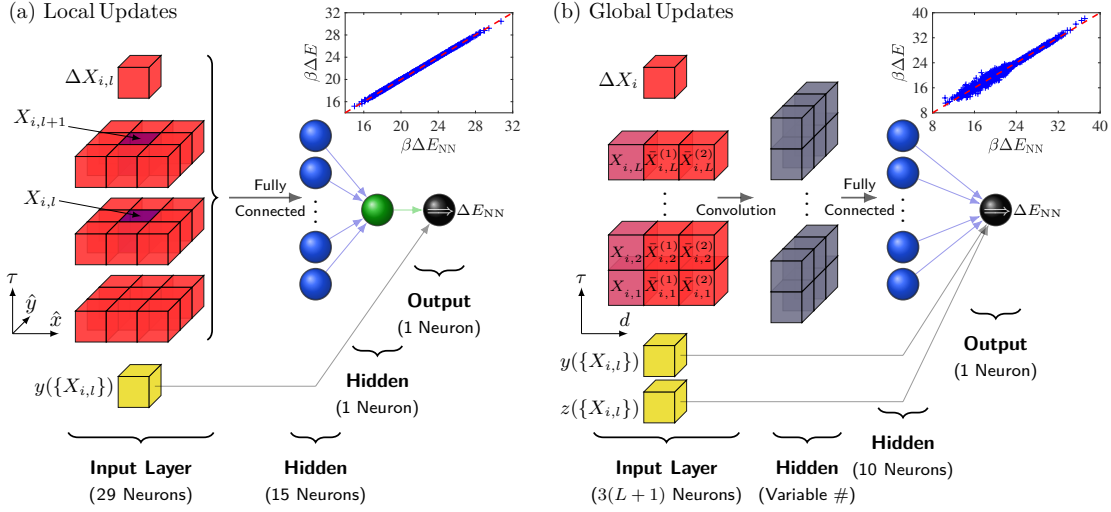
Figure 3.1: A sketch of the architecture of the (a) fully-connected and (b) convolutional neural networks (CNN) used to perform local and global updates of the auxiliary fields, respectively. The first and second hidden layers of the fully-connected neural network use softplus activation functions $f(x) = \ln(1+e^x)$, while the output layer uses a linear activation function. The first and second hidden layers of the CNN use sigmoid functions $f(x) = (1+e^{-x})^{-1}$, while the output layer uses a linear function. The number of neurons in the first hidden layer of the CNN is set by the stride and kernel. A measure of the performance of the two networks is presented in the insets, which compare the predicted $\beta\Delta E_{\mathrm{NN}}$ against the exact $\beta\Delta E$ for the fully-connected and the CNN, respectively. These results were obtained using networks trained on an $N = 6 \times 6$ cluster, an inverse temperature $\beta = 4.1/t$, filling $\langle \hat{n} \rangle = 1$, $\lambda = t/2$, and $\Omega = t/2$. Figure taken from our Ref. [2].

To facilitate a direct comparison with a recent state-of-the-art simulation [242], we focus on $\Omega = t/2$ and dimensionless e-ph coupling strength $\lambda = \frac{g^2}{8t\Omega^2} = 0.5$.

Determinant quantum Monte Carlo — DQMC is an auxiliary field, imaginary time technique that computes expectation values of an observable within the grand canonical ensemble. In a DQMC simulation, the imaginary time interval $\tau \in [0, \beta]$ is evenly divided into L discrete slices of length $\Delta\tau = \beta/L$ ($= 0.1$ in this work). Using the Trotter approximation, the partition function is then given by $Z = \text{Tr}\left(e^{-\Delta\tau LH}\right) \approx \text{Tr}\left(e^{-\Delta\tau H_{\text{e-ph}}}e^{-\Delta\tau(H_0+H_{\text{lat}})}\right)^L$. After integrating out the electronic degrees of freedom, the partition function can be reduced to $Z = \int W(\{X\})\,\mathrm{d}X$, where the configuration weight is $W(\{X\}) = e^{-S_{\text{ph}}\Delta\tau}\det M^\uparrow \det M^\downarrow$. Here, $\int \mathrm{d}X$ is shorthand for integrating over all of continuous displacements $X_{i,l}$ defined at each spacetime point (i, l), the matrices M^σ are defined as $M^\sigma = I + B^\sigma_L B^\sigma_{L-1} \cdots B^\sigma_1$, where I is an $N \times N$ identity matrix, and $B^\sigma_l = e^{-\Delta\tau H_{\text{e-ph}}}e^{-\Delta\tau H_0}$, and $S_{\text{ph}} = \frac{M}{2\Delta\tau^2}\sum_{i,l}(X_{i,l+1} - X_{i,l})^2 + \frac{M\Omega^2}{2}\sum_{i,l} X_{i,l}^2$ is lattice's contribution to the total action. Note that B^σ_l matrices for the Holstein model do not depend on spin but are implicitly dependent on the fields $X_{i,l}$ through $H_{\text{e-ph}}$. For more details, we refer the reader to Refs. [102, 145, 105].

As mentioned, two types of MC updates are needed in the simulation. The first are local updates of the type $X_{i,l} \to X'_{i,l} = X_{i,l} + \Delta X_{i,l}$, which are made at each spacetime point. The second are global or block updates, where the field for a given site are updated simultaneously at all timeslices $X_{i,l} \to X_{i,l} + \Delta X_i$, $\forall l \in [0, L]$. Such block updates are needed to help move phonon configurations out of local minima at low temperatures and large couplings [249, 105]. DQMC accepts both kinds of moves with a probability $p = W(\{X'\})/W(\{X\}) \equiv e^{-\beta\Delta E}$, which requires the costly evaluation of matrix determinants. Moreover, since the matrices M^σ depend on the fields, these must also be updated after every accepted change in the phonon fields. While an efficient update algorithm exists for performing local updates [102], no such algorithm is known for block updates. The computational cost for performing a full sweep of (fast) local updates and block updates is $\mathcal{O}(N^3 L)$ and $\mathcal{O}(N^4 L)$ [250], respectively.

To reduce this cost, we train our networks to predict $\beta\Delta E$ appearing in the definition of the configuration weight given only changes in, and local information of, the phonon fields and their expected behavior at large displacements as input. This reduces the total computational complexity of determining whether both kinds of updates will be accepted to

the time needed to evaluate the networks, which is $\mathcal{O}(1)$ for the case of the simply connected network and $\mathcal{O}(L)$ for the convolutional neural network. As with other SLMC methods, we then use the neural networks to propose many MC updates that are ultimately accepted or rejected based on the configuration weights of the original model. While determining this final acceptance probability requires the evaluation of the matrix determinants, this task can be done infrequently enough that a considerable speedup is achieved. Another advantage of our approach is that the networks can be trained using data generated by the conventional DQMC algorithm on inexpensive small clusters before being generalized to larger systems. In this way, our method combines the flexibility of neural networks with the inexpensive training costs seen in SLMC approaches making use of largely local effective models.

3.2.1 Local Updates

Local updates are performed using a fully-connected network with two hidden layers [Fig. 3.1(a)]. Assuming that the update is proposed at spacetime site (i, l), the learning objective is to predict $\beta \Delta E$ given only $\Delta X_{i,l}$ and the field values at the surrounding spacetime points as input features. Here, we include nearest- and next-nearest neighbor phonon fields in both space and imaginary time, and neglect long-range correlations. While there is justification for a short-range effective interaction in proximity to the CDW phase at half-filling [1], this approximation can also be systematically improved by taking more input features. We have found, however, that next-nearest-neighbor inputs are sufficient. We also supply an additional neuron in the input layer that enforces known behavior at large displacements [242] (CITESUPP).

3.2.2 Global Updates

Global updates are performed using a convolutional neural network (CNN) with four layers [Fig. 3.1(b)], where the objective again is to predict $\beta \Delta E$ given only local information about the phonon fields. Assuming the update occurs at site i, the input layer has three columns of input features: the first contains fields $X_{i,l}$ across all imaginary time slices; the second and third columns contain averages $\bar{X}_{i,l}^{(1)} = \frac{1}{4} \sum_{\langle j \rangle} X_{j,l}$ and $\bar{X}_{i,l}^{(2)} = \frac{1}{4} \sum_{\langle\langle j \rangle\rangle} X_{j,l}$, respectively, at

all time slices, where $\langle j \rangle$ and $\langle\langle j \rangle\rangle$ denote nearest- and next-nearest-neighbor sums around site i. The use of $\bar{X}_{i,l}^{(1)}$ and $\bar{X}_{i,l}^{(2)}$ enforces C_4 rotational symmetry and reduces the cost of training the CNN. The convolution operation from the input layer to the first hidden layer is standard (CITESUPP).

For each set of (fixed) input parameters $\{\beta, \mu, \Omega, g\}$ we train both networks using training examples generated with the conventional DQMC algorithm on a 6×6 cluster. Throughout, we generated 8×10^4 samples, which were randomly partitioned into 6×10^4 training and 2×10^4 test samples. We first show results for their performance; the insets of Figs. 3.1(a) and 3.1(b) compare the predicted $\beta\Delta E_{\mathrm{NN}}$ against the exact $\beta\Delta E$ values obtained from our test data sets for the local and global updates, respectively. This simulation was performed close to the CDW transition for the model [Fig. 3.3]. Both networks accurately predict the MC configure weights but the fully-connected neural network is slightly more accurate. While the accuracy can be systematically improved by taking more input features, we find that the knowledge learned by both networks can be transferred to larger clusters remarkably well based on Fig. 3.2 (a).

Once our networks have been trained and tested, we then define a full MC sweep as consisting of N_{u} complete sweeps of local updates performed at each spacetime point (i, l) using the fully-connected neural network, followed by N_{u} sweeps of global updates performed at *every* lattice site i using the CNN. (This sampling procedure differs from the conventional one [105], where global updates are performed on a subset of sites to minimize the total computational cost.) After performing these sweeps, the original field configuration $\{X\}$ is replaced with a newly proposed one $\{X'\}$ in a cumulative update [233, 238, 239] with a probability $\min[1, p_c]$, where

$$p_c = \frac{W(\{X'\})}{W(\{X\})} \frac{\exp(-\beta E_{\mathrm{NN}}[\{X\}])}{\exp(-\beta E_{\mathrm{NN}}[\{X'\}])}.$$

3.3 Benchmarks

To benchmark the neural network Monte Carlo (NNMC), we performed direct comparisons with the conventional DQMC algorithm for the half-filled model $\langle \hat{n} \rangle = 1$ at $\beta = 4.1/t$, which
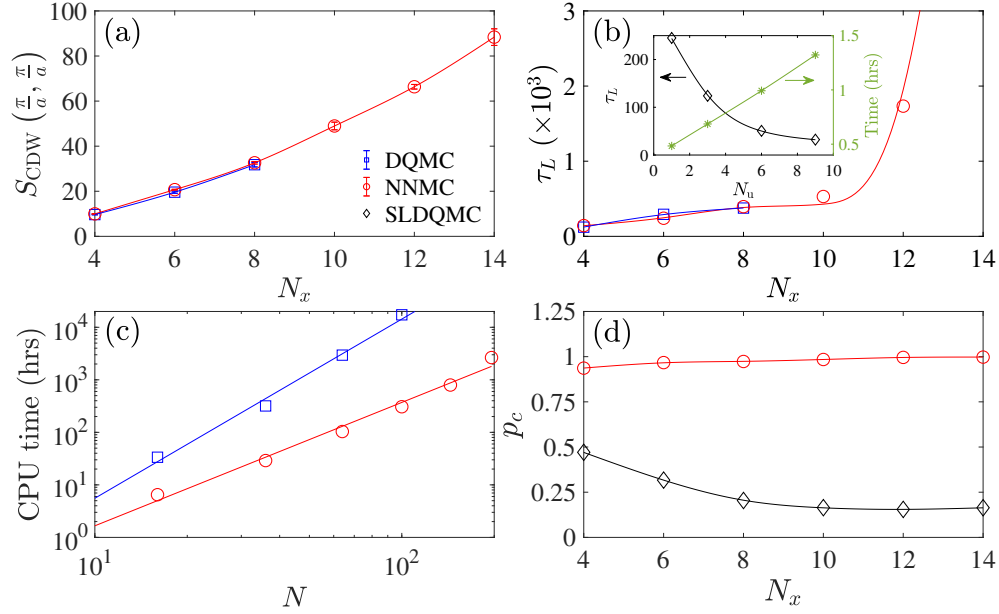
Figure 3.2: (a) The CDW structure factor $S_{\mathrm{CDW}}\left(\frac{\pi}{a},\frac{\pi}{a}\right)$ and (b) its autocorrelation time as a function of the linear cluster size N_x obtained with conventional DQMC and NNMC algorithms. The inset shows the reduction of the autocorrelation time and increase of the simulation runtime as the number of update sweeps per Monte Carlo sweep N_u is increased. (c) A comparison of CPU time to complete 8×10^4 warm-up and 8×10^4 measurement sweeps as a function of N_x using the conventional and neural network sampling schemes. In both cases, we performed global updates randomly at all sites in the cluster after every one full spacetime sweep of local updates. To make a robust comparison between the two methods, we took identical parameters for both sets of simulations. The solid lines are fits to the data of the form $t_{\mathrm{CPU}} = \alpha N^z$. (d) The cumulative update ratio of the NNMC algorithm compared against the values achieved using the SLMC method as described in Ref. [242]. Figure taken from our Ref. [2].

is close to the CDW transition temperature for this parameter set. We emphasize that both the DQMC and NNMC simulations used the same sampling protocol with $N_u = 1$. Figure 3.2(a) plots the CDW structure factor $S(\mathbf{q})$ at $\mathbf{q} = (\pi, \pi)/a$ (CITESUPP) as a function of the linear cluster size N_x, and demonstrates that the NNMC algorithm accurately reproduces the results of the conventional DQMC algorithm for the accessible lattice sizes. Figure 3.2(b) compares the autocorrelation time τ_L of $S_{\mathrm{CDW}}(\mathbf{q})$ for both techniques, which again yields similar results. We note, however, that the autocorrelation time can be reduced significantly by increasing the number of update sweeps N_u that are performed before computing the cumulative update acceptance probability, as shown in the inset of Fig. 3.2(b).

To address how NNMC reduces the computational cost, we compare the time to solution for both algorithms in Fig. 3.2(c). Fitting a power law $t_{\mathrm{CPU}} = \alpha N^z$ to the data yields $z = 3.41$ and 2.35 for DQMC and NNMC, respectively, a significant reduction in the scaling. We note that a similar speedup was obtained using SLMC [242]; however, the NNMC does not require the functional form of the effective model to be specified *a priori.* Moreover, the NNMC method is more efficient at generating accepted MC moves, particularly as it is generalized to larger system sizes. We highlight this aspect in Fig 3.2(d), which shows the cumulative acceptance ratio p_c obtained using NNMC and compares it with SLMC. As the methods are generalized to larger cluster sizes, p_c decreases for the SLMC method while the NNMC method proposes cumulative moves that are almost always accepted, and becomes more accurate on larger cluster sizes. The decrease of p_c in SLMC is due to the poor performance of the regression model for predicting global updates, which requires a more sophisticated effective model.

We now demonstrate that the NNMC approach can also be used to study the finite-size scaling of the CDW structure factor and obtain the transition temperature in the thermodynamic limit. Fig. 3.3 presents a similar analysis carried out in the same temperature region $\beta = 3.8/t \sim 4.5/t$ using the NNMC approach. At the critical point, the finite-size scaling behavior has the form $S_{\mathrm{CDW}}(\pi, \pi)/N_x^2 = N_x^{-2\gamma/\nu} f\left(N_x^{1/\nu} \frac{T-T_c}{T_c}\right)$, where $\gamma = \frac{1}{8}$ and $\nu = 1$ are the 2D Ising critical exponents. The critical temperature $T_c/t \approx 0.244$ ($\beta_c = 4.1/t$) is determined by the common intersection point of the curves. The inset of
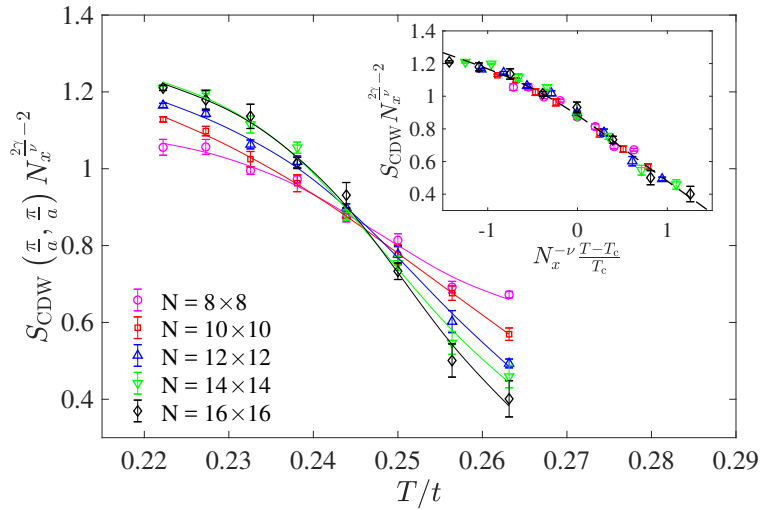
Figure 3.3: A finite size scaling analysis of the $\mathbf{q} = (\pi, \pi)/a$ CDW structure factor $S_{\mathrm{CDW}}(\mathbf{q}) N_x^{2\gamma/\nu-2}$ *vs.* T/t. The CDW transition is in the 2D Ising universality class with critical exponents $\gamma = 1/8$ and $\nu = 1$. The inset shows the collapse of the data when $S_{\mathrm{CDW}}(\mathbf{q}) N_x^{2\gamma/\nu-2}$ is plotted *vs.* $N_x^{-\nu}\frac{T-T_c}{T_c}$ with a critical temperature $T_c = 0.244$. Figure taken from our Ref. [2].

Fig. 3.3 replots $S_{\text{CDW}} N_x^{-7/4}$ against $N_x^{1/\nu} \frac{T - T_c}{T_c}$, showing the expected data collapsing to a single curve, consistent with Ref. [242].

3.4 Summary and Conclusions

We have extended the use of artificial neural networks in self-learning Monte Carlo methods to lattice Monte Carlo simulations. Our approach overcomes many of the scaling issues associated with other SLMC implementations and can be widely applied to classical and quantum Monte Carlo simulations on extended lattices. We then applied this methodology to DQMC studies of the Holstein model. In doing so, we designed fully-connected and convolutional neural networks capable of performing accurate *local* and, for the first time, *global* moves in configuration space. Using this method we are able to reproduce results of the charge-density-wave transition in this model but using an approach that does not require the form of the effective model to be specified in advance.

The success of our network architectures indicates that the effective interactions in the Holstein model are sufficiently short-ranged that the lattice dynamics can be captured using relatively small clusters. This observation is supported by our results in in Chapter 2 for the effective e-e interaction within the Migdal approximation [1]. In the future, one could envision examing the structure of the trained networks to infer information abou the effective interactions in other model Hamiltonians.

Our approach constitutes a generalizable method for performing machine-learning accelerated lattice Monte Carlo simulations (even the Fermi-Hubbard model), provided that the neural networks are sophisticated enough to learn the underlying effective model for the relevant parameter ranges. At last, We would like to stress that our approach allows to compute physical quantities that can be compared with experiments. Previous quantum Monte Carlo + machine learning approaches used to study the Hubbard model on extended lattices [224] have generally focused on classifying phases in the parameter space, while physical measurable quantities (such as one- and two-particle functions) are inaccessible.

Chapter 4

Nonlinear electron-phonon coupling in the Holstein model

Determining the range of validity of Migdal's approximation for electron-phonon (e-ph) coupled systems is a long-standing problem. Many attempts to answer this question employ the Holstein Hamiltonian, where the electron density couples linearly to local lattice displacements. When these displacements are large, however, nonlinear corrections to the interaction must also be included, which can significantly alter the physical picture obtained from this model. Using determinant quantum Monte Carlo and the self-consistent Migdal approximation, we compared superconducting and charge-density-wave correlations in the Holstein model with and without second-order nonlinear interactions. We find a disagreement between the two cases, even for relatively small values of the e-ph coupling strength, and, importantly, that this can occur in the same parameter regions where Migdal's approximation holds. Our results demonstrate that questions regarding the validity of Migdal's approximation go hand in hand with questions of the validity of a linear e-ph interaction. The content of this chapter is sourced from our Ref. [3], essentially verbatim.

4.1   Introduction

Our modern understanding of phonon-mediated superconductors is largely based on results from ab initio approaches [84] coupled with Migdal's approximation [92, 138, 165]. Migdal's

approximation [92] neglects corrections to the electron-phonon (e-ph) interaction vertex, which scale as $O(\lambda \frac{\hbar\Omega}{E_\mathrm{F}})$, where λ is a dimensionless measure of the e-ph coupling strength, $\hbar\Omega$ is the typical phonon energy, and E_F is the Fermi energy. Physically, this approximation neglects processes leading to polaron formation, and determining precisely when these processes become important and their impact on transport properties is a long-standing problem [251, 182, 252, 162, 98, 253, 254, 255].

Many attempts to address this question have utilized nonpertubative simulations of simplified effective models like the Holstein [79] or Fröhlich [256] Hamiltonians, where the electron density couples linearly with phonon fields. For example, owing to it's relative simplicity, the Holstein model and its extensions have been studied extensively using quantum Monte Carlo (QMC) [145, 140, 257, 258, 146, 147, 259, 148, 260, 251, 261, 262, 263, 242, 2, 264], and serves as a prototype for studying different polaronic regimes. Recently, it was shown that even if $\frac{\hbar\Omega}{E_\mathrm{F}} < 1$, one can find instances where vertex corrections (i.e. polaron formation) become important for $\lambda \approx 0.4 - 0.5$ [98, 162].

It is generally understood that small (large) polarons form when the polaron binding energy is larger (smaller) than the hopping energy of the carriers [265]. However, small polarons are often accompanied by sizable lattice distortions and a tendency toward localization and charge order. This observation has motivated some work to include higher-order nonlinear e-ph coupling terms to study changes in polaron formation [266] and on charge-density-wave (CDW) and superconducting (SC) pairing correlations [199, 151]. These studies found that small positive (negative) nonlinear terms decrease (increase) the effective mass of the carriers and contracts (enlarges) the local lattice distortions surrounding the carriers [266]. Furthermore, mean-field treatments aiming to recover a linear model via effective model parameters fail to capture the quantitative nature of the true nonlinear model [266, 199, 151], indicating that nonlinearities cannot be renormalized out of the problem. For example, one can tune the parameters of an effective linear model to capture either the electronic or phononic properties of the nonlinear model but not both simultaneously [151]. This failure is important to note in the context of polaron formation, where the electrons and phonons become highly intertwined. To capture this physics

accurately, an effective model must describe both degrees of freedom on an equal footing, and an effective linear description of a nonlinear *e*-ph model will not do this.

These results raise an important question about the priority of investigations into the validity of the aforementioned approximations. Are there scenarios where the breakdown of the linear approximation supersedes the breakdown of Migdal's approximation? In this work, we show that this is indeed the case. Specifically, by comparing QMC simulations of the (non)linear Holstein model with results obtained with the Migdal approximation's, we show that nonlinear corrections can be more important than vertex corrections, and that this can occur even when Migdal's approximation appears to be valid. Our results have consequences for any conclusions drawn about the validity of Migdal's approximation from model Hamiltonians and highlight a critical need to move beyond such models for a complete understanding of strong *e*-ph interactions.

4.2   Model and Methods

We study an extension of the Holstein model introduced in Section 1.2.5 that includes nonlinear *e*-ph interaction terms and defined on a two-dimensional (2D) square lattice. The Hamiltonian is $\hat{H} = \hat{H}_{\text{el}} + \hat{H}_{\text{ion}} + \hat{H}_{\text{int}}$, where

$$\hat{H}_{\text{el}} = -t \sum_{\langle i,j \rangle, \sigma} \hat{c}^{\dagger}_{i,\sigma} \hat{c}_{j,\sigma} - \mu \sum_i \hat{n}_i \tag{4.1}$$

and

$$\hat{H}_{\text{ion}} = \sum_i \left(\frac{\hat{P}_i^2}{2M} + \frac{M\Omega^2 \hat{X}_i^2}{2} \right) = \sum_i \hbar\Omega \left(\hat{a}^{\dagger}_i \hat{a}_i + \frac{1}{2} \right) \tag{4.2}$$

describe the noninteracting electronic and phononic parts, respectively, and

$$\hat{H}_{\text{int}} = \sum_{i,k} \alpha_k \hat{n}_i \hat{X}_i^k = \sum_{i,k} g_k \hat{n}_i \left(\hat{a}^{\dagger}_i + \hat{a}_i \right)^k \tag{4.3}$$

describes the *e*-ph interaction to k^{th} order in the atomic displacement. As a reminder, α_k and g_k are the *e*-ph interaction strengths related by $g_k = \alpha_k \left(\frac{\hbar}{2M\Omega} \right)^{\frac{k}{2}}$.

Following previous works on the nonlinear Holstein model [199, 151], we truncate the series in $\hat{H}_{\text{int}}$ to second order and introduce the ratio $\xi = g_2/g_1$ to quantify the relative size of the two e-ph couplings. (The standard Holstein model is recovered by setting $g_2 = 0$.) This simplification is sufficient to assess the relative importance of nonlinear interactions relative to Migdal's approximation. Additional orders up to $k = 4$ have been studied in the single carrier limit [266], where they produce the same qualitative picture.

To facilitate comparison with previous work, we set $k_B = \hbar = t = M = 1$. The scale of atomic displacements is set by the oscillation amplitude of the free harmonic oscillator $A = \sqrt{1/2\Omega}$ ($\sqrt{\hbar/2M\Omega}$ with the physical units restored). When reporting expectation values of X and its fluctuations, we explicitly divide by A in model units, thereby making the results dimensionless. To get an idea for what these values mean in reality, one can simply multiply the results by A in physical units. Later, we will consider FeSe to estimate the strength of the nonlinear interactions. In that case, the prefactor (in physical units) is $A \sim 0.036$ Å, which is obtained after adopting a selenium mass $M = 1.31 \times 10^{-25}$ kg and the experimental phonon energy $\hbar\Omega = 20.8$ meV of the A_{1g} mode. Alternatively, we obtain a comparable scale of $A \sim 0.051$ Å for the transition metal oxides, where $\hbar\Omega = 50$ meV and $M = 2.66 \times 10^{-26}$ kg are typical for the optical oxygen phonons. Finally, we adopt the standard definition for the dimensionless *linear* e-ph interaction strength $\lambda = 2g_1^2/W\Omega$, where $W = 8t$ is the bandwidth.

In what follows, we compare results obtained using determinant quantum Monte Carlo (DQMC) [102] and the self-consistent Migdal approximation (SCMA) [140, 1]. The details for our DQMC formulation are found in Section 1.3.2 and Appendix B, while Migdal's approximation and the SCMA are covered in Sections 1.3.1, 2.2, and 2.6. To determine the relative importance of nonlinear e-ph interactions against vertex corrections to Migdal's approximation, we juxtapose results obtained using these methods for the linear and nonlinear models. For example, comparing results obtained from DQMC and the SCMA for the linear model reveals the importance of vertex corrections. Analogously, comparing DQMC results for the linear and nonlinear models provides a measure for the importance of nonlinear interactions while treating the two models exactly. This methodology will allow us to isolate the source of any observed discrepancies. Deviations between SCMA and

98

DQMC for the linear model must be due to vertex corrections, while disagreement between DQMC results for the linear and nonlinear models must arise from the additional quadratic interaction.

The effects of nonlinear e-ph coupling or the omission of vertex corrections will manifest uniquely in different observables. Here, we focus on two-particle correlation functions. Specifically, we calculate the CDW susceptibility $\chi^{\mathrm{CDW}}(\pi, \pi)$ evaluated at the CDW wave vector $\mathbf{q}_{\mathrm{max}} = (\pi, \pi)$ and the singlet-pairing susceptibility χ^{SC}. Both of these functions were defined in Eqns. 2.12 and (2.14), respectively.

4.2.1 DQMC Simulation Details

In practice, we choose $\Delta\tau = 0.1$ in all our calculations. To reach equilibrium we use 80,000-100,000 warmup sweeps before collecting 80,000-120,000 measurement sweeps per Markov chain. With at least 8 Markov chains in each simulation, we collect between 10^5 and 10^6 total samples per data point averaged over 100-200 bins with jackknife error estimation. While QMC simulations of the (non)linear Holstein model face long autocorrelation times [248], they are free of a sign problem. As seen in our data, error bars (s.d.) are typically smaller than the symbol size and indicate our simulation parameters were sufficient to capture most of the important sample space.

4.3 Results

4.3.1 Comparison of susceptibilities at half-filling

We begin by comparing the susceptibilities for charge-density-wave (CDW) $\chi^{\mathrm{CDW}}(\pi, \pi)$ and pairing χ^{SC} correlations for a few illustrative cases. The first comparison takes place at half-filling $n \equiv \langle \hat{n}_i \rangle = 1$, where both CDW correlations and lattice displacements are significant. For example, at $\lambda = 0.2$, $\Omega = 0.5t$, and $T = 0.1t$, we obtain $|\langle X_{i,l} \rangle|/A \sim 1.97$ and 2.53 for $\xi = 0.05$ and $\xi = 0$, respectively. Taking $A \approx 0.036$ Å for FeSe, these values correspond to approximately 2.4% and 3.1% of the 2.95 Å Fe-Fe bond length. Similarly, taking $A \approx 0.051$ Å translates to 5.1% and 6.6% of the typical 1.96 Å Cu-O bond-distance in a high-T_{c}

superconducting cuprate. These displacements are not negligible (as we will show) when the nonlinearities are included, particularly given the weak values of the coupling we consider here. Later, we also discuss the size of the corresponding vibrational fluctuations.

Fig. 4.1 presents results for the temperature dependence of $\chi^{\mathrm{CDW}}(\pi, \pi)$ and χ^{SC} using $\Omega = 0.5t$, $N = 8 \times 8$, and $\lambda = 0.1$ and 0.2. This parameter set corresponds to weak coupling and satisfies the adiabatic criterion $\frac{\Omega}{E_{\mathrm{F}}} < 1$, where we expect the SCMA to hold. Indeed, when $\lambda = 0.1$ (Fig. 4.1a-b), there is fair agreement between the DQMC results obtained from both the linear ($\xi = 0$) and nonlinear ($\xi = 0.05$) e-ph models (symbols with solid curve), as well as the SCMA results for the linear model (dash-dot curve). When $\lambda = 0.2$ (Fig. 4.1c-d), however, we find significant disagreement between the results for $\xi = 0$ and $\xi = 0.05$ in both susceptibilities, especially at lower temperatures. In Fig. 4.1d the DQMC and SCMA results mostly agree for the linear Holstein model ($\xi = 0$), but a small nonlinear correction of $\xi = 0.05$ yields a marked suppression the CDW correlations. The rapid onset of CDW order in the $\xi = 0$ case (Fig. 4.1d) coincides with a sharp downturn in χ^{SC} (Fig. 4.1c), a feature which isn't captured by the SCMA result.

The suppression of CDW correlations (Fig. 4.1d) in the presence of nonlinear e-ph coupling demonstrates the importance of higher-order interactions over vertex corrections in this case. As we show later, the need for nonlinear e-ph coupling is greatest near half-filling, where the CDW correlations are strongest. Of course, the downturn of the pairing susceptibility obtained from DQMC ($\xi = 0$) at lower temperatures (Fig. 4.1c) appears to indicate that vertex corrections are also important for capturing the low temperature behavior of χ^{SC} at $\lambda \sim 0.2$. This value of λ is smaller than the breakdown values reported in Esterlis *et al.* [98], however, our models differ slightly. For one, they suppress the effects of Fermi-surface nesting by situating the electron density away from half-filling and also include hopping between next nearest-neighbors. Second, they use an alternate definition for $\lambda = \alpha^2 N_{\mathrm{F}}/M\Omega^2$, where N_{F} is the density of states evaluated at the Fermi energy. Nevertheless, the results in Fig. 4.1c-d reveal that the nonlinear corrections to the linear model are non-negligible at high temperature, even before the breakdown of Migdal's approximation becomes apparent.
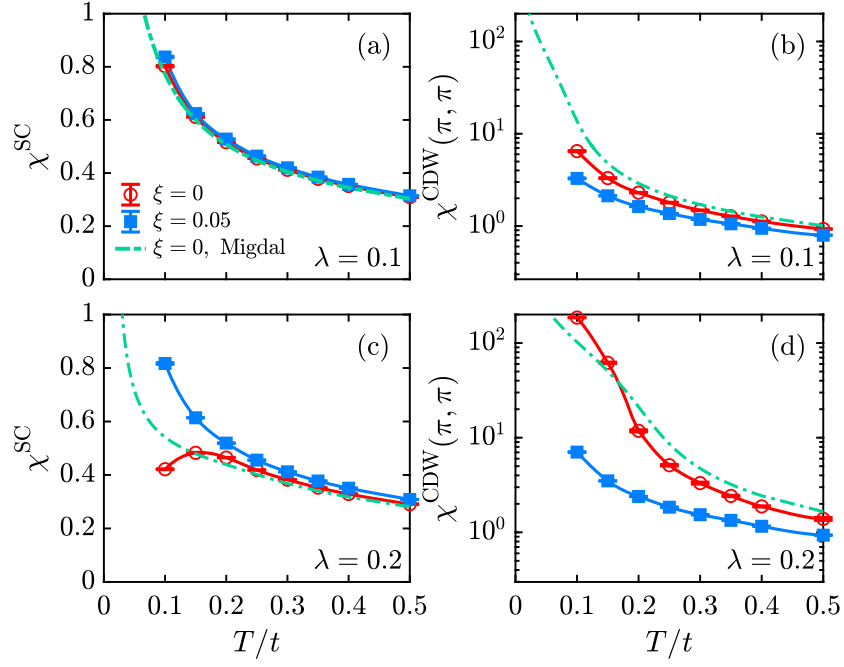
Figure 4.1: Comparison of the superconducting (SC) and charge susceptibilities at half-filling. The singlet-pairing (χ^{SC}) and charge-density-wave ($\chi^{\mathrm{CDW}}(\pi, \pi)$) susceptibilities vs. temperature for dimensionless e-ph couplings of $\lambda = 0.1$ (panels a-b) and 0.2 (panels c-d) at half-filling and $\Omega = 0.5t$. Results for the model with and without nonlinear corrections are shown using closed and open symbols, respectively. Error bars on the DQMC data points are one standard deviation statistical errors estimated using jackknife resampling. Figure taken from our Ref. [3].

4.3.2 Pairing susceptibilities for large phonon frequency

Now we consider a counter comparison in the antiadiabatic regime with intermediate coupling by setting $\lambda = 0.4$, $\Omega = 4t$, $N = 10 \times 10$, and $n = 0.55$ (Fig. 4.2). Away from half-filling, the pairing correlations grow more rapidly in part due to the larger Ω, but also because of less competition with (incommensurate) CDW correlations. Each of the curves in Fig. 4.2 show that the system has strong pairing correlations, but they would yield very different estimates for T_c. The SCMA significantly overestimates χ^{SC}, which is not surprising because Migdal's approximation is ill justified in this case (i.e., $\lambda \frac{\Omega}{E_F} \sim 1$). Interestingly, the nonlinear corrections become important at low temperature despite the presence of smaller lattice displacements (e.g. $|\langle X_{i,l} \rangle|/A \approx 0.22$).

4.3.3 Comparison over doping

Finally, Fig. 4.3 shows results for three combinations of λ and Ω/t over a wide range of electronic filling and at a fixed temperature $T = 0.25t$. The DQMC results for $\xi = 0$ ($\xi = 0.05$) are represented by open (closed) symbols in all three panels, while the SCMA results are shown as dashed or dotted lines in Fig. 4.3a-b. For reference, Fig. 4.3c shows the corresponding the average lattice displacement, obtained by averaging over *all* spacetime points $\langle X_{i,l} \rangle = \frac{1}{N^2 L} \sum_{i,l} X_{i,l}$. We caution that $\langle X_{i,l} \rangle$ provides a rough measure of the typical lattice displacements, and not a complete picture of the ionic subsystem. We will return to this subtle issue later, when we discuss the displacement fluctuations.

Case (1), $\lambda = 0.15$, $\Omega = 0.5t$: These parameters are nearly identical to those used in Fig. 4.1. The deviations in $\chi^{\text{CDW}}(\pi, \pi)$ for $\xi = 0$ and $\xi = 0.05$ (Fig. 4.3a) become apparent near $n \geq 0.6$ whereas the SCMA result starts to deviate from DQMC for $n \geq 0.8$. At this temperature, the results for χ^{SC} essentially agree (Fig. 4.3b), but the nonlinear model yields a smaller average displacement $\langle X_{i,l} \rangle/A$ (Fig. 4.3c). These results further reinforce our prior observation that Migdal's approximation and the linear model can break down in different parameter regimes (in this case doping).

Case (2), $\lambda = 0.3$, $\Omega = 0.5t$: Now we double λ while keeping the Ω fixed. The increase in λ produces larger average displacements (Fig. 4.3c) and more pronounced nonlinear
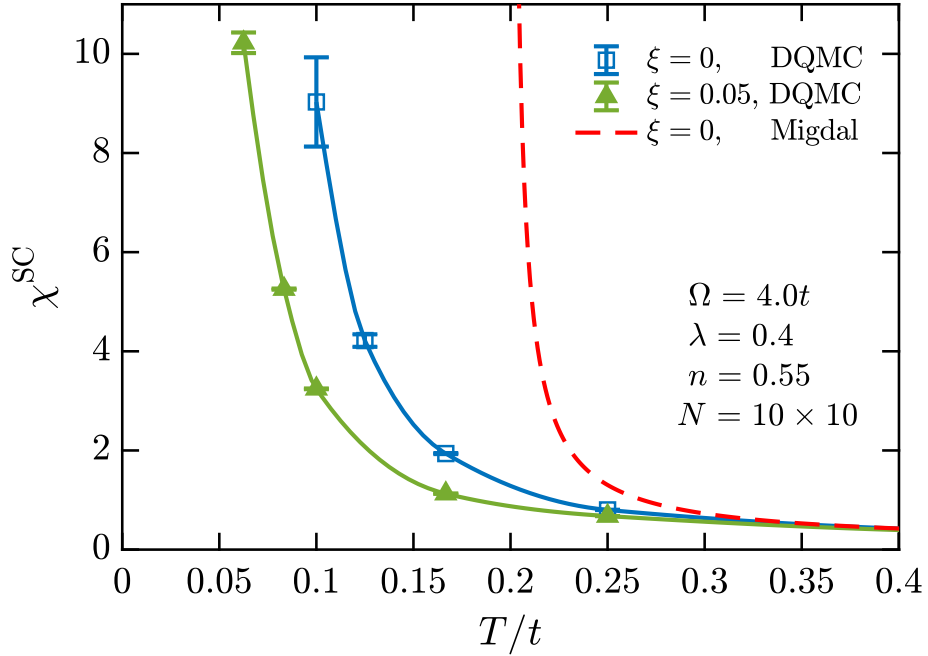
Figure 4.2: Temperature dependence of the superconducting susceptibility for a large phonon frequency $\Omega = 4.0t$. Results are shown for a filling of $n = 0.55$ and a lattice size $N = 10 \times 10$. Both the linear ($\xi = 0$, blue squares) and nonlinear ($\xi = 0.05$, green triangles) Holstein model results from determinant quantum Monte Carlo (DQMC) show a rapid growth of pairing correlations with decreasing temperature, but approach different asymptotes. The self-consistent Migdal approximation (SCMA) results (red dashed line), shown here for reference, yield a large and inaccurate estimate for the superconducting critical temperature due to the invalidity of Migdal's approximation. The lines connecting DQMC data are spline-interpolated and used only to guide the eye. Error bars on the DQMC data points are one standard deviation statistical errors estimated using jackknife resampling. Figure taken from our Ref. [3].
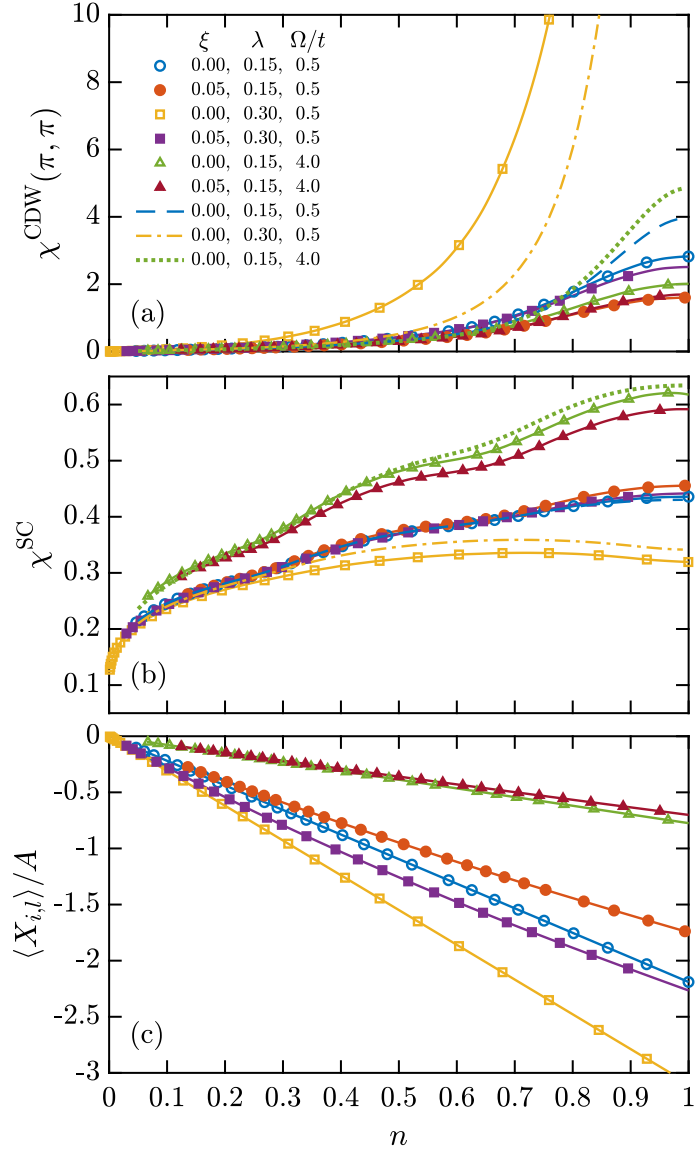
Figure 4.3: Doping dependence of the correlations at fixed temperature $T = 0.25t$. (a) The charge-density wave (CDW) susceptibility $\chi^{\mathrm{CDW}}(\pi, \pi)$, (b) superconducting (SC) pair-field susceptibility χ^{SC}, and (c) the average value of the phonon field $\langle X_{i,l} \rangle / A$ are shown for a lattice size of $N = 8 \times 8$. Symbols connected by solid lines depict determinant quantum Monte Carlo (DQMC) data where open (closed) symbols correspond to $\xi = 0$ ($\xi = 0.05$). Like symbol shapes between curves indicate the same pair of λ and Ω. Dashed and dotted lines correspond to self consistent Migdal approximation calculations for $\xi = 0$. Error bars on the DQMC data were estimated using jackknife resampling; however, all one-sigma error bars are smaller than the symbol size and have been suppressed for clarity. Lines connecting DQMC data are used only to guide the eye. Figure taken from our Ref. [3].

corrections. It also induces a stronger CDW (Fig. 4.3a) for the linear ($\xi = 0$) model. The SCMA qualitatively captures the CDW correlations of the linear model in panel (a), but underestimates their strength, which can be attributed to solely to the vertex corrections, consistent with the conclusions of Esterlis et al. [[98]]. Due to the large CDW correlations, there is a suppression [267, 268] in χ^{SC} for $\xi = 0$, which is mostly captured by the SCMA (Fig. 4.3b). The introduction of the nonlinear interaction significantly reduces the CDW correlations and their competition with SC, which enhances χ^{SC} at larger values of n.

Case (3), $\lambda = 0.15$, $\Omega = 4.0t$:   Now we look at the large phonon frequency results for DQMC (green and crimson triangles) and SCMA (green dotted line). The larger Ω boosts pairing correlations (Fig. 4.3b) across the entire doping range and all of the χ^{SC}'s are in fair agreement. However, we know from Fig. 4.2 that larger differences between each curve will emerge at lower temperatures. In fact, the SCMA already overestimates $\chi^{\text{CDW}}(\pi, \pi)$ near half-filling at this temperature, a feature we may attribute to antiadiabaticity. The increased value of Ω means that the lattice vibrations are characterized by stiffer spring constants. We obtain smaller average lattice displacements at all n as a result (Fig. 4.3c), which reduces the importance of the nonlinear interaction and produces better agreement between $\xi = 0$ and $\xi = 0.05$ DQMC results.

We should be careful in interpreting the results at lower filling in each of the cases above. On the one hand, our examples suggest that corrections to the e-ph interaction are most important for describing the CDW phase transition near half-filling, which appears at higher temperatures. On the other hand, corrections could become important in the dilute carrier region at much lower temperatures. Nonetheless, our results suggest that the linear Holstein model is sensitive to nonlinear corrections over a large parameter space and that regions of this space overlap with regions where Migdal's approximation is not valid. But perhaps more importantly, there are regions where the linear approximation breaks down before Migdal's approximation does.

4.3.4   Average lattice displacement and its fluctuations

In Fig. 4.3c we showed that the magnitude of the mean displacement $\langle X_{i,l} \rangle / A$ had an approximately linear dependence on the filling n. These displacements become larger when

the dimensionless e-ph coupling λ is increased or when the phonon energy Ω is decreased (or, equivalently, when the spring constants are softer). The behavior of $\langle X_{i,l} \rangle$ as a function of doping can be loosely understood by considering the atomic limit. In this case, the effect of the linear e-ph-interaction is to shift the equilibrium position of the lattice to $X_0 \approx -n\frac{\alpha_1}{M\Omega^2}$ [105]. Indeed, the results shown in Fig. 4.3c for the linear model are well described by this function. Based on this observation, one might then be tempted to try to eliminate the nonlinear interactions by defining new lattice operators $\hat{X}' = \hat{X} - X_0 = \hat{X}$ in hopes that the displacements of $\hat{X}'$ remain small. Unfortunately, this procedure is not viable for several reasons.

The first reason is that global shift of the equilibrium position will only be effective in the case of a uniform charge distribution. This certainly will not be the case when the CDW correlations are significant. For example, in the (π, π) CDW phase, half of the sites are doubly occupied with an average displacement of $\approx 2X_0$ while the remaining sites are unoccupied with an average displacement of zero. In this instance, $\langle X_{i,l} \rangle = X_0$, consistent with our results in Fig. 4.3c, but shifting the origin to $X = X_0$ will not eliminate the large lattice displacements at each site.

The second reason why redefining the origin will not work is that such transformations do not affect the displacement fluctuations, which are also significant for the linear Holstein model. To show this, we examine the root-mean-square (rms) displacement of $X_{i,l}$ in our system with a linear e-ph coupling strength λ, which is defined as

$$\sigma_X(\lambda) = \sqrt{\langle X_{i,l}^2 \rangle - \langle X_{i,l} \rangle^2} \tag{4.4}$$

and is formally identical to a standard deviation. The value of σ_X in the limit $n \to 0$ approaches the (thermal) rms displacement for the free harmonic oscillator, which we denote as $\sigma_X(0)$ and is given by

$$\sigma_X(0) = \sqrt{\frac{1}{2\Omega} [2n_{\mathrm{B}}(\Omega) + 1]}, \tag{4.5}$$

where $n_{\mathrm{B}}(\Omega) = [e^{\beta\Omega} - 1]^{-1}$ is the Bose occupation function.

Fig. 4.4 shows results for $[\sigma_X(\lambda) - \sigma_X(0)]/A$, as a function of filling for the same parameters used in Fig. 4.3. (For reference, for $\Omega/t = 0.5$ and 4.0, we obtain $\sigma_X(0)/A = 1.146$
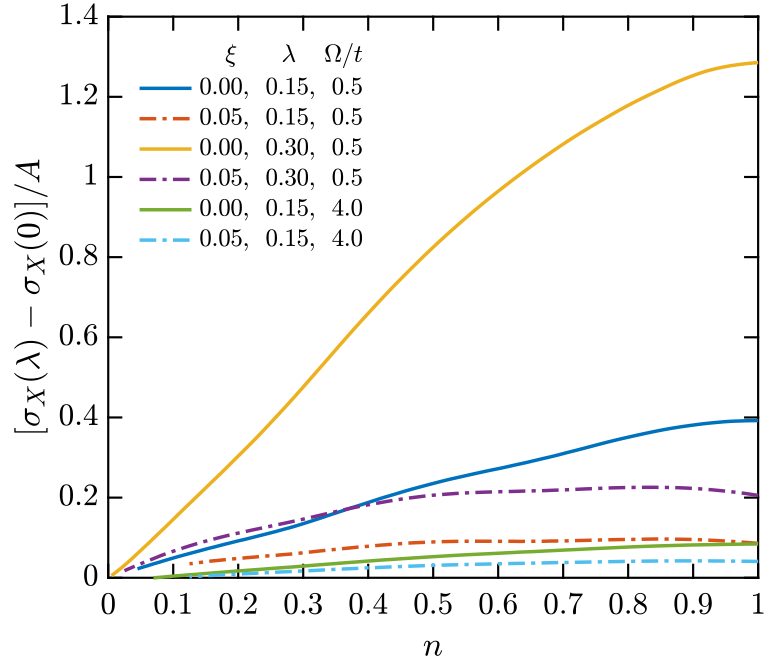
Figure 4.4: Doping dependence of the root-mean-square (rms) lattice fluctuations. Comparison of rms fluctuations beyond the (noninteracting) thermal oscillator value, denoted $[\sigma_X(\lambda) - \sigma_X(0)]/A$ as a function of filling for $T = t/4$ and $N = 8 \times 8$. Here, $\sigma_X(0)$ is the baseline contribution to the rms fluctuations from the noninteracting thermal oscillator and $\sigma_X(\lambda)$ is the fluctuation in the full interacting problem. Again, we find similar behavior to Fig. 4.3c only now we are looking at the growth of oscillations beyond zero-point fluctuations (which can also be large). Figure taken from our Ref. [3].

and 0.354, respectively.) Here, we see that the fluctuations of the linear Holstein model are quite sensitive to the size of the dimensionless linear e-ph interaction λ. Moreover, the magnitude of the fluctuations generally grow monotonically with filling until reaching a maximum at half-filling. There, the largest fluctuations shown correspond to $\sigma_X(\lambda = 0.3)/A \approx 2.43$, which is more than double the size of captured by $\sigma_X(0)/A$. Again, taking FeSe or a typical cuprate as references, these fluctuations correspond to $\sim 3.0\%$ and $\sim 6.3\%$ of the respective lattice constants. It is important to note that $\sigma_X(0)/A$ rises sharply for even smaller (and more realistic) model values of $\Omega/t \approx 0.02 - 0.1$. Such values, however, are typically inaccessible to DQMC due to prohibitively long autocorrelation times.

The overall effect of the nonlinear coupling is to suppress the rms displacements relative to the linear case, especially near half-filling. Only when $(\xi, \lambda, \Omega/t) = (0, 0.15, 4.0)$ and $(0.05, 0.15, 4.0)$ do we find close agreement between the linear and nonlinear models, and typical lattice displacements that are a small fraction of the lattice spacing.

4.3.5 How big are nonlinear interactions in materials?

Throughout this work we used $\xi = 0.05$, but how representative is this value for a realistic system? To address this question, we considered the case of bulk FeSe, a quasi-2D material where the position of the Se atoms influence the on-site energies of the Fe $3d$ orbitals [269], somewhat akin to the 2D Holstein model. To determine the strength of the linear and nonlinear e-ph coupling, we constructed a Wannier function basis from density functional theory (DFT) calculations to determine the on-site energy of the Fe 3d orbitals $\epsilon_{\text{diag}}(z_{\text{Se}})$ as a function of the Se atom's static displacement z_{Se} along the c-axis. We then applied a polynomial fit of the form $f(z_{\text{Se}}) = a_0 + a_1(z_{\text{Se}} - z_0) + a_2(z_{\text{Se}} - z_0)^2$ to the site energy $\epsilon_{\text{diag}}(z_{\text{Se}})$ for each orbital and computed $\xi = A\frac{a_2}{a_1}$. Here, the oscillation amplitude $A = \sqrt{\hbar/2M\Omega} \approx 0.036$ Å, adopting a selenium mass $M = 1.31 \times 10^{-25}$ kg, and the calculated phonon frequency $\Omega = 2\pi \cdot 5.02$ THz of the A_{1g} mode.

The results are summarized in Table 4.1, where ξ ranges from -0.1640 to 0.0148, with the strongest nonlinearity appearing for the d_{xy} orbital. We do not investigate $\xi < 0$ in our model calculations because others have shown that it leads to increased softening of

Table 4.1: Estimation of nonlinear e-ph coupling ratio ξ in FeSe. Results from fits of the on-site energy $\epsilon_{\mathrm{diag}}(z_{\mathrm{Se}})$ for each d-orbital of Fe as a function of the height of the Se atom z_{Se} measured with respect to the Fe-plane. Fitting $\epsilon_{\mathrm{diag}}(z_{\mathrm{Se}})$ with a simple polynomial of the form $f(z_{\mathrm{Se}}) = a_0 + a_1(z_{\mathrm{Se}} - z_0) + a_2(z_{\mathrm{Se}} - z_0)^2$, we estimate the nonlinear coupling ratio ξ from the fitting parameters a_2/a_1. Table from our Ref. [3].

Orbital	a_2/a_1 [Å^{-1}]	ξ
d_{xy}	-4.5936	-0.1641
d_{xz}/d_{yz}	-0.4804	-0.0172
d_{z^2}	0.0159	0.0006
$d_{x^2-y^2}$	0.4155	0.0148

the phonon dispersion and larger CDW correlations [151]. Nevertheless, our results show $|\xi| \approx 0.05$ is certainly not out of the question for a real material.

4.4 Discussion

We have demonstrated that the linear approximation to the e-ph interaction in the Holstein model breaks down in commonly studied parameter regimes. Importantly, this breakdown regime overlaps with ones where Migdal's approximation captures the DQMC result, even if only qualitatively. This observation indicates that nonlinear corrections to the underlying linear lattice model may be important even when vertex corrections are not. We also studied the example of bulk FeSe from first principles and found that nonlinear e-ph interactions in a real materials can be quite significant and on par with, or even larger than our model choice of $|\xi| = 0.05$.

It is natural to wonder which parameter regimes might be best for ensuring lattice displacements remain small enough justify the use of a linear interaction. We have found that tuning λ to smaller values suppresses the lattice displacements and their fluctuations, but also pushes the growth of correlations to lower temperatures, making computations more expensive. (Some groups [264] have recently managed to access such temperatures in QMC, however.) Alternatively, one could also shrink the displacements by choosing antiadiabatic parameters (i.e., $\Omega > E_\mathrm{F}$). But even for a strongly antiadiabatic choice of $(\lambda,\, \Omega/t,\, n) = (0.4, 4.0, 0.55)$, nonlinear corrections to the e-ph interaction produced considerable differences in the resulting temperature dependence of the superconducting susceptibility. Unfortunately, focusing on smaller phonon energies, which are relevant for real materials, will also produce larger lattice displacements and fluctuations that are inconsistent with a linear interaction. While our results are not comprehensive across the entire parameter space of the Holstein model, we are forced to conclude that they do call large portions of this space into question. For instance, our results imply that combinations of $\lambda \gtrsim 10^{-1}$ and $\Omega \lesssim 4t$ yield sizable displacements and displacement fluctuations, which would necessitate additional nonlinear interactions and/or anharmonic lattice potentials [261]. Our results

indicate a clear and present need for more work extending beyond the simplest effective models, especially when one is trying to describe the physics of a real system.

The Holstein model and Migdal's approximation have long served as cornerstones in the study of electron-phonon interactions. Their relative simplicity has helped shape our intuition about superconductivity, its competition with charge order, and polaron formation, and studying the Holstein model can address the essential physics of these processes. While it is clear that these models are built on the assumption of small lattice displacements, it is not always clear how large these displacements will be in practice or whether additional nonlinear interactions will modify the physics of the model. One must, therefore, be careful when extrapolating results from effective models to real materials when they are driven outside their range of validity. For example, we have shown that the Holstein model can produce displacements that begin to approach the Lindemann criteria for melting (particularly as Ω is reduced), but the model cannot describe such a transition. Instead, it over predicts various tendencies towards ordered phases in these cases. Similarly, it is unclear how one should map critical λ values derived for the breakdown of Migdal's approximation onto real materials.

Chapter 5

Two-component Hubbard Bilayer model

A hypothesis by Steve Kivelson [71] suggests that one can raise the superconducting transition temperature (T_c) in a large pairing scale superconductor, inhibited by phase fluctuations, by coupling the system to a metal. Subsequent model calculations added support to this idea using a composite bilayer model with disconnected negative-U sites coupled to a metal layer via single-particle tunneling. We study a more general version of this model using the dynamical cluster approximation in a less studied regime where the interaction $|U|$ is comparable with the electronic bandwidth. We find that the transition temperature follows a nonmonotonic dependence on the interlayer tunneling, peaking at some finite value comparable to the hopping in the metallic layer. However, unlike previous works, this boost in the critical temperature appears to be modest compared with the negative-U model in isolation. We show that while the tunneling enhances pair mobility, it also decreases the effective pairing interaction, creating the competition responsible for the nonmonotonic behavior of T_c. Much of the work in this chapter stems from a work in preparation [4] and describes the status of our work thus far.

5.1   Introduction

One of the curious observations of early cuprate superconductors was that they hosted a remarkably low carrier density and correspondingly low superfluid stiffness; yet, they have

a large pairing scale characterized by the superconducting gap and correspondingly short coherence length [270, 72]. The low superfluid stiffness and short coherence length, as seen in underdoped cuprates, means that phases fluctuations can prevent the system from achieving long-range phase coherence [72, 271, 272, 273, 274, 73]. As a result, long-range phase coherence occurs at a superconducting transition temperature T_c that is significantly lower than the corresponding mean-field temperature scale T_c^{MF}. Metallic superconductors, on the other hand, do realize the mean-field transition temperature because pairing and long-range phase coherence happen simultaneously [271].

A proposal by Kivelson [71] has suggested that it might be possible to raise T_c closer to its mean-field pairing scale in a superconductor with low superfluid stiffness and a large pairing scale by coupling it to a metallic layer. Using a disconnected (i.e., no in-plane hopping) negative-U Hubbard layer coupled to a metallic layer by single-particle tunneling $t_\perp$, this system was originally studied perturbatively [94] for $|U|$ and $t_\perp$ much smaller than the metallic bandwidth $W = 8t$, and later using quantum Monte Carlo (QMC) up to values of $|U|$ larger than the bandwidth [95]. In this model, the pairing layer has zero superfluid stiffness and the corresponding critical temperature vanishes when the interlayer tunneling is switched off (i.e. $t_\perp = 0$). For small and increasing $t_\perp$, phase coupling between pairing sites is enabled by Josephson tunneling through the metallic layer [94, 95] and T_c increases; however, T_c is eventually suppressed by the same delocalization effects beyond intermediate values of $t_\perp$. The numerical results [95] suggest that phase fluctuations produce an exponential suppression in T_c for small $t_\perp$. Moreover, this work found that the highest T_c that can be achieved by varying $t_\perp$ is three to four times smaller than T_c^{MF} for small and intermediate U/t, while for large U/t it is bounded by the highest T_c in the 2D attractive Hubbard model.

The intermediate regime $U \sim W$ was later addressed using QMC, but with intraplane hopping in the negative-U layer restored [96]. Here, the correlated layer has a small but nonzero superfluid stiffness, even when $t_\perp = 0$, and the superconducting transition follows the Berezinskii-Kosterlitz-Thouless (BKT) universality class of the XY model. For increasing $t_\perp$, the authors of Ref. [96] also found a proximity effect induced suppression of the pairing correlations in the correlated layer, while the metallic layer exhibited nonmonotonic behavior with a maximum at intermediate $t_\perp$. In other words, pairing is orbital (or layer)

dependent for small $t_\perp$, an observation that is reminiscent of the orbital selective Mott insulating phase observed in more sophisticated two-orbital models with repulsive-U and Hund's interactions [275, 276]. Finally, pairing is suppressed simultaneously in both layers beyond a critical value of $t_\perp$. These trends were also found to persist through a modest finite size scaling analysis of the QMC results.

Despite the finite size analysis in Ref. [96], an estimate of T_c as a function of $t_\perp$ is lacking in the literature in the parameter regime $U \sim W$. We address this issue here by studying an negative-U Hubbard model coupled to noninteracting layer with a representative parameter set and obtaining T_c as a function of $t_\perp$ using the dynamical cluster approximation (DCA). Since the DCA incorporates long range correlations in the thermodynamic limit through a coarse-graining of momentum space, it provides a different numerical perspective than finite cluster QMC methods. Our results show that for large clusters, T_c is enhanced for finite $t_\perp$ beyond the system T_c when $t_\perp = 0$, reaching a maximum in the vicinity of $t_\perp \sim 1.5$ - 2.0. That is, an increased single-particle tunneling between the layers reduces the effects of phase fluctuations present in negative-U layer. We also discuss the competition between an increasing pair mobility and reduced effective pairing interaction. These quantities suggest signs of crossover behavior as seen in the attractive Hubbard model.

5.2 Model and Methods

5.2.1 Two-component Model

Our composite system introduced in Section 1.2.6 consists of a correlated negative-U Hubbard layer and a non-interacting (metallic) layer connected through interlayer single-particle tunneling $t_\perp$ (See Fig. 5.1). Both layers have a square lattice geometry with identical lattice spacing. The associated bilayer Hamiltonian is defined as

$$\hat{H} = -\sum_{\langle ij \rangle, \alpha, \sigma} t_\alpha (\hat{c}^\dagger_{i\alpha\sigma} \hat{c}_{j\alpha\sigma} + \text{H.c}) - |U| \sum_i \hat{n}_{i1\uparrow} \hat{n}_{i1\downarrow} + \sum_{i,\alpha,\sigma} (\epsilon_2 \delta_{\alpha 2} - \mu) \hat{n}_{i\alpha\sigma} + t_\perp \sum_{i,\sigma} (\hat{c}^\dagger_{i1\sigma} \hat{c}_{i2\sigma} + \text{H.c.}),$$

(5.1)
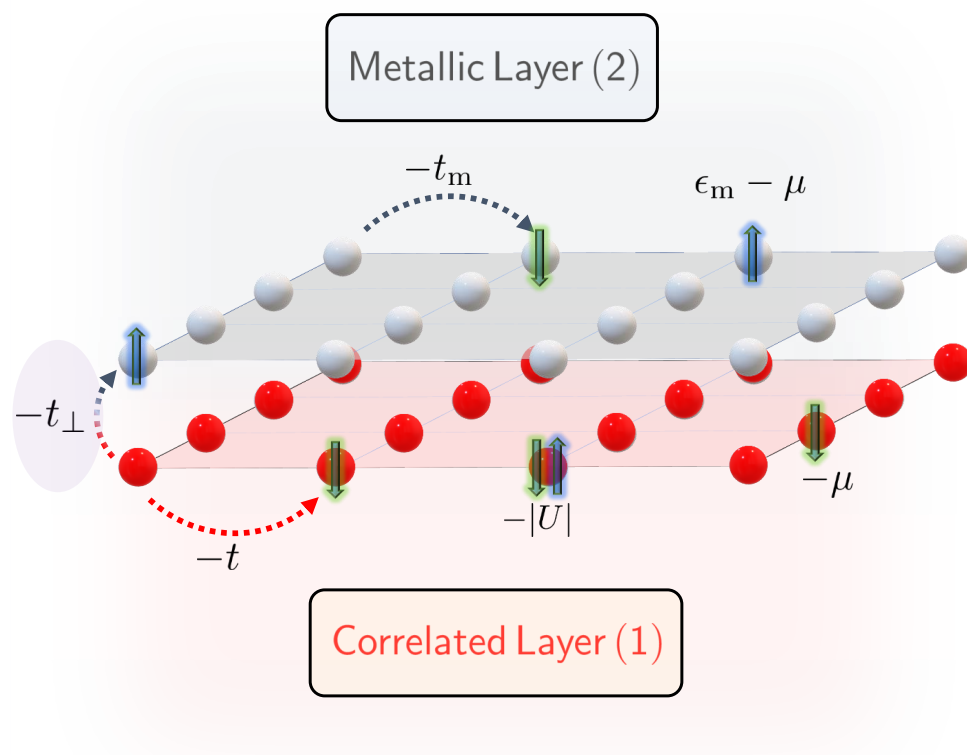
Figure 5.1: A schematic of the model described by Eqn. 5.1. Note that $t_{\mathrm{m}} \equiv t_2$ and $\epsilon_{\mathrm{m}} \equiv \epsilon_2$.

where $\hat{c}_{i\alpha\sigma}^\dagger$ $(\hat{c}_{j\alpha\sigma})$ creates (destroys) an electron on the ith site of the $\alpha = 1$ or 2 layer with spin σ $(=\uparrow,\downarrow)$ and $\hat{n}_{i\alpha\sigma} = \hat{c}_{i\alpha\sigma}^\dagger \hat{c}_{i\alpha\sigma}$. The in-plane nearest neighbor hoppings t_α are fixed such that $t_1 \equiv t = 1$ and $t_2 = 2t$, whereas the interlayer tunneling $t_\perp$ is a variable parameter. An attractive on-site Coulomb interaction U in the correlated layer $(\alpha = 1)$ is responsible for the formation of local (s-wave) Cooper pairs. Lastly, the noninteracting metallic layer $(\alpha = 2)$ has an additional on-site energy term that is used to shift the van Hove singularity slightly above the chemical potential μ (we set $\epsilon_2 - \mu = 0.2t$).

5.2.2   Methods

The Hamiltonian in Eqn. (5.1) is studied using DCA++ [113], a state-of-the-art implementation of the DCA method. In this formalism, the lattice problem is reduced to a finite-size cluster embedded in a mean-field that is self-consistently determined to represent the system beyond the cluster [107]. Our model is an effective two band model, with N_c unit cells arranged in an $N \times N$ square lattice. This arrangement results in a $2N_c$-site cluster problem that is solved using a continuous-time auxiliary-field QMC algorithm [110, 111, 112]. In this work, we examine three different clusters, namely 4×4 ($N_c = 16$), 6×6 ($N_c = 36$), and 8×8 ($N_c = 64$).

The QMC simulations utilized 6000 independent Markov chains to collect 2×10^6 to 5×10^6 total measurements per DCA iteration. The negative-U interaction tends to produce long autocorrelation times, so each of the contributing measurements was made after skipping 50-100 Monte Carlo updates to further ensure statistically independent sampling. A typical DCA calculation for our model (i.e., for a single set of model parameters) reaches numerical accuracy in 6-8 iterations. Convergence is attained when the difference in the DCA self-energy on subsequent iterations is either less than a small fixed numerical cutoff, or when the difference becomes smaller than the QMC statistical error.

The chemical potential μ is allowed to vary such that the filling in the correlated layer remains fixed at $n_1 \equiv \langle \hat{n}_{i1} \rangle = 0.75$, where $\hat{n}_{i1} = \hat{n}_{i1\uparrow} + \hat{n}_{i1\downarrow}$. As a result, the filling of the metallic layer is allowed to take whatever value is necessary to satisfy thermodynamic equilibrium. This choice of filling avoids any complications that might stem from a perfectly

nested Fermi surface as seen at half-filling and it still gives us access to the superconducting transition in the negative-U model at higher temperatures.

For the isolated ($t_\perp = 0$) 2D attractive Hubbard model away from half-filling, the system has an s-wave SC ground state. When $|U|/t \ll 1$, the system adopts a weak coupling BCS state and eventually crosses over to a Bose-Einstein condensate (BEC) of hard-core on-site bosons for $|U|/t \gg 1$ [277, 278, 279, 280, 281]. Consequently, the behavior of T_c as a function of $|U|/t$ is a non-monotonic function that peaks at intermediate $|U|/t \approx 4-6$, and gradually tapers off in the presence of increasingly stronger phase fluctuations at larger values of $|U|/t$ [278, 282, 280]. We are interested in the question of whether the reduction in T_c due to phase fluctuations can be reversed in the composite system, hence, we set $U = -10t$ in the correlated layer. As the interlayer hopping $t_\perp$ is gradually increased, we will study its effects on the T_c of the correlated layer.

We obtain estimates for the superconducting T_c by solving the Bethe-Salpeter equation

$$- \frac{T}{N_c} \sum_{k'} \Gamma_{pp}(k, k') G(k') G(-k') \phi_\alpha(k') = \lambda_\alpha \phi_\alpha(k) \,. \tag{5.2}$$

Here, ϕ_α and λ_α represent a possible eigenvector and eigenvalue, repectively; $G(k)$ is the dressed single-particle propagator and $\Gamma_{pp}(k, k')$ the irreducible particle-particle vertex, both obtained from the DCA and written compactly using the notation $k = (\mathbf{k}, i\omega_n)$, where $\mathbf{k}$ is the momentum and $i\omega_n$ is a fermionic Matsubara frequency $\omega_n = (2n+1)\pi T$. A superconducting transition occurs when the leading eigenvalue $\lambda_{\tilde{\alpha}}(T_c) = 1$. For our case of an attractive Hubbard layer, we find that the leading eigenvector ($\phi_{\tilde{\alpha}}$) has s-wave symmetry (i.e., $\phi_{\tilde{\alpha}}, \lambda_{\tilde{\alpha}} \to \phi_s, \lambda_s$) for all the values of $t_\perp$ we consider.

5.3 Results

We begin by fixing the temperature $T = t/4$ and varying the interlayer hopping. In Fig. 5.2, we plot λ_s as a function of $t_\perp/t$ for $N_c = 16$, revealing a monotonically decreasing function in $t_\perp/t$. For $t_\perp/t = 0$, the leading eigenvalue is greater than unity, indicating that when the layers are isolated, the correlated layer is in the superconducting phase for the given
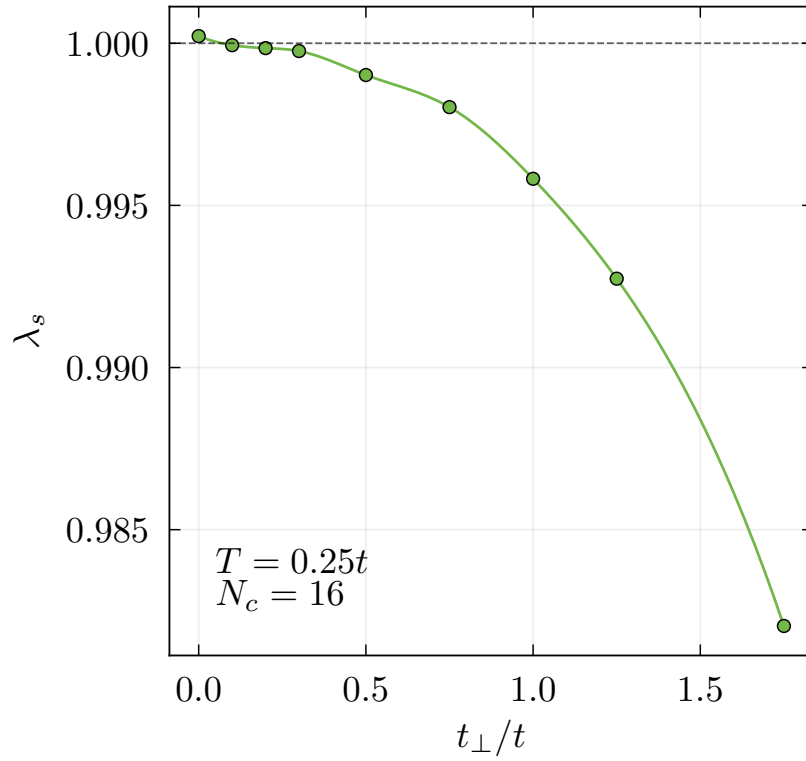
Figure 5.2: Interlayer hopping dependence of the s-wave eigenvalue λ_s for fixed temperature $T = 0.25t$, in-plane cluster size of $N_c = 16$, and filling of the correlated layer $n_1 = 0.75$. Figure taken from our Ref. [4].

parameters. For $t_\perp/t > 0$, $\lambda_s < 1$ indicating that the system is now in the normal state at $T = 0.25t$. As $t_\perp$ increases, the leading eigenvalue decreases, implying that the pairing correlations become weaker overall. However, there is a noticeable downturn in the leading eigenvalue for $t_\perp/t > 0.3$. This shift in the functional dependence of $\lambda_s(t_\perp)$ coincides with a growth of proximity-induced pairs in the metallic layer at $t_\perp/t > 0.5$ observed in Ref. [96] for similar parameters. For this $N_c = 16$ result, it is apparent that the superconducting transition is moved to lower temperatures as the interlayer tunneling is increased.

Next, we focus on the temperature dependence of $1 - \lambda_s(T)$ for several values of $t_\perp$ plotted in Fig. 5.3. Starting from high-temperature ($T/t = 2$), we cool the composite system down to T_c, the latter of which is identified by the temperature at which $1 - \lambda_s(T = T_c) = 0$. The family of curves depicted in Fig. 5.3 represent different values of the interlayer hopping between 0 and 2.5 but with all other model parameters identical (except for μ, which is adjusted to maintain $n_1 = 0.75$). All curves for $t_\perp/t \leq 1$ are denoted by filled circles and solid lines (to guide the eye) and the remaining curves with $t_\perp/t > 1$ are depicted with filled squares and dashed lines. This distinction is made because it roughly marks a change in convexity of the curves of $1 - \lambda_s(T)$ and consequently, the nature of the superconducting phase transition itself.

As noted, the supeconducting transition in this model is expected to follow the BKT universality class. Since the DCA embeds the finite-size cluster in a mean-field, the temperature dependence found in the DCA will cross over to mean-field behavior when the correlation length exceeds the cluster size. At higher temperatures, however, when the correlations are still contained within the cluster, the DCA results will exhibit the true temperature dependence of the system in the thermodynamic limit.

For small $t_\perp/t < 1$, the curves display convex behavior, indicating the presence of phase fluctuations and BKT behavior [73]. For larger $t_\perp/t > 1$, the temperature dependence of $1 - \lambda_s(T)$ changes qualitatively to a more BCS-like behavior, exhibiting logarithmic $\ln(T/T_c^{\mathrm{MF}})$ dependence. This change in the curvature of $1 - \lambda_s(T)$ with increasing $t_\perp$ is similar to the change found in the repulsive Hubbard model with increasing hole doping [73] and reflects the decreasing strength of phase fluctuations. Importantly, the gradual evolution of the

Figure 5.3: Temperature dependence of $1 - \lambda_s(T)$ for the composite bilayer system on a $N_c = 16$ site cluster for several different values of the interlayer hopping in the interval $t_\perp/t \in [0, 2.5]$. Filled circles (squares) with solid (dashed) lines depict results for $t_\perp/t \leq 1$ ($t_\perp/t > 1$). Figure taken from our Ref. [4].

temperature dependence of $1 - \lambda_s(T)$ with increasing $t_\perp/t$ does not appear to enhance the T_c.

As a rough measure of the finite-size effects for this system, we repeat part of the analysis just described for five illustrative values of $t_\perp/t$ using a 6×6 ($N_c = 36$) cluster (see Fig. 5.4). Again, one sees that $1 - \lambda_s(T)$ begins to follow the same pattern as before, changing to a more rapid dependence with increasing $t_\perp/t$. However, the larger cluster treats spatial fluctuations on longer length scales, and the resulting transition temperatures are, therefore, reduced.

The estimated T_c values obtained from $1 - \lambda_s(T)$ are depicted in Fig. 5.5 for all three cluster sizes $N_c = 16$, 36, and 64. The smaller cluster results ($N_c = 16$, 36) predictions are quantitatively different, but they describe the same qualitative result: the coupling $t_\perp$ to the metallic layer suppresses T_c in this parameter regime. The significant cluster size dependence at small tunneling values suggests that the larger cluster is needed to account for long-range spatial fluctuations that suppress T_c. Based on previous studies of the negative-U Hubbard model [278, 282], T_c is expected to fall in the range of 0.1 to 0.14 for our model parameters, which is smaller than the lowest temperature shown for $t_\perp = 0$. Therefore, we expect T_c to continue dropping for the smallest values of interlayer tunneling. However, we do not observe such a cluster size dependence for larger tunneling values, meaning that T_c will remain enhanced over some finite range of $t_\perp$. Since these curves are trending downward for the largest tunneling values, we expect the final peak to be in the range of 1.5 - 2.5.

The authors of Ref. [96] studied a wider set of parameters, some of which get close enough to ours for qualitative comparison. Unfortunately, these authors did not estimate T_c, meaning that an apples-to-apples comparison is not possible. They studied the relative size of real space pair correlations in each layer, finding a monotonic decrease in the correlations with increasing $t_\perp/t$. Even for increasingly larger finite-size lattices, their qualitative result remains the same. The metallic layer exhibited a nonmonotonic dependence of pairing correlations with respect to $t_\perp/t$, signaling an onset of induced pairing. In other words, the composite system at intermediate coupling $W \sim |U|$ gives rise to a significant proximity effect where local singlet-pairs are created in the metallic layer at the expense of T_c.
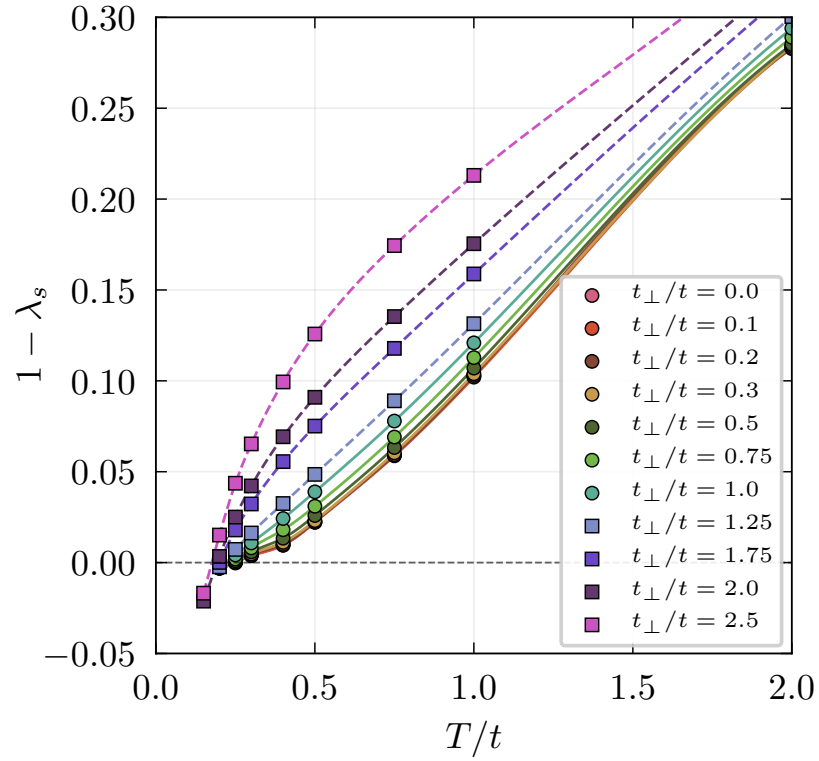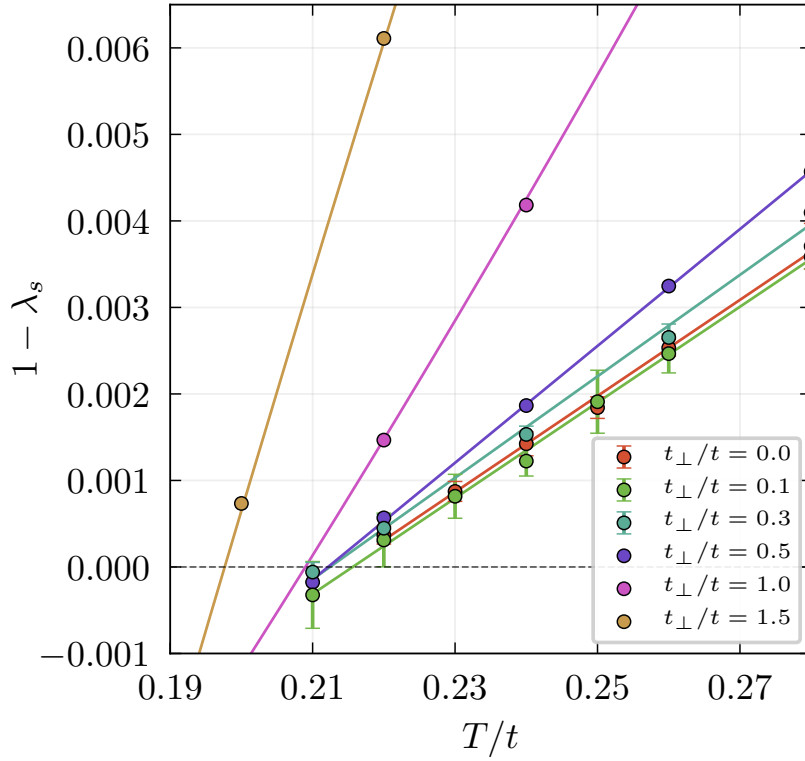
Figure 5.4: Temperature dependence of $1 - \lambda_s(T)$ for the composite bilayer system on a $N_c = 36$ site cluster for several different values of the interlayer hopping $t_\perp$. Error bars (s.d.) are shown for the smallest three values of $t_\perp/t = 0.0, 0.1, 0.3$ obtained by repeating the last DCA iteration using different random number seeds in the CTQMC cluster solver. The resulting T_c estimates for $t_\perp/t = 0.0, 0.1,$ and 0.3 fall within each other's range of uncertainty. Figure taken from our Ref. [4].
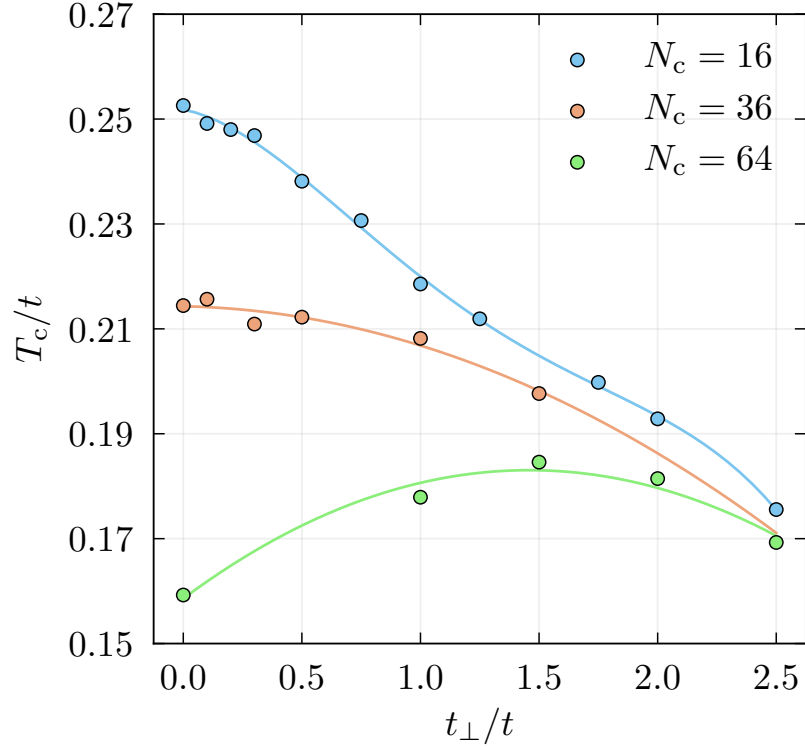
Figure 5.5: Superconducting critical temperature T_c/t as function of interlayer tunneling $t_\perp/t$ for $N_c = 16$, 36, and 64. For $N_c = 16$ and 36, T_c is monotonically decreasing function of $t_\perp$, but with strong indications of a cluster size dependence for small $t_\perp$. However, when $N_c = 64$, T_c is nonmonotonic as a function of $t_\perp$. This discrepancy suggests that large cluster sizes are required to capture the effects of phase fluctuations on T_c. The solid lines are intended to guide the eye. Figure taken from our Ref. [4].

5.3.1 Effective pairing interaction

We can view our results through the behavior of two renormalized quantities as a function of tunneling. Equipped with the leading eigenvalue λ_s and eigenvector ϕ_s from the BSE [Eqn. (5.2)], we use a separable approximation to decompose the leading eigenvalue as $\lambda_s \simeq V_s P_{0s}$, where the pairing interaction V_s and the "pair mobility" P_{0s} are given by [283]

$$V_s = -\frac{\sum_{k,k'} \phi_s(k)\Gamma_{pp}(k,k')\phi_s(k')}{\left[\sum_k \phi_s^2(k)\right]^2} \tag{5.3}$$

and

$$P_{s0} = \frac{T}{N_c} \sum_{k'} \phi_s(k')G(k')G(-k')\phi_s(k'), \tag{5.4}$$

respectively.

We find that this separable form, $V_s P_{s0}$, provides a very good approximation for the exact eigenvalue λ_s obtained from Eqn. (5.2) and only slightly overestimates λ_s by $\sim$ 5-10%. These results hold even if we restrict the sum over layer indices implicit in Eqs. (5.3) and (5.4) to the correlated layer only. At the temperatures studied here, the metallic layer is nearly devoid of pairing correlations. However, based on the results of Ref. [96], proximity-induced pairing in the metallic layer can occur at lower temperatures ($T/t \sim 0.1$). Others have explored the zero temperature picture for the case of a correlated t-J layer coupled to a metal, finding instances where the proximity induced superconducting gap in the metallic layer can exceed that in the correlated layer [284].

In Fig 5.6, we plot the effective pairing interaction $\tilde{V}_s(t_\perp) \equiv V_s(t_\perp)/V_s(0)$ and the pair mobility $\tilde{P}_{s0}(t_\perp) = P_{s0}(t_\perp)/P_{s0}(0)$ relative to their values at $t_\perp/t = 0$. As interlayer tunneling increases, $\tilde{V}_s(t_\perp)$ and $\tilde{P}_{s0}(t_\perp)$ exhibit the opposite monotonic behavior for $0 \leq t_\perp/t \leq 1.5$. While the increase in $\tilde{P}_{s0}(t_\perp)$ is good for T_c, it competes with a corresponding decrease in $\tilde{V}_s(t_\perp)$ for each value of $t_\perp/t$. Consequently, this weakening of the effective pairing interaction lowers the effective pairing scale Δ, and thus also the mean-field temperature scale $T_c^{\mathrm{MF}} \sim \Delta$.

A shortcoming of our analysis is that it considers a narrow range of model parameters. Previous work shows that the qualitative trends are insensitive to small variations in model parameters. For instance, Ref. [96] examined other filling factors ($n_1 = 0.6, 0.8, 1.0$) and attractive interaction strengths ($U = -4t, -6t, -10t$) and found that smaller values of n_1
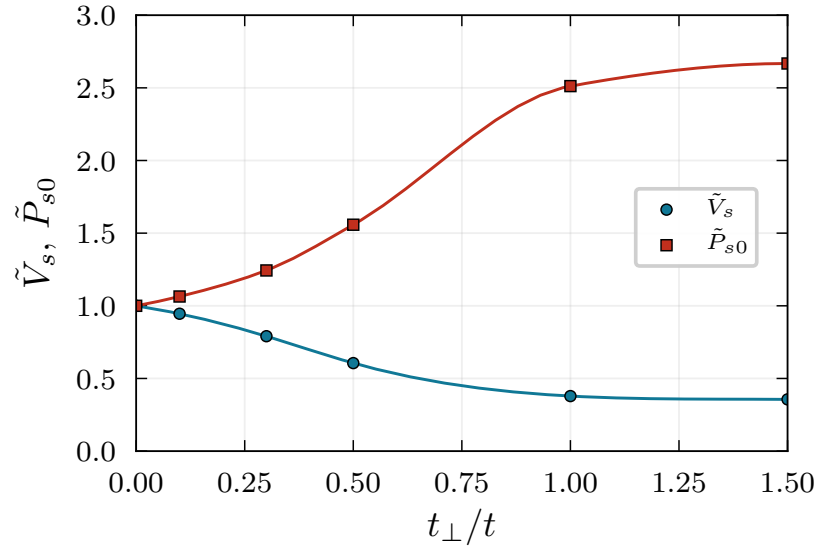
Figure 5.6: Effective interaction $\tilde{V}_s(t_\perp) = V_s(t_\perp)/V_s(0)$ and pair-mobility $\tilde{P}_{s0}(t_\perp) = P_{s0}(t_\perp)/P_{s0}(0)$ normalized by their values at $t_\perp/t = 0$. Results obtained on a cluster size of $N_c = 36$ at $T = 0.22t$. The solid lines are included to guide the eye. Figure taken from our Ref. [4].

are only marginally better for inducing pairing correlations in the metallic layer and that less negative values of U decrease pairing significantly in both layers. Thus, we expect our results to be representative of the regime where the size of the interaction and the bandwidth are comparable and pairing is more significant. Similar to earlier works showing that T_c increases in a composite superconductor-metal system, [94, 95] we also find an enhancement in T_c with increasing $t_\perp$. However, the enhancement is modest for the largest cluster size studied. Although a direct comparison with Ref. [96] is not possible, their calculations (for similar parameters) show that the pair structure factor decreases monotonically with increasing $t_\perp$ in the correlated layer and peaks in the metallic layer. However, the magnitude of the induced correlations in the metallic layer are small compared with the correlated layer and not representative of a transition. This suggests a need to compare our results directly to those from a method like determinant quantum Monte Carlo. There, we could better gauge the role of the mean-field in the DCA method in situations where phase fluctuations are strong.

The evolution of the superconducting transition from KT-like to BCS-like is reminiscent of the BCS-BEC crossover [285, 286] discussed in the context of the 2D attractive Hubbard model [277, 279]. In the latter scenario, one goes from BEC to BCS superconductivity by systematically lowering $|U|$ from the intermediate-strong coupling regime to the weak coupling regime. Importantly, $T_c(|U|)$ is found to have a maximum for $|U| \sim W$, where W is the bandwidth. In the bilayer model, although $|U|$ is kept constant, we find that the pairing interaction is effectively reduced through an increase in the interlayer tunneling amplitude $t_\perp$. Interestingly, like the purely 2D case, we find that T_c in the composite system has a maximum value with decreasing pairing interaction. We intend to expand the analysis of Fig 5.6 to larger values of $t_\perp$ in order to see if $\tilde{V}_s(t_\perp)$ and $\tilde{P}_{s0}(t_\perp)$ plateau, or reverse directions.

5.4 Conclusion

In this chapter, we used DCA calculations of a composite bilayer system to study the relationship between the superconducting transition temperature and the interlayer single-particle tunneling between an negative-U Hubbard layer and a non-interacting metallic layer. Specifically, we expanded on previous works [94, 95, 96] in the regime where the magnitude of the attractive interaction is comparable to the bandwidth ($W \sim |U|$). We showed that T_c has a nonmonotonic dependence on interlayer tunneling when the DCA cluster size becomes sufficiently large $N_c \geq 64$. For smaller clusters, phase fluctuations are suppressed by the mean-field and the T_c is overestimated, especially for small tunneling values. We showed that effective pairing interaction in the correlated layer decreases monotonically with increasing $t_\perp$, thereby lowering the pairing scale. However, we see a concomitant increase in the pair-mobility over the same range of tunneling values, which helps to increase T_c. The peak T_c may correspond to a crossover between tightly formed BEC pairs and longer range BCS pairs, much like in the attractive Hubbard model.

For small interlayer tunneling, the superconducting transition resembles a Kosterlitz-Thouless temperature dependence, as expected for a 2D negative-U Hubbard model. On finite-size clusters, the DCA will ultimately give a mean-field result close to the transition, but KT behavior is still noticeable across a range of higher temperatures. As the single-particle tunneling increases, we observed a shift toward a BCS-like logarithmic temperature dependence. Interestingly, this confirms that the superconducting transition in the composite system does inherit a more mean-field-like character through the interlayer hybridization. However, due to the concomitant reduction in pairing scale, T_c is reduced with respect to the isolated system.

Chapter 6

Conclusions

This dissertation presented four primary research questions. The first question (Chapter 2) was in the pursuit of finding out the temperature phase diagram of the Holstein model using many-body perturbation theory. It was known that the Holstein model hosted s-wave superconductivity and charge-density-wave correlations, but there was no consensus on where the phase boundaries fell as a function of filling or how they changed with phonon frequency or next-nearest neighbor hopping. Aided by a computationally efficient solution of the coupled many-body propagators under Migdal's approximation, we were able to study correlations on lattice sizes large enough to capture the thermodynamic limit. The phase diagrams revealed a high-temperature CDW phase at and around half-filling, giving way to a superconducting dome at finite doping. The superconducting T_c-dome was concomitant with an increase in the renormalized e-ph coupling and electronic density of states near the Fermi level, as well as a reduction in the renormalized phonon frequency. While these factors point to competition effects with the CDW as the primary reason for the reduction in T_c in the SCMA, there are factors beyond Migdal's approximation which also contribute, such as polaron and bipolaron formation. When polaronic effects are included (say, through DQMC simulations), one finds that increasing the e-ph coupling strength is not necessarily an effective route to high-temperature superconductivity in e-ph systems, especially near commensurate filling where bipolaron formation tends the system toward an insulating charge-ordered state [100].

The second question, considered in Chapter 3, asks if artificial neural networks are an effective means for accelerating DQMC simulations of the Holstein model. While DQMC effectively samples all possible Feynman diagrams, it is computationally expensive, limiting simulations to smaller lattices and higher temperatures. The neural networks learned an effective energy manifold used in Monte Carlo updates, bypassing the usual bottleneck in DQMC. We found that the networks could learn using the lattice configurations alone and that this was highly effective for studying the CDW phase at half-filling. The neural network model was trained on a small lattice and reused for several larger lattice sizes, an advantage made possible by the Hamiltonian's local nature. However, our network architecture was insufficient for capturing results at smaller fillings where superconductivity is present. Nevertheless, the NNMC approach lowers the computational complexity of simulations by a factor of the lattice size.

Applications of machine learning to many-body problems are in the early stages of development, and the field is moving fast [287, 288, 289]. In self-learning-type applications, it is still unclear if the neural networks can accurately extrapolate to lattices considerably larger than the training size. The effective energy learned by the networks is an extensive quantity that scales according to the system size. It would be interesting to formulate the NNMC to learn a size-independent manifold, like an energy density. Naively, one could add system size as an input parameter and train the models on different lattice sizes as well, but the training cost starts eating away at the runtime savings afforded by this approach. Even more ambitiously, one could formulate a new approach catered to machine learning utilization *ab initio*. Alternatively, our current NNMC approach is highly effective for the CDW phase of Holstein-like models. A large lattice NNMC simulation could be used to resolve the electronic spectral function as a function of temperature as the system undergoes a metal-to-insulator transition. One could attempt to resolve the e-ph induced kink in the electronic spectral function and study the apparent pseudogap at large coupling values [290].

The third question (Chapter 4) considered whether relatively small nonlinear e-ph coupling could become important in the parameter regime covered by Migdal's approximation. While this question may seem auxiliary to other concerns surrounding the e-ph problem, it is motivated by two recent and seemingly disparate efforts to map out the validity of

Migdal's approximation and gauge the importance of nonlinear e-ph coupling. Most efforts focused on the breakdown of Migdal's approximation take linear e-ph coupling for granted and push the model into scenarios that would otherwise face restraint from higher-order coupling effects present in actual materials. We found that a combination of increasing e-ph coupling and decreasing phonon frequency enhances sensitivity to small nonlinear coupling. More importantly, nonlinear corrections change the results significantly in the regime where Migdal's approximation is considered accurate (at least qualitatively). One of the glaring issues is the increasing sensitivity to nonlinear corrections as smaller and more realistic phonon frequencies are used in the model.

We have learned a great deal about the e-ph problem by studying the Holstein model, and there may be more to learn from it yet. However, our work highlights a need to reconsider some of our established ideas in the face of more realistic model systems. The Holstein model transitions from a Fermi liquid to a classical bipolaron gas at stronger couplings and becomes a commensurate CDW as the temperature decreases. Bipolaron formation and the CDW are favored when the interaction is strong and solely linear but suppressed in the face of nonlinearity and anharmonicity. A comprehensive intuition of how these factors alter the superconducting and charge order is underdeveloped in the literature. It will be a challenge to develop a systematic way of reintroducing interactions that are nonlinear and long-ranged.

The fourth and final question (Chapter 5) asks if coupling a metal to a phase fluctuating superconductor could raise T_c when the interaction $|U|$ is comparable with the electronic bandwidth W. This route to higher T_c has proven successful in similar models where the attractive interaction is small compared with the bandwidth and when hopping in the superconductor is neglected, but the general case is less explored. We used the DCA to access the superconducting phase transition via the Bethe-Salpeter equation and showed an enhancement in T_c for finite values of single-particle tunneling between the layers. The tunneling increases the pair mobility and thus also the overall phase stiffness, promoting superconductivity. However, the effective pairing interaction decreases with increasing interlayer tunneling, thereby lowering the pairing scale. The increasing mobility but decreasing interaction has similarities to the BCS-BEC crossover, moving from strong (BEC) to weak (BCS) interactions in the 2D attractive Hubbard model. When the

tunneling is small, and the interaction is comparable or larger than the bandwidth, then the superconductivity is well described by tightly bound pairs with a short coherence length. As the tunneling increases and the interaction weakens, the superconductivity becomes more BCS-like, as evidenced by the leading eigenvalue's temperature dependence. Our results suggest that growing a thin metallic film atop a phase fluctuating superconductor may be a viable way to boost T_c over a broader range of parameters than previously thought. However, the increase observed in our results appears to be modest at best and more work is needed to study the influence of other model parameters like in-plane hopping, electron density, and longer-range interactions.

In the ongoing quest for sustainable room-temperature superconductivity (under ambient pressure), there is still a sizable temperature chasm between the best candidates and 273 K. While high-pressure experiments are poised to teach us more about the phenomenology of conventional high-T_c, strategic heterostructure design is essential as well. For example, understanding how different dielectric environments screen the Coulomb interaction in correlated layered superconductors is vital for developing such strategies [291]. We need a more comprehensive set of design principles to optimize superconductivity developed through a combination of experiments, first principles, and model research.

We do not have a complete understanding of how or where unconventional superconductors save their energy in the transition or the various possible pairing mechanisms that could bind pairs of electrons. The BCS-BEC crossover in the attractive Hubbard model is a conventional example that suggests there is something special about kinetic and potential energy savings being nearly equal. It also suggests that there may be an optimal coherence length for which the superconducting phase is more robust against fluctuations and competing orders. Suppressing competing order, tuning the effective interaction, quelling large phase fluctuations, and many other adjustments may one day fill the table of contents of a compendium on how to get the highest possible T_c from any set of compatible materials.

Bibliography

[1] P. M. Dee, K. Nakatsukasa, Y. Wang, and S. Johnston. Temperature-filling phase diagram of the two-dimensional Holstein model in the thermodynamic limit by self-consistent Migdal approximation. *Phys. Rev. B*, 99:024514, Jan 2019. 1, 37, 44, 49, 52, 53, 55, 57, 58, 60, 63, 64, 66, 68, 70, 75, 86, 89, 94, 98

[2] Shaozhi Li, Philip M. Dee, Ehsan Khatami, and Steven Johnston. Accelerating lattice quantum Monte Carlo simulations using artificial neural networks: Application to the Holstein model. *Phys. Rev. B*, 100:020302, Jul 2019. 1, 84, 87, 91, 93, 96

[3] Philip M. Dee, Jennifer Coulter, Kevin G. Kleiner, and Steven Johnston. Relative importance of nonlinear electron-phonon coupling and vertex corrections in the Holstein model. *Communications Physics*, 3(1):145, Aug 2020. 1, 25, 26, 95, 101, 103, 104, 107, 109

[4] Philip M. Dee, Steven Johnston, and Thomas Maier. Pairing in a bilayer attractive Hubbard composite system: A dynamical cluster approximation study. Unpublished Manuscript, 2021. 1, 112, 118, 120, 122, 123, 125

[5] Maria N. Gastiasoro, Jonathan Ruhman, and Rafael M. Fernandes. Superconductivity in dilute SrTiO3: A review. *Annals of Physics*, 417:168107, 2020. Eliashberg theory at 60: Strong-coupling superconductivity and beyond. 1

[6] Elliot Snider, Nathan Dasenbrock-Gammon, Raymond McBride, Mathew Debessai, Hiranya Vindana, Kevin Vencatasamy, Keith V. Lawler, Ashkan Salamat, and Ranga P. Dias. Room-temperature superconductivity in a carbonaceous sulfur hydride. *Nature*, 586(7829):373–377, Oct 2020. 2

[7] N. W. Ashcroft. Metallic Hydrogen: A High-Temperature Superconductor? *Phys. Rev. Lett.*, 21:1748–1749, Dec 1968. 2

[8] J. Bardeen, L. N. Cooper, and J. R. Schrieffer. Theory of Superconductivity. *Phys. Rev.*, 108:1175–1204, Dec 1957. 2, 37

[9] P. W. Anderson and P. Morel. Generalized Bardeen-Cooper-Schrieffer States and Aligned Orbital Angular Momentum in the Proposed Low-Temperature Phase of Liquid He^3. *Phys. Rev. Lett.*, 5:136–138, Aug 1960. 2

[10] P. W. Anderson and P. Morel. Generalized Bardeen-Cooper-Schrieffer States and the Proposed Low-Temperature Phase of Liquid He^3. *Phys. Rev.*, 123:1911–1934, Sep 1961. 2

[11] R. Balian and N. R. Werthamer. Superconductivity with Pairs in a Relative p Wave. *Phys. Rev.*, 131:1553–1564, Aug 1963. 2

[12] Anthony J. Leggett. A theoretical description of the new phases of liquid ^{3}He. *Rev. Mod. Phys.*, 47:331–414, Apr 1975. 2

[13] L P Pitaevskii. ON SUPERFLUIDITY OF LIQUID Hesup3. *Zhur. Eksptl'. i Teoret. Fiz.*, Vol: 37, 12 1959. 2

[14] David J Thouless. Perturbation theory in statistical mechanics and the theory of superconductivity. *Annals of Physics*, 10(4):553–588, 1960. 2

[15] V. J. Emery and A. M. Sessler. Possible Phase Transition in Liquid He^3. *Phys. Rev.*, 119:43–49, Jul 1960. 2

[16] K. A. Brueckner, Toshio Soda, Philip W. Anderson, and Pierre Morel. Level Structure of Nuclear Matter and Liquid He^3. *Phys. Rev.*, 118:1442–1446, Jun 1960. 2

[17] A. J. Leggett. Interpretation of Recent Results on He^3 below 3 mK: A New Liquid Phase? *Phys. Rev. Lett.*, 29:1227–1230, Oct 1972. 3

[18] A. J. Leggett. Microscopic Theory of NMR in an Anisotropic Superfluid (^{3}HeA). *Phys. Rev. Lett.*, 31:352–355, Aug 1973. 3

[19] A J Leggett. NMR lineshifts and spontaneously broken spin-orbit symmetry. I. General concepts. *Journal of Physics C: Solid State Physics*, 6(21):3187–3204, Oct 1973. 3

[20] J. G. Bednorz and K. A. Müller. Possible high-T_c superconductivity in the Ba-La-Cu-O system. *Zeitschrift für Physik B Condensed Matter*, 64(2):189–193, Jun 1986. 3

[21] M. K. Wu, J. R. Ashburn, C. J. Torng, P. H. Hor, R. L. Meng, L. Gao, Z. J. Huang, Y. Q. Wang, and C. W. Chu. Superconductivity at 93 K in a new mixed-phase Y-Ba-Cu-O compound system at ambient pressure. *Phys. Rev. Lett.*, 58:908–910, Mar 1987. 3

[22] M. A. Subramanian, C. C. Torardi, J. C. Calabrese, J. Gopalakrishnan, K. J. Morrissey, T. R. Askew, R. B. Flippen, U. Chowdhry, and A. W. Sleight. A New High-Temperature Superconductor: Bi2Sr3-x Cax Cu2O8+y. *Science*, 239(4843):1015–1017, 1988. 3

[23] J. L. Tallon, R. G. Buckley, P. W. Gilberd, M. R. Presland, I. W. M. Brown, M. E. Bowden, L. A. Christian, and R. Goguel. High-Tc superconducting phases in the series $Bi_{2.1}(Ca, Sr)_{n+l}Cu_nO_{2n+4+\delta}$. *Nature*, 333(6169):153–156, May 1988. 3

[24] A. Schilling, M. Cantoni, J. D. Guo, and H. R. Ott. Superconductivity above 130 K in the Hg–Ba–Ca–Cu–O system. *Nature*, 363(6424):56–58, May 1993. 3

[25] L. Gao, Y. Y. Xue, F. Chen, Q. Xiong, R. L. Meng, D. Ramirez, C. W. Chu, J. H. Eggert, and H. K. Mao. Superconductivity up to 164 K in $HgBa_2Ca_{m-1} Cu_mO_{2m+2+\delta}$ (m=1, 2, and 3) under quasihydrostatic pressures. *Phys. Rev. B*, 50:4260–4263, Aug 1994. 3

[26] Yoichi Kamihara, Takumi Watanabe, Masahiro Hirano, and Hideo Hosono. Iron-Based Layered Superconductor $La[O_{1-x}F_x]FeAs$ (x = 0.05-0.12) with T_c = 26 K. *Journal of the American Chemical Society*, 130(11):3296–3297, 2008. PMID: 18293989. 3

[27] I. I. Mazin, D. J. Singh, M. D. Johannes, and M. H. Du. Unconventional Superconductivity with a Sign Reversal in the Order Parameter of $LaFeAsO_{1-x}F_x$. *Phys. Rev. Lett.*, 101:057003, Jul 2008. 3

[28] G. R. Stewart. Superconductivity in iron compounds. *Rev. Mod. Phys.*, 83:1589–1652, Dec 2011. 3

[29] Peter J. Hirschfeld. Using gap symmetry and structure to reveal the pairing mechanism in Fe-based superconductors. *Comptes Rendus Physique*, 17(1):197–231, 2016. Iron-based superconductors / Supraconducteurs à base de fer. 3

[30] Qimiao Si, Rong Yu, and Elihu Abrahams. High-temperature superconductivity in iron pnictides and chalcogenides. *Nature Reviews Materials*, 1(4):16017, Mar 2016. 3

[31] G. R. Stewart. Heavy-fermion systems. *Rev. Mod. Phys.*, 56:755–787, Oct 1984. 3

[32] Christian Pfleiderer. Superconducting phases of f-electron compounds. *Rev. Mod. Phys.*, 81:1551–1624, Nov 2009. 3

[33] Jérome, D., Mazaud, A., Ribault, M., and Bechgaard, K. Superconductivity in a synthetic organic conductor (TMTSF)2PF 6. *J. Physique Lett.*, 41(4):95–98, 1980. 3

[34] S. Lefebvre, P. Wzietek, S. Brown, C. Bourbonnais, D. Jérome, C. Mézière, M. Fourmigué, and P. Batail. Mott Transition, Antiferromagnetism, and Unconventional Superconductivity in Layered Organic Superconductors. *Phys. Rev. Lett.*, 85:5420–5423, Dec 2000. 3

[35] Danfeng Li, Kyuho Lee, Bai Yang Wang, Motoki Osada, Samuel Crossley, Hye Ryoung Lee, Yi Cui, Yasuyuki Hikita, and Harold Y. Hwang. Superconductivity in an infinite-layer nickelate. *Nature*, 572(7771):624–627, Aug 2019. 3

[36] Hirofumi Sakakibara, Hidetomo Usui, Katsuhiro Suzuki, Takao Kotani, Hideo Aoki, and Kazuhiko Kuroki. Model Construction and a Possibility of Cupratelike Pairing in a New d^9 Nickelate Superconductor $(Nd, Sr)NiO_2$. *Phys. Rev. Lett.*, 125:077003, Aug 2020. 3

[37] Yuan Cao, Valla Fatemi, Shiang Fang, Kenji Watanabe, Takashi Taniguchi, Efthimios Kaxiras, and Pablo Jarillo-Herrero. Unconventional superconductivity in magic-angle graphene superlattices. *Nature*, 556(7699):43–50, Apr 2018. 3

[38] Yuan Cao, Valla Fatemi, Ahmet Demir, Shiang Fang, Spencer L. Tomarken, Jason Y. Luo, Javier D. Sanchez-Yamagishi, Kenji Watanabe, Takashi Taniguchi, Efthimios

Kaxiras, Ray C. Ashoori, and Pablo Jarillo-Herrero. Correlated insulator behaviour at half-filling in magic-angle graphene superlattices. *Nature*, 556(7699):80–84, Apr 2018. 3

[39] G. R. Stewart. Unconventional superconductivity. *Advances in Physics*, 66(2):75–196, 2017. 3

[40] Defa Liu, Wenhao Zhang, Daixiang Mou, Junfeng He, Yun-Bo Ou, Qing-Yan Wang, Zhi Li, Lili Wang, Lin Zhao, Shaolong He, Yingying Peng, Xu Liu, Chaoyu Chen, Li Yu, Guodong Liu, Xiaoli Dong, Jun Zhang, Chuangtian Chen, Zuyan Xu, Jiangping Hu, Xi Chen, Xucun Ma, Qikun Xue, and X. J. Zhou. Electronic origin of high-temperature superconductivity in single-layer FeSe superconductor. *Nature Communications*, 3(1):931, Jul 2012. 4

[41] Shaolong He, Junfeng He, Wenhao Zhang, Lin Zhao, Defa Liu, Xu Liu, Daixiang Mou, Yun-Bo Ou, Qing-Yan Wang, Zhi Li, Lili Wang, Yingying Peng, Yan Liu, Chaoyu Chen, Li Yu, Guodong Liu, Xiaoli Dong, Jun Zhang, Chuangtian Chen, Zuyan Xu, Xi Chen, Xucun Ma, Qikun Xue, and X. J. Zhou. Phase diagram and electronic indication of high-temperature superconductivity at 65 K in single-layer FeSe films. *Nature Materials*, 12(7):605–610, Jul 2013. 4

[42] Qing-Yan Wang, Zhi Li, Wen-Hao Zhang, Zuo-Cheng Zhang, Jin-Song Zhang, Wei Li, Hao Ding, Yun-Bo Ou, Peng Deng, Kai Chang, Jing Wen, Can-Li Song, Ke He, Jin-Feng Jia, Shuai-Hua Ji, Ya-Yu Wang, Li-Li Wang, Xi Chen, Xu-Cun Ma, and Qi-Kun Xue. Interface-Induced High-Temperature Superconductivity in Single Unit-Cell FeSe Films on SrTiO3. *Chinese Physics Letters*, 29(3):037402, mar 2012. 4

[43] Fong-Chi Hsu, Jiu-Yong Luo, Kuo-Wei Yeh, Ta-Kun Chen, Tzu-Wen Huang, Phillip M. Wu, Yong-Chi Lee, Yi-Lin Huang, Yan-Yi Chu, Der-Chung Yan, and Maw-Kuen Wu. Superconductivity in the PbO-type structure α-FeSe. *Proceedings of the National Academy of Sciences*, 105(38):14262–14264, 2008. 4

[44] J. J. Lee, F. T. Schmitt, R. G. Moore, S. Johnston, Y.-T. Cui, W. Li, M. Yi, Z. K. Liu, M. Hashimoto, Y. Zhang, D. H. Lu, T. P. Devereaux, D.-H. Lee, and Z.-X. Shen.

Interfacial mode coupling as the origin of the enhancement of Tc in FeSe films on SrTiO3. *Nature*, 515:245, Nov 2014. 4, 39

[45] Zi-Xiang Li, T. P. Devereaux, and Dung-Hai Lee. Electronic and phononic properties of a two-dimensional electron gas coupled to dipolar phonons via small-momentum-transfer scattering. *Phys. Rev. B*, 100:241101, Dec 2019. 4

[46] Fabian Schrodi, Alex Aperis, and Peter M. Oppeneer. Multichannel superconductivity of monolayer FeSe on $SrTiO_3$: Interplay of spin fluctuations and electron-phonon interaction. *Phys. Rev. B*, 102:180501, Nov 2020. 4

[47] Louk Rademaker, Gustavo Alvarez-Suchini, Ken Nakatsukasa, Yan Wang, and Steven Johnston. Enhanced superconductivity in FeSe/$SrTiO_3$ from the combination of forward scattering phonons and spin fluctuations, 2021. 4

[48] Georgios Varelogiannis. Small-q electron–phonon interaction and the phase diagram of the cuprates. *Physica C: Superconductivity*, 460-462:1125–1126, 2007. Proceedings of the 8th International Conference on Materials and Mechanisms of Superconductivity and High Temperature Superconductors. 4

[49] S. Y. Savrasov and O. K. Andersen. Linear-Response Calculation of the Electron-Phonon Coupling in Doped $CaCuO_2$. *Phys. Rev. Lett.*, 77:4430–4433, Nov 1996. 4

[50] O. K. Andersen, S. Y. Savrasov, O. Jepsen, and A. I. Liechtenstein. Out-of-plane instability and electron-phonon contribution to *s*- and *d*-wave pairing in high-temperature superconductors; LDA linear-response calculation for doped $CaCuO_2$ and a generic tight-binding model. *Journal of Low Temperature Physics*, 105(3):285–304, Nov 1996. 4

[51] T. Sakai, D. Poilblanc, and D. J. Scalapino. Hole pairing and phonon dynamics in generalized two-dimensional $t - J$ Holstein models. *Phys. Rev. B*, 55:8445–8451, Apr 1997. 4

[52] O. Jepsen, O.K. Andersen, I. Dasgupta, and S. Savrasov. BUCKLING AND d-WAVE PAIRING IN HiTc SUPERCONDUCTORS. *Journal of Physics and Chemistry of Solids*, 59(10):1718–1722, 1998. 4

[53] Sumio Ishihara and Naoto Nagaosa. Interplay of electron-phonon interaction and electron correlation in high-temperature superconductivity. *Phys. Rev. B*, 69:144520, Apr 2004. 4

[54] S. Johnston, F. Vernay, B. Moritz, Z.-X. Shen, N. Nagaosa, J. Zaanen, and T. P. Devereaux. Systematic study of electron-phonon coupling to oxygen modes across the cuprates. *Phys. Rev. B*, 82:064513, Aug 2010. 4, 42

[55] D. Fausti, R. I. Tobey, N. Dean, S. Kaiser, A. Dienst, M. C. Hoffmann, S. Pyon, T. Takayama, H. Takagi, and A. Cavalleri. Light-Induced Superconductivity in a Stripe-Ordered Cuprate. *Science*, 331(6014):189–191, 2011. 4

[56] S. Kaiser, C. R. Hunt, D. Nicoletti, W. Hu, I. Gierz, H. Y. Liu, M. Le Tacon, T. Loew, D. Haug, B. Keimer, and A. Cavalleri. Optically induced coherent transport far above T_c in underdoped $YBa_2Cu_3O_{6+\delta}$. *Phys. Rev. B*, 89:184516, May 2014. 4

[57] W. Hu, S. Kaiser, D. Nicoletti, C. R. Hunt, I. Gierz, M. C. Hoffmann, M. Le Tacon, T. Loew, B. Keimer, and A. Cavalleri. Optically enhanced coherent transport in YBa2Cu3O6.5 by ultrafast redistribution of interlayer coupling. *Nature Materials*, 13(7):705–711, Jul 2014. 4

[58] Dante M. Kennes, Eli Y. Wilner, David R. Reichman, and Andrew J. Millis. Transient superconductivity from electronic squeezing of optically pumped phonons. *Nature Physics*, 13(5):479–483, May 2017. 4

[59] M. A. Sentef. Light-enhanced electron-phonon coupling from nonlinear electron-phonon coupling. *Phys. Rev. B*, 95:205111, May 2017. 4

[60] M. Raichle, D. Reznik, D. Lamago, R. Heid, Y. Li, M. Bakr, C. Ulrich, V. Hinkov, K. Hradil, C. T. Lin, and B. Keimer. Highly Anisotropic Anomaly in the Dispersion

of the Copper-Oxygen Bond-Bending Phonon in Superconducting $YBa_2Cu_3O_7$ from Inelastic Neutron Scattering. *Phys. Rev. Lett.*, 107:177004, Oct 2011. 4

[61] Lucio Braicovich, Matteo Rossi, Roberto Fumagalli, Yingying Peng, Yan Wang, Riccardo Arpaia, Davide Betto, Gabriella M. De Luca, Daniele Di Castro, Kurt Kummer, Marco Moretti Sala, Mattia Pagetti, Giuseppe Balestrino, Nicholas B. Brookes, Marco Salluzzo, Steven Johnston, Jeroen van den Brink, and Giacomo Ghiringhelli. Determining the electron-phonon coupling in superconducting cuprates by resonant inelastic x-ray scattering: Methods and results on $Nd_{1+x}Ba_{2-x}Cu_3O_{7-\delta}$. *Phys. Rev. Research*, 2:023231, May 2020. 4

[62] O Gunnarsson and O Rösch. Interplay between electron–phonon and Coulomb interactions in cuprates. *Journal of Physics: Condensed Matter*, 20(4):043201, Jan 2008. 4

[63] B. Keimer, S. A. Kivelson, M. R. Norman, S. Uchida, and J. Zaanen. From quantum matter to high-temperature superconductivity in copper oxides. *Nature*, 518(7538):179–186, Feb 2015. 5

[64] J. Hubbard. Electron Correlations in Narrow Energy Bands. *Proc. R. Soc. Lond. A*, 276(1365):238–257, 1963. 5, 7

[65] Martin C. Gutzwiller. Effect of Correlation on the Ferromagnetism of Transition Metals. *Phys. Rev. Lett.*, 10:159–162, Mar 1963. Gutzwiller wrote down the Hubbard model in Eqn. (11) of this work, independently of others. 5, 7

[66] Junjiro Kanamori. Electron Correlation and Ferromagnetism of Transition Metals. *Progress of Theoretical Physics*, 30(3):275–289, 09 1963. See Eqn. (1) for the first appearance of the famous Hubbard U. Again, this was done independently of others at the same time. 5, 7

[67] Can-Li Song, Yi-Lin Wang, Ye-Ping Jiang, Zhi Li, Lili Wang, Ke He, Xi Chen, Xu-Cun Ma, and Qi-Kun Xue. Molecular-beam epitaxy and robust superconductivity of

stoichiometric FeSe crystalline films on bilayer graphene. *Phys. Rev. B*, 84:020503, Jul 2011. 5

[68] Shiyong Tan, Yan Zhang, Miao Xia, Zirong Ye, Fei Chen, Xin Xie, Rui Peng, Difei Xu, Qin Fan, Haichao Xu, Juan Jiang, Tong Zhang, Xinchun Lai, Tao Xiang, Jiangping Hu, Binping Xie, and Donglai Feng. Interface-induced superconductivity and strain-dependent spin density waves in FeSe/SrTiO3 thin films. *Nature Materials*, 12(7):634–640, Jul 2013. 5

[69] Zhongpei Feng, Jie Yuan, Ge He, Wei Hu, Zefeng Lin, Dong Li, Xingyu Jiang, Yulong Huang, Shunli Ni, Jun Li, Beiyi Zhu, Xiaoli Dong, Fang Zhou, Huabing Wang, Zhongxian Zhao, and Kui Jin. Tunable critical temperature for superconductivity in FeSe thin films by pulsed laser deposition. *Scientific Reports*, 8(1):4039, Mar 2018. 5

[70] Rainer Wesche. *High-Temperature Superconductors*, pages 1–1. Springer International Publishing, Cham, 2017. 6

[71] S.A. Kivelson. Making high Tc higher: a theoretical proposal. *Physica B: Condensed Matter*, 318(1):61 – 67, 2002. The Future of Materials Physics: A Festschrift for Zachary Fisk. 6, 21, 112, 113

[72] V. J. Emery and S. A. Kivelson. Importance of phase fluctuations in superconductors with small superfluid density. *Nature*, 374(6521):434–437, Mar 1995. 6, 113

[73] Thomas A. Maier and Douglas J. Scalapino. Pairfield fluctuations of a 2D Hubbard model. *npj Quantum Materials*, 4(1):30, Jun 2019. 6, 113, 119

[74] J. P. F. LeBlanc, Andrey E. Antipov, Federico Becca, Ireneusz W. Bulik, Garnet Kin-Lic Chan, Chia-Min Chung, Youjin Deng, Michel Ferrero, Thomas M. Henderson, Carlos A. Jiménez-Hoyos, E. Kozik, Xuan-Wen Liu, Andrew J. Millis, N. V. Prokof'ev, Mingpu Qin, Gustavo E. Scuseria, Hao Shi, B. V. Svistunov, Luca F. Tocchio, I. S. Tupitsyn, Steven R. White, Shiwei Zhang, Bo-Xiao Zheng, Zhenyue Zhu, and Emanuel Gull. Solutions of the Two-Dimensional Hubbard Model: Benchmarks and Results from a Wide Range of Numerical Algorithms. *Phys. Rev. X*, 5:041041, Dec 2015. 7

[75] Bo-Xiao Zheng, Chia-Min Chung, Philippe Corboz, Georg Ehlers, Ming-Pu Qin, Reinhard M. Noack, Hao Shi, Steven R. White, Shiwei Zhang, and Garnet Kin-Lic Chan. Stripe order in the underdoped region of the two-dimensional Hubbard model. *Science*, 358(6367):1155–1160, 2017. 7

[76] Mingpu Qin, Chia-Min Chung, Hao Shi, Ettore Vitali, Claudius Hubig, Ulrich Schollwöck, Steven R. White, and Shiwei Zhang. Absence of Superconductivity in the Pure Two-Dimensional Hubbard Model. *Phys. Rev. X*, 10:031016, Jul 2020. 7

[77] Thomas Schäfer, Nils Wentzell, Fedor Šimkovic, Yuan-Yao He, Cornelia Hille, Marcel Klett, Christian J. Eckhardt, Behnam Arzhang, Viktor Harkov, François-Marie Le Régent, Alfred Kirsch, Yan Wang, Aaram J. Kim, Evgeny Kozik, Evgeny A. Stepanov, Anna Kauch, Sabine Andergassen, Philipp Hansmann, Daniel Rohe, Yuri M. Vilk, James P. F. LeBlanc, Shiwei Zhang, A.-M. S. Tremblay, Michel Ferrero, Olivier Parcollet, and Antoine Georges. Tracking the Footprints of Spin Fluctuations: A MultiMethod, MultiMessenger Study of the Two-Dimensional Hubbard Model. *Phys. Rev. X*, 11:011058, Mar 2021. 7

[78] Eduardo Fradkin, Steven A. Kivelson, and John M. Tranquada. Colloquium: Theory of intertwined orders in high temperature superconductors. *Rev. Mod. Phys.*, 87:457–482, May 2015. 7

[79] T Holstein. Studies of polaron motion: Part I. The molecular-crystal model. *Ann. Phys.*, 8(3):325–342, 1959. 7, 38, 86, 96

[80] T. Holstein. Studies of polaron motion: Part II. The "small" polaron. *Ann. Phys.*, 8(3):343–389, 1959. 7

[81] Gerald D. Mahan. *Many-Particle Physics.* Plenum Press, New York, NY, 2 edition, 1990. 7, 11, 13, 38

[82] H. Fröhlich. Theory of the Superconducting State. I. The Ground State at the Absolute Zero of Temperature. *Phys. Rev.*, 79:845–856, Sep 1950. 10

[83] Herbert Fröhlich. Interaction of electrons with lattice vibrations. *Proceedings of the Royal Society of London. Series A. Mathematical and Physical Sciences*, 215(1122):291–298, 1952. 10

[84] Feliciano Giustino. Electron-phonon interactions from first principles. *Rev. Mod. Phys.*, 89:015003, Feb 2017. 10, 11, 13, 38, 39, 95

[85] Piers Coleman. *Introduction to Many-Body Physics*. Cambridge University Press, 2015. 11, 22

[86] Otfried Madelung. *Electron-Phonon Interaction: Transport Phenomena*, pages 175–227. Springer Berlin Heidelberg, Berlin, Heidelberg, 1978. 11

[87] H. Bruus, K. Flensberg, and Oxford University Press. *Many-Body Quantum Theory in Condensed Matter Physics: An Introduction*. Oxford Graduate Texts. OUP Oxford, 2004. 11, 13, 15

[88] Philip Phillips. *Advanced Solid State Physics*. Cambridge University Press, 2 edition, 2012. 11

[89] Radi A. Jishi. *Feynman Diagram Techniques in Condensed Matter Physics*. Cambridge University Press, 2013. 11, 15

[90] Louk Rademaker, Yan Wang, Tom Berlijn, and Steve Johnston. Enhanced superconductivity due to forward scattering in FeSe thin films on SrTiO3substrates. *New Journal of Physics*, 18(2):022001, feb 2016. 18

[91] Charles P. Poole, John F. Zasadzinski, Roberta K. Zasadzinski, and Philip B. Allen. Chapter 9 - Characteristic parameters. In Charles P. Poole, editor, *Handbook of Superconductivity*, pages 433–489. Academic Press, San Diego, 2000. 19

[92] A. B. Migdal. Interaction between electrons and lattice vibrations in a normal metal. *Sov. Phys. JETP*, 7(6):996–1001, 1958. [Zh. Eksp. Teor. Fiz. **34**, 1438 (1958)]. 20, 22, 38, 39, 95, 96

[93] J. K. Freericks. Strong-coupling expansions for the attractive Holstein and Hubbard models. *Phys. Rev. B*, 48:3881–3891, Aug 1993. 21

[94] Erez Berg, Dror Orgad, and Steven A. Kivelson. Route to high-temperature superconductivity in composite systems. *Phys. Rev. B*, 78:094509, Sep 2008. 21, 113, 126, 127

[95] Gideon Wachtel, Assaf Bar-Yaacov, and Dror Orgad. Superfluid stiffness renormalization and critical temperature enhancement in a composite superconductor. *Phys. Rev. B*, 86:134531, Oct 2012. 21, 113, 126, 127

[96] Aleksander Zujev, Richard T Scalettar, George G Batrouni, and Pinaki Sengupta. Pairing correlations in the two-layer attractive Hubbard model. *New Journal of Physics*, 16(1):013004, jan 2014. 21, 113, 114, 119, 121, 124, 126, 127

[97] A.A. Abrikosov, L.P. Gor'kov, and I.E. Dzyaloshinski. *Methods of Quantum Field Theory in Statistical Physics*. Prentice-Hall, Englewood Cliffs, NJ, 1963. 22, 38, 79, 80

[98] I. Esterlis, B. Nosarzewski, E. W. Huang, B. Moritz, T. P. Devereaux, D. J. Scalapino, and S. A. Kivelson. Breakdown of the Migdal-Eliashberg theory: A determinant quantum Monte Carlo study. *Phys. Rev. B*, 97:140501(R), Apr 2018. 25, 38, 39, 96, 100, 105

[99] Andrey V. Chubukov, Artem Abanov, Ilya Esterlis, and Steven A. Kivelson. Eliashberg theory of phonon-mediated superconductivity — When it is valid and how it breaks down. *Annals of Physics*, 417:168190, 2020. Eliashberg theory at 60: Strong-coupling superconductivity and beyond. 25

[100] B. Nosarzewski, E. W. Huang, Philip M. Dee, I. Esterlis, B. Moritz, S. A. Kivelson, S. Johnston, and T. P. Devereaux. Superconductivity, Charge-Density-Waves, and Bipolarons in the Holstein model, 2021. 25, 128

[101] R. Blankenbecler, D. J. Scalapino, and R. L. Sugar. Monte Carlo calculations of coupled boson-fermion systems. I. *Phys. Rev. D*, 24:2278–2286, Oct 1981. 26, 27

[102] S. R. White, D. J. Scalapino, R. L. Sugar, E. Y. Loh, J. E. Gubernatis, and R. T. Scalettar. Numerical study of the two-dimensional Hubbard model. *Phys. Rev. B*, 40:506–516, Jul 1989. 26, 28, 88, 98, 173, 178, 191, 192

[103] Zhaojun Bai, Cherung Lee, Ren-Cang Li, and Shufang Xu. Stable solutions of linear systems involving long chain of matrix multiplications. *Linear Algebra and its Applications*, 435(3):659–673, 2011. Special Issue: Dedication to Pete Stewart on the occasion of his 70th birthday. 26

[104] F.F. Assaad and H.G. Evertz. *World-line and Determinantal Quantum Monte Carlo Methods for Spins, Phonons and Electrons*, pages 277–356. Springer Berlin Heidelberg, Berlin, Heidelberg, 2008. 26, 173, 201

[105] S. Johnston, E. A. Nowadnick, Y. F. Kung, B. Moritz, R. T. Scalettar, and T. P. Devereaux. Determinant quantum Monte Carlo study of the two-dimensional single-band Hubbard-Holstein model. *Phys. Rev. B*, 87:235133, Jun 2013. 26, 38, 86, 88, 90, 106

[106] F. Fucito, E. Marinari, G. Parisi, and C. Rebbi. A Proposal for Monte Carlo Simulations of Fermionic Systems. *Nucl. Phys. B*, 180:369, 1981. 27

[107] Thomas Maier, Mark Jarrell, Thomas Pruschke, and Matthias H. Hettler. Quantum cluster theories. *Rev. Mod. Phys.*, 77:1027–1080, Oct 2005. 30, 116

[108] M. H. Hettler, M. Mukherjee, M. Jarrell, and H. R. Krishnamurthy. Dynamical cluster approximation: Nonlocal dynamics of correlated electron systems. *Phys. Rev. B*, 61:12739–12756, May 2000. 30

[109] M. Jarrell, Th. Maier, C. Huscroft, and S. Moukouri. Quantum Monte Carlo algorithm for nonlocal corrections to the dynamical mean-field approximation. *Phys. Rev. B*, 64:195130, Oct 2001. 30

[110] E. Gull, P. Werner, O. Parcollet, and M. Troyer. Continuous-time auxiliary-field Monte Carlo for quantum impurity models. *EPL (Europhysics Letters)*, 82(5):57003, may 2008. 30, 116

[111] Emanuel Gull, Peter Staar, Sebastian Fuchs, Phani Nukala, Michael S. Summers, Thomas Pruschke, Thomas C. Schulthess, and Thomas Maier. Submatrix updates for the continuous-time auxiliary-field algorithm. *Phys. Rev. B*, 83:075122, Feb 2011. 30, 116

[112] Emanuel Gull, Andrew J. Millis, Alexander I. Lichtenstein, Alexey N. Rubtsov, Matthias Troyer, and Philipp Werner. Continuous-time Monte Carlo methods for quantum impurity models. *Rev. Mod. Phys.*, 83:349–404, May 2011. 30, 116

[113] Urs R. Hähner, Gonzalo Alvarez, Thomas A. Maier, Raffaele Solcà, Peter Staar, Michael S. Summers, and Thomas C. Schulthess. DCA++: A software framework to solve correlated electron problems with modern quantum cluster methods. *Computer Physics Communications*, 246:106709, 2020. 30, 116

[114] Autumn School on Correlated Electrons, Jülich (Germany), 21 Sep 2015 - 25 Sep 2015. *Many-Body Physics: From Kondo to Hubbard*, volume 5 of *Modeling and Simulation*, Jülich, Sep 2015. Forschungszentrum Jülich GmbH Zentralbibliothek, Verlag. 30, 31

[115] J. T. Devreese. Polarons. *Encyclopedia of Applied Physics*, 14:383, 1996. 37

[116] G. Grüner. The dynamics of charge-density waves. *Rev. Mod. Phys.*, 60:1129–1181, Oct 1988. 37

[117] D. J. Scalapino, J. R. Schrieffer, and J. W. Wilkins. Strong-Coupling Superconductivity. I. *Phys. Rev.*, 148:263–279, Aug 1966. 37, 38

[118] John Bardeen. Electron-Phonon Interactions and Superconductivity. *Science*, 181(4106):1209–1214, 1973. 37

[119] F. Marsiglio and J. P. Carbotte. *Electron-Phonon Superconductivity*, pages 73–162. Springer Berlin Heidelberg, Berlin, Heidelberg, 2008. 38

[120] J.J. Hamlin. Superconductivity in the metallic elements at high pressures. *Physica C*, 514:59–76, 2015. 38

[121] Cristina Buzea and Tsutomu Yamashita. Review of the superconducting properties of MgB 2. *Superconductor Science and Technology*, 14(11):R115, 2001. 38

[122] Jun Nagamatsu, Norimasa Nakagawa, Takahiro Muranaka, Yuji Zenitani, and Jun Akimitsu. Superconductivity at 39 K in magnesium diboride. *Nature*, 410(6824):63–64, 2001. 38

[123] A. P. Drozdov, M. I. Eremets, I. A. Troyan, V. Ksenofontov, and S. I. Shylin. Conventional superconductivity at 203 Kelvin at high pressures in the sulfur hydride system. *Nature*, 525:73–, aug 2015. 38

[124] Igor I. Mazin. Extraordinarily conventional. *Nature*, 525:40–, Aug 2015. 38

[125] A. P. Drozdov, V. S. Minkov, S. P. Besedin, P. P. Kong, M. A. Kuzovnikov, D. A. Knyazev, and M. I. Eremets. Superconductivity at 215 K in lanthanum hydride at high pressures. *ArXiv e-prints*, aug 2018. 38

[126] I. A. Kruglov, D. V. Semenok, R. Szczęśniak, M. Mahdi Davari Esfahani, A. G. Kvashnin, and A. R. Oganov. Superconductivity in *LaH_*10: a new twist of the story. *ArXiv e-prints*, Oct 2018. 38

[127] Mirko M. Möller, George A. Sawatzky, Marcel Franz, and Mona Berciu. Type-II Dirac semimetal stabilized by electron-phonon coupling. *Nat. Commun.*, 8(1):2267–, 2017. 38

[128] Stefano Baroni, Stefano de Gironcoli, Andrea Dal Corso, and Paolo Giannozzi. Phonons and related crystal properties from density-functional perturbation theory. *Rev. Mod. Phys.*, 73:515–562, Jul 2001. 38

[129] Hyoung Joon Choi, David Roundy, Hong Sun, Marvin L. Cohen, and Steven G. Louie. First-principles calculation of the superconducting transition in MgB_2 within the anisotropic Eliashberg formalism. *Phys. Rev. B*, 66:020513, Jul 2002. 38, 39

[130] M. Lüders, M. A. L. Marques, N. N. Lathiotakis, A. Floris, G. Profeta, L. Fast, A. Continenza, S. Massidda, and E. K. U. Gross. *Ab initio* theory of superconductivity.

I. Density functional formalism and approximate functionals. *Phys. Rev. B*, 72:024545, Jul 2005. 38

[131] M. A. L. Marques, M. Lüders, N. N. Lathiotakis, G. Profeta, A. Floris, L. Fast, A. Continenza, E. K. U. Gross, and S. Massidda. *Ab initio* theory of superconductivity. II. Application to elemental metals. *Phys. Rev. B*, 72:024546, Jul 2005. 38

[132] A. Floris, G. Profeta, N. N. Lathiotakis, M. Lüders, M. A. L. Marques, C. Franchini, E. K. U. Gross, A. Continenza, and S. Massidda. Superconducting Properties of MgB$_2$ from First Principles. *Phys. Rev. Lett.*, 94:037004, Jan 2005. 38

[133] E. R. Margine and F. Giustino. Anisotropic Migdal-Eliashberg theory using Wannier functions. *Phys. Rev. B*, 87:024505, Jan 2013. 38, 39

[134] Han Rongsheng, Lin Zijing, and Wang Kelin. Exact solutions for the two-site Holstein model. *Phys. Rev. B*, 65:174303, Apr 2002. 38

[135] Mona Berciu. Exact Green's functions for the two-site Hubbard-Holstein Hamiltonian. *Phys. Rev. B*, 75:081101, Feb 2007. 38

[136] Yu-Yu Zhang, Tao Liu, Qing-Hu Chen, Xiaoguang Wang, and Ke-Lin Wang. Ground-state properties of the two-site Hubbard-Holstein model: an exact solution. *J. Phys.: Condens. Matter*, 21(41):415601, 2009. 38

[137] Przemyslaw Grzybowski and P Micnas. Superconductivity and Charge-Density Wave Phase in the Holstein Model: a Weak Coupling Limit. *Acta Phys. Pol. A*, 111(4):455–466, 2007. 38, 76

[138] G. M. Eliashberg. Interactions between electrons and lattice vibrations in a superconductor. *Sov. Phys. JETP*, 11:696–702, 1960. [Zh. Eksp. Teor. Fiz. **38**, 966 (1960)]. 38, 95

[139] S. Engelsberg and J. R. Schrieffer. Coupled Electron-Phonon System. *Phys. Rev.*, 131:993–1008, Aug 1963. 38, 39

[140] F. Marsiglio. Pairing and charge-density-wave correlations in the Holstein model at half-filling. *Phys. Rev. B*, 42:2416–2424, Aug 1990. 38, 39, 40, 43, 96, 98, 217

[141] E. Berger, P. Valášek, and W. von der Linden. Two-dimensional Hubbard-Holstein model. *Phys. Rev. B*, 52:4806–4814, Aug 1995. 38

[142] Mona Berciu. Green's Function of a Dressed Particle. *Phys. Rev. Lett.*, 97:036402, Jul 2006. 38

[143] Hadi Ebrahimnejad and Mona Berciu. Perturbational study of the lifetime of a Holstein polaron in the presence of weak disorder. *Phys. Rev. B*, 86:205109, Nov 2012. 38

[144] Jorge E. Hirsch and Eduardo Fradkin. Effect of Quantum Fluctuations on the Peierls Instability: A Monte Carlo Study. *Phys. Rev. Lett.*, 49:402–405, Aug 1982. 38

[145] R. T. Scalettar, N. E. Bickers, and D. J. Scalapino. Competition of pairing and Peierls–charge-density-wave correlations in a two-dimensional electron-phonon model. *Phys. Rev. B*, 40:197–200, Jul 1989. 38, 54, 88, 96

[146] R. M. Noack, D. J. Scalapino, and R. T. Scalettar. Charge-density-wave and pairing susceptibilities in a two-dimensional electron-phonon model. *Phys. Rev. Lett.*, 66:778–781, Feb 1991. 38, 54, 96

[147] M. Vekić, R. M. Noack, and S. R. White. Charge-density waves versus superconductivity in the Holstein model with next-nearest-neighbor hopping. *Phys. Rev. B*, 46:271–278, Jul 1992. 38, 59, 96

[148] Parhat Niyaz, J. E. Gubernatis, R. T. Scalettar, and C. Y. Fong. Charge-density-wave-gap formation in the two-dimensional Holstein model at half-filling. *Phys. Rev. B*, 48:16011–16022, Dec 1993. 38, 96

[149] Martin Hohenadler, Hans Gerd Evertz, and Wolfgang von der Linden. Quantum Monte Carlo and variational approaches to the Holstein model. *Phys. Rev. B*, 69:024301, Jan 2004. 38

[150] Z. B. Huang, W. Hanke, E. Arrigoni, and D. J. Scalapino. Electron-phonon vertex in the two-dimensional one-band Hubbard model. *Phys. Rev. B*, 68:220507, Dec 2003. 38

[151] Shaozhi Li, E. A. Nowadnick, and S. Johnston. Quasiparticle properties of the nonlinear Holstein model at finite doping and temperature. *Phys. Rev. B*, 92:064301, Aug 2015. 38, 96, 98, 110

[152] N. C. Costa, T. Blommel, W.-T. Chiu, G. Batrouni, and R. T. Scalettar. Phonon Dispersion and the Competition between Pairing and Charge Order. *Phys. Rev. Lett.*, 120:187003, May 2018. 38, 47

[153] B. J. Alder, K. J. Runge, and R. T. Scalettar. Variational Monte Carlo Study of an Interacting Electron-Phonon Model. *Phys. Rev. Lett.*, 79:3022–3025, Oct 1997. 38

[154] Takahiro Ohgoe and Masatoshi Imada. Variational Monte Carlo method for electron-phonon coupled systems. *Phys. Rev. B*, 89:195139, May 2014. 38

[155] Takahiro Ohgoe and Masatoshi Imada. Competition among Superconducting, Antiferromagnetic, and Charge Orders with Intervention by Phase Separation in the 2D Holstein-Hubbard Model. *Phys. Rev. Lett.*, 119:197001, Nov 2017. 38, 39

[156] J. K. Freericks, M. Jarrell, and D. J. Scalapino. Holstein model in infinite dimensions. *Phys. Rev. B*, 48:6302–6314, Sep 1993. 38, 59

[157] S. Ciuchi, F. de Pasquale, S. Fratini, and D. Feinberg. Dynamical mean-field theory of the small polaron. *Phys. Rev. B*, 56:4494–4512, Aug 1997. 38

[158] J. K. Freericks, V. Zlatić, Woonki Chung, and Mark Jarrell. Vertex-corrected perturbation theory for the electron-phonon problem with nonconstant density of states. *Phys. Rev. B*, 58:11613–11623, Nov 1998. 38

[159] D. Meyer, A. C. Hewson, and R. Bulla. Gap Formation and Soft Phonon Mode in the Holstein Model. *Phys. Rev. Lett.*, 89:196401, Oct 2002. 38, 39

[160] M. Capone and S. Ciuchi. Polaron Crossover and Bipolaronic Metal-Insulator Transition in the Half-Filled Holstein Model. *Phys. Rev. Lett.*, 91:186405, Oct 2003. 38, 39

[161] J. P. Hague and N. d'Ambrumenil. Breakdown of Migdal–Eliashberg Theory via Catastrophic Vertex Divergence at Low Phonon Frequency. *J. Low Temp. Phys.*, 151(5):1149–1163, Jun 2008. 38, 39

[162] Johannes Bauer, Jong E. Han, and Olle Gunnarsson. Quantitative reliability study of the Migdal-Eliashberg theory for strong electron-phonon coupling in superconductors. *Phys. Rev. B*, 84:184531, Nov 2011. 38, 39, 96

[163] Yuta Murakami, Philipp Werner, Naoto Tsuji, and Hideo Aoki. Supersolid Phase Accompanied by a Quantum Critical Point in the Intermediate Coupling Regime of the Holstein Model. *Phys. Rev. Lett.*, 113:266404, Dec 2014. 38, 39, 76

[164] Masaki Tezuka, Ryotaro Arita, and Hideo Aoki. Phase diagram for the one-dimensional Hubbard-Holstein model: A density-matrix renormalization group study. *Phys. Rev. B*, 76:155114, Oct 2007. 39

[165] G. M. Eliashberg. Temperature Green's Function For Electrons In a Supercondutor. *Sov. Phys. JETP*, 12(5):1000–1002, may 1961. 39, 95

[166] Alex Aperis, Pablo Maldonado, and Peter M. Oppeneer. Ab initio theory of magnetic-field-induced odd-frequency two-band superconductivity in MgB_2. *Phys. Rev. B*, 92:054516, Aug 2015. 39

[167] S. Poncé, E.R. Margine, C. Verdi, and F. Giustino. EPW: Electron-phonon coupling, transport and superconducting properties using maximally localized Wannier functions. *Comput. Phys. Commun.*, 209:116–133, 2016. 39

[168] T. Cuk, F. Baumberger, D. H. Lu, N. Ingle, X. J. Zhou, H. Eisaki, N. Kaneko, Z. Hussain, T. P. Devereaux, N. Nagaosa, and Z.-X. Shen. Coupling of the B_{1g} Phonon to the Antinodal Electronic States of $Bi_2Sr_2Ca_{0.92}Y_{0.08}Cu_2O_{8+\delta}$. *Phys. Rev. Lett.*, 93:117003, Sep 2004. 39

[169] D. E. Shai, C. Adamo, D. W. Shen, C. M. Brooks, J. W. Harter, E. J. Monkman, B. Burganov, D. G. Schlom, and K. M. Shen. Quasiparticle Mass Enhancement and Temperature Dependence of the Electronic Structure of Ferromagnetic $SrRuO_3$ Thin Films. *Phys. Rev. Lett.*, 110:087004, Feb 2013. 39

[170] H. F. Yang, Z. T. Liu, C. C. Fan, Q. Yao, P. Xiang, K. L. Zhang, M. Y. Li, H. Li, J. S. Liu, D. W. Shen, and M. H. Jiang. Origin of the kink in the band dispersion of the ferromagnetic perovskite $SrRuO_3$: Electron-phonon coupling. *Phys. Rev. B*, 93:121102, Mar 2016. 39

[171] E. R. Margine, Henry Lambert, and Feliciano Giustino. Electron-phonon interaction and pairing mechanism in superconducting Ca-intercalated bilayer graphene. *Scientific Reports*, 6:21414, Feb 2016. 39

[172] Carla Verdi, Fabio Caruso, and Feliciano Giustino. Origin of the crossover from polarons to Fermi liquids in transition metal oxides. *Nature Communications*, 8:15769, Jun 2017. 39

[173] Adrian G. Swartz, Hisashi Inoue, Tyler A. Merz, Yasuyuki Hikita, Srinivas Raghu, Thomas P. Devereaux, Steven Johnston, and Harold Y. Hwang. Polaronic behavior in a weak-coupling superconductor. *Proceedings of the National Academy of Sciences*, 82:224304, 2018. 39

[174] C. Grimaldi, L. Pietronero, and S. Strässler. Nonadiabatic Superconductivity: Electron-Phonon Interaction Beyond Migdal's Theorem. *Phys. Rev. Lett.*, 75:1158–1161, Aug 1995. 39

[175] O. Gunnarsson. Superconductivity in fullerides. *Rev. Mod. Phys.*, 69:575–606, Apr 1997. 39

[176] Alaska Subedi and Lilia Boeri. Vibrational spectrum and electron-phonon coupling of doped solid picene from first principles. *Phys. Rev. B*, 84:020508, Jul 2011. 39

[177] Michele Casula, Matteo Calandra, Gianni Profeta, and Francesco Mauri. Intercalant and Intermolecular Phonon Assisted Superconductivity in K-Doped Picene. *Phys. Rev. Lett.*, 107:137006, Sep 2011. 39

[178] Lev P. Gor'kov. Phonon mechanism in the most dilute superconductor n-type SrTiO3. *Proceedings of the National Academy of Sciences*, 113(17):4646–4651, 2016. 39

[179] Peter Wölfle and Alexander V. Balatsky. Superconductivity at low density near a ferroelectric quantum critical point: Doped SrTiO$_3$. *Phys. Rev. B*, 98:104505, Sep 2018. 39

[180] Lev P. Gor'kov. Superconducting transition temperature: Interacting Fermi gas and phonon mechanisms in the nonadiabatic regime. *Phys. Rev. B*, 93:054517, Feb 2016. 39

[181] Patrizia Benedetti and Roland Zeyher. Holstein model in infinite dimensions at half-filling. *Phys. Rev. B*, 58:14320–14334, Dec 1998. 39

[182] A. S. Alexandrov. Breakdown of the Migdal-Eliashberg theory in the strong-coupling adiabatic regime. *EPL (Europhysics Letters)*, 56(1):92, 2001. 39, 96

[183] J. W. Serene and D. W. Hess. Quasiparticle properties of the two-dimensional Hubbard model in a propagator-renormalized fluctuation-exchange approximation. *Phys. Rev. B*, 44:3391–3394, Aug 1991. 40

[184] J. J. Deisz, D. W. Hess, and J. W. Serene. Phase diagram for the attractive Hubbard model in two dimensions in a conserving approximation. *Phys. Rev. B*, 66:014539, Jul 2002. 40

[185] Antoine Georges, Gabriel Kotliar, Werner Krauth, and Marcelo J. Rozenberg. Dynamical mean-field theory of strongly correlated fermion systems and the limit of infinite dimensions. *Rev. Mod. Phys.*, 68:13–125, Jan 1996. 40

[186] N. Bulut and D. J. Scalapino. $d_{x^2-y^2}$ symmetry and the pairing mechanism. *Phys. Rev. B*, 54:14971–14973, Dec 1996. 42

[187] A. W. Sandvik, D. J. Scalapino, and N. E. Bickers. Effect of an electron-phonon interaction on the one-electron spectral weight of a *d*-wave superconductor. *Phys. Rev. B*, 69:094523, Mar 2004. 42

[188] Fabian Schrodi, Alex Aperis, and Peter M. Oppeneer. Increased performance of Matsubara space calculations: A case study within Eliashberg theory. *Phys. Rev. B*, 99:184508, May 2019. 50

[189] Dominic Bergeron, Vasyl Hankevych, Bumsoo Kyung, and A. M. S. Tremblay. Optical and dc conductivity of the two-dimensional Hubbard model in the pseudogap regime and across the antiferromagnetic quantum critical point including vertex corrections. *Phys. Rev. B*, 84:085128, Aug 2011. 50

[190] Donald G. Anderson. Iterative Procedures for Nonlinear Integral Equations. *J. ACM*, 12(4):547–560, Oct 1965. 50

[191] V. Eyert. A Comparative Study on Methods for Convergence Acceleration of Iterative Vector Sequences. *J. Comput. Phys.*, 124(2):271–285, 1996. 50

[192] Homer F. Walker and Peng Ni. Anderson Acceleration for Fixed-Point Iterations. *SIAM J. Numer. Anal.*, 49(4):1715–1735, 2011. 50, 51

[193] J M Kosterlitz and D J Thouless. Ordering, metastability and phase transitions in two-dimensional systems. *J. Phys. C: Solid State Phys.*, 6(7):1181, 1973. 54

[194] J. E. Hirsch and D. J. Scalapino. Enhanced Superconductivity in Quasi Two-Dimensional Systems. *Phys. Rev. Lett.*, 56:2732–2735, Jun 1986. 59

[195] J. K. Freericks, Mark Jarrell, and G. D. Mahan. The Anharmonic Electron-Phonon Problem. *Phys. Rev. Lett.*, 77:4588–4591, Nov 1996. 61, 76, 77

[196] Carl J. Chandler, Christian Prosko, and F. Marsiglio. The Effect of Next-Nearest Neighbour Hopping in the One, Two, and Three Dimensional Holstein Model. *Sci. Rep.*, 6:32591–, September 2016. 61

[197] Christoph Heil, Samuel Poncé, Henry Lambert, Martin Schlipf, Elena R. Margine, and Feliciano Giustino. Origin of Superconductivity and Latent Charge Density Wave in NbS$_2$. *Phys. Rev. Lett.*, 119:087003, Aug 2017. 61

[198] H. J. Vidberg and J. W. Serene. Solving the Eliashberg equations by means of N-point Padé approximants. *J. Low Temp. Phys.*, 29(3):179–192, 1977. 65, 69

[199] Shaozhi Li and S. Johnston. The effects of non-linear electron-phonon interactions on superconductivity and charge-density-wave correlations. *EPL (Europhysics Letters)*, 109(2):27007, jan 2015. 65, 96, 98

[200] P. B. Allen and R. C. Dynes. Transition temperature of strong-coupled superconductors reanalyzed. *Phys. Rev. B*, 12:905–922, Aug 1975. 72, 82

[201] I. I. Mazin. The FeSe riddle. *Nature Materials*, 14:755, Jul 2015. 73

[202] E. Langmann, C. Triola, and A. V. Balatsky. Ubiquity of superconducting domes in BCS theory with finite-range potentials. *ArXiv e-prints*, oct 2018. 76, 78

[203] J. K. Freericks and G. D. Mahan. Strong-coupling expansions for the anharmonic Holstein model and for the Holstein-Hubbard model. *Phys. Rev. B*, 54:9372–9384, Oct 1996. 76, 77

[204] J. E. Gubernatis, D. J. Scalapino, R. L. Sugar, and W. D. Toussaint. Two-dimensional spin-polarized fermion lattice gases. *Phys. Rev. B*, 32:103–116, Jul 1985. 77

[205] H. Q. Lin and J. E. Hirsch. Condensation transition in the one-dimensional extended Hubbard model. *Phys. Rev. B*, 33:8155–8163, Jun 1986. 77

[206] R. Micnas, J. Ranninger, and S. Robaszkiewicz. Superconductivity in a narrow-band system with intersite electron pairing in two dimensions. II. Effects of nearest-neighbor exchange and correlated hopping. *Phys. Rev. B*, 39:11653–11662, Jun 1989. 77

[207] A. Macridin, M. Jarrell, and Th. Maier. Phase separation in the Hubbard model using the dynamical cluster approximation. *Phys. Rev. B*, 74:085104, Aug 2006. 77

[208] M. Aichhorn, E. Arrigoni, M. Potthoff, and W. Hanke. Phase separation and competition of superconductivity and magnetism in the two-dimensional Hubbard model: From strong to weak coupling. *Phys. Rev. B*, 76:224509, Dec 2007. 77

[209] C. Castellani, C. Di Castro, and M. Grilli. Singular Quasiparticle Scattering in the Proximity of Charge Instabilities. *Phys. Rev. Lett.*, 75:4650–4653, Dec 1995. 77

[210] Seher Karakuzu, Luca F. Tocchio, Sandro Sorella, and Federico Becca. Superconductivity, charge-density waves, antiferromagnetism, and phase separation in the Hubbard-Holstein model. *Phys. Rev. B*, 96:205145, Nov 2017. 77

[211] Georgios Varelogiannis. Phonon-mediated unconventional superconductivity in strongly correlated systems. *Phys. Rev. B*, 57:13743–13764, Jun 1998. 77

[212] W.H. Press, S.A. Teukolsky, W.T. Vetterling, and B.P. Flannery. *Numerical Recipes in FORTRAN: The Art of Scientific Computing*. Cambridge University Press, Cambridge, 2 edition, 1992. 80, 82

[213] Philip J. Davis and Philip Rabinowitz. *Methods of Numerical Integration*. Academic Press, San Diego, CA, 2 edition, 1984. 80

[214] J. P. Carbotte. Properties of boson-exchange superconductors. *Rev. Mod. Phys.*, 62:1027–1157, Oct 1990. 82

[215] Kevin Schawinski, Ce Zhang, Hantian Zhang, Lucas Fowler, and Gokula Krishnan Santhanam. Generative adversarial networks recover features in astrophysical images of galaxies beyond the deconvolution limit. *Monthly Notices of the Royal Astronomical Society: Letters*, 467(1):L110–L114, 2017. 85

[216] A. L. Edelen, S. G. Biedron, B. E. Chase, D. Edstrom, S. V. Milton, and P. Stabile. Neural Networks for Modeling and Control of Particle Accelerators. *IEEE Transactions on Nuclear Science*, 63(2):878–897, April 2016. 85

[217] Alexander Radovic, Mike Williams, David Rousseau, Michael Kagan, Daniele Bonacorsi, Alexander Himmel, Adam Aurisano, Kazuhiro Terao, and Taritree

Wongjirad. Machine learning at the energy and intensity frontiers of particle physics. *Nature*, 560(7716):41–48, 2018. 85

[218] Alexander Scheinker, Auralee Edelen, Dorian Bohler, Claudio Emma, and Alberto Lutman. Demonstration of Model-Independent Control of the Longitudinal Phase Space of Electron Beams in the Linac-Coherent Light Source with Femtosecond Resolution. *Phys. Rev. Lett.*, 121:044801, Jul 2018. 85

[219] Juan Carrasquilla and Roger G. Melko. Machine learning phases of matter. *Nat Phys*, 13(5):431–434, May 2017. Letter. 85

[220] Lei Wang. Discovering phase transitions with unsupervised learning. *Phys. Rev. B*, 94:195105, Nov 2016. 85

[221] Yi Zhang, A. Mesaros, K. Fujita, S. D. Edkins, M. H. Hamidian, K. Ch'ng, H. Eisaki, S. Uchida, J. C. Séamus Davis, Ehsan Khatami, and Eun-Ah Kim. Machine learning in electronic-quantum-matter imaging experiments. *Nature*, 570(7762):484–490, Jun 2019. 85

[222] Giuseppe Carleo and Matthias Troyer. Solving the quantum many-body problem with artificial neural networks. *Science*, 355(6325):602–606, 2017. 85

[223] Giacomo Torlai and Roger G. Melko. Learning thermodynamics with Boltzmann machines. *Phys. Rev. B*, 94:165134, Oct 2016. 85

[224] Kelvin Ch'ng, Juan Carrasquilla, Roger G. Melko, and Ehsan Khatami. Machine Learning Phases of Strongly Correlated Fermions. *Phys. Rev. X*, 7:031038, Aug 2017. 85, 94

[225] Dong-Ling Deng, Xiaopeng Li, and S. Das Sarma. Machine learning topological states. *Phys. Rev. B*, 96:195145, Nov 2017. 85

[226] Evert P. L. van Nieuwenburg, Ye-Hua Liu, and Sebastian D. Huber. Learning phase transitions by confusion. *Nat Phys*, 13(5):435–439, May 2017. Letter. 85

[227] Yi Zhang and Eun-Ah Kim. Quantum Loop Topography for Machine Learning. *Phys. Rev. Lett.*, 118:216401, May 2017. 85

[228] Sebastian J. Wetzel. Unsupervised learning of phase transitions: From principal component analysis to variational autoencoders. *Phys. Rev. E*, 96:022140, Aug 2017. 85

[229] Wenjian Hu, Rajiv R. P. Singh, and Richard T. Scalettar. Discovering phases, phase transitions, and crossovers through unsupervised machine learning: A critical examination. *Phys. Rev. E*, 95:062122, Jun 2017. 85

[230] Giacomo Torlai, Guglielmo Mazzola, Juan Carrasquilla, Matthias Troyer, Roger Melko, and Giuseppe Carleo. Neural-network quantum state tomography. *Nature Physics*, 14(5):447–450, 2018. 85

[231] Frank Schindler, Nicolas Regnault, and Titus Neupert. Probing many-body localization with neural networks. *Phys. Rev. B*, 95:245134, Jun 2017. 85

[232] Li Huang and Lei Wang. Accelerated Monte Carlo simulations with restricted Boltzmann machines. *Phys. Rev. B*, 95:035105, Jan 2017. 85

[233] Junwei Liu, Huitao Shen, Yang Qi, Zi Yang Meng, and Liang Fu. Self-learning Monte Carlo method and cumulative update in fermion systems. *Phys. Rev. B*, 95:241104(R), Jun 2017. 85, 90

[234] Shuo-Hui Li and Lei Wang. Neural Network Renormalization Group. *Phys. Rev. Lett.*, 121:260601, Dec 2018. 85

[235] Romain Fournier, Lei Wang, Oleg V. Yazyev, and QuanSheng Wu. Artificial Neural Network Approach to the Analytic Continuation Problem. *Phys. Rev. Lett.*, 124:056401, Feb 2020. 85

[236] James Nelson, Rajarshi Tiwari, and Stefano Sanvito. Machine learning density functional theory for the Hubbard model. *Phys. Rev. B*, 99:075132, Feb 2019. 85

[237] Hidemaro Suwa, Justin S. Smith, Nicholas Lubbers, Cristian D. Batista, Gia-Wei Chern, and Kipton Barros. Machine learning for molecular dynamics with strongly correlated electrons. *Phys. Rev. B*, 99:161107, Apr 2019. 85

[238] Junwei Liu, Yang Qi, Zi Yang Meng, and Liang Fu. Self-learning Monte Carlo method. *Phys. Rev. B*, 95:041101(R), Jan 2017. 85, 90

[239] Xiao Yan Xu, Yang Qi, Junwei Liu, Liang Fu, and Zi Yang Meng. Self-learning quantum Monte Carlo method in interacting fermion systems. *Phys. Rev. B*, 96:041119(R), Jul 2017. 85, 90

[240] Yuki Nagai, Huitao Shen, Yang Qi, Junwei Liu, and Liang Fu. Self-learning Monte Carlo method: Continuous-time algorithm. *Phys. Rev. B*, 96:161102(R), Oct 2017. 85

[241] Huitao Shen, Junwei Liu, and Liang Fu. Self-learning Monte Carlo with deep neural networks. *Phys. Rev. B*, 97:205140, May 2018. 85

[242] Chuang Chen, Xiao Yan Xu, Junwei Liu, George Batrouni, Richard Scalettar, and Zi Yang Meng. Symmetry-enforced self-learning Monte Carlo method applied to the Holstein model. *Phys. Rev. B*, 98:041102(R), Jul 2018. 85, 88, 89, 91, 92, 94, 96

[243] Yuki Nagai, Masahiko Okumura, and Akinori Tanaka. Self-learning Monte Carlo method with Behler-Parrinello neural networks. *Phys. Rev. B*, 101:115111, Mar 2020. 85

[244] E. M. Inack, G. E. Santoro, L. Dell'Anna, and S. Pilati. Projective quantum Monte Carlo simulations guided by unrestricted neural network states. *Phys. Rev. B*, 98:235145, Dec 2018. 85

[245] Taegeun Song and Hunpyo Lee. Accelerated continuous time quantum Monte Carlo method with machine learning. *Phys. Rev. B*, 100:045153, Jul 2019. 85

[246] Asok K. Sen, Robert Mills, Theodore Kaplan, and L. J. Gray. Traveling-cluster approximation for uncorrelated amorphous systems. *Phys. Rev. B*, 30:5686–5695, Nov 1984. 86

[247] Anamitra Mukherjee, Niravkumar D. Patel, Chris Bishop, and Elbio Dagotto. Parallelized traveling cluster approximation to study numerically spin-fermion models on large lattices. *Phys. Rev. E*, 91:063303, Jun 2015. 86

[248] M. Hohenadler and T. C. Lang. Autocorrelations in Quantum Monte Carlo Simulations of Electron-Phonon Models. In H. Fehske, Schneider R., and Weisse A., editors, *Computational Many-Particle Physics*, pages 357–366. Springer, Berlin, 2008. 86, 99

[249] Richard T. Scalettar, Reinhard M. Noack, and Rajiv R. P. Singh. Ergodicity at large couplings with the determinant Monte Carlo algorithm. *Phys. Rev. B*, 44:10502–10507, Nov 1991. 86, 88

[250] Chen-Rung Lee, I-Hsin Chung, and Zhaojun Bai. Parallelization of DQMC simulation for strongly correlated electron systems. *In Proceedings of 24th IEEE International Parallel and Distributed Processing Symposium*, (11309863), 2010. 88

[251] J. K. Freericks, E. J. Nicol, A. Y. Liu, and A. A. Quong. Vertex-corrected tunneling inversion in electron-phonon mediated superconductors: Pb. *Phys. Rev. B*, 55:11651–11658, May 1997. 96

[252] J P Hague. Electron and phonon dispersions of the two-dimensional Holstein model: effects of vertex and non-local corrections. *Journal of Physics: Condensed Matter*, 15(17):2535–2550, apr 2003. 96

[253] Fabian Schrodi, Peter M. Oppeneer, and Alex Aperis. Full-bandwidth Eliashberg theory of superconductivity beyond Migdal's approximation. *Phys. Rev. B*, 102:024503, Jul 2020. 96

[254] Maria N. Gastiasoro, Andrey V. Chubukov, and Rafael M. Fernandes. Phonon-mediated superconductivity in low carrier-density systems. *Phys. Rev. B*, 99:094524, Mar 2019. 96

[255] Guo-Zhu Liu, Zhao-Kun Yang, Xiao-Yin Pan, and Jing-Rong Wang. Towards exact solutions for the superconducting T_c induced by electron-phonon interaction. *Phys. Rev. B*, 103:094501, Mar 2021. 96

[256] H. Fröhlich. Electrons in lattice fields. *Advances in Physics*, 3(11):325–361, 1954. 96

[257] G. Levine and W. P. Su. Pairing of charge carriers in the two-dimensional molecular crystal model. *Phys. Rev. B*, 42:4143–4149, Sep 1990. 96

[258] G. Levine and W. P. Su. Finite-cluster study of superconductivity in the two-dimensional molecular-crystal model. *Phys. Rev. B*, 43:10413–10421, May 1991. 96

[259] M. Vekić and S. R. White. Gap formation in the density of states for the Holstein model. *Phys. Rev. B*, 48:7643–7650, Sep 1993. 96

[260] J. K. Freericks and Mark Jarrell. Competition between Electron-Phonon Attraction and Weak Coulomb Repulsion. *Phys. Rev. Lett.*, 75:2570–2573, Sep 1995. 96

[261] J. K. Freericks, Mark Jarrell, and G. D. Mahan. The Anharmonic Electron-Phonon Problem [Phys. Rev. Lett. 77, 4588 (1996)]. *Phys. Rev. Lett.*, 79:1783–1783, Sep 1997. 96, 110

[262] H. Zheng and S. Y. Zhu. Charge-density-wave and superconducting states in the Holstein model on a square lattice. *Phys. Rev. B*, 55:3803–3815, Feb 1997. 96

[263] Glen L. Goodvin, Mona Berciu, and George A. Sawatzky. Green's function of the Holstein polaron. *Phys. Rev. B*, 74:245104, Dec 2006. 96

[264] M. Hohenadler and G. G. Batrouni. Dominant charge density wave correlations in the Holstein model on the half-filled square lattice. *Phys. Rev. B*, 100:165114, Oct 2019. 96, 110

[265] J. T. Devreese. Polarons. *Encyclopedia of Applied Physics*, 14:383, 1996. 96

[266] C. P. J. Adolphs and M. Berciu. Going beyond the linear approximation in describing electron-phonon coupling: Relevance for the Holstein model. *EPL (Europhysics Letters)*, 102(4):47003, 2013. 96, 98

[267] Zhou Li and F. Marsiglio. The Polaron-Like Nature of an Electron Coupled to Phonons. *Journal of Superconductivity and Novel Magnetism*, 25(5):1313–1317, 2012. 105

[268] F. Marsiglio. Eliashberg theory: A short review. *Annals of Physics*, 417:168102, 2020. Eliashberg theory at 60: Strong-coupling superconductivity and beyond. 105

[269] S. Gerber, S.-L. Yang, D. Zhu, H. Soifer, J. A. Sobota, S. Rebec, J. J. Lee, T. Jia, B. Moritz, C. Jia, A. Gauthier, Y. Li, D. Leuenberger, Y. Zhang, L. Chaix, W. Li, H. Jang, J.-S. Lee, M. Yi, G. L. Dakovski, S. Song, J. M. Glownia, S. Nelson, K. W. Kim, Y.-D. Chuang, Z. Hussain, R. G. Moore, T. P. Devereaux, W.-S. Lee, P. S. Kirchmann, and Z.-X. Shen. Femtosecond electron-phonon lock-in by photoemission and x-ray free-electron laser. *Science*, 357(6346):71–75, 2017. 108

[270] Y. J. Uemura, G. M. Luke, B. J. Sternlieb, J. H. Brewer, J. F. Carolan, W. N. Hardy, R. Kadono, J. R. Kempton, R. F. Kiefl, S. R. Kreitzman, P. Mulhern, T. M. Riseman, D. Ll. Williams, B. X. Yang, S. Uchida, H. Takagi, J. Gopalakrishnan, A. W. Sleight, M. A. Subramanian, C. L. Chien, M. Z. Cieplak, Gang Xiao, V. Y. Lee, B. W. Statt, C. E. Stronach, W. J. Kossler, and X. H. Yu. Universal Correlations between T_c and $\frac{n_s}{m^*}$ (Carrier Density over Effective Mass) in High-T_c Cuprate Superconductors. *Phys. Rev. Lett.*, 62:2317–2320, May 1989. 113

[271] J. Corson, R. Mallozzi, J. Orenstein, J. N. Eckstein, and I. Bozovic. Vanishing of phase coherence in underdoped $Bi_2Sr_2CaCu_2O_{8+\delta}$. *Nature*, 398(6724):221–223, Mar 1999. 113

[272] Z. A. Xu, N. P. Ong, Y. Wang, T. Kakeshita, and S. Uchida. Vortex-like excitations and the onset of superconducting phase fluctuation in underdoped $La_{2-x}Sr_xCuO_4$. *Nature*, 406(6795):486–488, Aug 2000. 113

[273] Yayu Wang, Lu Li, M. J. Naughton, G. D. Gu, S. Uchida, and N. P. Ong. Field-Enhanced Diamagnetism in the Pseudogap State of the Cuprate $Bi_2Sr_2CaCu_2O_{8+\delta}$ Superconductor in an Intense Magnetic Field. *Phys. Rev. Lett.*, 95:247002, Dec 2005. 113

[274] Patrick M. C. Rourke, Ioanna Mouzopoulou, Xiaofeng Xu, Christos Panagopoulos, Yue Wang, Baptiste Vignolle, Cyril Proust, Evgenia V. Kurganova, Uli Zeitler,

Yoichi Tanabe, Tadashi Adachi, Yoji Koike, and Nigel E. Hussey. Phase-fluctuating superconductivity in overdoped $La_{2-x}Sr_xCuO_4$. *Nature Physics*, 7(6):455–458, Jun 2011. 113

[275] Philipp Werner and Andrew J. Millis. High-Spin to Low-Spin and Orbital Polarization Transitions in Multiorbital Mott Systems. *Phys. Rev. Lett.*, 99:126405, Sep 2007. 114

[276] Luca F. Tocchio, Federico Becca, and Sandro Sorella. Hidden Mott transition and large-U superconductivity in the two-dimensional Hubbard model. *Phys. Rev. B*, 94:195126, Nov 2016. 114

[277] R. T. Scalettar, E. Y. Loh, J. E. Gubernatis, A. Moreo, S. R. White, D. J. Scalapino, R. L. Sugar, and E. Dagotto. Phase diagram of the two-dimensional negative-U Hubbard model. *Phys. Rev. Lett.*, 62:1407–1410, Mar 1989. 117, 126

[278] A. Moreo and D. J. Scalapino. Two-dimensional negative-U Hubbard model. *Phys. Rev. Lett.*, 66:946–948, Feb 1991. 117, 121

[279] M. Keller, W. Metzner, and U. Schollwöck. Dynamical Mean-Field Theory for Pairing and Spin Gap in the Attractive Hubbard Model. *Phys. Rev. Lett.*, 86:4612–4615, May 2001. 117, 126

[280] Tatsuya Kaneko and Yukinori Ohta. BCS–BEC Crossover in the Two-Dimensional Attractive Hubbard Model: Variational Cluster Approach. *Journal of the Physical Society of Japan*, 83(2):024711, 2014. 117

[281] Tamaghna Hazra, Nishchhal Verma, and Mohit Randeria. Bounds on the Superconducting Transition Temperature: Applications to Twisted Bilayer Graphene and Cold Atoms. *Phys. Rev. X*, 9:031049, Sep 2019. 117

[282] Thereza Paiva, Richard Scalettar, Mohit Randeria, and Nandini Trivedi. Fermions in 2D Optical Lattices: Temperature and Entropy Scales for Observing Antiferromagnetism and Superfluidity. *Phys. Rev. Lett.*, 104:066406, Feb 2010. 117, 121

[283] Thomas A Maier, Seher Karakuzu, and Douglas J Scalapino. Overdoped end of the cuprate phase diagram. *Phys. Rev. Res.*, 2(3):33132, 2020. 124

[284] Chun Chen, Yan Chen, Z. D. Wang, and C. S. Ting. Enhanced superconducting proximity effect in strongly correlated heterostructures. *Phys. Rev. B*, 82:174502, Nov 2010. 124

[285] A. J. Leggett. Diatomic molecules and cooper pairs. In Andrzej Pękalski and Jerzy A. Przystawa, editors, *Modern Trends in the Theory of Condensed Matter*, pages 13–27, Berlin, Heidelberg, 1980. Springer Berlin Heidelberg. 126

[286] M. G. Ries, A. N. Wenz, G. Zürn, L. Bayha, I. Boettcher, D. Kedar, P. A. Murthy, M. Neidig, T. Lompe, and S. Jochim. Observation of Pair Condensation in the Quasi-2D BEC-BCS Crossover. *Phys. Rev. Lett.*, 114:230401, Jun 2015. 126

[287] Giuseppe Carleo, Ignacio Cirac, Kyle Cranmer, Laurent Daudet, Maria Schuld, Naftali Tishby, Leslie Vogt-Maranto, and Lenka Zdeborová. Machine learning and the physical sciences. *Rev. Mod. Phys.*, 91:045002, Dec 2019. 129

[288] Filippo Vicentini. Machine learning toolbox for quantum many body physics. *Nature Reviews Physics*, 3(3):156–156, Mar 2021. 129

[289] Juan Carrasquilla and Giacomo Torlai. Neural networks in quantum many-body physics: a hands-on tutorial, 2021. 129

[290] I. Esterlis, S. A. Kivelson, and D. J. Scalapino. Pseudogap crossover in the electron-phonon system. *Phys. Rev. B*, 99:174516, May 2019. 129

[291] A. Alexandradinata, N. P. Armitage, Andrey Baydin, Wenli Bi, Yue Cao, Hitesh J. Changlani, Eli Chertkov, Eduardo H. da Silva Neto, Luca Delacretaz, Ismail El Baggari, G. M. Ferguson, William J. Gannon, Sayed Ali Akbar Ghorashi, Berit H. Goodge, Olga Goulko, G. Grissonnanche, Alannah Hallas, Ian M. Hayes, Yu He, Edwin W. Huang, Anshul Kogar, Divine Kumah, Jong Yeon Lee, A. Legros, Fahad Mahmood, Yulia Maximenko, Nick Pellatz, Hryhoriy Polshyn, Tarapada

Sarkar, Allen Scheie, Kyle L. Seyler, Zhenzhong Shi, Brian Skinner, Lucia Steinke, K. Thirunavukkuarasu, Thaís Victa Trevisan, Michael Vogl, Pavel A. Volkov, Yao Wang, Yishu Wang, Di Wei, Kaya Wei, Shuolong Yang, Xian Zhang, Ya-Hui Zhang, Liuyan Zhao, and Alfred Zong. The Future of the Correlated Electron Problem, 2020. 131

[292] Steven Johnston. *Electron-phonon Coupling in Quasi-Two-Dimensional Correlated Systems*. PhD thesis, University of Waterloo, University of Waterloo Library, Jun 2010. The author is my Ph.D. advisor. 173, 201

[293] Naomichi Hatano and Masuo Suzuki. *Finding Exponential Product Formulas of Higher Orders*, pages 37–68. Springer Berlin Heidelberg, Berlin, Heidelberg, 2005. 175

[294] Masuo Suzuki. Relationship between d-Dimensional Quantal Spin Systems and (d+1)-Dimensional Ising Systems: Equivalence, Critical Exponents and Systematic Approximants of the Partition Function and Spin Correlations. *Progress of Theoretical Physics*, 56(5):1454–1469, 1976. 175

[295] J. E. Hirsch. Discrete Hubbard-Stratonovich transformation for fermion lattice models. *Phys. Rev. B*, 28:4059–4061, Oct 1983. 176

[296] Matthias Troyer and Uwe-Jens Wiese. Computational Complexity and Fundamental Limitations to Fermionic Quantum Monte Carlo Simulations. *Phys. Rev. Lett.*, 94:170201, May 2005. 195

[297] Z. C. Wei, Congjun Wu, Yi Li, Shiwei Zhang, and T. Xiang. Majorana Positivity and the Fermion Sign Problem of Quantum Monte Carlo Simulations. *Phys. Rev. Lett.*, 116:250601, Jun 2016. 196

[298] Zi-Xiang Li, Fa Wang, Hong Yao, and Dung-Hai Lee. What makes the T(c) of monolayer FeSe on SrTiO(3) so high: a sign-problem-free quantum Monte Carlo study. *Sci Bull (Beijing)*, 61:925–930, Apr 2016. 1087[PII]. 196, 197

Appendices

A Momentum-Space representation of the 2D Holstein model

In this appendix, we will evaluate the Fourier transform of the 2D singleband Holstein model. A **k**-space form of the Holstein model is especially useful for the diagrammatic approach of Chapter 2. The real space version that we will start with is given by

$$\hat{H} = -\sum_{i,j,\sigma} t_{ij}\left(\hat{c}^{\dagger}_{i,\sigma}\hat{c}_{j,\sigma} + \hat{c}^{\dagger}_{j,\sigma}\hat{c}_{i,\sigma}\right) - \mu\sum_{i,\sigma}\hat{n}_{i,\sigma} + \sum_{i}\left[\frac{\hat{P}^2_i}{2M} + \frac{1}{2}K\hat{X}^2_i\right] - \alpha\sum_{i,\sigma}\hat{X}_i\left(\hat{n}_{i,\sigma} - \frac{1}{2}\right).$$
(A.1)

Here, $\hat{c}^{\dagger}_{i,\sigma}$ ($\hat{c}_{i,\sigma}$) creates (annihilates) an electron with spin σ at site i, and the number operator $\hat{n}_{i,\sigma} = \hat{c}^{\dagger}_{i,\sigma}\hat{c}_{i,\sigma}$. The electrons may tunnel to neighboring sites according to the hopping-matrix element t_{ij}, which is usually limited to nearest or next-nearest neighbors only. Thanks to the $-1/2$ in the last term of Eqn. (A.1), this Hamiltonian exhibits particle-hole symmetry when the chemical potential $\mu = 0$, but only if $t_{i,j}$ is limited to nearest neighbors only. Next, $\hat{X}_i$ and $\hat{P}_i$ are the position and momentum operators for the ion with mass M at site i. These ionic oscillators are considered to be independent harmonic with the spring constant $K = M\Omega^2$, each with an "Einstein" phonon frequency Ω. Finally, α is the e-ph interaction strength corresponding to a linear coupling between the local electron density at site i and the lattice displacement at the same location. A discussion of this Hamiltonian and other details regarding the approximations leading to such simple models of e-ph coupling can be found in Section 1.2.

If we move the factor of $-1/2$ out of the interaction term and group it with the phonon energy terms, we can show that acts to shift the displacement datum. To proceed, we simply

complete the square as follows:

$$\hat{H}_{\text{ph}} + \hat{H}_{\text{e-ph}} = \sum_i \left[\frac{\hat{P}_i^2}{2M} + \frac{1}{2}K\hat{X}_i^2 \right] - \alpha \sum_{i,\sigma} \hat{X}_i \left(\hat{n}_{i,\sigma} - \frac{1}{2} \right)$$

$$= \sum_i \left[\frac{\hat{P}_i^2}{2M} + \frac{1}{2}K\hat{X}_i^2 - \alpha \sum_\sigma \hat{X}_i \left(\hat{n}_{i,\sigma} - \frac{1}{2} \right) \right]$$

$$= \sum_i \left[\frac{\hat{P}_i^2}{2M} + \frac{1}{2}K \left(\hat{X}_i^2 + \frac{2\alpha}{K}\hat{X}_i \right) - \alpha\hat{X}_i \sum_\sigma \hat{n}_{i,\sigma} \right]$$

$$= \sum_i \left[\frac{\hat{P}_i^2}{2M} + \frac{1}{2}K \left[\left(\hat{X}_i + \frac{\alpha}{K} \right)^2 - \frac{\alpha^2}{K^2} \right] - \alpha\hat{X}_i \sum_\sigma \hat{n}_{i,\sigma} \right]$$

$$= \sum_i \left[\frac{\hat{P}_i^2}{2M} + \frac{1}{2}K \left(\hat{X}_i + \frac{\alpha}{K} \right)^2 - \frac{\alpha^2}{2K} - \alpha\hat{X}_i \sum_\sigma \hat{n}_{i,\sigma} \right] \qquad \text{(A.2)}$$

In the last line of Eqn. (A.2) above, we will henceforth drop the $-\frac{\alpha^2}{2K}$ term, as it does not contain any operators and thus has no influence on the dynamics of the system. The shift in $\hat{X}$ is now given by $\hat{X}'_i \equiv \hat{X}_i + \frac{\alpha}{K}$. With these changes, Eqn. (A.2) can be written as:

$$\hat{H}_{\text{ph}} + \hat{H}_{\text{e-ph}} = \sum_i \left[\frac{\hat{P}_i^2}{2M} + \frac{1}{2}K\hat{X}'^2_i - \alpha\hat{X}'_i \sum_\sigma \hat{n}_{i,\sigma} + \frac{\alpha^2}{K} \sum_\sigma \hat{n}_{i,\sigma} \right]. \qquad \text{(A.3)}$$

The 'prime' on the position operator can be treated analogously to a dummy index and be removed from this point forward (i.e., all position operators in this section will now be the newly transformed ones). Let us write the new form of Eqn. (A.1)

$$\hat{H} = -\sum_{i,j,\sigma} t_{ij} \left(\hat{c}^\dagger_{i,\sigma}\hat{c}_{j,\sigma} + \hat{c}^\dagger_{j,\sigma}\hat{c}_{i,\sigma} \right) - \left(\mu - \frac{\alpha^2}{K} \right) \sum_{i,\sigma} \hat{n}_{i,\sigma} + \sum_i \left[\frac{\hat{P}_i^2}{2M} + \frac{1}{2}K\hat{X}_i^2 - \alpha\hat{X}_i \sum_\sigma \hat{n}_{i,\sigma} \right],$$

$$\text{(A.4)}$$

where it is now clear that the particle-hole symmetric transformation mentioned earlier is just a shift in the chemical potential by a factor $\frac{\alpha^2}{K}$. It is customary to pose the problem in reciprocal space, where at least for Eqn. (A.1), the mathematics will simplify. First we introduce the Fourier transform of the relevant operators from crystal space to momentum space:

$$\hat{c}_{i,\sigma} = \frac{1}{\sqrt{N_s}} \sum_{\mathbf{k}} e^{i\mathbf{k}\cdot\mathbf{r}_i}\hat{c}_{\mathbf{k},\sigma} \qquad\qquad \hat{c}^\dagger_{i,\sigma} = \frac{1}{\sqrt{N_s}} \sum_{\mathbf{k}} e^{-i\mathbf{k}\cdot\mathbf{r}_i}\hat{c}^\dagger_{\mathbf{k},\sigma} \qquad \text{(A.5)}$$

and

$$\hat{X}_i = \sqrt{\frac{\hbar}{2M\Omega}} \left(\hat{a}_i + \hat{a}_i^\dagger \right) \qquad \hat{P}_i = \mathrm{i}\sqrt{\frac{M\hbar\Omega}{2}} \left(-\hat{a}_i + \hat{a}_i^\dagger \right), \qquad (A.6)$$

where N_s is the number of sites, $\mathbf{k}$ is an electron (momentum) wave vector[1], and $\mathbf{r}_i$ is the position of the ith site. We can now proceed to find $\hat{X}_i^2$:

$$\begin{aligned}
\hat{X}_i^2 &= \frac{\hbar}{2M\Omega} \left(\hat{a}_i + \hat{a}_i^\dagger \right)^2 \\
&= \frac{\hbar}{2M\Omega} \left((\hat{a}_i)^2 + \hat{a}_i \hat{a}_i^\dagger + \hat{a}_i^\dagger \hat{a}_i + (\hat{a}_i^\dagger)^2 \right) \\
&= \frac{\hbar}{2M\Omega} \left((\hat{a}_i)^2 + 2\hat{a}_i^\dagger \hat{a}_i + (\hat{a}_i^\dagger)^2 + \hat{\mathbb{1}} \right),
\end{aligned} \qquad (A.7)$$

and similarly for $\hat{P}_i^2$,

$$\begin{aligned}
\hat{P}_i^2 &= -\frac{M\hbar\Omega}{2} \left(-\hat{a}_i + \hat{a}_i^\dagger \right)^2 \\
&= -\frac{M\hbar\Omega}{2} \left((\hat{a}_i)^2 - \hat{a}_i \hat{a}_i^\dagger - \hat{a}_i^\dagger \hat{a}_i + (\hat{a}_i^\dagger)^2 \right) \\
&= -\frac{M\hbar\Omega}{2} \left((\hat{a}_i)^2 - 2\hat{a}_i^\dagger \hat{a}_i + (\hat{a}_i^\dagger)^2 - \hat{\mathbb{1}} \right).
\end{aligned} \qquad (A.8)$$

With these expressions we can work on obtaining the phonon energy in terms of the bosonic operators $\hat{a}_i^\dagger$ and $\hat{a}_i$:

$$\begin{aligned}
\frac{\hat{P}_i^2}{2M} + \frac{1}{2}K\hat{X}_i^2 &= -\frac{\hbar\Omega}{4} \left((\hat{a}_i)^2 - 2\hat{a}_i^\dagger \hat{a}_i + (\hat{a}_i^\dagger)^2 - \hat{\mathbb{1}} \right) + \frac{\hbar\Omega}{4} \left((\hat{a}_i)^2 + 2\hat{a}_i^\dagger \hat{a}_i + (\hat{a}_i^\dagger)^2 + \hat{\mathbb{1}} \right) \\
&= \hbar\Omega \left(\hat{a}_i^\dagger \hat{a}_i + \frac{\hat{\mathbb{1}}}{2} \right),
\end{aligned} \qquad (A.9)$$

which gives us the canonical energy levels for the harmonic oscillator in second quantization. From this point forward we will set $\hbar \equiv 1$ to simplify notation. We can now transform these phonon operators into reciprocal space:

$$\hat{a}_i = \frac{1}{\sqrt{N_s}} \sum_{\mathbf{k}} e^{\mathrm{i}\mathbf{k}\cdot\mathbf{r}_i} \hat{a}_{\mathbf{k}} \qquad \text{and} \qquad \hat{a}_i^\dagger = \frac{1}{\sqrt{N_s}} \sum_{\mathbf{k}} e^{-\mathrm{i}\mathbf{k}\cdot\mathbf{r}_i} \hat{a}_{\mathbf{k}}^\dagger \qquad (A.10)$$

---

[1]The sum in A.5 is to consist of all the $\mathbf{k}$'s in the first Brillouin Zone (FBZ), which could be denoted explicitly as $\sum_{\mathbf{k}\in\text{FBZ}}$. However, we will omit the $\in$ FBZ in all cases where it need not be specified otherwise.

All of the terms in A.1 will need to be evaluated with the transforms outlined above, and we will do this term by term.

1. Restricting the hopping to nearest-neighbors (NN) only, the hopping energy matrix element $-t_{ij}$ is replaced by $-t$. The sum over i and j is can be replaced by a sum over i and $\mathbf{r}_\eta$, where the index η runs over the four NN sites surrounding the ith site. As a consequence, the entire expression for electron hopping can be rewritten and then transformed using Eqns. (A.5):

$$
\begin{aligned}
\hat{H}_e &= -\sum_{i,j,\sigma} t_{ij} \left(\hat{c}_{i,\sigma}^\dagger \hat{c}_{j,\sigma} + \hat{c}_{j,\sigma}^\dagger \hat{c}_{i,\sigma} \right) \\
&= -t \sum_{i,\eta,\sigma} \left(\hat{c}_{i,\sigma}^\dagger \hat{c}_{i+\eta,\sigma} + \hat{c}_{i+\eta,\sigma}^\dagger \hat{c}_{i,\sigma} \right) \\
&= -t \sum_{i,\eta,\sigma} \left(\frac{1}{N_s} \sum_{\mathbf{k},\mathbf{k}'} \mathrm{e}^{-\mathrm{i}(\mathbf{k}'-\mathbf{k})\cdot\mathbf{r}_i} \mathrm{e}^{\mathrm{i}\mathbf{k}\cdot\mathbf{r}_\eta} \hat{c}_{\mathbf{k}',\sigma}^\dagger \hat{c}_{\mathbf{k},\sigma} + \frac{1}{N_s} \sum_{\mathbf{k},\mathbf{k}'} \mathrm{e}^{-\mathrm{i}(\mathbf{k}-\mathbf{k}')\cdot\mathbf{r}_i} \mathrm{e}^{-\mathrm{i}\mathbf{k}'\cdot\mathbf{r}_\eta} \hat{c}_{\mathbf{k},\sigma}^\dagger \hat{c}_{\mathbf{k}',\sigma} \right) \\
&= -t \sum_{\eta,\sigma} \sum_{\mathbf{k},\mathbf{k}'} \left(\mathrm{e}^{\mathrm{i}\mathbf{k}\cdot\mathbf{r}_\eta} \hat{c}_{\mathbf{k}',\sigma}^\dagger \hat{c}_{\mathbf{k},\sigma} \delta_{\mathbf{k}',\mathbf{k}} + \mathrm{e}^{-\mathrm{i}\mathbf{k}'\cdot\mathbf{r}_\eta} \hat{c}_{\mathbf{k},\sigma}^\dagger \hat{c}_{\mathbf{k}',\sigma} \delta_{\mathbf{k}',\mathbf{k}} \right) \\
&= -t \sum_{\eta,\sigma} \sum_{\mathbf{k}} \hat{c}_{\mathbf{k},\sigma}^\dagger \hat{c}_{\mathbf{k},\sigma} \left(\mathrm{e}^{\mathrm{i}\mathbf{k}\cdot\mathbf{r}_\eta} + \mathrm{e}^{-\mathrm{i}\mathbf{k}\cdot\mathbf{r}_\eta} \right) \\
&= -2t \sum_{\eta,\sigma} \sum_{\mathbf{k}} \hat{c}_{\mathbf{k},\sigma}^\dagger \hat{c}_{\mathbf{k},\sigma} \cos(\mathbf{k}\cdot\mathbf{r}_\eta). \\
&= -2t \sum_{\mathbf{k},\sigma} \hat{c}_{\mathbf{k},\sigma}^\dagger \hat{c}_{\mathbf{k},\sigma} \left(\cos(k_x a) + \cos(k_y a) \right).
\end{aligned}
\tag{A.11}
$$

where we have used that $N_s^{-1} \sum_i \mathrm{e}^{-\mathrm{i}(\mathbf{k}'-\mathbf{k})\cdot\mathbf{r}_i} = \delta_{\mathbf{k}',\mathbf{k}}$. The vector $\mathbf{r}_\eta$ can take the values $(a,0)$, $(0,a)$, $(-a,0)$, and $(0,-a)$, where a is the spacing between sites in the square lattice.

2. The second term is the chemical potential term, which effectively tells us how much energy would be required to add another electron to the system.

$$
\begin{aligned}
-\left(\mu - \frac{\alpha^2}{K}\right)\sum_{i,\sigma}\hat{n}_{i,\sigma} &= -\left(\mu - \frac{\alpha^2}{K}\right)\sum_{i,\sigma}\hat{c}^\dagger_{i,\sigma}\hat{c}_{i,\sigma} \\
&= -\left(\mu - \frac{\alpha^2}{K}\right)\frac{1}{N_s}\sum_{i,\sigma}\sum_{\mathbf{k},\mathbf{k}'}\mathrm{e}^{-\mathrm{i}(\mathbf{k}'-\mathbf{k})\cdot\mathbf{r}_i}\hat{c}^\dagger_{\mathbf{k}',\sigma}\hat{c}_{\mathbf{k},\sigma} \\
&= -\left(\mu - \frac{\alpha^2}{K}\right)\sum_{\mathbf{k},\sigma}\hat{c}^\dagger_{\mathbf{k},\sigma}\hat{c}_{\mathbf{k},\sigma}
\end{aligned}
\tag{A.12}
$$

3. The third term is carried out similarly to the previous term except that now we use the transforms depicted in A.10. Thus, we simply state the result without revealing the extra steps

$$
\Omega\sum_i\left(\hat{a}^\dagger_i\hat{a}_i + \frac{\hat{\mathbb{I}}}{2}\right) = \Omega\sum_{\mathbf{k}}\left(\hat{a}^\dagger_{\mathbf{k}}\hat{a}_{\mathbf{k}} + \frac{\hat{\mathbb{I}}}{2}\right).
\tag{A.13}
$$

4. Lastly, we need to find the **k**-space representation of the e-ph coupling term:

$$
\begin{aligned}
-\alpha\sum_{i,\sigma}\hat{X}_i\hat{n}_{i,\sigma} &= -\frac{\alpha}{\sqrt{2M\Omega}}\sum_{i,\sigma}\left(\hat{a}_i + \hat{a}^\dagger_i\right)\hat{c}^\dagger_{i,\sigma}\hat{c}_{i,\sigma} \\
&= -\frac{\alpha}{\sqrt{2N_sM\Omega}}\sum_{i,\sigma}\sum_{\mathbf{q}}\left(\mathrm{e}^{\mathrm{i}\mathbf{q}\cdot\mathbf{r}_i}\hat{a}_{\mathbf{q}} + \mathrm{e}^{-\mathrm{i}\mathbf{q}\cdot\mathbf{r}_i}\hat{a}^\dagger_{\mathbf{q}}\right)\left(\frac{1}{N_s}\sum_{\mathbf{k},\mathbf{k}'}\mathrm{e}^{-\mathrm{i}(\mathbf{k}'-\mathbf{k})\cdot\mathbf{r}_i}\hat{c}^\dagger_{\mathbf{k}',\sigma}\hat{c}_{\mathbf{k},\sigma}\right) \\
&= -\frac{\alpha}{\sqrt{2N_sM\Omega}}\sum_{i,\sigma}\left[\frac{1}{N_s}\sum_{\mathbf{q},\mathbf{k},\mathbf{k}'}\left(\mathrm{e}^{\mathrm{i}(\mathbf{q}-(\mathbf{k}'-\mathbf{k}))\cdot\mathbf{r}_i}\hat{a}_{\mathbf{q}} + \mathrm{e}^{-\mathrm{i}(\mathbf{q}-(\mathbf{k}-\mathbf{k}'))\cdot\mathbf{r}_i}\hat{a}^\dagger_{\mathbf{q}}\right)\hat{c}^\dagger_{\mathbf{k}',\sigma}\hat{c}_{\mathbf{k},\sigma}\right] \\
&= -\frac{\alpha}{\sqrt{2N_sM\Omega}}\sum_{\sigma}\left[\sum_{\mathbf{q},\mathbf{k},\mathbf{k}'}\left(\delta_{\mathbf{q},\mathbf{k}'-\mathbf{k}}\hat{a}_{\mathbf{q}} + \delta_{\mathbf{q},-(\mathbf{k}'-\mathbf{k})}\hat{a}^\dagger_{\mathbf{q}}\right)\hat{c}^\dagger_{\mathbf{k}',\sigma}\hat{c}_{\mathbf{k},\sigma}\right] \\
&= -\frac{\alpha}{\sqrt{2N_sM\Omega}}\sum_{\sigma}\left[\sum_{\mathbf{k},\mathbf{k}'}\left(\hat{a}_{\mathbf{k}'-\mathbf{k}} + \hat{a}^\dagger_{-(\mathbf{k}'-\mathbf{k})}\right)\hat{c}^\dagger_{\mathbf{k}',\sigma}\hat{c}_{\mathbf{k},\sigma}\right] \\
&= -\frac{\alpha}{\sqrt{2N_sM\Omega}}\left[\sum_{\mathbf{k},\mathbf{k}',\sigma}\left(\hat{a}_{\mathbf{k}'-\mathbf{k}} + \hat{a}^\dagger_{-(\mathbf{k}'-\mathbf{k})}\right)\hat{c}^\dagger_{\mathbf{k}',\sigma}\hat{c}_{\mathbf{k},\sigma}.\right]
\end{aligned}
\tag{A.14}
$$

This completes our derivation of the e-ph coupling term in **k**-space. Now we can proceed with the new representation of the Hamiltonian

5. The results in Eqns. (A.11) and (A.12) have the same operators $\hat{c}^\dagger_{\mathbf{k},\sigma}\hat{c}_{\mathbf{k},\sigma}$ and can be grouped into a term that contains a dispersion like term $\epsilon_{\mathbf{k}}$ and the operators $\hat{c}^\dagger_{\mathbf{k},\sigma}\hat{c}_{\mathbf{k},\sigma}$.

The quantity $\epsilon_{\mathbf{k}}$ can be defined as follows:

$$\epsilon_{\mathbf{k}} = -2t \left(\cos(k_x a) + \cos(k_y a)\right) - \left(\mu - \frac{\alpha^2}{K}\right).$$

(A.15)

Note that in most computational applications, such as the Migdal-Eliashberg theory, we take the lattice spacing $a = 1$.

With the expressions above we can represent the original Hamiltonian A.1 in momentum space

$$\hat{H} = \sum_{\mathbf{k},\sigma} \epsilon_{\mathbf{k}} \hat{c}^{\dagger}_{\mathbf{k},\sigma} \hat{c}_{\mathbf{k},\sigma} + \Omega \sum_{\mathbf{k}} \left(\hat{a}^{\dagger}_{\mathbf{k}} \hat{a}_{\mathbf{k}} + \frac{\hat{\mathbb{I}}}{2}\right) - \frac{\alpha}{\sqrt{2N_s M\Omega}} \sum_{\mathbf{k},\mathbf{k}',\sigma} \left(\hat{a}_{\mathbf{k}'-\mathbf{k}} + \hat{a}^{\dagger}_{-(\mathbf{k}'-\mathbf{k})}\right) \hat{c}^{\dagger}_{\mathbf{k}',\sigma} \hat{c}_{\mathbf{k},\sigma}$$

(A.16)

B Details and background for DQMC

In this section, we present a fairly comprehensive and detailed account of the algorithmic details and derivations of DQMC. The notation and discussion is based heavily on the paper by S.R. White *et al* listed under Ref. [102], while further details were taken from many of the invaluable resources (papers, dissertations, etc.) available on Fakher Assaad's webpage (Universität Würzburg). Of the latter references, I can attribute most of this citation to Ref.[104]. The details about the algorithm and its scaling that appear in later subsections were based on Prof. Johnston's (my Ph.D. advisor) dissertation document[292]. I have made a considerable effort to compose many of the derivations to my own standards and would greatly appreciate notification of any typos or mistakes noticed by the reader.

B.1 The Hubbard Model

Working in the grand-canonical ensemble, the expectation value of a physical observable, $\hat{O}$, is given by

$$\langle \hat{O} \rangle = \frac{\text{Tr}\left[\text{e}^{-\beta(\hat{H}-\mu\hat{N})}\hat{O}\right]}{\text{Tr}\left[\text{e}^{-\beta(\hat{H}-\mu\hat{N})}\right]}, \tag{B.1}$$

where $\beta \equiv 1/k_B T \rightarrow 1/T$ where $k_B = 1$ in natural units. The expression in the denominator represents the partition function $\mathcal{Z} \equiv \text{Tr}\left[\text{e}^{-\beta(\hat{H}-\mu\hat{N})}\right]$ in the grand canonical ensemble, and we should note that for the rest of this section we will assume that the $-\mu\hat{N}$ is absorbed into $\hat{H}$.

To better facilitate the discussion on the DQMC formalism, we will work with the singleband Hubbard-Hamiltonian as it appears in Ref.[102]:

$$\hat{H} = -t \sum_{\langle i,j \rangle,\sigma} \left(\hat{c}_{i\sigma}^{\dagger}\hat{c}_{j\sigma} + \hat{c}_{j\sigma}^{\dagger}\hat{c}_{i\sigma}\right) + U \sum_i \left(\hat{n}_{i\uparrow} - \frac{1}{2}\right)\left(\hat{n}_{i\downarrow} - \frac{1}{2}\right) - \mu \sum_i \left(\hat{n}_{i\uparrow} + \hat{n}_{i\downarrow}\right). \tag{B.2}$$

Here, we have that $\hat{c}_{i\sigma}^{\dagger}$ and $\hat{c}_{i\sigma}$ are the creation and annihilation operators for electrons on site i, with a z component of spin σ equal to $\uparrow$ or $\downarrow$. The sum notation $\langle i,j \rangle$ restricts i and j to nearest neighbor lattice sites, $-t$ is the hopping matrix element, μ is the chemical

potential, and U is the same-site Coulomb interaction energy (with $U > 0$ for repulsion). The occupation number operator $\hat{n}_{i\sigma} = \hat{c}_{i\sigma}^{\dagger}\hat{c}_{i\sigma}$ has the following useful relations:

$$\hat{n}_{i\sigma}\left|0\right\rangle = 0 \tag{B.3}$$

where $\left|0\right\rangle$ is the vacuum state with no particles,

$$\hat{n}_{i\sigma}\left|n_{1\uparrow}, n_{1\downarrow}, ..., n_{i\uparrow}, n_{i\downarrow}, ..., n_{N\uparrow}, n_{N\downarrow}\right\rangle = \begin{cases} n_{i\uparrow}\left|n_{1\uparrow}, n_{1\downarrow}, ..., n_{i\uparrow}, n_{i\downarrow}, ..., n_{N\uparrow}, n_{N\downarrow}\right\rangle & \text{for } \sigma = \uparrow \\ n_{i\downarrow}\left|n_{1\uparrow}, n_{1\downarrow}, ..., n_{i\uparrow}, n_{i\downarrow}, ..., n_{N\uparrow}, n_{N\downarrow}\right\rangle & \text{for } \sigma = \downarrow \end{cases} \tag{B.4}$$

where $n_{i\sigma}$ is the number of electrons on site i with spin σ, and

$$[\hat{n}_{i\sigma}, \hat{n}_{j\sigma'}] = 0 . \tag{B.5}$$

B.2 Suzuki-Trotter Decomposition

Referring again to our Hamiltonian Eqn. (B.2), we can break the expression into two distinct pieces,

$$\hat{H} = \hat{K} + \hat{V} , \tag{B.6}$$

where $\hat{K}$ corresponds to kinetic energy terms and the $\hat{V}$ corresponds to interaction terms. Explicitly, $\hat{K}$ and $\hat{V}$ are given by

$$\hat{K} = -t \sum_{\langle i,j\rangle,\sigma} \left(\hat{c}_{i\sigma}^{\dagger}\hat{c}_{j\sigma} + \hat{c}_{j\sigma}^{\dagger}\hat{c}_{i\sigma}\right) - \mu \sum_{i} \left(\hat{n}_{i\uparrow} + \hat{n}_{i\downarrow}\right) , \tag{B.7}$$

and

$$\hat{V} = U \sum_{i} \left(\hat{n}_{i\uparrow} - \frac{1}{2}\right)\left(\hat{n}_{i\downarrow} - \frac{1}{2}\right) , \tag{B.8}$$

respectively. Using the Wick rotation, one can treat β in the same way one would treat $it/\hbar$ in the path integral approach by partitioning the time interval into discrete "time slices". The difference here is that we are not dealing with real-time slices, but rather, "imaginary time slices" arising in the finite-temperature formalism. Various substitutions will be made

to reflect the algorithmic structure of DQMC. First, we define $\tau = it$ and set $\hbar = 1$ such that $\beta = \tau$. The imaginary time τ is generally defined on the continuous interval $\tau \in [0, \beta]$, but we will discretize this interval into L steps of size $\Delta\tau = \beta/L$. Therefore, $\beta = \Delta\tau L$ and our partition function can be written as

$$\mathcal{Z} = \mathrm{Tr}\left[\mathrm{e}^{-\Delta\tau L \hat{H}}\right],\tag{B.9}$$

which can be rewritten again using Eqn. (B.6) as

$$\mathcal{Z} = \mathrm{Tr}\left[\left(\mathrm{e}^{-\Delta\tau(\hat{K}+\hat{V})}\right)^{L}\right].\tag{B.10}$$

We can use the Suzuki-Trotter decomposition (see Refs. [293, 294]) of the exponential product to simplify the expression in the trace:

$$
\begin{aligned}
\mathrm{e}^{-\Delta\tau(\hat{K}+\hat{V})} &= \mathrm{e}^{-\Delta\tau\hat{K}}\mathrm{e}^{-\Delta\tau\hat{V}}\mathrm{e}^{-\frac{1}{2}(\Delta\tau)^2\left[\hat{K},\hat{V}\right]} \\
&= \mathrm{e}^{-\Delta\tau\hat{K}}\mathrm{e}^{-\Delta\tau\hat{V}}\left[\hat{\mathbb{1}} - \frac{1}{2}(\Delta\tau)^2\left[\hat{K},\hat{V}\right] + \mathcal{O}\left((\Delta\tau)^4\right)\right] \\
&\approx \mathrm{e}^{-\Delta\tau\hat{K}}\mathrm{e}^{-\Delta\tau\hat{V}}.
\end{aligned}\tag{B.11}
$$

Here, we neglect terms that account for the commutation of $\hat{K}$ and $\hat{V}$ as they tend to be of $\sim \mathcal{O}(1)$, and their pre-factor $\frac{1}{2}(\Delta\tau)^2$ is relatively small [2]. Thus, we find that DQMC uses an approximation that introduces systematic errors of $\mathcal{O}\left((\Delta\tau)^2\right)$, and since we specify the value of $\Delta\tau$ at the beginning of simulations, we can tune the corrections to be small. Updating the trace to its new form, we have

$$\mathcal{Z} = \mathrm{Tr}\left[\left(\mathrm{e}^{-\Delta\tau\hat{K}}\mathrm{e}^{-\Delta\tau\hat{V}}\right)^{L}\right],\tag{B.12}$$

where we have split the exponential into two distinct pieces.

---

[2]It is small because $\Delta\tau$ is a tunable parameter in the algorithm which we can choose to be small. For this approximation to be effective, it usually suffices to use $\Delta\tau \sim \mathcal{O}\left(10^{-1}\right)$ since going much smaller will increase computation time.

B.3 Discrete Hubbard-Stratonovich Transformation

Many problems that use DQMC have Hamiltonians with interaction terms that are not bilinear in creation and annihilation operators $\hat{c}^\dagger$ and $\hat{c}$, and the interactions are commonly on the order of the nearest neighbor hopping integral t (i.e. $V \sim \mathcal{O}(t)$), ruling out the efficacy of perturbative expansions. For two-particle interactions such as the same-site Coulomb repulsion U term $\hat{H}_{\text{e-e}} = \sum_j \hat{c}^\dagger_{j,\uparrow} \hat{c}_{j,\uparrow} \hat{c}^\dagger_{j,\downarrow} \hat{c}_{j,\downarrow}$ in our Hubbard model example, the fermion operators appear in a quartic rather than quadratic form. This quartic form makes manipulations with the interaction terms rather challenging to work with since we cannot group them with the bilinear terms. One way to proceed is to parameterize interaction terms with bosonic auxiliary fields that possess the same eigenvalues as seen by the trace. This procedure is known as Hirsch's discrete Hubbard-Stratonovich transformation (DHST) and is outlined in Ref. [295].

The term we wish to simplify is $\mathrm{e}^{-\Delta\tau\hat{V}}$. The potential $\hat{V}$ defined in Eqn. (B.8) will yield products of two $\hat{n}$ operators, thereby yielding terms quartic in fermion creation and annihilation operators. Let us consider the term explicitly

$$\mathrm{e}^{-\Delta\tau U \sum_i \left(\hat{n}_{i\uparrow}-\frac{1}{2}\right)\left(\hat{n}_{i\downarrow}-\frac{1}{2}\right)}, \tag{B.13}$$

where the product the sum can be expanded as

$$\left(\hat{n}_{i\uparrow} - \frac{1}{2}\right)\left(\hat{n}_{i\downarrow} - \frac{1}{2}\right) = \hat{n}_{i\uparrow}\hat{n}_{i\downarrow} - \frac{1}{2}\left(\hat{n}_{i\uparrow} + \hat{n}_{i\uparrow}\right) - \frac{1}{4}. \tag{B.14}$$

We can put this into Eq.(B.13) and obtain

$$\mathrm{e}^{-\Delta\tau U \sum_i \left(\hat{n}_{i\uparrow}\hat{n}_{i\downarrow}-\frac{1}{2}\left(\hat{n}_{i\uparrow}+\hat{n}_{i\uparrow}\right)-\frac{1}{4}\right)}, \tag{B.15}$$

which shows the problematic term $\hat{n}_{i\uparrow}\hat{n}_{i\downarrow}$ that is quartic in the fermion operators. One could ask: what are all the possible values that the product $\left(\hat{n}_{i\uparrow} - \frac{1}{2}\right)\left(\hat{n}_{i\downarrow} - \frac{1}{2}\right)$ can take when projected out of an eigenstate? That question is readily answered for fermions since the eigenvalues of the number operators can only take the values of 0 or 1.

Table B.1: Possible eigenvalues for fermion number operators in the occupation representation.

$\hat{n}_{i\uparrow}$	$\hat{n}_{i\downarrow}$	$\left(\hat{n}_{i\uparrow} - \frac{1}{2}\right)\left(\hat{n}_{i\downarrow} - \frac{1}{2}\right)$
0	0	+1/4
0	1	- 1/4
1	0	- 1/4
1	1	+1/4

Given that the values are limited to $\pm 1/4$, we can now consider replacing the troublesome term, $\left(\hat{n}_{i\uparrow} - \frac{1}{2}\right)\left(\hat{n}_{i\downarrow} - \frac{1}{2}\right)$, with a term quadratic in fermion operators that arrives at the same results. We are clearly limited to expressions that are, at most, linear in the operators $\hat{n}_{i\uparrow}$ and $\hat{n}_{i\downarrow}$. Crafting a new expression that no longer contains the pesky quartic dependence on fermion operators and the constants must be done in a way that the preserves the possible eigenvalues in the previous interaction term. To better reflect the approach taken in Ref.[102], we use the DHST to find the following expression

$$\mathrm{e}^{-\Delta\tau U \sum_i \left(\hat{n}_{i\uparrow} - \frac{1}{2}\right)\left(\hat{n}_{i\downarrow} - \frac{1}{2}\right)} = \alpha \sum_{\{s_{i,l}\}=\pm 1} \mathrm{e}^{-\Delta\tau\lambda \sum_i s_{i,l}(\hat{n}_{i,\uparrow} - \hat{n}_{i,\downarrow})}, \tag{B.16}$$

where $\{s_{i,l}\} = s_{1,l}, s_{2,l}, \ldots, s_{N,l}$, and each field on site i and time-slice l, denoted $s_{i,l}$, can take only the values ± 1. We can show what values α and λ take upon substituting the possible eigenvalues of the number operators in a site-by-site term comparison:

For the cases where $\hat{n}_{i\uparrow} \to 0$, $\hat{n}_{i\downarrow} \to 0$ and $\hat{n}_{i\uparrow} \to 1$, $\hat{n}_{i\downarrow} \to 1$ one has

$$\mathrm{e}^{-\frac{1}{4}U\Delta\tau} = 2\alpha \quad \Rightarrow \quad \alpha = \frac{1}{2}\mathrm{e}^{-\frac{1}{4}U\Delta\tau}, \tag{B.17}$$

and similarly for the cases where $\hat{n}_{i\uparrow} \to 0$, $\hat{n}_{i\downarrow} \to 1$ and $\hat{n}_{i\uparrow} \to 1$, $\hat{n}_{i\downarrow} \to 0$ one has

$$\mathrm{e}^{\frac{1}{4}U\Delta\tau} = \alpha \left[\mathrm{e}^{\Delta\tau\lambda} + \mathrm{e}^{-\Delta\tau\lambda}\right] \quad \Rightarrow \quad \mathrm{e}^{\frac{1}{4}U\Delta\tau}(2\alpha)^{-1} = \cosh(\Delta\tau\lambda). \tag{B.18}$$

Upon substituting the value attained for α we find the relation between λ, U, and $\Delta\tau$

$$\cosh(\Delta\tau\lambda) = \mathrm{e}^{\frac{1}{2}U\Delta\tau}. \tag{B.19}$$

Now that all the components of Eqn. (B.16) are defined, we can write the trace as

$$\mathcal{Z} = \text{Tr}\left[\left(e^{-\Delta\tau\hat{K}}e^{-\Delta\tau\hat{V}}\right)^L\right]$$

$$\mathcal{Z} = \text{Tr}\left[\left(\frac{1}{2}e^{-\frac{1}{4}U\Delta\tau}e^{\Delta\tau\left(t\sum_{\langle i,j\rangle,\sigma}\left(\hat{c}_{i\sigma}^\dagger\hat{c}_{j\sigma}+\hat{c}_{j\sigma}^\dagger\hat{c}_{i\sigma}\right)+\mu\sum_i\left(\hat{n}_{i\uparrow}+\hat{n}_{i\downarrow}\right)\right)}\sum_{\{s_{i,l}\}}e^{-\Delta\tau\lambda\sum_i s_{i,l}(\hat{n}_{i,\uparrow}-\hat{n}_{i,\downarrow})}\right)^L\right],$$

$$(\text{B.20})$$

which contains the expanded form of the kinetic energy operator.

B.4   Compacting the Partition Function

Notice that we can condense the chemical potential term as

$$\mu\sum_i\left(\hat{n}_{i\uparrow}+\hat{n}_{i\downarrow}\right) = \mu\sum_{i,\sigma}\hat{c}_{i\sigma}^\dagger\hat{c}_{i\sigma} \tag{B.21}$$

so that the kinetic energy can be expressed in a simple bilinear form

$$\hat{K} = t\sum_{\langle i,j\rangle,\sigma}\left(\hat{c}_{i\sigma}^\dagger\hat{c}_{j\sigma}+\hat{c}_{j\sigma}^\dagger\hat{c}_{i\sigma}\right)+\mu\sum_{i,\sigma}\hat{c}_{i\sigma}^\dagger\hat{c}_{i\sigma}$$

$$= \sum_{i,j,\sigma}\hat{c}_{i\sigma}^\dagger K_{i\sigma,j\sigma}\hat{c}_{j\sigma}, \tag{B.22}$$

where the matrix element[3] $K_{i\sigma,j\sigma} \equiv (\text{K})_{i\sigma,j\sigma}$ where K is an $N \times N$ matrix with N being the number of lattice sites:

$$\text{K} = \begin{bmatrix} \mu & t & 0 & 0 & \dots & t \\ t & \mu & t & 0 & \dots & 0 \\ 0 & t & \mu & t & \dots & 0 \\ 0 & 0 & t & \mu & \dots & \vdots \\ \vdots & \vdots & \vdots & \vdots & \ddots & t \\ t & 0 & 0 & \dots & t & \mu \end{bmatrix}. \tag{B.23}$$

---

[3]We need not specify the NN summation constraint on i and j since the matrix elements $K_{i\sigma,j\sigma}$ vanish for $i\sigma, j\sigma$ pairs that fall outside the relevancy of the original Hamiltonian.

The upper right and lower left appearances of the hopping t signify that we are using periodic boundary conditions.

We can put Eqn. (B.22) into the partition function to give us

$$\mathcal{Z} = \text{Tr}\left[\left(\frac{1}{2}e^{-\frac{1}{4}U\Delta\tau}e^{\Delta\tau\sum_{i,j,\sigma}\hat{c}_{i\sigma}^{\dagger}K_{i\sigma,j\sigma}\hat{c}_{j\sigma}}\sum_{\{s_{i,l}\}}e^{-\Delta\tau\lambda\sum_{i}s_{i,l}(\hat{n}_{i,\uparrow}-\hat{n}_{i,\downarrow})}\right)^{L}\right],\qquad\text{(B.24)}$$

which can be expressed equivalently [4] as

$$\mathcal{Z} = \frac{1}{2^{L}}e^{-\frac{1}{4}\beta U}\text{Tr}\left[\left(e^{\Delta\tau\sum_{i,j,\sigma}\hat{c}_{i\sigma}^{\dagger}K_{i\sigma,j\sigma}\hat{c}_{j\sigma}}\sum_{\{s_{i,L}\}}e^{-\Delta\tau\lambda\sum_{i}s_{i,L}(\hat{n}_{i,\uparrow}-\hat{n}_{i,\downarrow})}\right)\right.$$
$$\left.\ldots\left(e^{\Delta\tau\sum_{i,j,\sigma}\hat{c}_{i\sigma}^{\dagger}K_{i\sigma,j\sigma}\hat{c}_{j\sigma}}\sum_{\{s_{i,1}\}}e^{-\Delta\tau\lambda\sum_{i}s_{i,1}(\hat{n}_{i,\uparrow}-\hat{n}_{i,\downarrow})}\right)\right].\qquad\text{(B.25)}$$

Integrating out the Fermion DOF

In Eqn. (B.25) it is implied that there are L (equivalent) parenthesized terms in the trace which are multiplied in succession. Handling the evaluation of the trace over the L terms is rather complicated procedure if one wants to be rigorous. We will proceed with the intention of showing the main ideas and not a rigorous proof[5]. Let us begin by introducing slightly more compact notation:

$$e^{\Delta\tau\sum_{\sigma}\hat{c}_{\sigma}^{\dagger}K^{\sigma}\hat{c}_{\sigma}} \equiv e^{\Delta\tau\sum_{i,j,\sigma}\hat{c}_{i\sigma}^{\dagger}K_{i\sigma,j\sigma}\hat{c}_{j\sigma}},\qquad\text{(B.26)}$$

---

[4]This is trick related to the path integral discretization of a time interval into L time-slices. The notation $\text{Tr}\left[(f(l))^{L}\right]$ implies $\text{Tr}\left[\hat{T}_{\tau}\prod_{l=1}^{L}f(l)\right] = \text{Tr}\left[f(L)f(L-1)\ldots f(1)\right]$ where $\hat{T}_{\tau}$ time orders the product from right to left. Normally f depends on τ explicitly, but in our problem the imaginary time τ is given by $\tau_{l} = l\Delta\tau$, and thus we show l dependence instead.

[5]See Appendix FIX

where $\hat{c}_\sigma^\dagger = [\hat{c}_{1,\sigma}^\dagger, \hat{c}_{2,\sigma}^\dagger, \ldots, \hat{c}_{n,\sigma}^\dagger]$. For the potential energy term [6] we write

$$\sum_{\{s_{i,l}\}} e^{\Delta\tau \sum_\sigma \hat{c}_\sigma^\dagger \tilde{V}^\sigma(s_{i,l}) \hat{c}_\sigma} \equiv \sum_{\{s_{i,l}\}} e^{-\Delta\tau\lambda \sum_i s_{i,l}(\hat{n}_{i,\uparrow} - \hat{n}_{i,\downarrow})} . \tag{B.27}$$

Hence, the partition function can be expressed as

$$\mathcal{Z} = \frac{1}{2^L} e^{-\frac{1}{4}\beta U} \mathrm{Tr}\left[\left(e^{\Delta\tau \sum_\sigma \hat{c}_\sigma^\dagger K^\sigma \hat{c}_\sigma} \sum_{\{s_{i,L}\}} e^{\Delta\tau \sum_\sigma \hat{c}_\sigma^\dagger \tilde{V}^\sigma(s_{i,L})\hat{c}_\sigma}\right) \cdots \left(e^{\Delta\tau \sum_\sigma \hat{c}_\sigma^\dagger K^\sigma \hat{c}_\sigma} \sum_{\{s_{i,1}\}} e^{\Delta\tau \sum_\sigma \hat{c}_\sigma^\dagger \tilde{V}^\sigma(s_{i,1})\hat{c}_\sigma}\right)\right] .$$
$$\tag{B.28}$$

The exponential operators in the terms of the trace have a bilinear form, and as such, the trace over operators can be replaced with determinants over the corresponding matrices.

Although we could proceed using the trace-to-determinant identity, it is common to separate the spin components of the exponential terms. This procedure can be done without a commutation penalty since we would be commuting terms like $\hat{c}_{i\sigma}^\dagger \hat{c}_{j\sigma}$ with $\hat{c}_{m\sigma'}^\dagger \hat{c}_{m\sigma'}$, which would yield 0 due to $\sigma \neq \sigma'$ terms we are commuting obey Bose-commutation relations and never correspond to the same set of quantum numbers (hence their commutators=0). We proceed as follows:

$$\mathrm{Tr}\left[\left(e^{\Delta\tau \sum_\sigma \hat{c}_\sigma^\dagger K^\sigma \hat{c}_\sigma} \sum_{\{s_{i,L}\}} e^{\Delta\tau \sum_\sigma \hat{c}_\sigma^\dagger \tilde{V}^\sigma(s_{i,L})\hat{c}_\sigma}\right) \cdots \left(e^{\Delta\tau \sum_\sigma \hat{c}_\sigma^\dagger K^\sigma \hat{c}_\sigma} \sum_{\{s_{i,1}\}} e^{\Delta\tau \sum_\sigma \hat{c}_\sigma^\dagger \tilde{V}^\sigma(s_{i,1})\hat{c}_\sigma}\right)\right]$$

$$= \mathrm{Tr}\left[\sum_{\{s_{i,l}\}} \prod_\sigma \left(e^{\Delta\tau \hat{c}_\sigma^\dagger K^\sigma \hat{c}_\sigma} e^{\Delta\tau \hat{c}_\sigma^\dagger \tilde{V}^\sigma(s_{i,L})\hat{c}_\sigma}\right) \cdots \left(e^{\Delta\tau \hat{c}_\sigma^\dagger K^\sigma \hat{c}_\sigma} e^{\Delta\tau \hat{c}_\sigma^\dagger \tilde{V}^\sigma(s_{i,1})\hat{c}_\sigma}\right)\right]$$

$$= \sum_{\{s_{i,l}\}} \mathrm{Tr}\left[\hat{B}_s^\uparrow(\beta, 0) \hat{B}_s^\downarrow(\beta, 0)\right] \tag{B.29}$$

---

[6]The intermediate steps look like

$$e^{-\Delta\tau\lambda \sum_i s_{i,l}(\hat{n}_{i,\uparrow} - \hat{n}_{i,\downarrow})} = e^{\Delta\tau \sum_{i,j,\sigma} \hat{c}_{i\sigma}^\dagger \tilde{V}_{i\sigma,j\sigma}(s_{i,l})\hat{c}_{j\sigma}}$$

where the minus sign has be absorbed into the matrix elements $\tilde{V}_{i\sigma,j\sigma}(s_{i,l})$.

where we have made a substitution

$$\hat{B}_s^\sigma(\beta,0) = \left(e^{\Delta\tau\hat{c}_\sigma^\dagger K^\sigma\hat{c}_\sigma}e^{\Delta\tau\hat{c}_\sigma^\dagger \tilde{V}^\sigma(s_{i,L})\hat{c}_\sigma}\right)\cdots\left(e^{\Delta\tau\hat{c}_\sigma^\dagger K^\sigma\hat{c}_\sigma}e^{\Delta\tau\hat{c}_\sigma^\dagger \tilde{V}^\sigma(s_{i,1})\hat{c}_\sigma}\right)$$

$$= \prod_{l=L}^{1} e^{\Delta\tau\hat{c}_\sigma^\dagger K^\sigma\hat{c}_\sigma}e^{\Delta\tau\hat{c}_\sigma^\dagger \tilde{V}^\sigma(s_{i,l})\hat{c}_\sigma}.$$

We can think of $\hat{B}_s^\sigma(\beta,0)$ as a time-evolution operator that incrementally evolves the system from $\tau = 0$ to $\tau = \beta$ in discrete steps of $\Delta\tau$.

The trace could be expanded in the occupation number basis states $|\{n_{i,\uparrow}\},\{n_{i,\downarrow}\}\rangle$:

$$\text{Tr}\left[\hat{B}_s^\uparrow(\beta,0)\hat{B}_s^\downarrow(\beta,0)\right] = \sum_{\{n_{i,\uparrow}\},\{n_{i,\downarrow}\}} \langle\{n_{i,\uparrow}\},\{n_{i,\downarrow}\}|\hat{B}_s^\uparrow(\beta,0)\hat{B}_s^\downarrow(\beta,0)|\{n_{i,\uparrow}\},\{n_{i,\downarrow}\}\rangle$$

$$= \sum_{\{n_{i,\uparrow}\}} \langle\{n_{i,\uparrow}\}|\hat{B}_s^\uparrow(\beta,0)|\{n_{i,\uparrow}\}\rangle \sum_{\{n_{i,\downarrow}\}} \langle\{n_{i,\downarrow}\}|\hat{B}_s^\downarrow(\beta,0)|\{n_{i,\downarrow}\}\rangle$$

$$= \text{Tr}\left[\hat{B}_s^\uparrow(\beta,0)\right]\text{Tr}\left[\hat{B}_s^\downarrow(\beta,0)\right] \tag{B.30}$$

which is a result related to the identity $\text{Tr}\left[\hat{A}\otimes\hat{B}\right] = \text{Tr}\left[\hat{A}\right]\text{Tr}\left[\hat{B}\right]$ where $\otimes$ is a Kronecker product (a special case of the tensor product). With the last equation we are ready to employ an important identity mentioned previously:

$$\text{Tr}\left[\hat{B}_{s,L}^\sigma\ldots\hat{B}_{s,1}^\sigma\right] = \det\left[\mathbb{1} + B_{s,L}^\sigma\ldots B_{s,1}^\sigma\right], \tag{B.31}$$

wherein our problem suggests that the following definitions must be true

$$\hat{B}_{s,l}^\sigma \equiv e^{\Delta\tau\hat{c}_\sigma^\dagger K^\sigma\hat{c}_\sigma}e^{\Delta\tau\hat{c}_\sigma^\dagger \tilde{V}^\sigma(s_{i,l})\hat{c}_\sigma} \tag{B.32}$$

and

$$B_{s,l}^\sigma \equiv e^{\Delta\tau(-1)^\sigma\lambda v(l)}e^{\Delta\tau K^\sigma}. \tag{B.33}$$

where $v_{i,j}(l) = \delta_{i,j}s_{i,l}$ is the matrix element of the diagonal matrix $v(l)$, and $(-1)^\sigma$ is equal to -1 for $\sigma =\uparrow \implies 1$ or -1 for $\sigma =\downarrow \implies -1$. We are now in a position to put the results

182

seen in Eqns. (B.28)-(B.33) together to find the partition function $\mathcal{Z}$

$$\mathcal{Z} = \Lambda \sum_{\{s_{i,l}\}} \det\left(\mathrm{M}_s^\uparrow\right) \det\left(\mathrm{M}_s^\downarrow\right), \tag{B.34}$$

whereby we have again compacted the equation with substitutions given below as

$$\Lambda = \frac{1}{2^L} \mathrm{e}^{-\frac{1}{4}\beta U}, \tag{B.35}$$

and

$$\mathrm{M}_s^\sigma = \mathbb{1} + \mathrm{B}_{s,L}^\sigma \ldots \mathrm{B}_{s,1}^\sigma. \tag{B.36}$$

We should emphasize that the DHST for this Hamiltonian gave us Hubbard-Stratonovich fields $s_{i,l}$ that can only take the values $+1$ or -1, but it is possible to use this transformation on other interactions that yield continuous fields. Note also that we can write $\hat{B}_s^\sigma(\beta, 0)$ and its matrix counterpart $\mathrm{B}_s^\sigma(\beta, 0)$, in terms of the $\hat{B}_{s,l}^\sigma$ and $\mathrm{B}_{s,l}^\sigma$ quantities

$$\hat{B}_s^\sigma(\beta, 0) \equiv \prod_{l=L}^{1} \hat{B}_{s,l}^\sigma, \tag{B.37}$$

and

$$\mathrm{B}_s^\sigma(\beta, 0) \equiv \prod_{l=L}^{1} \mathrm{B}_{s,l}^\sigma. \tag{B.38}$$

B.5   Expectation Values

The form of the partition function we have obtained required some rather important steps that can be recycled when evaluating the expectation value of observables, which was the motivation of all of the discussion thus far. For some "well behaved" observable $\hat{O}$ the expectation value can be evaluated to an accuracy tuned by errors from the Trotter decomposition

$$\langle \hat{O} \rangle = \frac{\mathrm{Tr}\left[\mathrm{e}^{-\beta(\hat{H}-\mu\hat{N})}\hat{O}\right]}{\mathrm{Tr}\left[\mathrm{e}^{-\beta(\hat{H}-\mu\hat{N})}\right]} = \sum_{\{s_{i,l}\}} p_s \langle \hat{O} \rangle_s + \mathcal{O}(\Delta\tau^2), \tag{B.39}$$

where p_s is

$$p_s = \frac{\det(\mathbb{1} + \mathrm{B}^{\sigma}_s(\beta, 0))}{\sum_{\{s_{i,l}\}} \det(\mathbb{1} + \mathrm{B}^{\sigma}_s(\beta, 0))}, \tag{B.40}$$

and

$$\langle \hat{O} \rangle_s = \frac{\mathrm{Tr}\left[\hat{B}^{\sigma}_s(\beta, \tau)\hat{O}\hat{B}^{\sigma}_s(\tau, 0)\right]}{\mathrm{Tr}\left[\hat{B}^{\sigma}_s(\beta, 0)\right]}. \tag{B.41}$$

If we assume the operator $\hat{O}$ can be written as $\hat{O} = \hat{c}^{\dagger}O\hat{c}$, then the calculation of Eqn. (B.41) can be evaluated as follows:

$$\langle \hat{O} \rangle_s = \frac{\mathrm{Tr}\left[\hat{B}^{\sigma}_s(\beta, \tau)\hat{O}\hat{B}^{\sigma}_s(\tau, 0)\right]}{\mathrm{Tr}\left[\hat{B}^{\sigma}_s(\beta, 0)\right]}$$

$$= \frac{\partial}{\partial \eta} \ln\left(\mathrm{Tr}\left[\hat{B}^{\sigma}_s(\beta, \tau)\mathrm{e}^{\eta\hat{O}}\hat{B}^{\sigma}_s(\tau, 0)\right]\right)\bigg|_{\eta=0}$$

$$= \frac{\partial}{\partial \eta} \ln\left(\det\left[\mathbb{1} + \mathrm{B}^{\sigma}_s(\beta, \tau)\mathrm{e}^{\eta O}\mathrm{B}^{\sigma}_s(\tau, 0)\right]\right)\bigg|_{\eta=0}$$

Use the identity : $\ln(\det[A]) = \mathrm{Tr}[\ln(A)]$

$$= \frac{\partial}{\partial \eta} \mathrm{Tr}\left[\ln\left(\mathbb{1} + \mathrm{B}^{\sigma}_s(\beta, \tau)\mathrm{e}^{\eta O}\mathrm{B}^{\sigma}_s(\tau, 0)\right)\right]\bigg|_{\eta=0}$$

$$= \mathrm{Tr}\left[\frac{\partial}{\partial \eta} \ln\left(\mathbb{1} + \mathrm{B}^{\sigma}_s(\beta, \tau)\mathrm{e}^{\eta O}\mathrm{B}^{\sigma}_s(\tau, 0)\right)\right]\bigg|_{\eta=0}$$

$$= \mathrm{Tr}\left[\frac{\mathrm{B}^{\sigma}_s(\beta, \tau)\mathrm{e}^{\eta O}O\mathrm{B}^{\sigma}_s(\tau, 0)}{\mathbb{1} + \mathrm{B}^{\sigma}_s(\beta, \tau)\mathrm{e}^{\eta O}\mathrm{B}^{\sigma}_s(\tau, 0)}\right]\bigg|_{\eta=0}$$

$$= \mathrm{Tr}\left[\frac{\mathrm{B}^{\sigma}_s(\beta, \tau)O\mathrm{B}^{\sigma}_s(\tau, 0)}{\mathbb{1} + \mathrm{B}^{\sigma}_s(\beta, 0)}\right]$$

$$= \mathrm{Tr}\left[\mathrm{B}^{\sigma}_s(\beta, \tau)O\mathrm{B}^{\sigma}_s(\tau, 0)(\mathbb{1} + \mathrm{B}^{\sigma}_s(\beta, 0))^{-1}\right]$$

$$= \mathrm{Tr}\left[\mathrm{B}^{\sigma}_s(\tau, 0)(\mathbb{1} + \mathrm{B}^{\sigma}_s(\beta, 0))^{-1}\mathrm{B}^{\sigma}_s(\beta, \tau)O\right] \text{ (Used cyclic property of trace)}$$

$$= \mathrm{Tr}\left[\frac{\mathbb{1} + \mathrm{B}^{\sigma}_s(\tau, 0)\mathrm{B}^{\sigma}_s(\beta, \tau)}{\mathbb{1} + \mathrm{B}^{\sigma}_s(\tau, 0)\mathrm{B}^{\sigma}_s(\beta, \tau)}\mathrm{B}^{\sigma}_s(\tau, 0)(\mathbb{1} + \mathrm{B}^{\sigma}_s(\beta, 0))^{-1}\mathrm{B}^{\sigma}_s(\beta, \tau)O\right]$$

$$= \mathrm{Tr}\left[\frac{\mathrm{B}^{\sigma}_s(\tau, 0) + \mathrm{B}^{\sigma}_s(\tau, 0)\mathrm{B}^{\sigma}_s(\beta, 0)}{\mathbb{1} + \mathrm{B}^{\sigma}_s(\tau, 0)\mathrm{B}^{\sigma}_s(\beta, \tau)}(\mathbb{1} + \mathrm{B}^{\sigma}_s(\beta, 0))^{-1}\mathrm{B}^{\sigma}_s(\beta, \tau)O\right]$$

$$= \mathrm{Tr}\left[\frac{\mathrm{B}^{\sigma}_s(\tau, 0)\mathrm{B}^{\sigma}_s(\beta, \tau)}{\mathbb{1} + \mathrm{B}^{\sigma}_s(\tau, 0)\mathrm{B}^{\sigma}_s(\beta, \tau)}O\right]$$

$$= \mathrm{Tr}\left[\left(\mathbb{1} - (\mathbb{1} + \mathrm{B}^{\sigma}_s(\tau, 0)\mathrm{B}^{\sigma}_s(\beta, \tau))^{-1}\right)O\right]. \tag{B.42}$$

If we adhere to a notation that commonly appears in the literature we can define new quantity $A_s^\sigma(l)$ which simplifies the split product of matrices

$$A_s^\sigma(l) \equiv B_s^\sigma(\tau, 0) B_s^\sigma(\beta, \tau) = B_{s,l}^\sigma \ldots B_{s,1}^\sigma B_{s,L}^\sigma \ldots B_{s,l+1}^\sigma \, , \qquad (B.43)$$

so that the Eqn. (B.42) becomes

$$\langle \hat{O} \rangle_s = \mathrm{Tr} \left[\left(\mathbb{1} - (\mathbb{1} + A_s^\sigma(l))^{-1} \right) O \right] \, . \qquad (B.44)$$

This expression along with the expression for p_s gives a way to evaluate the thermal expectation value for any observable $\langle \hat{O} \rangle$ in the DQMC formalism. In the next section we find practical expressions for the equal time Green's function as a demonstration of the expressions derived in this section.

B.6 Equal Time Single-Particle Green's Functions

Now we turn our attention to the equal time Matsubara Green's function $\mathcal{G}_{s,i,j}^\sigma(l)$ for a given HS field $s \equiv s_{i,l}$. This propagator describes a response of the single-particle electron system for the given field configuration at a time-slice l, which corresponds to an imaginary time [7] $\tau = \tau_l = l\Delta\tau$.

$$\mathcal{G}_{s,i,j}^\sigma(l) = - \langle \, \hat{T}_\tau \{ \hat{c}_{i,\sigma}(\tau) \hat{c}_{j,\sigma}^\dagger(\tau) \} \, \rangle_s \qquad (B.45)$$

Before evaluating this quantity explicitly, lets look at the full single-electron Green's function $\mathcal{G}_{i,j}^\sigma(l)$ for equal times $\tau = l\Delta\tau$ momentarily by expanding the operators in the Heisenberg representation and use the definition of the expectation value $\langle \cdots \rangle$ defined earlier. The conventional way to proceed is to attribute an infinitesimal imaginary time increment η to the argument one of the operators as to allow time-ordering of the $\hat{c}$ and $\hat{c}^\dagger$ operators and then taking the limit as $\eta \to 0^+$. Convention usually prescribes that for equal-times, the destruction operator appear to the right and therefore we attribute the infinitesimal to the

---

[7]The decision to promote the imaginary time slice index l to the argument for G is one of convention. Green's functions are usually written as functions of time t or imaginary time τ, but in this case the τ is replaced with its respective integer index l to better emphasize the algorithmic structure of DQMC. Discussing quantities in terms of time slice indices lends more to the actual algorithmic implementation.

creation operator that appears rightmost in the standard definition of the single-particle Green's function

$$
\begin{aligned}
\mathcal{G}_{i,j}^{\sigma}(l) &= -\langle\, \hat{T}_{\tau}\{\hat{c}_{i,\sigma}(\tau)\hat{c}_{j,\sigma}^{\dagger}(\tau)\} \,\rangle \\
&= -\lim_{\eta\to 0^{+}} \langle\, \hat{T}_{\tau}\{\hat{c}_{i,\sigma}(\tau)\hat{c}_{j,\sigma}^{\dagger}(\tau^{+})\} \,\rangle\,, \quad \text{where } \tau^{+} = \tau + \eta \\
&= -\lim_{\eta\to 0^{+}} \mathrm{Tr}\left[\hat{\rho}\,\hat{T}_{\tau}\{\hat{c}_{i,\sigma}(\tau)\hat{c}_{j,\sigma}^{\dagger}(\tau^{+})\}\right] \\
&= \lim_{\eta\to 0^{+}} \mathrm{Tr}\left[\hat{\rho}\,\hat{c}_{j,\sigma}^{\dagger}(\tau^{+})\hat{c}_{i,\sigma}(\tau)\right] \\
&= \mathrm{Tr}\left[e^{\beta(\hat{\Omega}-\hat{\mathsf{H}})}e^{\hat{\mathsf{H}}\tau}\hat{c}_{j,\sigma}^{\dagger}e^{-\hat{\mathsf{H}}\tau}e^{\hat{\mathsf{H}}\tau}\hat{c}_{i,\sigma}e^{-\hat{\mathsf{H}}\tau}\right] \\
&= \mathrm{Tr}\left[e^{\beta(\hat{\Omega}-\hat{\mathsf{H}})}e^{\hat{\mathsf{H}}\tau}\hat{c}_{j,\sigma}^{\dagger}\hat{c}_{i,\sigma}e^{-\hat{\mathsf{H}}\tau}\right] \\
&= \mathrm{Tr}\left[e^{\beta(\hat{\Omega}-\hat{\mathsf{H}})}\hat{c}_{j,\sigma}^{\dagger}\hat{c}_{i,\sigma}\right]\,, \quad \text{(Used cyclic property of trace)} \\
&= \langle\, \hat{c}_{j,\sigma}^{\dagger}\hat{c}_{i,\sigma} \,\rangle\,.
\end{aligned}
\tag{B.46}
$$

Here we used the invariance of the trace under cyclic permutation of operators and the fact that all the exponentials commute with each other to obtain Eqn. (B.46); the operators $\hat{\rho}$, $\hat{\mathsf{H}}$, and $\hat{\Omega}$ have been defined in the discussion around Eqns. (??) and (??). Note that the use of $\hat{\mathsf{H}} = \hat{H} - \mu\hat{N}$ corresponds to a general situation where the chemical potential terms are excluded from $\hat{H}$, however, in our Hamiltonian (Eqn. (B.2)) the chemical potential was included in $\hat{H}$ by definition, such that $\hat{\mathsf{H}} \equiv \hat{H}$.

Consider now that we choose the destruction operator to have the τ^{+} argument instead, the expectation value is:

$$
\begin{aligned}
\mathcal{G}_{i,j}^{\sigma}(l) &= -\langle\, \hat{T}_{\tau}\{\hat{c}_{i,\sigma}(\tau)\hat{c}_{j,\sigma}^{\dagger}(\tau)\} \,\rangle \\
&= -\lim_{\eta\to 0^{+}} \langle\, \hat{T}_{\tau}\{\hat{c}_{i,\sigma}(\tau^{+})\hat{c}_{j,\sigma}^{\dagger}(\tau)\} \,\rangle \\
&= -\langle\, \hat{c}_{i,\sigma}(\tau)\hat{c}_{j,\sigma}^{\dagger}(\tau) \,\rangle \\
&= -\langle\, \delta_{i,j}\hat{\mathbb{1}} - \hat{c}_{j,\sigma}^{\dagger}(\tau)\hat{c}_{i,\sigma}(\tau) \,\rangle \\
&= -\langle\, \delta_{i,j}\hat{\mathbb{1}} \,\rangle + \langle\, \hat{c}_{j,\sigma}^{\dagger}(\tau)\hat{c}_{i,\sigma}(\tau) \,\rangle \\
&= \langle\, \hat{c}_{j,\sigma}^{\dagger}\hat{c}_{i,\sigma} \,\rangle - \delta_{i,j}\,,
\end{aligned}
\tag{B.47}
$$

which is expected from the commutation relation $\langle\, [\hat{c}_{i,\sigma}, \hat{c}^{\dagger}_{j,\sigma}]\, \rangle = \delta_{i,j}$. To calculate the equal-time Green's function used in our DQMC algorithm, we will change our approach slightly. First, we will drop the minus sign from the definition of the Green's function, a decision which we must be consistent with moving forward. Second, we will start our problem with the unconventional time ordering from the last calculation. Lastly we will assume that our operator can be expressed as $\hat{O} = \hat{c}_{i,\sigma}\hat{c}^{\dagger}_{j,\sigma} = \delta_{i,j}\hat{\mathbb{1}} - \hat{c}^{\dagger}O^{j,i}\hat{c}$ where $O^{j,i}$ is a matrix with elements given by $O^{j,i}_{j',i'} = \delta_{j',j}\delta_{i',i}$. Using these changes, we can jump straight into the evaluation of Eqn. (B.45)

$$
\begin{aligned}
\mathcal{G}^{\sigma}_{s,i,j}(l) &= \langle\, \hat{c}_{i,\sigma}\hat{c}^{\dagger}_{j,\sigma}\, \rangle_s \\
&= \langle\, \delta_{i,j}\hat{\mathbb{1}} - \hat{c}^{\dagger}_{j,\sigma}\hat{c}_{i,\sigma}\, \rangle_s \\
&= \langle\, \delta_{i,j}\hat{\mathbb{1}}\, \rangle_s - \langle\, \hat{c}^{\dagger}O^{j,i}\hat{c}\, \rangle_s \\
&= \frac{\mathrm{Tr}\left[\hat{B}^{\sigma}_s(\beta,\tau)\delta_{i,j}\hat{\mathbb{1}}\hat{B}^{\sigma}_s(\tau,0)\right]}{\mathrm{Tr}\left[\hat{B}^{\sigma}_s(\beta,0)\right]} - \frac{\mathrm{Tr}\left[\hat{B}^{\sigma}_s(\beta,\tau)\hat{c}^{\dagger}O^{j,i}\hat{c}\hat{B}^{\sigma}_s(\tau,0)\right]}{\mathrm{Tr}\left[\hat{B}^{\sigma}_s(\beta,0)\right]} \\
&= \delta_{i,j}\mathbb{1} - \mathrm{Tr}\left[\left(\mathbb{1} - (\mathbb{1} + \mathrm{B}^{\sigma}_s(\tau,0)\mathrm{B}^{\sigma}_s(\beta,\tau))^{-1}\right)O^{j,i}\right] \\
&= (\mathbb{1} + \mathrm{B}^{\sigma}_s(\tau,0)\mathrm{B}^{\sigma}_s(\beta,\tau))^{-1}_{i,j}\,, \quad\quad\quad\quad\quad\quad\quad\quad\quad\quad\quad (B.48)
\end{aligned}
$$

where one should notice that the trace operation (by definition) limits the matrix elements included to those along the diagonal of matrix inside the trace. This result is what we set out to obtain and it is important enough to express again in a slightly more compact form

$$
\mathcal{G}^{\sigma}_{s,i,j}(l) = (\mathbb{1} + \mathrm{A}^{\sigma}_s(l))^{-1}_{i,j}\,. \quad\quad\quad\quad\quad\quad\quad\quad (B.49)
$$

The importance of this expression cannot be understated since it is essential to evaluate all the correlation functions we might be interested in, and as we will see, the unequal-time Green's functions can be written in terms of the equal-time functions.

B.7 Updating the Local HS Fields

The procedure for updating a local HS field variable $s_{i,l}$ is usually accomplished with standard approaches such as the heat bath or Metropolis algorithms, and within these approaches we

must examine the change in the fermion determinants when we have a spin flip $s_{i,l} \to -s_{i,l}$. This results in a change in $A_s^\sigma(l)$ denoted by

$$A_s^\sigma(l) \to A_{-s}^\sigma(l) = [\mathbb{1} + \Delta_s^\sigma(i,l)]A_s^\sigma(l) \tag{B.50}$$

where $\Delta_s^\sigma(i,l)$ is a matrix with only one nonzero element

$$\Delta_{s,j,k}^\pm(i,l) = \delta_{j,i}\delta_{k,i}(e^{\pm\Delta\tau\lambda s_{i,l}} - 1). \tag{B.51}$$

The probability for any particular field configuration $s_{i,l}$ denoted by p_s was given before by

$$p_s = \frac{\det(M_s^\sigma)}{\mathcal{Z}}. \tag{B.52}$$

In the Metropolis routine we calculate the probability of acceptance of the system going from one configuration $\mathscr{C}$ to another $\mathscr{C}'$ expressed simply by

$$acc(\mathscr{C} \to \mathscr{C}') = \min\left\{1, \frac{p(\mathscr{C}')}{p(\mathscr{C})}\right\}. \tag{B.53}$$

Therefore we must calculate a similar ratio, denoted R^σ of probabilities for this local spin-flip update

$$
\begin{aligned}
R^\sigma &= \frac{\det(M_{-s}^{\sigma'})}{\det(M_s^\sigma)} \\
&= \det(M_{-s}^{\sigma'})\det((M_s^\sigma)^{-1}) = \det((M_s^\sigma)^{-1})\det(M_{-s}^{\sigma'}) \\
&= \det((M_s^\sigma)^{-1}M_{-s}^{\sigma'}) \\
&= \det\left([\mathbb{1} + A_s^\sigma(l)]^{-1}[\mathbb{1} + A_{-s}^{\sigma'}(l)]\right) \\
&= \det\left([\mathbb{1} + A_s^\sigma(l)]^{-1}[\mathbb{1} + [\mathbb{1} + \Delta_s^\sigma(i,l)]A_s^\sigma(l)]\right) \\
&= \det\left(\underbrace{[\mathbb{1} + A_s^\sigma(l)]^{-1}[\mathbb{1} + A_s^\sigma(l)]}_{=\mathbb{1}} + \underbrace{[\mathbb{1} + A_s^\sigma(l)]^{-1}}_{=\mathcal{G}_s^\sigma(l)}\Delta_s^\sigma(i,l)A_s^\sigma(l)\right) \\
&= \det\left(\mathbb{1} + \mathcal{G}_s^\sigma(l)\Delta_s^\sigma(i,l)A_s^\sigma(l)\right) \tag{B.54}
\end{aligned}
$$

188

We can express this in another way by noticing that we can rewrite the argument inside the determinant as

$$
\begin{aligned}
\mathbb{1} + \mathcal{G}_s^\sigma(l)\Delta_s^\sigma(i,l)\mathrm{A}_s^\sigma(l) &= \mathbb{1} + \mathrm{A}_s^\sigma(l)^{-1}\mathrm{A}_s^\sigma(l)\mathcal{G}_s^\sigma(l)\Delta_s^\sigma(i,l)\mathrm{A}_s^\sigma(l) \\
&= \mathbb{1} + \mathrm{A}_s^\sigma(l)^{-1}\mathrm{A}_s^\sigma(l)[\mathbb{1} + \mathrm{A}_s^\sigma(l)]^{-1}\Delta_s^\sigma(i,l)\mathrm{A}_s^\sigma(l) \\
&= \mathbb{1} + \mathrm{A}_s^\sigma(l)^{-1}[\mathbb{1} - \mathcal{G}_s^\sigma(l)]\Delta_s^\sigma(i,l)\mathrm{A}_s^\sigma(l) \, .
\end{aligned}
\tag{B.55}
$$

Now we can use the following determinant identity for similarity transformations:

$$
\det\left(\lambda\mathbb{1} + \mathrm{S}^{-1}\mathrm{MS}\right) = \det\left(\lambda\mathbb{1} + \mathrm{M}\right) \, ,
\tag{B.56}
$$

where it is clear that our determinant has such a form with the A matrices serving as the S's in this case. Using this result and the definition we gave to the δ matrix in Eqn. (B.51), we can find a new form for R

$$
\begin{aligned}
R^\sigma &= \det\left(\mathbb{1} + [\mathbb{1} - \mathcal{G}_s^\sigma(l)]\Delta_s^\sigma(i,l)\right) \\
&= 1 + [1 - \mathcal{G}_{s,i,i}^\sigma(l)]\Delta_{s,i,i}^\sigma(i,l) \, .
\end{aligned}
\tag{B.57}
$$

The full ratio for accepting a proposed change is $R = R^\uparrow R^\downarrow$, and it can be calculated from the Green's function for the current configuration and imaginary time-slice.

If the change is rejected, the update scheme restarts with a new proposed change for the same system configuration. Otherwise the change is accepted and the Green's function updates accordingly $\mathcal{G}_s^\sigma(l) \rightarrow \mathcal{G}_{s'}^{\sigma'}(l)$. Computation of $\mathcal{G}_s^\sigma(l)$ by Eqn. (B.48) involves a multiplication sequence of L, $N \times N$ matrices, which has a costly computational scaling of LN^3. Employing a so-called "Sherman-Morrison" update scheme reduces the scaling cost to N^2 by exploiting the fact that only a single row and column of $G^\sigma(l)$ are affected by a single flip of $s_{i,l}$. The new Green's function after an update can be obtained from the previous one by noticing first that since

$$
[\mathcal{G}_s^\sigma(l)]^{-1} = (\mathbb{1} + \mathrm{A}_s^\sigma(l)) \, ,
\tag{B.58}
$$

then we must have that

$$[\mathcal{G}_{s'}^{\sigma'}(l)]^{-1} = (\mathbb{1} + [\mathbb{1} + \Delta_s^\sigma(l)]\mathrm{A}_s^\sigma(l)) \,, \tag{B.59}$$

where all of the quantities above are assumed to be matrices over site indices. Rewriting $\mathrm{A} = \mathcal{G}^{-1} - 1$ and temporarily dropping spin/field indices and time-slice arguments, we can substitute this into the expression for the updated Green's function

$$\begin{aligned}
[\mathcal{G}']^{-1} &= \mathbb{1} + [\mathbb{1} + \Delta][\mathcal{G}^{-1} - 1] \\
&= \mathbb{1} + \mathcal{G}^{-1} - \mathbb{1} + \Delta\mathcal{G}^{-1} - \Delta \\
&= [\mathbb{1} + \Delta]\mathcal{G}^{-1} - \Delta \,.
\end{aligned}$$

Solving for $\mathcal{G}'$ from this matrix equation yields

$$\mathcal{G}' = (\mathbb{1} + \Delta[1 - \mathcal{G}])^{-1}\mathcal{G} = \frac{\mathbb{1}}{\mathbb{1} + \Delta[\mathbb{1} - \mathcal{G}]}\mathcal{G} \tag{B.60}$$

which is essentially a rearranged version of Dyson's equation and contains a piece that can be rewritten according to the Woodbury-Sherman-Morrison formula

$$\frac{\mathbb{1}}{\mathrm{A} - \mathrm{BC}} = \frac{\mathbb{1}}{\mathrm{A}} + \frac{\mathbb{1}}{\mathrm{A}}\mathrm{B}\frac{\mathbb{1}}{\mathbb{1} - \mathrm{CA}^{-1}\mathrm{B}}\mathrm{C}\frac{\mathbb{1}}{\mathrm{A}} \,. \tag{B.61}$$

This formula can be obtained by an infinite geometric series

$$\frac{\mathbb{1}}{\mathrm{A} - \mathrm{BC}} = \frac{\mathbb{1}}{\mathrm{A}}\left(\mathbb{1} + \mathrm{BCA}^{-1} + \mathrm{BCA}^{-1}\mathrm{BCA}^{-1} + \ldots\right) \tag{B.62}$$

$$= \frac{\mathbb{1}}{\mathrm{A}} + \frac{\mathbb{1}}{\mathrm{A}}\mathrm{B}\left(\mathbb{1} + \mathrm{CA}^{-1}\mathrm{B} + \ldots\right)\mathrm{C}\frac{\mathbb{1}}{\mathrm{A}} \tag{B.63}$$

$$= \frac{\mathbb{1}}{\mathrm{A}} + \frac{\mathbb{1}}{\mathrm{A}}\mathrm{B}\frac{\mathbb{1}}{\mathbb{1} - \mathrm{CA}^{-1}\mathrm{B}}\mathrm{C}\frac{\mathbb{1}}{\mathrm{A}} \,. \tag{B.64}$$

In order to apply this formula above to the one we have obtained with the Green's functions, we need to specify a formality related to the matrix Δ. As we have stated before, Δ is matrix with only one nonzero element and it can be constructed using two rectangular matrices we denote Υ_1 and Υ_2 such that $\Delta = \Upsilon_1\Delta_s\Upsilon_2$, and where Δ_s is the small but nonzero HS field

dependent part of Δ. If we define

$$A = \mathbb{1}\,, \qquad B = -\Upsilon_1\,, \qquad \text{and} \qquad C = \Delta_s \Upsilon_2 (\mathbb{1} - \mathcal{G})\,, \tag{B.65}$$

then we can apply the formula to obtain

$$\mathcal{G}' = \mathcal{G} - \mathcal{G} \Upsilon_1 \frac{\mathbb{1}}{\mathbb{1} - \Delta_s \Upsilon_2 (\mathbb{1} - \mathcal{G}) \Upsilon_1} \Delta_s \Upsilon_2 (\mathbb{1} - \mathcal{G})\,. \tag{B.66}$$

Bringing back the full regalia of indices, we now summarize this result in the form that matches Ref.[102]

$$\mathcal{G}_{s'}^{\sigma'}(l) = \mathcal{G}_s^{\sigma}(l) - \frac{\mathcal{G}_s^{\sigma}(l) \Delta_s^{\sigma}(l)(\mathbb{1} - \mathcal{G}_s^{\sigma}(l))}{\mathbb{1} - \Delta_s^{\sigma}(l)(\mathbb{1} - \mathcal{G}_s^{\sigma}(l))}\,. \tag{B.67}$$

Thus we have shown that an update of the equal-time Green's function is a straight forward calculation that was simplified from a more complicated matrix-matrix multiplication scheme of cost LN^3 to one without matrix multiplication of computational cost N^2.

How do we proceed to the next time slice? Once the algorithm sweeps through all of the sites at time slice l and all proposed changes and updates have been made, we advance the propagator to the next time-slice by using the B-matrices. As mentioned before, these behave analogously to the standard time-evolution operator and thus we simply have to apply them to $\mathcal{G}_s^{\sigma}(l)$ in the usual way (i.e. $\hat{O}_{\mathrm{H}}(t) = \hat{U}^{\dagger}(t,0)\hat{O}_{\mathrm{S}}\hat{U}(t,0) = \hat{U}^{-1}(t,0)\hat{O}_{\mathrm{S}}\hat{U}(t,0)$)

$$\mathcal{G}_s^{\sigma}(l+1) = \mathrm{B}_{s,l+1}^{\sigma} \mathcal{G}_s^{\sigma}(l)(\mathrm{B}_{s,l+1}^{\sigma})^{-1}\,. \tag{B.68}$$

B.8   UDR Decomposition

Updating configurations on the same time slice across the lattice, as it turns out, is not significantly prone to numerical errors. On the other hand, advancing the equal-time Green's function to a subsequent time-slice according to Eqn. (B.68) does introduce numerical error. Therefore, one must calculate the matrices $\mathrm{A}_s^{\sigma}(l)$ to sufficient accuracy in order to preserve information about its small eigenvalues. The discrepancy between the largest and smallest eigenvalues in the non-interacting limit of the 2D Hubbard model ($U = 0$) is governed by the fact that the largest eigenvalues are as proportionally large as $\exp(+\beta\tilde{E})$ while the smallest

are proportional to $\exp(-\beta \tilde{E})$ where $\tilde{E} \sim 4t$. We are usually interested in performing simulations for large values of β and thus we must also segregate the contributions between large and small eigenvalues. Failing to do so would mean that the small eigenvalues are completely overshadowed by round-off errors.

The solutions to this problem are commonly framed as matrix factorization methods and a few different approaches exist amongst the variations of QMC. We will utilize the UDR decomposition procedure outlined in Ref.[102], keeping much of the discussion and notation. Let us define m as the number of matrices $\mathrm{B}^\sigma_{s,l}$ we can multiply without loss of numerical accuracy. Using the Gram-Schmidt orthogonalization procedure to write this product in the form

$$\begin{aligned} \mathrm{a}^\sigma_{1,s}(l) &= \mathrm{B}^\sigma_{s,l+m} \mathrm{B}^\sigma_{s,l+m-1} \cdots \mathrm{B}^\sigma_{s,l+1} \\ &= \mathrm{U}^\sigma_1 \mathrm{D}^\sigma_1 \mathrm{R}^\sigma_1 \end{aligned} \tag{B.69}$$

where U^σ_1 is an orthogonal matrix, D^σ_1 is a diagonal matrix, and R^σ_1 is a right triangular matrix with diagonal elements equal to unity. By construction, U^σ_1 is necessarily *well conditioned* [8]; theoretically, R^σ_1 need not be well conditioned , but it tends to be in practice. The large variations in the size of matrix elements appears in the diagonal matrix D^σ_1. We now form a second UDR form

$$\begin{aligned} \mathrm{a}^\sigma_{2,s}(l) &= \mathrm{B}^\sigma_{s,l+2m} \mathrm{B}^\sigma_{s,l+m-1} \cdots \mathrm{B}^\sigma_{s,l+1} \\ &= \mathrm{B}^\sigma_{s,l+2m} \mathrm{B}^\sigma_{s,l+2m-1} \cdots \mathrm{B}^\sigma_{s,l+m+1} \mathrm{U}^\sigma_1 \mathrm{D}^\sigma_1 \mathrm{R}^\sigma_1 \\ &= \mathrm{U}^\sigma_2 \mathrm{D}^\sigma_2 \mathrm{R}^\sigma_2 \,. \end{aligned} \tag{B.70}$$

The order of operations in Eqn. (B.70) is important and implies that one first multiplies U^σ_1 by $\mathrm{B}^\sigma_{s,l+2m} \mathrm{B}^\sigma_{s,l+2m-1} \cdots \mathrm{B}^\sigma_{s,l+m+1}$. It follows that we multiply it on the right by D^σ_1. This rescales the columns of the matrix and avoids incurring numerical instability in the next step, a UDR decomposition of the partial product we have so far. We then multiply teh

---

[8]A *well conditioned* matrix is generally characterized by a *condition number* C that obeys $\log(C) <$(precision of matrix entries). This number C is the ratio of the largest to smallest singular value in the *singular value decomposition* of the matrix. On the contrary, an *ill conditioned* matrix is one where $\log(C) \gtrsim$(precision of matrix entries).

resulting triangular matrix on the right by R_1^σ to obtain the last line, $U_2^\sigma D_2^\sigma R_2^\sigma$. Repeating this process L/m times gives us

$$A_s^\sigma(l) = a_{L/m,s}^\sigma(l) = U_{L/m}^\sigma D_{L/m}^\sigma R_{L/m}^\sigma. \tag{B.71}$$

Recall that the equal time Green's function is related to $A_s^\sigma(l)$ via $(\mathcal{G}_s^\sigma)^{-1}(l) = \mathbb{1} + A_s^\sigma(l)$. Since we must add the unit matrix $\mathbb{1}$ to $A_s^\sigma(l)$, we must be careful to isolate the diagonal matrix $D_{L/m}^\sigma$, whose elements vary greatly in size. We will replace the unit matrix by $\mathbb{1} = U_{L/m}^\sigma (U_{L/m}^\sigma)^{-1}(R_{L/m}^\sigma)^{-1}R_{L/m}^\sigma$ and find

$$
\begin{aligned}
(\mathcal{G}_s^\sigma)^{-1}(l) &= \mathbb{1} + A_s^\sigma(l) \\
&= U_{L/m}^\sigma \left((U_{L/m}^\sigma)^{-1}(R_{L/m}^\sigma)^{-1} + D_{L/m}^\sigma \right) R_{L/m}^\sigma \\
&= U_{L/m}^\sigma \left(\tilde{U}^\sigma \tilde{D}^\sigma \tilde{R}^\sigma \right) R_{L/m}^\sigma \\
&= U^\sigma D^\sigma R^\sigma.
\end{aligned}
\tag{B.72}
$$

The second to last step contains a numerically stable UDR decomposition because we have separated the large and small matrix elements.

B.9 Unequal Time Green's Functions

In order to measure dynamic quantities in DQMC we need to obtain the full time-dependent Green's function $\mathcal{G}(\tau, \tau') = \mathcal{G}(\tau - \tau')$. As we have seen, time evolution is governed by the matrices $B_{s,l}^\sigma$, however we have only discussed how to evolve the equal time Green's functions. These equal time propagators can be thought of as diagonal elements of some matrix G with the off diagonal elements representing the unequal time propagators throughout the discretized space-time (under Wick rotation).

$$
G =
\begin{bmatrix}
\mathcal{G}(\tau_1, \tau_1) & \mathcal{G}(\tau_1, \tau_2) & \cdots & \mathcal{G}(\tau_1, \tau_L) \\
\mathcal{G}(\tau_2, \tau_1) & \mathcal{G}(\tau_2, \tau_2) & \cdots & \mathcal{G}(\tau_2, \tau_L) \\
\vdots & \vdots & \cdots & \vdots \\
\mathcal{G}(\tau_L, \tau_1) & \mathcal{G}(\tau_L, \tau_2) & \cdots & \mathcal{G}(\tau_L, \tau_L)
\end{bmatrix}
\tag{B.73}
$$

In the expression above, it should be understood that the matrix elements $G_{i,j}$ are also matrices of size $N \times N$. This can be seen more clearly by noting the inverse of the above matrix is

$$
G^{-1} = \begin{bmatrix}
\mathbb{1} & 0 & 0 & \cdots & 0 & B_s(\tau_1, 0) \\
-B_s(\tau_2, \tau_1) & \mathbb{1} & 0 & \cdots & 0 & 0 \\
0 & -B_s(\tau_3, \tau_2) & \mathbb{1} & \cdots & 0 & 0 \\
0 & 0 & -B_s(\tau_4, \tau_3) & \ddots & 0 & 0 \\
\vdots & \vdots & \vdots & \ddots & \ddots & \vdots \\
0 & 0 & 0 & \cdots & B_s(\tau_L, \tau_{L-1}) & \mathbb{1}
\end{bmatrix} \tag{B.74}
$$

which is has dimensions $NL \times NL$. Despite the order in which we introduced them here, one typically is faced with the task of inverting $G^{-1} \rightarrow G$. Matrix inversion scales as $t_{\mathrm{inv}} \sim D^3$ where D is the linear dimension of the matrix, and thus it can be rather expensive for $(G^{-1})^{-1} \implies t_{\mathrm{inv}} \sim (NL)^3$. Fortunately for us, G^{-1} is a *sparse block matrix* [9] and when we require that $G^{-1}G = \mathbb{1}$ we find that the matrix elements

$$
\begin{aligned}
G_{i,i} &= [\mathbb{1} + B^\sigma_{s,i-1} \ldots B^\sigma_{s,1} B^\sigma_{s,L} \ldots B^\sigma_{s,i}]^{-1} \\
G^{i>j}_{i,j} &= G_{j,j}[B^\sigma_{s,i-1} \ldots B^\sigma_{s,j}] \\
G^{i<j}_{i,j} &= -G_{j,j}[\mathbb{1} + B^\sigma_{s,i-1} \ldots B^\sigma_{s,1} B^\sigma_{s,L} \ldots B^\sigma_{s,j}].
\end{aligned}
$$

The topmost expression is the equal time Green's function while the remaining two are essentially the retarded and advanced Green's functions valid only for $\tau_i > \tau_j$ and $\tau_i < \tau_j$ respectively. The computational cost for $G_{i,i}$ and $G_{i,j}$ is N^2 and $2N^2$ respectively.

---

[9] A *sparse matrix* is a matrix for which most of the elements are zero. By contrast, a *dense matrix* is one where most of the elements are nonzero. A measure of the *sparsity* is found by taking the ratio between the number of zero-valued elements and the total number of element. The closer to one this ratio is, the more sparse the matrix.

B.10 The Fermion Sign Problem in DQMC

In this section we review some basics of the fermion sign problem as it pertains to QMC. My primary reference for this section is the PRL (2005) by Matthias Troyer and Uwe-Jens Wiese (Ref.[296]).

One of the primary reasons one uses some flavor of the QMC approach to the many-body problem is that it gives us access to interacting models in higher dimensional systems with strong correlations. Analytical methods that solve such problems have yet to be developed (or at least become widely known), and analytical exact solutions are still only available through some sort of perturbative or mean-field type arguments. These QMC methods unintentionally suffer from the adage of "ain't no such thing as a free lunch", and they are plagued by the infamous fermion sign problem which makes it practically infeasible to study large finite-size lattices and very low temperatures.

Suppose we would like to find the expectation value of some observable $\hat{O}$ at finite temperature in the grand canonical ensemble :

$$\langle \hat{O} \rangle = \frac{\text{Tr}\left[e^{-\beta \hat{\mathsf{H}}}\hat{O}\right]}{\text{Tr}\left[e^{-\beta \hat{\mathsf{H}}}\right]} \tag{B.75}$$

where $\hat{\mathsf{H}} = \hat{H} - \mu\hat{N}$. If we map this to a classical problem, this expectation value effectively becomes

$$\langle O \rangle = \frac{\sum_i O_i p_i}{\sum_i p_i} \tag{B.76}$$

where p_i, the probability for each configuration of the system is defined in the partition function $\mathcal{Z} = \text{Tr}\left[e^{-\beta H}\right] = \sum_i p_i$. The "sign problem" appears if any of the $p_i < 0$. Positivity is a fundamental axiom in the interpretation of probabilities and it without it we lose information about the statistics of the system. In fermionic systems, the Pauli principle introduces a minus sign upon the exchange in quantum numbers of two particles, and it is here where the sign problem begins its propagation that ends in the partition function. If one samples the probability distrubution with respect to the absolute sign of the weights $|p_i|$

then the expectation value becomes

$$\langle O \rangle = \frac{\sum_i O_i p_i}{\sum_i p_i} = \frac{(\sum_i O_i \operatorname{sgn}(p_i)|p_i|/\sum_i p_i)}{(\sum_i \operatorname{sgn}(p_i)|p_i|/\sum_i p_i)} = \frac{\langle O \cdot \operatorname{sgn}(p) \rangle_{|p|}}{\langle \operatorname{sgn}(p) \rangle_{|p|}} . \tag{B.77}$$

In the DQMC problem, the factor $\det(M^\uparrow)\det(M^\downarrow)$ is not generally positive definite leading to sampling over an unrenormalized probability distribution which is, in turn, not generally positive definite. As outlined above, we circumvent this issue by using the absolute value $|\det(M^\uparrow)\det(M^\downarrow)|$ instead.

The cancellation in the sign grows exponentially

$$\langle \operatorname{sign} \rangle = \frac{\sum_i p_i}{\sum_i |p_i|} = e^{-\beta N \Delta f} \tag{B.78}$$

where N is the particle number and $\Delta f = f - f_{|p|}$ is the differences in the free energy densities. Consequently, the relative error $\Delta \operatorname{sign}/\langle \operatorname{sign} \rangle$ increases exponentially with increasing particle number and inverse temperature

$$\frac{\Delta \operatorname{sign}}{\langle \operatorname{sign} \rangle} \sim \frac{e^{\beta N \Delta f}}{\sqrt{N_{\mathscr{C}}}} \tag{B.79}$$

where $N_{\mathscr{C}}$ is the number of configurations in the set $\{\mathscr{C}_i\}$ chosen by a classical Monte Carlo method according to the probability distribution $p(\mathscr{C}_i)$. The takeaway here is the worsening of the sign-problem with increasing β and N. This dependence is the origin of the statement above that the sign problem makes it practically infeasible to study large finite-size lattices and low temperatures. Limitations aside, DQMC can still simulate systems large enough and at low enough temperatures to yield beneficial results.

Lastly, we should note that efforts surrounding the fermion sign problem are pretty significant since a definitive solution to the sign problem in polynomial time will solve the P=NP problem relevant to many computational science subfields. One interesting side-effect of the tremendous effort surrounding this problem is (at least in the QMC community) the discovery of sign-problem-free Hamiltonians and the symmetries that protect them. Two recent studies have claimed to prove definitively that only two fundamental sign-problem-free symmetry classes exist: Kramers class and Majorana class [297, 298]. With these

insights, it is possible to look for more sign-problem free Hamiltonians relevant to many-body physics. In particular, Hamiltonians describing topological superconductors with time-reversal symmetry are candidates for the Majorana class of sign-free problems [298].

B.11   Hubbard-Holstein Model

Thus far, we have described DQMC with the Hubbard model alone, which is the simplest interacting canonical model for e-e interactions. Adding phonons into the problem via the simplest e-ph model available, the Holstein model presents an opportunity to examine the competition between the two types of interactions. This Hubbard-Holstein (HH) model is described by $\hat{H} = \hat{H}_{\text{Hub}} + \hat{H}_{\text{ph}} + \hat{H}_{\text{e-ph}}$ where $\hat{H}_{\text{Hub}}$ is the Hubbard model described previously. The extra Holstein terms are

$$\hat{H}_{\text{ph}} = \sum_i \left[\frac{\hat{P}_i^2}{2M} + \frac{K}{2}\hat{X}_i^2 \right] \tag{B.80}$$

and

$$\hat{H}_{\text{e-ph}} = g \sum_{i,\sigma} \hat{X}_i \left(\hat{n}_{i,\sigma} - \frac{1}{2} \right) . \tag{B.81}$$

After this makes it through the Trotter decomposition and the terms are partitioned into their respective values on each time slice l, we have

$$\hat{H}_{\text{ph},l} = \sum_i \left[\frac{\hat{P}_{i,l}^2}{2M} + \frac{1}{2}M\Omega^2\hat{X}_{i,l}^2 \right] \tag{B.82}$$

and

$$\hat{H}_{\text{e-ph},l} = \alpha \sum_{i,\sigma} \hat{n}_{i,\sigma}\hat{X}_{i,l} . \tag{B.83}$$

where Ω is the phonon frequency of a dispersionless optical mode, and $\hat{X}_{i,l}, \hat{P}_{i,l}$ are the position and momentum operators for the oscillator at site i during time-slice l. The e-ph interaction strength, α, tunes the strength of the e-ph interaction and is isotropic (independent of momentum). The lattice DOF are handled by replacing the position operator with a continuous variable $X_{i,l}$, which changes the momentum operator to a discrete

difference step on the imaginary time grid

$$P_{i,l} = \frac{X_{i,l+1} - X_{i,l}}{\delta\tau} . \tag{B.84}$$

The procedure for dealing with the interaction is the same as before except now the matrices $\mathrm{B}_{s,l}^\sigma$ are modified to

$$\mathrm{B}_{s,l}^\sigma \equiv \mathrm{e}^{\Delta\tau(-1)^\sigma \lambda \mathrm{v}(l) - \Delta\tau g \mathrm{X}(l)} \mathrm{e}^{\Delta\tau \mathrm{K}^\sigma} . \tag{B.85}$$

where now $\mathrm{X}(l)$ represents a matrix with an ith diagonal element equal to the lattice displacement $X_{i,l}$.

With the inclusion of phonons, we must update both the HS and phonon fields. The displacement field $X_{i,l}$ can be updated in two different ways, (i) local site update and (ii) block updates. We won't discuss the scheme in detail here, but note that the local update proposes a displacement field shift ΔX weighted by a uniform probability distribution centered at 0. This new displacement field relates to the old one via $X'_{i,l} \rightarrow X_{i,l} + \Delta X$ and with it the acceptance ratio for a configuration update changes to $R = R^\uparrow R^\downarrow \mathrm{e}^{\Delta\tau g \Delta E_{\text{ph}}}$ where ΔE_{ph} is the change in kinetic and potential energy of the phonon fields in the update.

The second update procedure is known as a *block update* and refers to the simultaneous update of the entire set of displacements along a block of imaginary time slices. The imaginary time interval's size to be updated simultaneously is set by the need to recover Bose statistics. Unfortunately, the fast updates allowed by the Sherman-Morrison updating scheme outlined before are not viable when using block updates. The block updates' primary purpose is to counter a slowing of single-site updates' acceptance rate at low temperatures. Low-T values correspond to low phonon momentum, and thus the changes in the displacement field correspond to relatively large momentum shifts. The likelihood of acceptance for such changes becomes small, and thus the phonon configuration becomes 'frozen' in place. One must obtain statistically independent configurations for sampling, and thus static phonon field configurations need to be unfrozen by more uniform changes.

B.12 Equilibration, Auto-Correlation, and Measurements

This section will briefly discuss how measurements are organized and what additional constraints need to be considered to justify the simulation as producing physically meaningful results.

Equilibration Time: One cannot simply begin keeping measurements too soon after the first configuration on the lattice is updated. Our theoretical framework aims to find finite temperature expectation values at thermal equilibrium, and therefore we must wait until enough updates have equilibrated the system. We call these preliminary steps through non-equilibrated configurations *warmup sweeps*, and the amount required for equilibrium depends on the interaction parameters and temperature to a significant degree. Generally speaking, a conservative estimate for typical calculations on an 8×8 lattice, with $\Omega \sim t$ and $\beta \sim t \dots 10t$ is $N_{\text{warmup}} \sim 2 \times 10^4 \dots 5 \times 10^4$.

Autocorrelation Time: To guarantee that measurements are drawn from statistically independent field configurations, one must update the system several times between actual measurements. The amount of time one must wait in order to eliminate this statistical bias is known as the autocorrelation time. We can estimate this time by calculating the autocorrelation function for various quantities such as the phonon displacement fields X_l which we denote $\mathcal{X}_l$,

$$\mathcal{X}_l = \frac{\langle X_{n+l} X_n \rangle - \langle X_n \rangle^2}{\langle X_n^2 \rangle - \langle X_n \rangle^2} \, . \tag{B.86}$$

Here we have used that $\langle X_{n+l} X_n \rangle = \frac{1}{N_{\text{sweeps}}} \sum_{n=1}^{N_{\text{sweeps}}} X_{n+l} X_n$ with l as the sweep number and N_{sweeps} as the total number of Monte Carlo sweeps. Long autocorrelation times add to the total CPU runtime for the calculation and should be minimized within reason (if possible). Although methods for reducing autocorrelation times exist, we will not discuss them here.

Measurements: Computing the expectation values and estimating the statistical error requires the calculation of mean measurements and their respective variances (in equilibrium of course). The total number of measurement sweeps in the entire simulation denoted N_{sweeps} is divided into N_{bin} number of intervals and the values in each bin are averaged, thereby creating N_{bin} measurements. The binned measurements are considered to be statistically

independent and used to find a sample mean

$$\bar{x} = \frac{1}{N_{\text{bin}}} \sum_{i=1}^{N_{\text{bin}}} x_i \tag{B.87}$$

and a sample variance

$$\sigma_x^2 = \frac{1}{N-1} \sum_{i=1}^{N_{\text{bin}}} (x_i - \bar{x})^2 \tag{B.88}$$

which are taken to be the final measurement and square of the error estimate respectively. Error bars, wherever they may appear, are given from the estimate σ_x for each measured quantity.

C Proof of Identity $\text{Tr}[\hat{W}] = \det[1 + \text{e}^{\text{T}}]$

In the previous section, we used Eqn. B.31 to state (without proof) that the trace over imaginary-time evolution operators, $\hat{B}^{\sigma}_{s,l}$, was equivalent to a determinant containing their matrix-form counterparts. In this section, we provide a detailed proof of this identity with pedagogy in mind. Again, I am indebted to the detailed notes found in my advisor's dissertation [292] and the source of those notes written by Assaad et al.[104] I consider this discussion as a an "update" with more details and corrections of mistakes found in those references. I have made a considerable effort to compose many of the derivations to my standards and greatly appreciate any typos or mistakes noticed by the reader.

C.1 Tracing out the Fermion degrees of freedom.

A crucial step in simplifying the trace over the Fermion degrees of freedom (d.o.f.) was to utilize the identity

$$\text{Tr}\left[\text{e}^{\hat{c}^{\dagger}\hat{T}_1\hat{c}}\text{e}^{\hat{c}^{\dagger}\hat{T}_2\hat{c}}\ldots\text{e}^{\hat{c}^{\dagger}\hat{T}_n\hat{c}}\right] = \det\left[\mathbb{1} + \text{e}^{\text{T}_1}\text{e}^{\text{T}_2}\ldots\text{e}^{\text{T}_n}\right] \tag{C.1}$$

A proof of this identity will now be presented (in a pedagogical way) within this appendix using Slater determinants.

A Slater determinant is comprised of fermion operators and it preserves the anti-symmetric exchange of fermions in multi-particle states. These operators are essential for expressing the second quantized Hamiltonian for a particular physical system. Let us first consider a single particle Hamiltonian $\hat{H}_0 = \sum_{i,j}\hat{c}^{\dagger}_i(\text{H}_0)_{i,j}\hat{c}_j$ which is bilinear in the fermion creation and annihilation operators $\hat{c}^{\dagger}_i$ and $\hat{c}_j$ with i running over all of the N single particle states. The matrix element $(\text{H}_0)_{i,j}$ belongs to the $N \times N$ matrix H_0, and H_0 is always Hermitian. This implies that some orthogonal transformation U exists such that $\text{U}^{\dagger}\text{H}_0\text{U} = \text{H}_{\text{d}}$ where H_{d} is a diagonal matrix. Starting with Hamiltonian already introduced, we will show the transformation first, in a matrix form, using $\hat{c}^{\dagger} = [\hat{c}^{\dagger}_1, \hat{c}^{\dagger}_2, \ldots, \hat{c}^{\dagger}_n]$ and an analogous column

vector for $\hat{c}$:

$$
\begin{aligned}
\hat{H}_0 &= \hat{c}^\dagger H_0 \hat{c} \\
&= \hat{c}^\dagger U U^\dagger H_0 U U^\dagger \hat{c} \\
&= \hat{c}^\dagger U H_d U^\dagger \hat{c} \\
&= \hat{\gamma}^\dagger H_d \hat{\gamma} \quad\quad\quad\quad\quad\quad\quad\quad \text{(C.2)}
\end{aligned}
$$

where the unitarity of U was used to insert the identity matrix between terms since $U^\dagger U = U U^\dagger = \mathbb{1}$.

The last equation C.2 represents the diagonal form of our Hamiltonian, and it can be alternatively expressed as a sum across the diagonal elements of H_d:

$$
\hat{H}_0 = \sum_i (H_d)_{i,i}\, \hat{\gamma}_i^\dagger \hat{\gamma}_i \quad\quad\quad\quad\quad\quad \text{(C.3)}
$$

The fermion operators in the diagonal basis are then clearly given by

$$
\hat{\gamma}_i^\dagger = \sum_j \hat{c}_j^\dagger U_{ji} \quad\quad\quad \hat{\gamma}_i = \sum_j U_{ij}^\dagger \hat{c}_j \quad\quad\quad\quad \text{(C.4)}
$$

which satisfy the anti-commutation relations $\left\{ \hat{\gamma}_i^\dagger, \hat{\gamma}_j \right\} = \delta_{i,j}$, and $\left\{ \hat{\gamma}_i^\dagger, \hat{\gamma}_j^\dagger \right\} = \left\{ \hat{\gamma}_i, \hat{\gamma}_j \right\} = 0$ due to the unitarity of U. We will need to create multi-particle states of fermions by using the fermion operators $\hat{\gamma}_i^\dagger$ and $\hat{\gamma}_i$, which can be used express an arbitrary p-particle state eigenstate of the Hamiltonian as

$$
\hat{\gamma}_{\alpha_1}^\dagger \hat{\gamma}_{\alpha_2}^\dagger \dots \hat{\gamma}_{\alpha_p}^\dagger \left| 0 \right\rangle = \prod_{n=1}^{p} \left(\sum_j \hat{c}_j^\dagger U_{j,\alpha_n} \right) \left| 0 \right\rangle = \prod_{n=1}^{p} \left(\hat{c}^\dagger P \right)_n \left| 0 \right\rangle \quad\quad \text{(C.5)}
$$

The above features the vacuum state $\left| 0 \right\rangle$, the rectangular $N \times p$ matrix P, and the matrix product $\left(\hat{c}^\dagger P \right)_n$ which denotes that the product be evaluated using only the nth column of the $1 \times p$ row vector $\left(\hat{c}^\dagger P \right)$. The last equation, $\prod_{n=1}^{p} \left(\hat{c}^\dagger P \right)_n \left| 0 \right\rangle$ provides a definition for the Slater determinant, which is completely characterized by the rectangular matrix P. Since it must be true that $N \geq p$, the matrix P is actually a $N \times p$ submatrix of the $N \times N$ unitary

matrix U. It may not be completely clear from the last expression in Eqn.(C.5), but the different permutations of the creation operators (arising from the multiplication through all terms in the product series), yields the familiar (antisymmetric) minus signs of the Slater determinant[10]. Moreover some of the terms will contain two or more of the same creation operator, thus yielding zero on the vacuum state. The (single-particle) bilinear Hamiltonian as seen in Eqn.(C.3) is solved by the Slater determinant.

With the above arguments used to give us a working form of the p-particle state, let us return to our task at hand. Recall that we need to evaluate the trace $\text{Tr}\left\{e^{\hat{c}^\dagger \hat{T}_1 \hat{c}} e^{\hat{c}^\dagger \hat{T}_2 \hat{c}} \ldots e^{\hat{c}^\dagger \hat{T}_n \hat{c}}\right\}$, which has a general form

$$\text{Tr}\left\{e^{\hat{c}^\dagger \hat{T}_1 \hat{c}} e^{\hat{c}^\dagger \hat{T}_2 \hat{c}} \ldots e^{\hat{c}^\dagger \hat{T}_n \hat{c}}\right\} = \sum_m \langle m| \, e^{\hat{c}^\dagger \hat{T}_1 \hat{c}} e^{\hat{c}^\dagger \hat{T}_2 \hat{c}} \ldots e^{\hat{c}^\dagger \hat{T}_n \hat{c}} \, |m\rangle \tag{C.6}$$

where the basis set $\{|m\rangle\}$ can be any orthonormal basis set, but is ideally the set of many-particle eigenstates of an operator in the trace. Our states are the p-particle Slater determinants, which means we'll need to know how to evaluate something like

$$e^{\hat{c}^\dagger \hat{T} \hat{c}} \prod_{n=1}^{p} \left(\hat{c}^\dagger P\right)_n |0\rangle \tag{C.7}$$

The result of this operation is well known, and it can be stated with a subsidiary declaration followed by a proof of this lemma.

Lemma 1: When a Slater determinant is multiplied by the operator $\exp\left(\hat{c}^\dagger T \hat{c}\right)$ where T is a Hermitian (or anti-Hermitian) matrix, the result is also a Slater determinant as in

$$e^{\hat{c}^\dagger T \hat{c}} \prod_{n=1}^{p} \left(\hat{c}^\dagger P\right)_n |0\rangle = \prod_{n=1}^{p} \left(\hat{c}^\dagger e^{T} P\right)_n |0\rangle . \tag{C.8}$$

This is effectively a propagation of a Slater determinant with a single-particle propagator.

Proof: Let us transform T into a diagonal form with a unitary transformation like the one used on the Hamiltonian, namely, $U^\dagger T U = \lambda$. Again U is a unitary matrix and λ and if

---

[10]This is because we can anticommute all of the operators back to the proper numerical ordering. For example, if $N = p = 3$ one of the nonzero terms will be $\hat{c}_2^\dagger \hat{c}_1^\dagger \hat{c}_3^\dagger P_{2,1} P_{1,2} P_{3,3} = -\hat{c}_1^\dagger \hat{c}_2^\dagger \hat{c}_3^\dagger P_{2,1} P_{1,2} P_{3,3}$

T is a Hermitian (or anti-Hermitian) matrix, λ is a real (purely imaginary) diagonal matrix. The steps are identical to what was done for the result seen in Eqn.(C.2), and we will be using the gamma vector $\hat{\gamma}^\dagger = \hat{c}^\dagger U$ (implying that $\hat{\gamma}^\dagger U^\dagger = \hat{c}^\dagger$).

$$
\begin{aligned}
e^{\hat{c}^\dagger T \hat{c}} \prod_{n=1}^{p} \left(\hat{c}^\dagger P\right)_n |0\rangle &= e^{\hat{\gamma}^\dagger \lambda \hat{\gamma}} \prod_{n=1}^{p} \left(\hat{\gamma}^\dagger U^\dagger P\right)_n |0\rangle \\
&= e^{\hat{\gamma}^\dagger \lambda \hat{\gamma}} \left(\hat{\gamma}^\dagger U^\dagger P\right)_{\alpha_1} \left(\hat{\gamma}^\dagger U^\dagger P\right)_{\alpha_2} \cdots \left(\hat{\gamma}^\dagger U^\dagger P\right)_{\alpha_p} |0\rangle
\end{aligned} \tag{C.9}
$$

Each term in parenthesis can be unpacked as a sum over fermion operators multiplied by a specific column vector generated within the matrix product of $U^\dagger P$. For example, take the ith term $\left(\hat{\gamma}^\dagger U^\dagger P\right)_{\alpha_i}$,

$$
\left(\hat{\gamma}^\dagger U^\dagger P\right)_{\alpha_i} = \hat{\gamma}_1^\dagger \left(U^\dagger P\right)_{1,\alpha_i} + \ldots + \hat{\gamma}_N^\dagger \left(U^\dagger P\right)_{N,\alpha_i} = \sum_{j=1}^{N} \hat{\gamma}_j^\dagger \left(U^\dagger P\right)_{j,\alpha_i} \tag{C.10}
$$

which suggests another representation of Eqn.(C.9) as

$$
e^{\hat{c}^\dagger T \hat{c}} \prod_{n=1}^{p} \left(\hat{c}^\dagger P\right)_n |0\rangle = e^{\hat{\gamma}^\dagger \lambda \hat{\gamma}} \prod_{n=1}^{p} \left(\sum_{j=1}^{N} \hat{\gamma}_j^\dagger \left(U^\dagger P\right)_{j,\alpha_n} \right) |0\rangle. \tag{C.11}
$$

This expression will result in terms that have carry a product of p fermion creation operators, but we know that wherever they may appear, terms like $\left(\hat{\gamma}_j^\dagger\right)^k |0\rangle = 0$ for $k > 1$. This implies that the only t erms in Eqn.(C.11) that survive are those in which any fermion creation operator $\hat{\gamma}_j^\dagger$ appears only once. As it turns out, for N single particle states and p-particles, there will be $\binom{N}{p} = N!/(N-p)!$ different terms that survive since there are $\binom{N}{p}$ possible permutations of the product $\hat{\gamma}_j^\dagger \hat{\gamma}_k^\dagger \ldots \hat{\gamma}_l^\dagger$ where there are p terms in total for each product.

Since λ is diagonal, we can write

$$
\begin{aligned}
e^{\hat{\gamma}^\dagger \lambda \hat{\gamma}} &= e^{\sum_i \lambda_{i,i} \hat{\gamma}_i^\dagger \hat{\gamma}_i} \\
&= \left(e^{\lambda_{1,1} \hat{\gamma}_1^\dagger \hat{\gamma}_1}\right) \left(e^{\lambda_{2,2} \hat{\gamma}_2^\dagger \hat{\gamma}_2}\right) \cdots \left(e^{\lambda_{N,N} \hat{\gamma}_N^\dagger \hat{\gamma}_N}\right)
\end{aligned} \tag{C.12}
$$

which is exact since $\left[\hat{\gamma}_i^\dagger \hat{\gamma}_i, \hat{\gamma}_j^\dagger \hat{\gamma}_j\right] = 0$. Moreover, the many-particle states these exponentials act upon can also be rewritten for practical purposes:

$$\prod_{n=1}^{p} \left(\sum_{j=1}^{N} \hat{\gamma}_j^\dagger \left(\mathrm{U}^\dagger\mathrm{P}\right)_{j,\alpha_n}\right) |0\rangle = \left(\sum_{j_1\ldots j_p} \hat{\gamma}_{j_1}^\dagger \ldots \hat{\gamma}_{j_p}^\dagger \left(\mathrm{U}^\dagger\mathrm{P}\right)_{j_1,\alpha_1} \ldots \left(\mathrm{U}^\dagger\mathrm{P}\right)_{j_p,\alpha_p}\right) |0\rangle . \qquad \text{(C.13)}$$

Brief interlude on commuting the exponential operator with the creation operator:

If we wanted to commute the exponentials through the creation operators to get to and act upon the vacuum state, we would need to recall the relation for commuting an exponential operator with another operator. Say we have the operators $\hat{A}$ and $\hat{B}$ and a scalar λ, it can be shown easily that

$$\left[\hat{A}, e^{\lambda\hat{B}}\right] = \hat{A}e^{\lambda\hat{B}} - e^{\lambda\hat{B}}\hat{A} = \lambda\left[\hat{A}, \hat{B}\right]e^{\lambda\hat{B}} \qquad \text{(C.14)}$$

which implies that

$$e^{\lambda\hat{B}}\hat{A} = \hat{A}e^{\lambda\hat{B}} - \lambda\left[\hat{A}, \hat{B}\right]e^{\lambda\hat{B}}. \qquad \text{(C.15)}$$

For our problem, we will need to examine

$$\left[\hat{\gamma}_j^\dagger, \hat{\gamma}_i^\dagger\hat{\gamma}_i\right] \qquad \text{(C.16)}$$

which is motivated by our desire to commute the exponential operators through some arbitrary amount of creation operators. So naturally, we are looking to replace terms like $e^{\lambda_{i,i}\hat{\gamma}_i^\dagger\hat{\gamma}_i}\hat{\gamma}_j^\dagger$ with their commutation relations, as is shown with $e^{\lambda\hat{B}}\hat{A}$ in Eqn.(C.15):

$$e^{\lambda_{i,i}\hat{\gamma}_i^\dagger\hat{\gamma}_i}\hat{\gamma}_j^\dagger = \hat{\gamma}_j^\dagger e^{\lambda_{i,i}\hat{\gamma}_i^\dagger\hat{\gamma}_i} - \lambda_{i,i}\left[\hat{\gamma}_j^\dagger, \hat{\gamma}_i^\dagger\hat{\gamma}_i\right]e^{\lambda_{i,i}\hat{\gamma}_i^\dagger\hat{\gamma}_i}. \qquad \text{(C.17)}$$

Evaluating the unknown commutator is as follows:

$$\begin{aligned}
\left[\hat{\gamma}_j^\dagger, \hat{\gamma}_i^\dagger\hat{\gamma}_i\right] &= \hat{\gamma}_j^\dagger\hat{\gamma}_i^\dagger\hat{\gamma}_i - \hat{\gamma}_i^\dagger\underbrace{\hat{\gamma}_i\hat{\gamma}_j^\dagger}_{\{\rightsquigarrow\}} \\
&= \hat{\gamma}_j^\dagger\hat{\gamma}_i^\dagger\hat{\gamma}_i - \hat{\gamma}_i^\dagger\left(\delta_{i,j} - \hat{\gamma}_j^\dagger\hat{\gamma}_i\right) \\
&= \hat{\gamma}_j^\dagger\hat{\gamma}_i^\dagger\hat{\gamma}_i - \hat{\gamma}_i^\dagger\delta_{i,j} + \underbrace{\hat{\gamma}_i^\dagger\hat{\gamma}_j^\dagger}_{\{\rightsquigarrow\}}\hat{\gamma}_i \\
&= \cancel{\hat{\gamma}_j^\dagger\hat{\gamma}_i^\dagger\hat{\gamma}_i} - \hat{\gamma}_i^\dagger\delta_{i,j} - \cancel{\hat{\gamma}_j^\dagger\hat{\gamma}_i^\dagger\hat{\gamma}_i} \\
&= -\hat{\gamma}_i^\dagger\delta_{i,j}. \qquad \text{(C.18)}
\end{aligned}$$

Now we can rewrite Eqn.($C.17$) with this result,

$$e^{\lambda_{i,i}\hat{\gamma}_i^\dagger\hat{\gamma}_i}\,\hat{\gamma}_j^\dagger = \hat{\gamma}_j^\dagger e^{\lambda_{i,i}\hat{\gamma}_i^\dagger\hat{\gamma}_i} + \lambda_{i,i}\hat{\gamma}_i^\dagger\delta_{i,j}e^{\lambda_{i,i}\hat{\gamma}_i^\dagger\hat{\gamma}_i}\,,$$

$$= (1 + \lambda_{i,i}\delta_{i,j})\,\hat{\gamma}_j^\dagger e^{\lambda_{i,i}\hat{\gamma}_i^\dagger\hat{\gamma}_i}\,. \tag{C.19}$$

In summary, we only pay the commutator penalty if $i = j$, so we might consider avoiding the exchange of terms where $i = j$ in the remaining steps.

End interlude

Let us revisit the main term we are interested in working with:

$$\left(e^{\lambda_{1,1}\hat{\gamma}_1^\dagger\hat{\gamma}_1}\right)\cdots\left(e^{\lambda_{N,N}\hat{\gamma}_N^\dagger\hat{\gamma}_N}\right)\left(\sum_{j_1\ldots j_p}^N \hat{\gamma}_{j_1}^\dagger\cdots\hat{\gamma}_{j_p}^\dagger\left(\mathrm{U}^\dagger\mathrm{P}\right)_{j_1,\alpha_1}\cdots\left(\mathrm{U}^\dagger\mathrm{P}\right)_{j_p,\alpha_p}\right)|0\rangle\,. \tag{C.20}$$

As stated earlier, only those permutations with creation operators appearing once (and only once) for each state will survive the multiple summation. Thus, our summations reduce to a summation over all permutations π as in

$$\left(e^{\lambda_{1,1}\hat{\gamma}_1^\dagger\hat{\gamma}_1}\right)\cdots\left(e^{\lambda_{N,N}\hat{\gamma}_N^\dagger\hat{\gamma}_N}\right)\left(\sum_\pi \hat{\gamma}_{\pi(1)}^\dagger\cdots\hat{\gamma}_{\pi(p)}^\dagger\left(\mathrm{U}^\dagger\mathrm{P}\right)_{\pi(1),\alpha_1}\cdots\left(\mathrm{U}^\dagger\mathrm{P}\right)_{\pi(p),\alpha_p}\right)|0\rangle\,. \tag{C.21}$$

For each of the $\binom{N}{p}$ possible permutations, we can move the respective exponential term to just before the creation operator that shares the same indicies (as not to incur any commutation penalties) and all of the other $(N-p)$ remaining exponentials can be placed wherever as they commute with everything[11]. This leaves us with the permutation sum

$$\sum_\pi e^{\lambda_{\pi(1),\pi(1)}\hat{\gamma}_{\pi(1)}^\dagger\hat{\gamma}_{\pi(1)}}\hat{\gamma}_{\pi(1)}^\dagger\cdots e^{\lambda_{\pi(p),\pi(p)}\hat{\gamma}_{\pi(p)}^\dagger\hat{\gamma}_{\pi(p)}}\hat{\gamma}_{\pi(p)}^\dagger\left(\mathrm{U}^\dagger\mathrm{P}\right)_{\pi(1),\alpha_1}\cdots\left(\mathrm{U}^\dagger\mathrm{P}\right)_{\pi(p),\alpha_p}|0\rangle\,. \tag{C.22}$$

The above expression reveals that every relevant exponential in each permutation will adopt an eigenvalue 1 and becomes a scalar $e^{\lambda_{\pi(n),\pi(n)}}$. If the p-particle state-ket (resulting from the

---

[11]They could be commuted through to the vacuum state, which will result in an eigenvalue of 0 in the exponential, and be equal to unity (i.e., $e^{\lambda_{i,i}\hat{\gamma}_i^\dagger\hat{\gamma}_i}|0\rangle = e^0|0\rangle = |0\rangle$).

creation operators only) for a particular permutation is $|\psi_\pi\rangle$ then we could write

$$\sum_\pi e^{\lambda_{\pi(1),\pi(1)}\hat{\gamma}^\dagger_{\pi(1)}\hat{\gamma}_{\pi(1)}}\hat{\gamma}^\dagger_{\pi(1)}\cdots e^{\lambda_{\pi(p),\pi(p)}\hat{\gamma}^\dagger_{\pi(p)}\hat{\gamma}_{\pi(p)}}\hat{\gamma}^\dagger_{\pi(p)}\left(U^\dagger P\right)_{\pi(1),\alpha_1}\cdots\left(U^\dagger P\right)_{\pi(p),\alpha_p}|0\rangle$$

$$= \sum_\pi e^{\lambda_{\pi(1),\pi(1)}}\cdots e^{\lambda_{\pi(p),\pi(p)}}|\psi_\pi\rangle\left(U^\dagger P\right)_{\pi(1),\alpha_1}\cdots\left(U^\dagger P\right)_{\pi(p),\alpha_p}$$

$$= \sum_\pi e^{\sum_\pi \lambda_{\pi,\pi}}|\psi_\pi\rangle\left(U^\dagger P\right)_{\pi(1),\alpha_1}\cdots\left(U^\dagger P\right)_{\pi(p),\alpha_p}. \tag{C.23}$$

It becomes clear that the exponential operator we started with becomes a simple scalar quantity that can be placed anywhere. Taking some steps back toward the original form we find

$$\sum_\pi e^{\sum_\pi \lambda_{\pi,\pi}}|\psi_\pi\rangle\left(U^\dagger P\right)_{\pi(1),\alpha_1}\cdots\left(U^\dagger P\right)_{\pi(p),\alpha_p}$$

$$= \sum_\pi |\psi_\pi\rangle e^{\sum_\pi \lambda_{\pi,\pi}}\left(U^\dagger P\right)_{\pi(1),\alpha_1}\cdots\left(U^\dagger P\right)_{\pi(p),\alpha_p}$$

$$= \sum_\pi \hat{\gamma}^\dagger_{\pi(1)}\cdots\hat{\gamma}^\dagger_{\pi(p)}|0\rangle e^{\sum_\pi \lambda_{\pi,\pi}}\left(U^\dagger P\right)_{\pi(1),\alpha_1}\cdots\left(U^\dagger P\right)_{\pi(p),\alpha_p}$$

$$= \sum_\pi \hat{\gamma}^\dagger_{\pi(1)}\cdots\hat{\gamma}^\dagger_{\pi(p)}e^{\sum_\pi \lambda_{\pi,\pi}}\left(U^\dagger P\right)_{\pi(1),\alpha_1}\cdots\left(U^\dagger P\right)_{\pi(p),\alpha_p}|0\rangle \tag{C.24}$$

$$= \prod_{n=1}^p\left(\sum_{j=1}^N\hat{\gamma}^\dagger_j e^{\lambda_{j,j}}\left(U^\dagger P\right)_{j,\alpha_n}\right)|0\rangle \tag{C.25}$$

$$= \prod_{n=1}^p\left(\hat{\gamma}^\dagger e^\lambda U^\dagger P\right)_n|0\rangle$$

$$= \prod_{n=1}^p\left(\hat{c}^\dagger U e^\lambda U^\dagger P\right)_n|0\rangle$$

$$= \prod_{n=1}^p\left(\hat{c}^\dagger e^T P\right)_n|0\rangle \quad \text{q.e.d.} \tag{C.26}$$

The leap from Eqn.(C.24) to Eqn.(C.25) is related to an observation that analogously took us from Eqn.(C.20) to Eqn.(C.21), and it can be shown by proper expansion of the matrix multiplication, product series, and elimination of all terms with repeated (same-state) creation operators that the two expressions are equivalent. In effect we have proved Lemma (1) expressed in Eqn.(C.8).

Lemma 2: The scalar product of two Slater determinants $|\psi\rangle = \prod_{n=1}^p\left(\hat{c}^\dagger P\right)_n|0\rangle$ and

$|\tilde{\psi}\,\rangle = \prod_{n=1}^{p} \left(\hat{c}^{\dagger}\tilde{P}\right)_n |0\rangle$ can be expressed by

$$\langle\psi|\tilde{\psi}\rangle = \det\left[P^{\dagger}\tilde{P}\right]. \tag{C.27}$$

This expression can be obtained by working through the scalar product of the two states as follows:

$$
\begin{aligned}
\langle\psi|\tilde{\psi}\rangle &= \langle 0| \prod_{n=p}^{0} \left(P^{\dagger}\hat{c}\right)_n \prod_{n=1}^{p} \left(\hat{c}^{\dagger}\tilde{P}\right)_n |0\rangle \qquad \text{*notice product series limits} \\
&= \langle 0| \prod_{n=p}^{1} \left(\sum_{j=1}^{N} P^{\dagger}_{\alpha_n,j}\hat{c}_j\right) \prod_{n=1}^{p} \left(\sum_{\tilde{j}=1}^{N} \hat{c}^{\dagger}_{\tilde{j}}\tilde{P}_{\tilde{j},\alpha_n}\right) |0\rangle \\
&= \langle 0| \left(P^{\dagger}_{\alpha_p,1}\hat{c}_1 + \ldots + P^{\dagger}_{\alpha_p,N}\hat{c}_N\right) \ldots \left(P^{\dagger}_{\alpha_1,1}\hat{c}_1 + \ldots + P^{\dagger}_{\alpha_1,N}\hat{c}_N\right) \\
&\quad \left(\hat{c}^{\dagger}_{\tilde{1}}\tilde{P}_{\tilde{1},\alpha_1} + \ldots + \hat{c}^{\dagger}_{\tilde{N}}\tilde{P}_{\tilde{N},\alpha_1}\right) \left(\hat{c}^{\dagger}_{\tilde{1}}\tilde{P}_{\tilde{1},\alpha_p} + \ldots + \hat{c}^{\dagger}_{\tilde{N}}\tilde{P}_{\tilde{N},\alpha_p}\right) |0\rangle \\
&= \sum_{\substack{j_1\ldots j_p \\ \tilde{j}_1\ldots\tilde{j}_p}} P^{\dagger}_{\alpha_p,j_p} \ldots P^{\dagger}_{\alpha_1,j_1} \tilde{P}_{\tilde{j}_1,\alpha_1} \ldots \tilde{P}_{\tilde{j}_p,\alpha_p} \langle 0| \hat{c}_{j_p}\ldots\hat{c}_{j_1}\hat{c}^{\dagger}_{\tilde{j}_1}\ldots\hat{c}^{\dagger}_{\tilde{j}_p} |0\rangle
\end{aligned} \tag{C.28}
$$

In this last expression we have all possible permutations of creation and annihilation operators permitted by the sums, and as in the previous lemma, we must recognize that only certain permutations will result in nonzero values of $\langle 0| \hat{c}_{j_p}\ldots\hat{c}_{j_1}\hat{c}^{\dagger}_{\tilde{j}_1}\ldots\hat{c}^{\dagger}_{\tilde{j}_p} |0\rangle$. In this case, we must have that all the $j_i : i \in \{1,2,\ldots,p\}$ take different values and that there is a permutation π, of the p numbers such that

$$\tilde{j}_i = j_{\pi(i)}. \tag{C.29}$$

This result implies that all of the matrix elements will resolve to the sign of the permutation $(-1)^{\pi}$. The scalar product can be written as

$$\langle\psi|\tilde{\psi}\rangle = \sum_{j_1\ldots j_p} \left|\hat{c}^{\dagger}_{j_1}\ldots\hat{c}^{\dagger}_{j_p} |0\rangle\right|^2 \sum_{\pi}(-1)^{\pi} P^{\dagger}_{\alpha_p,j_p} \ldots P^{\dagger}_{\alpha_1,j_1} \tilde{P}_{j_{\pi(1)},\alpha_1} \ldots \tilde{P}_{j_{\pi(p)},\alpha_p} \tag{C.30}$$

where $\pi \in \mathcal{S}_p$, with $\mathcal{S}_p$ being defined as the a group of permutations with p elements to permute. The Pauli exclusion principle keeps the terms with $j_i = j_k$ from contributing. Moreover, we can omit the matrix element term since the sum over permutations vanishes

208

for $j_i = j_k$ for any $i \neq k$. This is seen more easily if we consider an example where $p = 2$ and $j_1 = j_2 = j$:

$$\sum_{\pi \in \mathcal{S}_2} (-1)^\pi P^\dagger_{\alpha_p, j_p} \ldots P^\dagger_{\alpha_1, j_1} \tilde{P}_{j_{\pi(1)}, \alpha_1} \ldots \tilde{P}_{j_{\pi(p)}, \alpha_p} = P^\dagger_{\alpha_2, j} P^\dagger_{\alpha_1, j} \tilde{P}_{j, \alpha_1} \tilde{P}_{j, \alpha_2} \sum_{\pi \in \mathcal{S}_2} (-1)^\pi = 0 \quad \text{(C.31)}$$

$$\text{since} \quad \sum_{\pi \in \mathcal{S}_2} (-1)^\pi = 1 - 1 = 0 \,.$$

We can now rewrite the overlap

$$\langle \psi | \tilde{\psi} \rangle = \sum_{j_1 \ldots j_p} \sum_{\pi \in \mathcal{S}_p} (-1)^\pi P^\dagger_{\alpha_p, j_p} \ldots P^\dagger_{\alpha_1, j_1} \tilde{P}_{j_{\pi(1)}, \alpha_1} \ldots \tilde{P}_{j_{\pi(p)}, \alpha_p}$$

$$= \sum_{j_1 \ldots j_p} \sum_{\pi \in \mathcal{S}_p} (-1)^{\pi^{-1}} P^\dagger_{\alpha_p, j_p} \ldots P^\dagger_{\alpha_1, j_1} \tilde{P}_{j_1, \pi^{-1}(1)} \ldots \tilde{P}_{j_p, \pi^{-1}(p)} \quad \text{(C.32)}$$

To get from the first line to the second line we need to recognize that the following is true:

$$\sum_{\substack{j_1 \ldots j_p \\ \pi \in \mathcal{S}_p}} (-1)^\pi P^\dagger_{\alpha_p, j_p} \ldots P^\dagger_{\alpha_1, j_1} \tilde{P}_{j_{\pi(1)}, \alpha_1} \ldots \tilde{P}_{j_{\pi(p)}, \alpha_p} = \sum_{\substack{j_1 \ldots j_p \\ \pi \in \mathcal{S}_p}} (-1)^{\pi^{-1}} P^\dagger_{\alpha_p, j_p} \ldots P^\dagger_{\alpha_1, j_1} \tilde{P}_{j_1, \pi^{-1}(1)} \ldots \tilde{P}_{j_p, \pi^{-1}(p)}$$

$$\text{(C.33)}$$

Another interlude section on some pertinent details of permutations will follow. Skip ahead if necessary.

Brief interlude on permutations.

Consider a set A of N sequential integers $S = \{1, 2, \ldots, N\}$ (though they could be more general variables $x_1, x_2, \ldots x_N$). A permutation of set S is a bijective (one-to-one) function $\pi : S \to S$. We can express π in a matrix form

$$\pi = \begin{pmatrix} 1 & 2 & \ldots & N \\ \pi(1) & \pi(2) & \ldots & \pi(N) \end{pmatrix} \quad \text{(C.34)}$$

which is useful in visually applying operations. There exists an identity permutation ε which just maps every element to itself again.

$$\varepsilon = \begin{pmatrix} 1 & 2 & \ldots & N \\ 1 & 2 & \ldots & N \end{pmatrix} \quad \text{(C.35)}$$

We can also evaluate group compositions between permutations π and σ such denoted $\pi\sigma = \pi \circ \sigma$. As an example, lets say we have a set $A = \{1, 2, 3, 4\}$ and the permutations π and σ defined as:

$$\pi = \begin{pmatrix} 1 & 2 & 3 & 4 \\ 1 & 3 & 4 & 2 \end{pmatrix} \quad , \quad \sigma = \begin{pmatrix} 1 & 2 & 3 & 4 \\ 4 & 1 & 2 & 3 \end{pmatrix}. \tag{C.36}$$

Let us find $\pi\sigma$ by going top-bottom and right-left fashion evaluating the mapping of each element one-by-one:

$$\pi\sigma = \begin{pmatrix} 1 & 2 & 3 & 4 \\ 1 & 3 & 4 & 2 \end{pmatrix} \begin{pmatrix} 1 & 2 & 3 & 4 \\ 4 & 1 & 2 & 3 \end{pmatrix} = \begin{pmatrix} 1 & 2 & 3 & 4 \\ 2 & 1 & 3 & 4 \end{pmatrix} \tag{C.37}$$

This was found by following through the mapping operations

$$1 \mapsto 4 \mapsto 2$$

$$2 \mapsto 1 \mapsto 1$$

$$3 \mapsto 2 \mapsto 3$$

$$4 \mapsto 3 \mapsto 4$$

which is the same procedure one would use to show that the identity returns the original permutation, i.e. $\pi\varepsilon = \varepsilon\pi = \pi$. For some permutation π there exists an inverse π^{-1} that satisfies $\pi\pi^{-1} = \pi^{-1}\pi = \varepsilon$. Let us use the previously defined π to demonstrate how one would find the inverse π^{-1}:

$$\pi^{-1}\pi = \begin{pmatrix} 1 & 2 & 3 & 4 \\ \pi^{-1}(1) & \pi^{-1}(2) & \pi^{-1}(3) & \pi^{-1}(4) \end{pmatrix} \begin{pmatrix} 1 & 2 & 3 & 4 \\ 1 & 3 & 4 & 2 \end{pmatrix} = \begin{pmatrix} 1 & 2 & 3 & 4 \\ 1 & 2 & 3 & 4 \end{pmatrix} \tag{C.38}$$

which gives us the mappings

$$1 \mapsto 1 \mapsto \pi^{-1}(1) = 1$$

$$2 \mapsto 3 \mapsto \pi^{-1}(3) = 2$$

$$3 \mapsto 4 \mapsto \pi^{-1}(4) = 3$$

$$4 \mapsto 2 \mapsto \pi^{-1}(2) = 4$$

hence

$$\pi^{-1} = \begin{pmatrix} 1 & 2 & 3 & 4 \\ 1 & 4 & 2 & 3 \end{pmatrix}. \tag{C.39}$$

To make a connection to the manipulations made in Eqns.(A.32) and (C.33) we should discuss the group of permutations that appears in our summations over π, where π is shorthand for π_i where i indexes the particular permutation. Lets consider $\pi_i \in \mathcal{S}_3$ where $\mathcal{S}_3$ contains all the permutations of the integers $1, 2$, and 3. The possible permutations can be expressed explicitly:

$$\pi_0 = \begin{pmatrix} 1 & 2 & 3 \\ 1 & 2 & 3 \end{pmatrix}, \ \pi_1 = \begin{pmatrix} 1 & 2 & 3 \\ 1 & 3 & 2 \end{pmatrix}, \ \pi_2 = \begin{pmatrix} 1 & 2 & 3 \\ 2 & 1 & 3 \end{pmatrix}, \ \pi_3 = \begin{pmatrix} 1 & 2 & 3 \\ 2 & 3 & 1 \end{pmatrix}, \ \pi_4 = \begin{pmatrix} 1 & 2 & 3 \\ 3 & 2 & 1 \end{pmatrix}, \ \pi_5 = \begin{pmatrix} 1 & 2 & 3 \\ 3 & 1 & 2 \end{pmatrix}$$
$$\text{(C.40)}$$

where it is apparent that $\pi_0 = \varepsilon$ (the identity permutation) and that there are $3!$ permutations of $\mathcal{S}_3$. The inverse permutations π^{-1} are easy to obtain by eye:

$$\pi_0^{-1} = \begin{pmatrix} 1 & 2 & 3 \\ 1 & 2 & 3 \end{pmatrix} = \pi_0 \,, \ \pi_1^{-1} = \begin{pmatrix} 1 & 2 & 3 \\ 1 & 3 & 2 \end{pmatrix} = \pi_1 \,, \ \pi_2^{-1} = \begin{pmatrix} 1 & 2 & 3 \\ 2 & 1 & 3 \end{pmatrix} = \pi_2 \qquad \text{(C.41)}$$

$$\pi_3^{-1} = \begin{pmatrix} 1 & 2 & 3 \\ 3 & 1 & 2 \end{pmatrix} = \pi_5 \,, \ \pi_4^{-1} = \begin{pmatrix} 1 & 2 & 3 \\ 3 & 2 & 1 \end{pmatrix} = \pi_4 \,, \ \pi_5^{-1} = \begin{pmatrix} 1 & 2 & 3 \\ 2 & 3 & 1 \end{pmatrix} = \pi_3 \qquad \text{(C.42)}$$

where we have extended the equations to show that all of the original permutations are collectively reproduced by the inverse permutations. We can use this to show that Eqn.(C.33) is true.

End interlude

Returning to the problem at hand we can now recognize that the sum over all permutations that belong to $\mathcal{S}_p$ will contain all of the inverse permutations as well. Consider again the case where we have $\mathcal{S}_3$. If we expand the sum over the permutations we get

$$\sum_{\substack{j_1,j_2,j_3 \\ \pi \in \mathcal{S}_3}} (-1)^\pi P^\dagger_{3,j_3} P^\dagger_{2,j_2} P^\dagger_{1,j_1} \tilde{P}_{j_{\pi(1)},1} \tilde{P}_{j_{\pi(2)},2} \tilde{P}_{j_{\pi(3)},3} = \sum_{j_1,j_2,j_3} \Big[(-1)^{\pi_0} P^\dagger_{3,j_3} P^\dagger_{2,j_2} P^\dagger_{1,j_1} \tilde{P}_{j_{\pi_0(1)},1} \tilde{P}_{j_{\pi_0(2)},2} \tilde{P}_{j_{\pi_0(3)},3}$$

$$+ (-1)^{\pi_1} P^\dagger_{3,j_3} P^\dagger_{2,j_2} P^\dagger_{1,j_1} \tilde{P}_{j_{\pi_1(1)},1} \tilde{P}_{j_{\pi_1(2)},2} \tilde{P}_{j_{\pi_1(3)},3} + (-1)^{\pi_2} P^\dagger_{3,j_3} P^\dagger_{2,j_2} P^\dagger_{1,j_1} \tilde{P}_{j_{\pi_2(1)},1} \tilde{P}_{j_{\pi_2(2)},2} \tilde{P}_{j_{\pi_2(3)},3}$$

$$+ (-1)^{\pi_3} P^\dagger_{3,j_3} P^\dagger_{2,j_2} P^\dagger_{1,j_1} \tilde{P}_{j_{\pi_3(1)},1} \tilde{P}_{j_{\pi_3(2)},2} \tilde{P}_{j_{\pi_3(3)},3} + (-1)^{\pi_4} P^\dagger_{3,j_3} P^\dagger_{2,j_2} P^\dagger_{1,j_1} \tilde{P}_{j_{\pi_4(1)},1} \tilde{P}_{j_{\pi_4(2)},2} \tilde{P}_{j_{\pi_4(3)},3}$$

$$+ (-1)^{\pi_5} P^\dagger_{3,j_3} P^\dagger_{2,j_2} P^\dagger_{1,j_1} \tilde{P}_{j_{\pi_5(1)},1} \tilde{P}_{j_{\pi_5(2)},2} \tilde{P}_{j_{\pi_5(3)},3}. \qquad \text{(C.43)}$$

Lets examine a couple of the terms in the expansion on the rhs of the above expression. First, notice that the most trivial term (the first term for π_0) contains a symmetry about its

indices which would remain even if we had swapped location of permutation in $(j_{\pi_0(i)}, i)$ with the ordinary particle index i and replaced the newly located permutation with its inverse as in $(j_{\pi_0(i)}, i) \to (j_i, \pi_0^{-1}(i))$. More explicitly with the first term, we have

$$\tilde{P}_{j_{\pi_0(1)},1}\tilde{P}_{j_{\pi_0(2)},2}\tilde{P}_{j_{\pi_0(3)},3} = \tilde{P}_{j_1,1}\tilde{P}_{j_2,2}\tilde{P}_{j_3,3} = \tilde{P}_{j_1,\pi_0^{-1}(1)}\tilde{P}_{j_2,\pi_0^{-1}(2)}\tilde{P}_{j_3,\pi_0^{-1}(3)} \tag{C.44}$$

Lets examine a term with a more varied permutation such as the term for π_3 (see Eqn.(C.40)).

$$\begin{aligned}
\tilde{P}_{j_{\pi_3(1)},1}\tilde{P}_{j_{\pi_3(2)},2}\tilde{P}_{j_{\pi_3(3)},3} &= \tilde{P}_{j_2,1}\tilde{P}_{j_3,2}\tilde{P}_{j_1,3} \\
&= \tilde{P}_{j_1,3}\tilde{P}_{j_2,1}\tilde{P}_{j_3,2} \\
&= \tilde{P}_{j_1,\pi_3^{-1}(1)}\tilde{P}_{j_2,\pi_3^{-1}(2)}\tilde{P}_{j_3,\pi_3^{-1}(3)}
\end{aligned} \tag{C.45}$$

As it happens, this will occur for all of the terms, and moreover, it will occur for any p in the context of $\pi_i \in \mathcal{S}_p : \forall\, i \in \{1, 2, \ldots, p\}$. Hence we have proved Eqn.(C.33). Moving forward, notice Eqn.(C.33) possesses matrix multiplication implicit in the notation of the sums over j_i. We have terms like $\sum_{j_i}^N P^\dagger_{\alpha_i,j_i}\tilde{P}_{j_i,\pi^{-1}(i)}$, which is simply equal to the element in the ith-row and $\pi^{-1}(i)$- column of the matrix formed by $\text{P}^\dagger\tilde{\text{P}}$. So we will use the expression

$$\sum_{j_i}^N P^\dagger_{\alpha_i,j_i}\tilde{P}_{j_i,\pi^{-1}(i)} = \left(\text{P}^\dagger\tilde{\text{P}}\right)_{i,\pi^{-1}(i)} \tag{C.46}$$

to rewrite the scalar product $\langle\psi|\tilde\psi\rangle$ as

$$\begin{aligned}
\langle\psi|\tilde\psi\rangle &= \sum_{\substack{j_1\ldots j_p \\ \pi \in \mathcal{S}_p}} (-1)^{\pi^{-1}} P^\dagger_{\alpha_p,j_p}\ldots P^\dagger_{\alpha_1,j_1}\tilde{P}_{j_1,\pi^{-1}(1)}\ldots\tilde{P}_{j_p,\pi^{-1}(p)} \\
&= \sum_{\pi \in \mathcal{S}_p} (-1)^{\pi^{-1}} \left(\text{P}^\dagger\tilde{\text{P}}\right)_{1,\pi^{-1}(1)}\ldots\left(\text{P}^\dagger\tilde{\text{P}}\right)_{p,\pi^{-1}(p)} \\
&= \sum_{\pi \in \mathcal{S}_p} (-1)^{\pi} \left(\text{P}^\dagger\tilde{\text{P}}\right)_{1,\pi(1)}\ldots\left(\text{P}^\dagger\tilde{\text{P}}\right)_{p,\pi(p)} \\
&= \det\left[\text{P}^\dagger\tilde{\text{P}}\right] \quad \text{q.e.d.}
\end{aligned} \tag{C.47}$$

Two comments should be made here: (1) The step from the second line to the third line is valid because both contain identical terms when expanded out, thus we may replace

the inverse permutations with the standard ones. (2) The third expression is precisely the *definition*[12] of the determinant of a matrix $P^\dagger \tilde{P}$.

With the completed lemmas above we are now ready to establish the relation

$$\text{Tr}\left[e^{\hat{c}^\dagger \hat{T}_1 \hat{c}} e^{\hat{c}^\dagger \hat{T}_2 \hat{c}} \ldots e^{\hat{c}^\dagger \hat{T}_n \hat{c}}\right] = \det\left[\mathbb{1} + e^{T_1} e^{T_2} \ldots e^{T_3}\right] \tag{C.48}$$

where the trace will be made over the Fock space $\mathcal{F}$. Conventionally, the following substitutions are made:

$$B = e^{T_1} e^{T_2} \ldots e^{T_N} \tag{C.49}$$

$$\hat{W} = e^{\hat{c}^\dagger \hat{T}_1 \hat{c}} e^{\hat{c}^\dagger \hat{T}_2 \hat{c}} \ldots e^{\hat{c}^\dagger \hat{T}_N \hat{c}}. \tag{C.50}$$

We may start with the determinant term and expand it to search for an expression that reveals equivalence to the trace evaluated in the space of $\mathcal{F}$.

$$
\begin{aligned}
\det[\mathbb{1} + B] &= \sum_{\pi \in \mathcal{S}_N} (-1)^\pi \, (\mathbb{1} + B)_{1,\pi(1)} \ldots (\mathbb{1} + B)_{N,\pi(N)} \\
&= \sum_{\pi \in \mathcal{S}_N} (-1)^\pi \left(\delta_{1,\pi(1)} + B_{1,\pi(1)}\right) \ldots \left(\delta_{N,\pi(N)} + B_{N,\pi(N)}\right) \\
&= \sum_{\pi \in \mathcal{S}_N} (-1)^\pi \left[\delta_{1,\pi(1)} \ldots \delta_{N,\pi(N)} + \sum_{i=1}^N B_{i,\pi(i)} \delta_{1,\pi(1)} \ldots \overline{\delta_{i,\pi(i)}} \ldots \delta_{N,\pi(N)} \right. \\
&\quad + \sum_{i<j}^N B_{i,\pi(i)} B_{j,\pi(j)} \delta_{1,\pi(1)} \ldots \overline{\delta_{i,\pi(i)}} \ldots \overline{\delta_{j,\pi(j)}} \ldots \delta_{N,\pi(N)} \\
&\quad + \sum_{i<j<k}^N B_{i,\pi(i)} B_{j,\pi(j)} B_{k,\pi(k)} \delta_{1,\pi(1)} \ldots \overline{\delta_{i,\pi(i)}} \ldots \overline{\delta_{j,\pi(j)}} \ldots \overline{\delta_{j,\pi(j)}} \ldots \delta_{N,\pi(N)} + \ldots \\
&\quad \left. \ldots + B_{1,\pi(1)} B_{2,\pi(2)} \ldots B_{N,\pi(N)} \right]
\end{aligned}
\tag{C.51}
$$

---

[12]We should recall the definitions for determinants and permanents of some $n \times n$ matrix M:

$$\det[M] \equiv \sum_{\pi \in \mathcal{S}_n} (-1)^\pi \, (M)_{1,\pi(1)} \ldots (M)_{n,\pi(n)}$$

$$\text{Per}[M] \equiv \sum_{\pi \in \mathcal{S}_n} (M)_{1,\pi(1)} \ldots (M)_{n,\pi(n)}$$

The last expression has some notation which can be further clarified:

- The sums with inequalities have condensed notation

$$\sum_{i<j}^{N} = \sum_{\substack{i=1 \\ j=2 \\ i<j}}^{N}, \quad \sum_{i<j<k}^{N} = \sum_{\substack{i=1,j=2 \\ k=3 \\ i<j<k}}^{N} \tag{C.52}$$

Note that inside the bracketed term of Eqn.(C.51), there are $(N-4)$ additional sums implied between the $+\ldots+$ after the i,j,k-term

- The wide over-bar on a Kronecker delta (e.g. $\overline{\delta_{i,\pi(i)}}$) indicate that the term is excluded from the product $\prod_{m=1}^{N} \delta_{m,\pi(m)}$ that appears in most terms of the expansion.

Attending to each term in Eqn.(C.51), we can evaluate as follows:

The first term is

$$\sum_{\pi \in \mathcal{S}_N} (-1)^{\pi} \delta_{1,\pi(1)} \ldots \delta_{N,\pi(N)} = 1 \tag{C.53}$$

where the identity permutation ε is the only π to contribute. Now we look at the second term, which is also easily simplified as

$$\sum_{\pi \in \mathcal{S}_N} (-1)^{\pi} \sum_{i=1}^{N} B_{i,\pi(i)} \delta_{1,\pi(1)} \ldots \overline{\delta_{i,\pi(i)}} \ldots \delta_{N,\pi(N)} = \sum_{i=1}^{N} B_{i,i},$$

since the only surviving permutation is again the identity permutation. A more interesting term is the one containing two matrix elements, where it is now possible for both the identity permutation $(\pi(i) = i, \pi(j) = j)$ and transposition permutations $(\pi(i) = j, \pi(j) = i)$ to survive the delta product. The transposition introduces a minus sign on its respective term due to the $(-1)^{\pi} = (-1)^{1}$ prefactor.

$$\sum_{\pi \in \mathcal{S}_N} (-1)^{\pi} \sum_{i<j}^{N} B_{i,\pi(i)} B_{j,\pi(j)} \delta_{1,\pi(1)} \ldots \overline{\delta_{i,\pi(i)}} \ldots \overline{\delta_{j,\pi(j)}} \ldots \delta_{N,\pi(N)}$$

$$= \sum_{i<j}^{N} (B_{i,i} B_{j,j} - B_{i,j} B_{j,i})$$

$$= \sum_{i<j}^{N} \det \left[\mathrm{P}_{(i,j)}^{\dagger} \mathrm{B} \mathrm{P}_{(i,j)} \right] \tag{C.54}$$

214

where $P_{(i,j)}$ is *defined* to be a rectangular matrix of dimension $N \times 2$ with entries of the first (second) column set to 1 at row i (j) and 0 otherwise. An example of this matrix is shown below.

$$
P_{(i,j)} = \begin{array}{cc} 1 & 2 \end{array} \\
\begin{pmatrix}
0 & 0 \\
0 & 0 \\
\vdots & \vdots \\
1 & 1 \\
\vdots & \vdots \\
1 & 1 \\
\vdots & \vdots \\
0 & 0
\end{pmatrix}
\begin{array}{l}
1 \\
2 \\
3:(i\text{-}1) \\
i \\
(i+1):(j\text{-}1) \\
j \\
(j+1):(N\text{-}1) \\
N
\end{array}
$$

The matrix multiplication $P_{(i,j)}^{\dagger} B P_{(i,j)}$ then yields a simple 2×2 matrix:

$$
P_{(i,j)}^{\dagger} B P_{(i,j)} = \begin{bmatrix} B_{i,i} & B_{i,j} \\ B_{j,i} & B_{j,j} \end{bmatrix} \tag{C.55}
$$

from which it becomes obvious that $\det\left[P_{(i,j)}^{\dagger} B P_{(i,j)} \right] = B_{i,i} B_{j,j} - B_{i,j} B_{j,i}$. This trend can continue with the next term with three matrix elements where the matrix $P_{(i,j)}$ becomes $P_{(i,j,k)}$, which is an $N \times 3$ matrix.

The new determinant bears resemblance to a form which invites the application of Eqn.(C.8) and Eqn.(C.27):

$$
\det\left[P^{\dagger} B P \right] = \det\left[P^{\dagger} \tilde{P} \right] = \langle \psi | \tilde{\psi} \rangle \tag{C.56}
$$

where we have used Eqn.(C.8) to enforce the finding that if P represents some $N \times p$ Slater determinant, and B is of the form $e^{T_1} e^{T_2} \dots e^{T_N}$ (as defined earlier) then BP is also a Slater determinant in which we denote by $\tilde{P}$. It then follows from the second lemma that this is simply equal to the overlap $\langle \psi | \tilde{\psi} \rangle$. Now we can resume looking at the $p = 2$-case with our

215

newly obtained relation in Eqn.(C.56). For purposes of generalization, we will change the previous notation for $P_{(i,j)}$ with $P_{(2)}$ such that for higher order terms with, say, p-particles we could write $P_{(p)}$

$$\det\left[P_{(2)}^\dagger B P_{(2)}\right] = \det\left[P_{(2)}^\dagger \tilde{P}_{(2)}\right] = \langle\psi_{(2)}|\tilde{\psi}_{(2)}\rangle = \langle\psi_{(2)}|\hat{W}|\psi_{(2)}\rangle = \langle 0|\hat{c}_i\hat{c}_j\hat{W}\hat{c}_j^\dagger\hat{c}_i^\dagger|0\rangle \quad \text{(C.57)}$$

where we used *lemma* 1 to equate $|\tilde{\psi}_{(2)}\rangle = \hat{W}|\psi_{(2)}\rangle$ and steps similar to what was seen in the equations leading to Eqn.(C.28) to get the last expression[13] Gathering all we have found thus far, we are equipped to present the final relations explicitly:

$$\det\left[\mathbb{1} + e^T\right] = \langle 0|0\rangle + \sum_i \langle 0|\hat{c}_i\hat{W}\hat{c}_i^\dagger|0\rangle + \sum_{i<j} \langle 0|\hat{c}_i\hat{c}_j\hat{W}\hat{c}_j^\dagger\hat{c}_i^\dagger|0\rangle + \sum_{i<j<k} \langle 0|\hat{c}_i\hat{c}_j\hat{c}_k\hat{W}\hat{c}_k^\dagger\hat{c}_j^\dagger\hat{c}_i^\dagger|0\rangle + \dots$$
$$\text{(C.58)}$$

which is recognized to be the definition of $\text{Tr}\left[\hat{W}\right]$ evaluated in $\mathcal{F}$. This concludes the proof of Eqn.(C.48).

---

[13]In this case all of the coefficients of the Slater determinant terms which we denoted P_{i,α_i} previously are equal to either 0 or 1 in this case. Hence the only surviving terms have a value of unity, and only their respective creation or annihilation operators are shown.

D   Self-consistent Migdal's Approximation

In this section, I will discuss the Feynman diagrams used in Migdal's approximation in the self-consistent formalism pioneered by Marsiglio [140]. The important difference between Ref. [140] and most of the treatments prior is the use of the full phonon propagator in the equations for the self-energy. This allows for electron and phonon self energy to be treated on equal footing, and includes renormalization effects. What follows is a simple assembly of the self energies based on the Feynman diagram rules. If anything, this short appendix could prove useful to students getting their feet wet with the approach.

D.1   Diagrams for the single-particle propagators:

Our desire is to calculate the one-electron Matsubara Green's function

$$\mathcal{G}_\sigma(\mathbf{k}, i\omega_n) = \left[i\omega_n - \epsilon_\mathbf{k} - \Sigma_\sigma(\mathbf{k}, i\omega_n)\right]^{-1}, \tag{D.1}$$

where $i\omega_n = i\pi T(2n-1)$ (with $n \in \mathbb{Z}$) are the fermion Matsubara frequencies and $\Sigma(\mathbf{k}, i\omega_n)$ is the electron self-energy due to the e-ph interaction[14]. We will use a diagrammatic approach for the propagators and susceptibilities and discuss the expressions associated with such diagrams. We first assemble Dyson's equations (diagrammatically) for both the electron and phonon (dressed) Green's functions starting with the propagators.

According to Fig.(D.1), the dressed electron Green's function $\mathcal{G}(\mathbf{k}, i\omega_n)$ is shown in a Dyson's equation for $\mathcal{G}$ in the Hartree-Fock approximation. The first non-interacting line, $\mathcal{G}_0(\mathbf{k}, i\omega_n)$, is the zeroth order term in the expansion. The other diagrams are the first order terms describing the electron self-energy $\Sigma(\mathbf{k}, i\omega_n)$ which utilize dressed propagators $\mathcal{G}$ and $\mathcal{D}$ in some places, a fact which makes the approximation a self-consistent one. The dressed phonon propagator in Fig.(D.2), $\mathcal{D}_\lambda(\mathbf{q}, i\nu_n)$, is written in using Dyson's equation whereby the zeroth-order line is just the non-interacting phonon Green's function $\mathcal{D}_0(\mathbf{q}, i\nu_n)$ and the

---

[14]The convention $k_B \equiv \hbar \equiv 1$ is used along with the expression of all energies in units of the hopping, t.

$$\underset{(\mathbf{k},\sigma,\mathrm{i}\omega_n)}{} = \underset{(\mathbf{k},\sigma,\mathrm{i}\omega_n)}{} + \underset{(\mathbf{k},\sigma,\mathrm{i}\omega_n)(\mathbf{k}',\sigma,\mathrm{i}\omega_{n'})(\mathbf{k},\sigma,\mathrm{i}\omega_n)}{\overset{(\mathbf{k}-\mathbf{k}',\lambda,\mathrm{i}(\omega_n-\omega_{n'}))}{}} + \underset{(\mathbf{k},\sigma,i\omega_n)(\mathbf{k},\sigma,\mathrm{i}\omega_n)}{\overset{(\mathbf{k}',\sigma',\mathrm{i}\omega_{n'})}{\underset{(0,\lambda,0)}{}}}$$

Figure D.1: Dressed electron Green's Function in Migdal-Eliashberg theory.

second term is the polarizability of interacting electrons, $\Pi(\mathbf{q}, i\nu_n)$. Note that λ is a phonon branch index.

The equations represented by figures (D.1) and (D.2) can be written explicitly as

$$\mathcal{G}_\sigma(\mathbf{k}, i\omega_n) = \mathcal{G}_\sigma^0(\mathbf{k}, i\omega_n) + \mathcal{G}_\sigma^0(\mathbf{k}, i\omega_n)\Sigma_\sigma(\mathbf{k}, i\omega_n)\mathcal{G}_\sigma(\mathbf{k}, i\omega_n) \tag{D.2}$$

and

$$\mathcal{D}_\lambda(\mathbf{q}, i\nu_n) = \mathcal{D}_\lambda^0(\mathbf{k}, i\nu_n) + \mathcal{D}_\lambda^0(\mathbf{k}, i\nu_n)\Pi_\lambda(\mathbf{q}, i\nu_n)\mathcal{D}_\lambda(\mathbf{q}, i\nu_n), \tag{D.3}$$

respectively. These expressions have the form $x = a + ab(x)x$, which can be partially solved for x :

$$x = a + ab(x)x \implies x = \frac{a}{1 - ab(x)} = \frac{1}{a^{-1} - b(x)}, \tag{D.4}$$

whereupon substitution of the actual Green's functions and self-energies gives

$$\mathcal{G}_\sigma(\mathbf{k}, i\omega_n) = [i\omega_n - \epsilon_\mathbf{k} - \Sigma_\sigma(\mathbf{k}, i\omega_n)]^{-1} \tag{D.5}$$

for the electron Greens's function (as seen before) and

$$\mathcal{D}_\lambda(\mathbf{q}, i\nu_n) = \left[\left((i\nu_n)^2 - (\Omega_{\mathbf{q},\lambda})^2\right)/(2\Omega_{\mathbf{q},\lambda}) - |M_{\mathbf{q},\lambda}|^2\Pi_\lambda(\mathbf{q}, i\nu_n)\right]^{-1} \tag{D.6}$$

for the phonon propagator. To arrive at the above expressions, we used the Matsubara form of the non-interacting Green's functions $\mathcal{G}_0$ and $\mathcal{D}_0$ for electrons and phonons, respectively:

$$\mathcal{G}_0(\mathbf{k}, i\omega_n) = \frac{1}{i\omega_n - \epsilon_\mathbf{k}} \tag{D.7}$$

and

$$\mathcal{D}_\lambda^0(\mathbf{q}, i\nu_n) = \frac{2\Omega_{\mathbf{q},\lambda}}{(i\nu_n)^2 - (\Omega_{\mathbf{q},\lambda})^2} . \tag{D.8}$$

The non-interacting Hamiltonian for free electrons is $\hat{H} = \sum_\mathbf{k} \epsilon_\mathbf{k}\hat{c}_\mathbf{k}^\dagger\hat{c}_\mathbf{k}$ where the band dispersion shifted by a chemical potential μ is $\epsilon_\mathbf{k} = \epsilon_\mathbf{k}^0 - \mu$. Analogously, the phonon non-interacting Hamiltonian $\hat{H} = \sum_\mathbf{q} \Omega_\mathbf{q}\hat{a}_\mathbf{q}^\dagger\hat{a}_\mathbf{q}$ and associated phonon dispersion $\Omega_\mathbf{q}$ plays the same role in the non-interacting propagator.

Figure D.2: Dressed phonon Green's Function in Migdal-Eliashberg theory.

Feynman Rules for e-ph Interaction

When treating the e-ph interaction as a perturbation, we can expand the electron Green's Function to various orders in that perturbation. The thermal average of the product of an odd number of phonon field operators $\hat{\phi}_{\mathbf{q},\lambda}(\tau) = e^{\hat{H}\tau}\hat{\phi}_{\mathbf{q},\lambda}(0)e^{-\hat{H}\tau}$, where $\hat{\phi}_{\mathbf{q},\lambda}(0) = \hat{a}_{\mathbf{q},\lambda} + \hat{a}^{\dagger}_{-\mathbf{q},\lambda}$, yields zero, and thus we only have even orders of the expansion that survive. One can derive the rules by using Wick's theorem to evaluate the various propagator arrangements, but we will only cite the rules here:

1. Draw all the topologically distinct diagrams with N_{ph} lines, with two external electron lines and $(2N_{ph} - 1)$ internal electron lines at order $2N_{ph}$ in the e-ph interaction.

2. For each normal electron line of coordinates $(\mathbf{k}, \sigma, i\omega_n)$, assign a non-interacting Green's function $\mathcal{G}^0_{\sigma}(\mathbf{k}, i\omega_n)$. For each double electron line of coordinates $(\mathbf{k}, \sigma, i\omega_n)$, assign a dressed Green's function $\mathcal{G}_{\sigma}(\mathbf{k}, i\omega_n)$.

3. For each normal phonon line of coordinates $(\mathbf{q}, \lambda, i\nu_n)$, assign a product of the non-interacting phonon Green's function and coupling matrix element, $|M_{\mathbf{q},\lambda}|^2\mathcal{D}^0_{\lambda}(\mathbf{q}, i\nu_n)$. For each double phonon line of coordinates $(\mathbf{q}, \lambda, i\nu_n)$, assign a product of the dressed phonon Green's function and matrix element $|M_{\mathbf{q},\lambda}|^2\mathcal{D}_{\lambda}(\mathbf{q}, i\nu_n)$.

4. At each vertex, conserve momentum (wave vector), frequency, and spin with delta functions.

5. Sum over all internal coordinates.

6. Multiply each fermion (electron) loop by -1.

7. Multiply by the factor $\left(\frac{1}{\hbar}\right)^{2N_{ph}} \left(\frac{-1}{\beta\hbar}\right)^{N_{ph}}$

With all of the rules summarized, we can now construct the proper mathematical equivalents to the Feynman diagrams in the figures. In the next section, we will start with the electron propagator.

Interacting Electron Green's Function $\mathcal{G}$

Examining Fig.(D.1) and Eqn.(D.2) reveals that the internal diagrams are described completely by the self energy $\Sigma_\sigma(\mathbf{k}, i\omega_n)$, which comes in two parts. The first diagram represents the self-consistently renormalized electron self energy due to e-ph scattering processes completely categorized by "rainbow" diagrams. The second term is known as the Hartree contribution to the self-energy, and it represents a sort of mean-field interaction with the background. Let us apply the rules for the diagrams starting with the first one on the rhs:

1. There is only one dressed phonon line, hence $N_{ph} = 1$.

2. The internal dressed electron propagator gives us a $\mathcal{G}_{\sigma'}(\mathbf{k}', i\omega_{n'})$.

3. The internal dressed phonon propagator yields $|M_{\mathbf{q},\lambda}|^2 \mathcal{D}_\lambda(\mathbf{q}, i\nu_{n''})$.

4. We need to conserve spin, momentum, and frequency at the vertices with appropriate delta functions:

   - spin conservation with incoming σ and internal σ' implies $\delta_{\sigma,\sigma'}$,

   - momentum conservation with incoming $\mathbf{k}$, outgoing (internal electron) $\mathbf{k}'$, and outgoing (internal phonon) $\mathbf{q}$ is expressed as $\mathbf{k} - \mathbf{k}' - \mathbf{q} = 0 \implies \delta_{(\mathbf{k}-\mathbf{k}'),\mathbf{q}}$.

   - The frequency conservation at the first vertex yields $i(\omega_n - \omega_{n'} - \nu_{n''}) = 0$ such that $\delta_{(\omega_n-\omega_{n'}),\nu_{n''}}$.

5. We now need to sum over all the internal coordinates, thus we will have $\sum_{\mathbf{k}',\sigma'} \sum_{\mathbf{q},\lambda} \sum_{n',n''}$.

6. There are no electron loops in the diagram, so $F = 0$ and thus this prefactor is $(-1)^F = 1$.

7. Lastly, since $N_{ph} = 1$, we will have a prefactor contribution of $(1/\hbar)^2(-1/\beta\hbar) = (-1/\beta\hbar^3)$.

Figure D.3: Dressed electron Green's Function showing self-energy explicitly.

Now we are in a position to assemble the first diagram depicted in Fig.(D.3):

$$\Sigma_\sigma^M(\mathbf{k}, i\omega_n) = \frac{-1}{\beta\hbar^3} \sum_{\mathbf{k}',\sigma'} \sum_{\mathbf{q},\lambda} \sum_{n',n''} |M_{\mathbf{q},\lambda}|^2 \mathcal{D}_\lambda(\mathbf{q}, i\nu_{n''}) \mathcal{G}_{\sigma'}(\mathbf{k}', i\omega_{n'}) \delta_{\sigma,\sigma'} \delta_{(\mathbf{k}-\mathbf{k}'),\mathbf{q}} \delta_{(\omega_n - \omega_{n'}),\nu_{n''}} \,, \quad \text{(D.9)}$$

which can be further reduced after application of all of the delta functions

$$\Sigma_\sigma^M(\mathbf{k}, i\omega_n) = \frac{-1}{\beta\hbar^3} \sum_{\mathbf{k}'} \sum_{\lambda,n'} |M_{\mathbf{k}-\mathbf{k}',\lambda}|^2 \mathcal{D}_\lambda(\mathbf{k} - \mathbf{k}', i(\omega_n - \omega_{n'})) \mathcal{G}_\sigma(\mathbf{k}', i\omega_{n'}) \,. \quad \text{(D.10)}$$

This term accounts for the contribution of certain types of scatterings between electrons and phonons in the fully renormalized case. We will revisit this term later to discuss it further, but for now we will evaluate the second self-energy contribution given by the balloon-like diagram in Fig.(D.3).

The second diagram is often referred to as the Hartree self-energy term $\Sigma_\sigma^H(\mathbf{k}, i\omega_n)$, from Hartree-Fock mean field theory. Before we stripped the external fermion lines from the internal part, we actually had the so-called Hartree diagram $\mathcal{G}_\sigma^H(\mathbf{k}, i\omega_n)$, which is 0 particular cases where: (i) if we didn't include the $\mathbf{q} = 0$ vector, since it corresponds to infinite wavelength (moving entire crystal), and (ii) if the phonon line was instead a Coulomb line, and we had a charge compensating background. To be clear, the diagram is not equal to zero in magnitude, rather it is momentum and energy independent. This independence makes the term a simple constant, and thus it is common to simply absorb it into the definition chemical potential μ. The vertical self-closing electron line is sometimes called a non-propagating line[15], and it means that we must include a convergence factor $\exp(i\omega_{n'}\eta^+)$ when translating these lines into functions. The factor η^+ is a positive infinitesimal such that its product with infinity is still infinite ($\eta^+ \cdot \infty = \infty$). If we assemble the terms according to the rules, then the diagram yields:

1. There is one phonon line, hence $N_{ph} = 1$.

2. The internal non-propagating dressed electron propagator gives us a $\mathcal{G}_{\sigma'}(\mathbf{k}', i\omega_{n'}) \exp(i\omega_{n'}\eta^+)$.

---

[15]This happens if same-time operators are contracted. The circular line emerges from and reenters the same vertex.

3. The internal free phonon propagator yields $|M_{0,\lambda}|^2 \mathcal{D}_\lambda^{(0)}(0,0)$.

4. In this case, no additional conservation needs to be added via delta functions. This is due to the fact that vertices all occur at the same time (or imaginary time).

5. We now need to sum over all the internal coordinates, thus we will have $\sum_{\mathbf{k}',\sigma'} \sum_\lambda \sum_{n'}$

.

6. There is one electron loop in the diagram, so $F = 1$ and thus this prefactor is $(-1)^1 = -1$.

7. Lastly, since $N_{ph} = 1$, we will have a prefactor contribution of $(1/\hbar)^2(-1/\beta\hbar) = (-1/\beta\hbar^3)$.

Putting all the pieces together gives us the second self-energy contribution

$$\Sigma^H(\mathbf{k}, i\omega_n) = \frac{2}{\beta\hbar^3} \sum_{\mathbf{k}',n'} \sum_\lambda |M_{0,\lambda}|^2 \mathcal{D}_\lambda^{(0)}(0,0) \mathcal{G}(\mathbf{k}', i\omega_{n'}) e^{i\omega_{n'}\eta^+} \tag{D.11}$$

where the factor of 2 arises from the sum over spin. In its current form, Eqn.(D.11) can be further modified by examining the sum over n' given by

$$\frac{1}{\beta\hbar} \sum_{n'} \mathcal{G}(\mathbf{k}', i\omega_{n'}) e^{i\omega_{n'}\eta^+} . \tag{D.12}$$

The positive infinitesimal η^+ is related to the negative infinitesimal η^- via $\eta^+ = -\eta^-$, and thus we can write the expression above as one that looks like a Fourier transform to imaginary time $\tau^- = \eta^-$:

$$\frac{1}{\beta\hbar} \sum_{n'} \mathcal{G}(\mathbf{k}', i\omega_{n'}) e^{-i\omega_{n'}\eta^-} = \mathcal{G}(\mathbf{k}', \tau^-; \mathbf{k}', 0) \tag{D.13}$$

where $\mathcal{G}(\mathbf{k}', \tau^-; \mathbf{k}', 0)$ is usually evaluated with a thermal trace

$$\mathcal{G}(\mathbf{k}', \tau^-; \mathbf{k}', 0) = -\mathrm{Tr}\left[e^{\beta(\hat{\Omega}-\hat{H})} \hat{T}_\tau \left\{\hat{c}_{\mathbf{k}'}(\tau^-) \hat{c}_{\mathbf{k}'}^\dagger(0)\right\}\right] . \tag{D.14}$$

The respective fermion creation and annihilation operators $\hat{c}^{\dagger}_{\mathbf{k}'}(\tau)$ and $\hat{c}_{\mathbf{k}'}(\tau)$ have an imaginary time dependence given in the Heisenberg representation, as in $\hat{c}^{\dagger}_{\mathbf{k}'}(\tau) = \mathrm{e}^{\hat{\mathsf{H}}\tau}\hat{c}^{\dagger}_{\mathbf{k}'}\mathrm{e}^{-\hat{\mathsf{H}}\tau}$ where $\hat{\mathsf{H}} = \hat{H} - \mu\hat{N}$ and the thermodynamic potential Ω appears as a trivial operator $\hat{\Omega} \equiv \hat{\mathbb{1}} \cdot \Omega$. The imaginary time ordering operator $\hat{T}_{\tau}$ orders the smallest τ (closest to $-\beta$) to the rightmost position, and orders the remaining terms leftward from least to greatest (e.g. $\hat{T}_{\tau}\{f_1(\tau_1)f_2(\tau_2)\} = f_2(\tau_2)f_1(\tau_1)$ for $\tau_1 < \tau_2$) Lets work out the trace operation:

$$
\begin{aligned}
\mathcal{G}(\mathbf{k}', \tau^-; \mathbf{k}', 0) &= -\mathrm{Tr}\left[\mathrm{e}^{\beta(\hat{\Omega}-\hat{\mathsf{H}})}\hat{T}_{\tau}\left\{\hat{c}_{\mathbf{k}'}(\tau^-)\hat{c}^{\dagger}_{\mathbf{k}'}(0)\right\}\right] \\
&= \mathrm{Tr}\left[\mathrm{e}^{\beta(\hat{\Omega}-\hat{\mathsf{H}})}\hat{c}^{\dagger}_{\mathbf{k}'}(0)\hat{c}_{\mathbf{k}'}(\tau^-)\right] \\
&= \mathrm{e}^{\beta\Omega}\mathrm{Tr}\left[\mathrm{e}^{-\beta\hat{\mathsf{H}}}\hat{c}^{\dagger}_{\mathbf{k}'}\mathrm{e}^{\hat{\mathsf{H}}\tau^-}\hat{c}_{\mathbf{k}'}\mathrm{e}^{-\hat{\mathsf{H}}\tau^-}\right] .
\end{aligned}
$$

Now we can take the limit as τ^- goes to zero:

$$
\begin{aligned}
\left.\mathcal{G}(\mathbf{k}', \tau^-)\right|_{\tau^-=0} &= \mathrm{e}^{\beta\Omega}\mathrm{Tr}\left[\mathrm{e}^{-\beta\hat{\mathsf{H}}}\hat{c}^{\dagger}_{\mathbf{k}'}\hat{c}_{\mathbf{k}'}\right] = \left\langle\hat{c}^{\dagger}_{\mathbf{k}'}\hat{c}_{\mathbf{k}'}\right\rangle = n_f(\epsilon_{\mathbf{k}'}) && \text{(D.15)} \\
\text{or alternatively } &= \mathrm{e}^{\beta\Omega}\mathrm{Tr}\left[\mathrm{e}^{-\beta\hat{\mathsf{H}}}\left(\hat{\mathbb{1}} - \hat{c}_{\mathbf{k}'}\hat{c}^{\dagger}_{\mathbf{k}'}\right)\right] \\
&= \mathrm{e}^{\beta\Omega}\underbrace{\mathrm{Tr}\left[\mathrm{e}^{-\beta\hat{\mathsf{H}}}\right]}_{\mathrm{e}^{-\beta\Omega}} - \mathrm{e}^{\beta\Omega}\mathrm{Tr}\left[\mathrm{e}^{-\beta\hat{\mathsf{H}}}\hat{c}_{\mathbf{k}'}\hat{c}^{\dagger}_{\mathbf{k}'}\right] \\
&= 1 - \left\langle\hat{c}_{\mathbf{k}'}\hat{c}^{\dagger}_{\mathbf{k}'}\right\rangle \\
&= \mathcal{G}^0(\mathbf{k}', 0^+) + 1 , && \text{(D.16)}
\end{aligned}
$$

where the last step utilized the relation $\mathcal{G}^0(\mathbf{k}', \tau = 0^+) = -\left\langle\hat{c}_{\mathbf{k}'}\hat{c}^{\dagger}_{\mathbf{k}'}\right\rangle$. If we use the result that $\left.\mathcal{G}(\mathbf{k}', \tau^-)\right|_{\tau^-=0} = n_f(\epsilon_{\mathbf{k}'})$ in the self energy expression that remains, we obtain a sum over $\mathbf{k}'$ across the Fermi-distribution $n_f(\epsilon_{\mathbf{k}'})$:

$$
\begin{aligned}
\Sigma^H(\mathbf{k}, \mathrm{i}\omega_n) &= \frac{2}{\hbar^2}\sum_{\lambda}|M_{0,\lambda}|^2\mathcal{D}^{(0)}_{\lambda}(0, 0)\sum_{\mathbf{k}'}n_f(\epsilon_{\mathbf{k}'}) \\
&= \frac{N}{\hbar^2}\sum_{\lambda}|M_{0,\lambda}|^2\mathcal{D}^{(0)}_{\lambda}(0, 0).
\end{aligned}
$$

As one can see, the Hartree contribution is independent of momentum and frequency and related to the number of fermions in the system.

Vita

Philip M. Dee was born and raised in Northeast Ohio. He attended Cleveland State University, attaining a B.Sc. in Physics and a B.E. in civil engineering in 2013. After a year of Master's research at the same university, Phil and his wife Hannah left for Knoxville, where Phil began work toward a Ph.D. in physics at The University of Tennessee. In late 2016, he began research in the group of Professor Steve Johnston on models of superconductivity and electron-phonon coupling. Phil received two awards for teaching and was granted an SCGSR fellowship from the Department of Energy in fall 2018. He spent much of his later Ph.D. working with Thomas Maier at Oak Ridge National Lab and has four published papers with several more in preparation. In early May of 2021, Phil will receive his Ph.D. and begin a postdoctoral appointment with Professors Peter Hirschfeld and Richard Hennig at the University of Florida with a primary focus on discovering new superconductors.